Final Report

Project Title:	"Development of Ultra-Low Platinum Alloy Cathode Catalysts for PEM Fuel Cells"
Project Period:	September 01, 2010 - Dec 31, 2015
Reporting Date:	January 7, 2016
Company Address:	University of South Carolina Research Foundation 301 Main St. Department of Chemical Engineering, University of South Carolina, Columbia, SC 29208.
Award Number:	DE-EE0000460
Working Partners:	Dr. Branko N. Popov (PI) (University of South Carolina)
	Dr. John Weidner (Co-PI) (University of South Carolina)
Cost-Sharing Partners:	University of South Carolina
Contact: Tel: FAX: E-mail:	Branko N. Popov (803) 777-7314 (803) 777-8265 popov@cec.sc.edu
DOE Manger: Phone: Email:	Donna Lee Ho (202) 586-8000 Donna.Ho@ee.doe.gov
Project Officer/Manager: Phone: E-Mail:	Peterson David (720) 356-1747 david.peterson@go.doe.gov
Project Monitor: Phone: E-Mail:	Cierpik Kim (720) 356-1266 kim.cierpik@go.doe.gov

Financial Assistance Contacts

Contract Officer/Manager: Phone: E-Mail:	Wilson Todd (720) 356-1815 todd.wilson@go.doe.gov
Contract Specialist: Phone: E-mail:	Nucci Thomas (303) 275-6040 thomas.nucci@go.doe.gov

1. Introduction

Polymer electrolyte membrane fuel cells (PEMFCs) are attractive power sources of the future for variety of applications including portable electronics, stationary power, and electric vehicles. However, sluggish cathode kinetics, high Pt cost, and durability issues inhibit the use of PEMFCs for automobile applications [1, 2]. A number of factors contribute to the performance degradation of PEMFCs including catalyst dissolution [3-8], catalyst sintering [7, 9], membrane degradation [10-12], and carbon support corrosion [13-17]. The current progress in support development, Pt-alloy catalyst development, and effect of Pt loading on the catalyst mass and specific activities reported in the literature is summarized below.

1.1. Literature Overview of Progress in Support Development

High surface area carbon (HSAC) is widely used as the catalyst support to improve Pt utilization because of its good electrical conductivity, pore structure suitable for Pt anchorage, high-surface-area for uniform Pt particle dispersion, easy availability, and low cost [18, 19]. However, many studies have shown that HSAC has low resistance towards thermal and electrochemical oxidation because of the HSAC structure containing mainly amorphous carbon and a small portion of plane graphite carbon, which has an abundance of dangling bonds and defects [20]. The dangling bonds can easily form surface oxides, which results in a higher corrosion rate under electrochemical oxidation.

To improve the electrochemical stability of the carbon support and overall Pt/C catalyst, new carbon materials have been tested as supports for PEMFC, including nano-diamonds [21-23], carbon nanotubes (CNT) [24-26], carbon nanofibers (CNF) [25, 27, 28], carbon nanocages (CNC) [27, 29], graphene [30, 31], etc. These carbon materials have shown enhanced thermal and electrochemical stability due to higher degree of graphitization of carbon and inert surface structures toward carbon oxidation [24]. However, these properties also act as drawbacks in the preparation of Pt/C catalysts since they do not provide proper active sites for Pt deposition. Furthermore, hydrophobic nature of their surfaces impedes dispersion in a polar solvent thus preventing the Pt deposition on the surfaces [28]. It may cause difficulty in controlling the particle size, uniform distribution of Pt particles, and achieving high metal loading, which results in low activity of catalysts [32].

In order to enhance Pt deposition on these carbons, a surface functionalization is required, which makes the catalyst preparation more complex and increases the cost. In addition, after attaching the functional groups on carbons, the surface properties are usually changed which results in a decrease in the stability of functionalized material [28]. Relatively high cost of the alternative carbon supports is another huge obstacle although the cost of these materials has fallen continuously in recent years [33].

To examine the electrochemical stability of carbon support material in PEMFC condition, various methods have been suggested [34]. Generally, it is required to operate more than 5000 h to apply PEMFCs to the automotive application [35]. However, it is impractical and inefficient to estimate the stability under practical conditions because of long testing time and cost. The U.S. Department of Energy (DOE), U.S. Fuel Cell Council (USFCC), and the Fuel Cell Commercialization Conference of Japan (FCCJ) proposed several effective accelerated stress test (AST) methods to test the stability of Pt-based catalysts [36-39]. A good AST method should meet several conditions: (i) relatively short testing time, (ii) good selectivity of carbon degradation, and (iii) good degradation behavior of fuel cell performance [40]. To establish appropriate AST protocol to meet all the conditions mentioned above, it is important to understand the mechanism of carbon corrosion at various potential regions and potential profiles (constant potential, triangular cycling, rectangular cycling, etc).

Reiser et al. suggested that a cathode interfacial potential difference increases up to ~1.5 V due to the "H_2/air front" mechanism in the case of start-up/shut-down process [41]. The same phenomenon also occurs in the case of local hydrogen starvation in the MEA [42]. Furthermore, it has been shown that the cathode potential behavior follows a triangular change with the maximum potential of ~1.5 V when H_2 introduced to the anode compartment [39]. Recently, Hashimasa et al. studied the effects of the potential waveform on carbon corrosion rate by comparing 1.3 V constant potential and 0.9-1.3 V potential [40]. If the carbon corrosion is only affected by high potential, holding the potential at high value would show high carbon corrosion rate. However, the carbon corrosion rate of 0.9-1.3 V potential cycling was higher than that of 1.3 V constant potential. Park et al. proposed the reason of this phenomenon that de-passivated Pt at the lower potential catalyzes carbon corrosion when potential is increased [43]. The result shows that the potential cycling is more effective than potential holding to test carbon corrosion. But there is still an issue about the lower potential limit of potential cycling; lower potentials

than 0.9 V in the potential cycling would also result in Pt degradation through the Pt oxidation and reduction processes [44]. Therefore, the performance loss by carbon corrosion and the one by Pt degradation will be mixed resulting in the poor selectivity of carbon support degradation.

Thus, the potential above 1.0 V at which Pt is passivated all the time should be used as the lower potential limit of a potential cycling test to study the carbon support stability without the contribution of Pt degradation. According to these studies, the potential cycling between 1.0 and 1.5 V would be a good AST protocol to test the carbon support stability in PEMFC. Actually, the FCCJ suggested a potential cycling protocol (1.0-1.5 V, 5000 cycles, 500 mV s−1) to test the support stability in 2011 [39], and the U.S. DOE revised their previous protocol (1.2 V constant potential for 400 h) with the same protocol as the FCCJ in 2013 [45]. This protocol also reduces the testing time (2 sec cycle−1, < 3 h total). Mukundan reported the comparison of the old protocol (1.2 V constant potential for 400 h) and the new protocol (1.0-1.5 V, 5000 cycles, 500 mV s−1) of U.S. DOE [46]. It was observed that 200 h constant potential at 1.2 V is equivalent to 2000 cycles at 1.0-1.5 V. According to the result, the author concluded that the new protocol could reduce the testing time significantly (~100 times) when compared to the old protocol with the same performance decay.

1.2. Literature Overview of Progress in Pt-based Cathode Catalyst Development

Durability, cost, and performance are the key issues for the commercialization of polymer electrolyte membrane fuel cells (PEMFCs) for variety of applications including portable electronics, automotive and stationary power. Platinum, due to its low overpotential and high catalytic activity, is currently used in PEMFCs for hydrogen oxidation at the anode and oxygen reduction reaction (ORR) at the cathode [47]. However, high-cost and limited supply of Pt together with its sluggish ORR kinetics triggered the research and development of various Pt-alloy cathode catalysts such as Pt-Fe, Pt-Co, Pt-Ni, and Pt-Cr [3, 48-52]. The requirements for fuel cell lifetime significantly vary for different applications; 5,000 h for cars, 20,000 h for buses, and 40,000 h of continuous operation for stationary applications [4].

One of the efforts in achieving increased catalytic activity is by alloying Pt with 3d transition metals to obtain high mass activity at 0.9 $V_{iR\text{-}free}$ for oxygen reduction reaction (ORR) [48, 53-57]. In PEMFCs, Pt-alloys with various transition metals such as Cr, Co, Ni, etc. have been extensively studied and shown superior electrocatalytic activity for the ORR when compared to pure Pt [49, 55-58]. The enhancement in measured activity over Pt by alloying Pt

with transition metals is due to various factors including lowering of the Pt oxidation state [26], suppression of Pt oxide formation [59, 60], formation of a new electronic structure with higher Pt 5d orbital vacancies [53], decrease in the Pt-Pt interatomic distance and therefore a more favorable O_2 adsorption [53], formation of a thin Pt skin on the surface of the alloy core [61-63], and the altered electronic structures of the topmost Pt atoms [55, 56, 64].

Amongst the Pt-alloy catalysts, the PtCo catalyst has attracted much attention due to its high activity and stability in acidic environment [49, 65]. Paulus et al. studied the bulk compositions of 50 and 75 at. % Pt with Ni and Co as alloying elements [54, 66]. In comparison to pure Pt, the results revealed a small activity enhancement of ca. 1.5 times for the 25 at. % Ni and Co catalysts, and a more significant enhancement by a factor of 2-3 for the 50 at.% Co. Huang et al. showed that PtCo alloy nanoparticles exhibit measured activity and specific activity enhancements by a factor of ~1.3-3.2 and ~1.2−2.2, respectively for the ORR when compared to pure Pt [67]. Antolini et al. reviewed the catalyst activity and stability, and concluded that PtCr and PtCo are more stable than PtV, PtNi, and PtFe due to their high degree of alloying and particle size [49]. Jayasayee et al. studied the activity and durability of PtCo, PtNi, and PtCu in PEMFC cathodes as a function of alloying elements in a systematic manner [57]. They showed that the performance of PtCo and PtCu catalysts was found to be most attractive when compared to PtNi and Pt catalysts. Mani et al. investigated the activity of dealloyed PtCu, PtCo, and PtNi in PEMFCs [58]. They found that Pt-alloy with Co and Cu are more active than PtNi. Mass and specific activities of PtCo and PtCu were enhanced by a factor of 3–4 times, compared to the commercial Pt/C catalyst.

Platinum based catalysts dissolve during fuel cell operation when the cathode is subjected to potential cycles [68-73]. Pt dissolution occurs in a narrow potential and pH window near 1.0 V vs. RHE [68, 69] A kinetic model developed by Darling and Meyers [70] indicates that platinum dissolution in PEMFC is negligible at low and high potentials but significantly large at intermediate potentials. The effect of potential on Pt dissolution was explained by considering three possible reactions:

$$Pt \rightarrow Pt^{2+} + 2e^- \quad (1)$$

$$Pt + H_2O \rightarrow PtO + 2H^+ + 2e^- \quad (2)$$

$$PtO + 2H^+ \rightarrow Pt^{2+} + H_2O \quad (3)$$

The model showed that the equilibrium concentration of dissolved Pt decreased between 1.1 and 1.5 V due to the formation of passivating oxides at high potentials [70].

Accelerated durability test (ADT) and accelerated stress test (AST) have been used to evaluate the durability of Pt and Pt-alloy catalysts since it allows degradation in the catalyst activity to be observed within several days, rather than several weeks otherwise required before any significant decrease in fuel cell performance is noticed [74]. A large number of studies have been reported in the literature for the degradation of Pt and Pt-alloy cathode catalysts using RRDE in three-electrode cell [75-87] and MEA [2, 88-97]. The losses in catalyst mass activity (in A/mg_{Pt}) measured at 0.9 $V_{iR\text{-}free}$, electrochemical surface area (ECSA, in m^2/g_{Pt}), and fuel cell performance under H_2-O_2 or H_2-air were used to evaluate the catalyst stability. The catalyst durability studies using three-electrode electrochemical cell in flooded electrolyte is very different from the actual fuel cell operating conditions and they provide only a fundamental understanding of Pt-based catalysts' degradation under potential cycling conditions. A more reliable means of acquiring in-depth knowledge would be the performance evaluation of Pt and Pt-alloy catalysts in MEAs subjected to potential cycling experiment and measuring the decay in mass activity, ECSA loss, and H_2-air fuel cell performance. The Pt/C catalyst stability in PEMFCs has been reported in the literature by measuring the fuel cell performance under H_2-air [90-94] or under H_2-O_2 [95, 96]. The fuel cell performances were evaluated after subjecting to triangular wave cycling (TWC) [90-92, 95, 96] or square wave cycling (SWC) [90, 93, 94]. The potential cycling experiments were performed either under H_2-N_2 [90-93, 95, 96] or under H_2-air [94] supplied to the anode and cathode compartments, respectively.

The durability of carbon-supported PtCo catalysts is the core advantage as cathode catalysts in PEMFCs. Yu et al. studied the durability of Pt/C and PtCo/C cathode catalysts with continuous water fluxing on the cathode under a potential cycling test between 0.87 and 1.2 V vs. RHE [88]. The authors found that cobalt dissolution neither detrimentally reduced the cell voltage nor dramatically affected the membrane conductance. Cell performance enhancement by PtCo/C over Pt/C catalyst was sustained over 2400 cycles and the overall performance loss of the PtCo/C membrane electrode assemblies (MEAs) was less than that of the Pt/C MEA.

Uchimura et al [89] suggested a hypothesis to attribute the higher dissolution under higher anodic sweep rates to the lower coverage of Pt with oxides which exposed bare Pt to high

potentials. Other durability studies such as particle size effect [90] Pt loading effect [91] and the effect of nature of solvent used for making the catalyst ink [92] have also been reported.

Arico et al. reported the performance and durability of carbon-supported PtCo under high temperature (110-130 °C) operation in PEMFCs [98]. A potential cycling test at 130 °C in a pressurized PEMFC showed a better stability for the PtCo alloy than pure Pt/C. Furthermore, better performance was obtained at high temperatures for the pre-leached PtCo/C than the Pt/C catalyst. They observed that the amount of Pt oxides on the outermost atomic layers was much smaller in PtCo than in Pt catalyst. These characteristics appeared to influence catalysts' performance and durability. Stassi et al. investigated the effect of thermal treatment on the structure and surface composition of PtCo catalysts during AST [99]. They reported that different thermal treatments caused significant structural and morphological modifications in the PtCo catalysts. Yu et al. studied the cycling stability of dealloyed $PtCo_3$ and $PtCu_3$ catalysts between 0.6 and 1.0 V (vs. RHE) for up to 30,000 cycles [100]. In situ X-ray absorption spectroscopy (XAS) analysis showed stronger bulk Pt-Pt compressive strains and higher bulk d-band vacancies for the dealloyed $PtCu_3$ than the dealloyed $PtCo_3$ which was correlated to the higher initial activity of dealloyed $PtCu_3$. MEA tests showed poor durability towards voltage cycling for the dealloyed $PtCu_3$ catalyst when compared to dealloyed $PtCo_3$ catalyst due to Cu plating on the anode.

Based on the catalyst durability studies available in the literature, it is evident that Pt based catalysts are not stable under PEMFC operating conditions and Pt degradation occurs through Pt dissolution/re-deposition and Ostwald ripening mechanisms. Pt alloy catalysts appear to provide enhanced ORR activities even in the absence of alloying elements on the surface layer which are leached out when exposed to acids leaving Pt-rich surface for ORR [97]. Furthermore, the catalyst supports play an important role in determining the overall stability of the catalyst when subjected to potential cycling or high constant potentials. Carbon supports with high degree of graphitization as support materials is proved to be effective ways to improve the catalyst durability [20, 94]. However, the durability studies of Pt and Pt-alloy catalysts with ultra-low loading (0.1-0.2 mg_{Pt}/cm^2) in practical fuel cells are scarce. Most of the catalyst and support durability studies available in the literature do not fulfill the automotive PEM fuel cell cathode catalyst requirements described by U.S. DRIVE Fuel Cell Tech Team in "Cell Component Accelerated Stress Test Protocols for PEM Fuel Cells" [45].

1.3. Impact of Catalyst Loading on Pt Mass and Specific Activities

Mass activity is defined as the current density measured at 0.9 V (iR-corrected) and normalized by the cathode mass loading [101, 102]. It is frequently applied for the comparison of the activity of different catalysts in fuel cells [1, 58, 103-105]. In spite of the broad application of mass activity there are still uncertainties, that which material and experimental parameters influence the measured values.

Mass and specific activity were first applied to characterize the technical activity of the dispersed Pt particles in phosphoric acid fuel cells [106, 107]. The analysis of nano-scale effects on catalyst activity at low and high currents [101, 107-109] revealed the influence of catalyst-support interactions [110-112], support surface area [113, 114], catalyst layer thickness [115, 116], and diffusion profiles [117, 118]. Particularly, a maximum of mass activity was found at 3-5 nm Pt particle size. It was assumed that the small particles have more low coordination Pt atoms which may increase the strength of adsorption of surface oxide species [101]. Watanabe [113] showed that the inter-crystallite distance is also an important factor which can cause a similar relationship in mass activity as it was found by Peuckert [107].

Recently, density functional theory calculation showed that the OH is more strongly adsorbed at steps, edges and kinks of the Pt catalyst particles. Consequently, the contribution of these under-coordinated Pt site to the ORR are negligible [108]. Nesselberger et al. [109] compared 6 different commercial Pt electrocatalysts having different particle sizes deposited on the same support and found no particle size effect in the range of 1-5 nm and the effect is noticeable only in the range of 5-30 nm and poly-Pt samples. At macro-scale (i.e. catalyst layer level) the nano-scale effects can be eliminated by depositing the catalyst layer prepared using the same catalyst (same particle size and support area). Gasteiger et al. [119] in their study of dependence of polymer electrolyte membrane (PEM) fuel cell performance at three different Pt catalyst loadings (0.4, 0.24, and 0.15 mg_{Pt}/cm^2) concluded that the mass activity and electrochemical active surface area (ECSA) in cathode catalyst membranes (CCMs) are essentially independent of Pt loading. However, Saha [116] found that the utilization of a screen printed CCM layer decreased as the loading of the catalyst layer increased from 0.02 to 0.12 mg cm^{-2}. Lee et al. [115] observed that the mass activity measured in membrane electrode assemblies (MEAs) is only 10-30% of the ring disk electrode's (RDE) mass activity, and increased as loading decreased while the utilization was unchanged. They assumed that O_2 may

access the catalyst particles more effectively when it exhibits thin layer geometry, or higher porosities at lower catalyst loadings. According to our experimental data on the dependence of mass and specific activity indicated [102] that the simple Tafel-approximation is not fully valid and complex models are needed to be applied for better understanding of the loading effect. Different agglomerate models have been developed to theoretically analyze the effect of the decrease of loading on the PEM fuel cell performance. Yoon [120] varied the thickness of the active layer for the simulation of different loadings and kept all the specific properties constant, such as Pt utilization, volumetric surface area etc. Kamarajugadda [121] kept the layer thickness constant and varied the Pt loading and the macroporosity. They all used a macrohomogeneous and agglomerate model, which assumes a linear expression between catalyst loading and ECSA. These types of models do not describe the exact geometric details of the catalyst layer. Instead, the material properties are averaged over the electrode volume. In the case of agglomerate models, the catalyst layer is considered as randomly distributed spherical particles in which the catalyst is supported on the surface of carbon particles and is wetted and covered by the ionomer (electrolyte) film [122-125]. Void spaces, characterized by the porosity, are also randomly distributed between the agglomerates forming gas channels. However, it is difficult to describe the real geometry of a disordered system with a small number of structural parameters. Pore scale models can generate realistic pore structures, but only with a loss of generality [126-127].

Siddique et al. [128] developed a catalyst layer microscopic model mimicking the experimental fabrication of the catalyst layer. The variation of the number of agglomerates varied the ECSA due to reduced connectivity and increased isolation. Large agglomerates correspond to insufficient mixing of ionomer and Pt/C and consequently limited the triple phase boundaries. Too small agglomerate size may lead to the loss of connectivity or entanglement between them. The commonly assumed random structure is not always adequate and fractal type structure has been found by Martin et al. [129]. They analyzed the effect electro spraying method on the structure of the catalyst layer at different Pt loading and Nafion® contents. SEM images revealed a fractal type structure in which the building blocks are clusters consisting of a few catalyst particles. The single particles size corresponds to the original nanoparticle in the Pt/Vulcan powder. These observations indicate that the agglomerates form a self-assembled layer rather than a random structure.

2. Project Objectives

- Develop unique hybrid cathode catalyst (HCC) through interaction of highly-active and stable compressive Pt-lattice catalyst (Pt*) with activated carbon composite support (A-CCS) having high activity for oxygen reduction reaction (ORR).
- Enhance the activity of HCC by increasing the synergistic effect of catalytic active sites present in the supports and those in Pt* catalyst.
- The specific objectives are to:
    - Perform optimization studies to develop a catalyst support with high kinetic activity and stability.
    - Estimate the role of Brunauer-Emmett-Teller (BET) surface area, porosity, pore-size, pore-size distribution and hydrophilic/hydrophobic properties on the support stability.
    - Synthesize low-PGM cathode catalyst for automotive application by decreasing the PGM loading while simultaneously increasing the catalytic activity and stability of A-CCS and the activity of Pt*.
    - Develop low cost procedures to synthesize Pt/ACCS-1, Pt/ACCS-2, Pt^*/ACCS-1, and Pt^*/ACCS-2.
- Demonstrate mass activity of $\geq$0.44 A/mg_{PGM} in H_2/O_2 fuel cell, initial high current performance under H_2/air (<0.125 g_{PGM}/kW rated power density) and stability of mass activity ($\leq$ 40% loss) and stability of high current density performance under H_2/air using DOE potential cycling (0.6-1.0 V for 30k cycles) and potential cycling (1.0-1.5 V for 5,000 cycles) tests.

The goal is to synthesize a low cost catalyst with optimized average mass activity, stability of mass activity, initial high current density performance under H_2 /air (power density), catalyst and support stability able to meet 2017 DOE targets for electrocatalysts for transportation applications.

3. Approach

This project is based on a major breakthrough research at USC that resulted in the development of highly-stable and kinetically-active carbon composite supports, namely Pt/ACCS-2 as well as development of highly-active and stable hybrid cathode catalyst,

Pt*/ACCS-2. The hybrid cathode catalyst (HCC) technology developed at USC is based on a two-step patented process to synthesize highly-active and stable ultra-low platinum group metal (PGM) hybrid cathode catalyst. The research at USC was aimed in developing catalytically-active and stable supports to sustain load cycling and startup/shut-down conditions. In the first step, the following major constraints were addressed when developing cathode catalyst supports: (a) the support should be chemically and electrochemically stable at high potentials, low pH, and high temperature and (b) an onset potential and kinetic activity for ORR similar to that of the platinum catalyst. To accomplish these requirements, ACCS-2 was synthesized with optimized (i) BET surface area, porosity, pore size and pore size distribution, (ii) hydrophilic/hydrophobic ratio, (iii) structural properties (amorphous/crystalline ratio), (iv) number of catalytic active sites through metal catalyzed pyrolysis, (v) Pt/Pt*-support interaction was optimized by inclusion of active surface functional groups and (vi) transition metal necessary for the formation of Pt* is encapsulated in the graphitic carbon structure.

In the second step, compressive Pt-lattice catalyst (Pt*) was synthesized through a USC-developed annealing procedure that controls the particle size during annealing. Monolayers of Pt* were formed by diffusing Co atoms present in the support in to Pt which is deposited on A-CCS support. Mathematical model developed at USC was used to optimize the Co diffusion time, annealing temperature, and Pt/Co stoichiometric ratio.

4. Results and Discussions

4.1. The effect of Pt loading on the performance of PEM fuel cells - Better understanding of the effect of microstructure

A systematic work for the characterization of mass and specific activities of PEM fuel cells at different Pt loadings resulted in a new self-assembled (rather than randomly distributed particles) catalyst layer model. This new model opens up a new possibility in characterizing the relationship between the microstructure of the active layer and the performance of PEM fuel cells under H_2-O_2 and H_2-air operating conditions. Our results showed that, as the Pt loading decreased from 0.4 to 0.05 mg/cm^2, the mass activity (at 0.9 $V_{iR\text{-}free}$) increased by a factor of 2.7 while specific activity increased by 50%.

Polymer electrolyte membrane fuel cells for automotive applications require cathode catalysts with platinum group metal content (PGM) lower than 0.2 g_{PGM}/kW and approach 0.1

g_{PGM}/kW. In the recent years, extensive efforts have been undertaken in order to develop different PtM (M=Co, Ni, Fe, Cu) alloys or Pt-skin catalysts. The activities of these catalysts were found to be 2-4 times higher than that of the state-of-the-art Pt/C catalysts. It is a common belief that the lower performance at ultra-low Pt loading would be compensated with catalysts with higher mass activity [105]. It was found by Gasteiger et al. [119] in their study of the dependence of polymer electrolyte membrane (PEM) fuel cell performance at different Pt catalyst loadings (0.4, 0.24, and 0.15 mg_{Pt}/cm^2), it have been concluded that mass activity (MA) and ECSA (utilization) in cathode catalyst membranes (CCMs) are essentially independent of Pt loading. Consequently high mass activity catalyst allows the decrease of overall catalyst (and Pt loading) loading and the thickness of electro active layer. However, at loadings below 0.2 mg/cm^2 Wagner [130] and Geszler [131] found that MEAs' performance is likely to suffer large losses at high power (high current). In spite of the high mass activity, these catalyst layers are unsuitable for automotive application without mitigation of the increased resistance and poor performance at high current densities. **The deterioration of performance at ultra-low loading is not fully understood, thus it is necessary to evaluate the processes that control the impact of Pt loading on the mass activity and the mass transport losses.**

4.1.1. Experimental

4.1.1.1. Preparation of MEAs of different catalyst loading

The catalyst inks used in the MEAs were prepared by ultrasonically mixing 46% Pt/C catalyst synthesized at USC with water and absolute ethanol. The ionomer in the catalyst ink was maintained at 30 and 20 wt.% for the anode and cathode, respectively. The cathode catalyst ink was sprayed directly on Nafion® 212 membrane and the anode was sprayed on the SGL 10 BC gas diffusion layer (GDL). The Pt loading was periodically measured using X-ray fluorescence spectroscopy (XRF, Fischer XDAC) until the desired catalyst loading was achieved. Finally, the cathode catalyst coated membrane was sandwiched between the catalyst coated gas diffusion layer (GDL) (anode) and bare SGL10 BC (from SGL Carbon) under a pressure of 25 kg/cm^2 at 140^oC. The Pt loading was accurately measured using a 5 digit accuracy balance and compared with the results obtained using X-ray fluorescence measurements. The difference in the two measurements of Pt loading was 0.01 mg/cm^2, which was taken into consideration for the calculation of absolute error in the mass loading.

4.1.1.2. Electrochemical characterization

All the electrochemical characterization studies were performed in 0.1 M $HClO_4$ using a Pine bipotentiostat (Model AFCBP1), a Pt-wire counter electrode, and a saturated Ag/AgCl reference electrode (0.258 V vs. reversible hydrogen electrode (RHE) in 0.1 HClO4 electrolyte). A rotating ring-disk electrode (RRDE) with a Pt ring and glassy carbon disk (surface area of 0.247 cm^2) was used as the working electrode. The catalyst ink was prepared by blending the catalyst powder with ethanol in an ultrasonic bath. Cyclic voltammograms (CVs) recorded in nitrogen were used to obtain the background capacitive currents and ECSA of the Pt catalysts.

The fuel cell performance of the 46% Pt/C catalyst at different Pt loadings was evaluated in a 25 cm^2 single cell under conditions suggested by the U.S. DRIVE Partnership, Fuel Cell Technical Team Cell Component Accelerated Stress Test and Polarization Curve Protocols for Polymer Electrolyte Membrane Fuel Cells. Catalyst MA and polarization studies were performed under H_2/O_2, at 80^{o}C and 100% relative humidity (RH). Other fuel cell operating conditions are provided in the respective figures. The MA and SA were determined by measuring the current at 0.9 $V_{iR\text{-}free}$.

Prior to the ECSA measurements in the MEA and the RRDE, the Pt catalyst particle surface was cleaned using the following procedures: In the case of MEA, the potential was kept constant at 0.6 V under H_2/O_2 until the current reached a stable value. For the RRDE measurements, the surface cleaning was performed by cycling the potential between 0.3 and 0.8 V (vs. RHE). These surface activation procedures resulted in reliable ECSA measurements and prevented the catalyst agglomeration that occurs during high potential limits.

The ECSA of Pt was determined by charge integration under the hydrogen desorption peaks appearing between 0 and 0.35 V, by assuming a charge of 210 μC/cm^2 for the electroactive Pt surface. Then, the specific ECSA was calculated based on the following relation [132]:

$$A_{\mathrm{Pt,el}} = \frac{Q_{\mathrm{H}}}{m \times q_{\mathrm{H}}} \tag{4}$$

where Q_H (μC) is the charge of hydrogen desorption, m (μg/cm^2) is the Pt metal loading, and qH (μC/cm^2) is the charge required for desorbing a monolayer of hydrogen on a Pt surface.

The porosity of the catalyst coated membrane (CCM) was measured by a mercury porosimeter (Micromeritics Autopore 9500). The cumulative pore volume as a function of pore diameter was

determined from the mercury intrusion data, i.e. the volume of mercury penetrating into the pores versus the applied pressure. Under the assumption that all pores are cylindrical, the pore diameter d_p was calculated from the value of the applied pressure p using the capillary law [133]:

$$d_p = \frac{4\gamma \cos\theta}{p} \tag{5}$$

where γ and θ denote the surface tension of mercury and the contact angle between mercury and the sample.

4.1.2. Numerical experiments and parameter estimation

A novel approach has been developed for the estimation of semi-quantitative information from an operating fuel cell [9-11, 102]. Our main focus was the analysis of mass activity and of the variation of transport coefficients with loading, such as diffusion resistance in the Nafion® film, Thiele modulus and the effective gas phase diffusion coefficient. Five consecutive steps have been performed which are summarized in Fig. 1.

1. Characterization of the catalyst by RDE experiments.
2. Characterization of the structure of the catalyst layer by Hg-porosimetry.
3. Characterization of the cathode at low current densities. It is assumed that only the ORR is the rate determining step. The utilization, the mass activity, and non-linear scaling factor have been determined.
4. Characterization of the MEA in O_2 is performed by fitting the model to the performance curve. The gas phase diffusion was neglected and the effectiveness factor and the Nafion® film diffusion resistance have been calculated.
5. Characterization of the MEA in air is performed by fitting the numerical model to the performance curve. The Nafion® film diffusion resistance and the effectiveness factor were substituted from the previous steps and the effective gas phase diffusion coefficient has been determined.

The parameters determined in the predecessor step have been used as an input in the further steps. The polarization curves and the mass activity have been simulated by using Matlab® partial differential equation (PDE) solver.

A simulated annealing (SA) algorithm was used for the parameter estimation developed by Horváth and Havasi [134] for fuel cells. The commonly applied Levenberg-Marquardt (LM) method [135] locates (estimates) a local minimum, however it is not guaranteed to be a global

minimum [134, 136]. The LM method usually stops, but it is evidently very far from the data measured. The SA method is a combination of LM and a random parameter set. During the fitting, the control parameter typically kicks off high and is gently "cooled" or decreased in every step, slowly lowering the probability of the random steps.

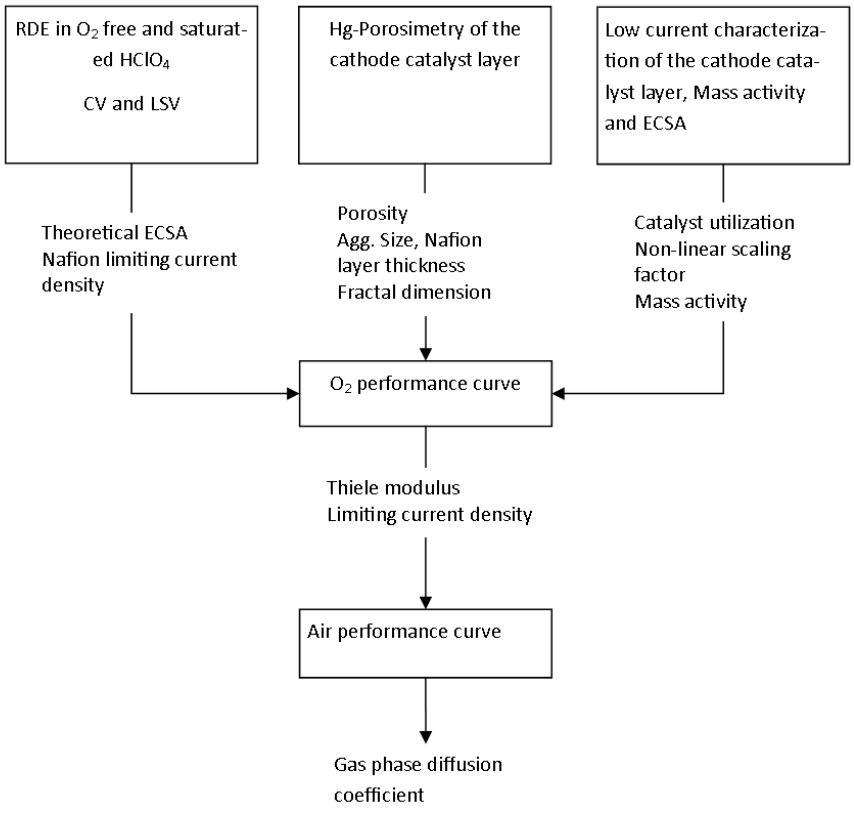

Figure 1. Flow chart for simulation and parameter estimation.

4.1.3. Mass Activity

Mass activity is defined as the normalized current density measured at 0.9 V (iR-corrected) divided by the cathode PGM loading in A/mg_{PGM}. The MA, catalyst loading (L), specific activity (SA), specific electrochemical surface area (ECSA), or surface enhancement factor (SEF) can be calculated if three of the five parameters are known by using the following equations:

$$MA = \frac{i_{0.9V}}{L} \tag{6}$$

$$SA = \frac{i_{0.9V}}{L \cdot ECSA_{MEA}} \quad (7)$$

$$SEF_{MEA} = ECSA_{MEA} \cdot L \quad (8)$$

where $i_{0.9V}$ is the current density measured at 0.9 $V_{iR\text{-}free}$ and normalized to the geometrical surface area (A/cm^2), here L is specifically the Pt loading (mg/cm^2), SEF_{MEA} is the surface enhancement factor (cm_{Pt}^2/cm^2), SA is the specific activity (A/cm_{Pt}^2) and MA is the mass activity (A/mg_{Pt}).

MA is evaluated by Tafel equation. This equation is valid under the assumption that the surface area of the individual particles can be linearly added and is linearly proportional to the mass of the catalyst.

$$\eta = TS\log\left(j_{cell} + j_{H_2}\right) - TS\left[ECSA \cdot m_{Pt} j_0\right] \quad (9)$$

where TS is the Tafel slope, j_{cell} is the measured total cell current density (A/cm^2), jH_2 is the hydrogen crossover current density. m_{Pt} is the Pt cathode loading (mg_{Pt}/cm^2). It has been reported in the literature that $j_{cell} = j + j_x$, where j_x is the measured hydrogen cross-over current with a value of 3.3 mA/cm^2 [119]. The hydrogen cross-over current can vary depending on the experimental conditions.

4.1.4. Experimental Results

Table 1 demonstrates that the catalyst utilization for the MEAs increased from 48.33% to 82.56% when the Pt loading was decreased from 0.4 to 0.05 mg_{Pt}/cm^2, consequently ECSA is dependent on the Pt loading. As shown in Table 1, the mass activity increases when the loading decreases which can be related to the increase in ECSA from 41.08 to 70.18 m^2/g. The result shows (Table 1) that the specific activity increased from 209 $\mu A/cm_{Pt}^2$ to 328 $\mu A/cm_{Pt}^2$ when the loading was decreased from 0.4 mg/cm^2 to 0.05 mg/cm^2. The mass and specific activities increased by a factor of 2.7 and 1.6, respectively while, the ECSA increased to 1.7 times from its original value. This implies that the variation of ECSA only partially accounted for the increase in mass activity. When MA is plotted**,** the following should yield identical slopes: $E_{iR\text{-}free}$ vs. the $\log(\frac{j_{cell} + j_{H_2}}{m_{Pt}})$ and $E_{iR\text{-}free}$ vs. log of mass activity A/mg_{Pt} (the mass specific current density, j_m).

With this assumption, the cathode performance is controlled only by the ORR kinetics and the Ohmic losses (R_Ω), or:

$$[\frac{\Delta E_{iR-free}}{\Delta \log[i_m]}]_{p_{O_2}, p_{H_2}, T, A_{Pt,el}} = -TS \quad (10)$$

Table 1. Comparison of the electrochemical properties for different Pt loadings.

Pt loading (mg/cm^2)	**Utilization (%)**	**ECSA (m^2/g)**	**Current Density @0.9$V_{iR\text{-}free}$ (A/cm^2)**	**Tafel-slope (V/decade)**	**specific activity ($\mu A/cm_{Pt}^2$)**	**mass activity (mA/mg_{Pt})**
0.05	82%	70.18	0.012	−0.065	328	240
0.1	79%	67.86	0.0185	−0.065	261	185
0.2	58%	49.45	0.03	−0.063	296	150
0.3	56%	47.63	0.0321	−0.064	218	107
0.4	48%	41.08	0.035	−0.063	209	87.5

Figure 2 shows the MA and SA at different loadings. An increase of MA up to 0.23 A/mg_{Pt} was observed for 0.05 mg_{metal}/cm^2 loadings, compared with a MA of 0.085 A/mg_{Pt} measured for Pt loadings of 0.4 mg/cm^2. Both in Fig. 2 (a) and (b) the lines are parallel and fit to the apparent Tafel-slope predicted by Eq. (10).

Table 2 shows the specific surface area, the average pore size, the porosity and the fractal dimension of the catalyst layer at different loadings. The data clearly shows that the loading highly influenced the physical properties of the catalyst layer. At a loading of 0.05 mg/cm^2, the specific surface area of the agglomerates is 754 m^2/g which decreases to 212 m^2/g as the loading increases to 0.4 mg/cm^2. Accordingly, the calculated agglomerate radius increases from 40 nm to 135 nm. It suggests that the newly deposited particles stick to the previously deposited ones and screen each other's surfaces. The variation of the pore diameter is shown in Table 2. At 0.05 mg/ cm^2 loadings, the pore size between the agglomerates is less than 10 nm, but at higher loadings (0.4 mg/cm^2) it shifts to around 40 nm. Simultaneously, the pores that are smaller than 20 nm diminish. It indicates that not only the particles agglomerated but the void spaces also agglomerate when increasing the catalyst loading from 0.05 to 0.4 mg/cm^2. Furthermore, the macro porosity shows relative fixedness over the loading. At 0.05 mg/cm^2, the macro porosity is

39% while at 0.4 mg/cm^2 it is 43%, however it increases from 31% to 43% as the loading increases from 0.1 mg/cm^2 to 0.4 mg/cm^2 loading.

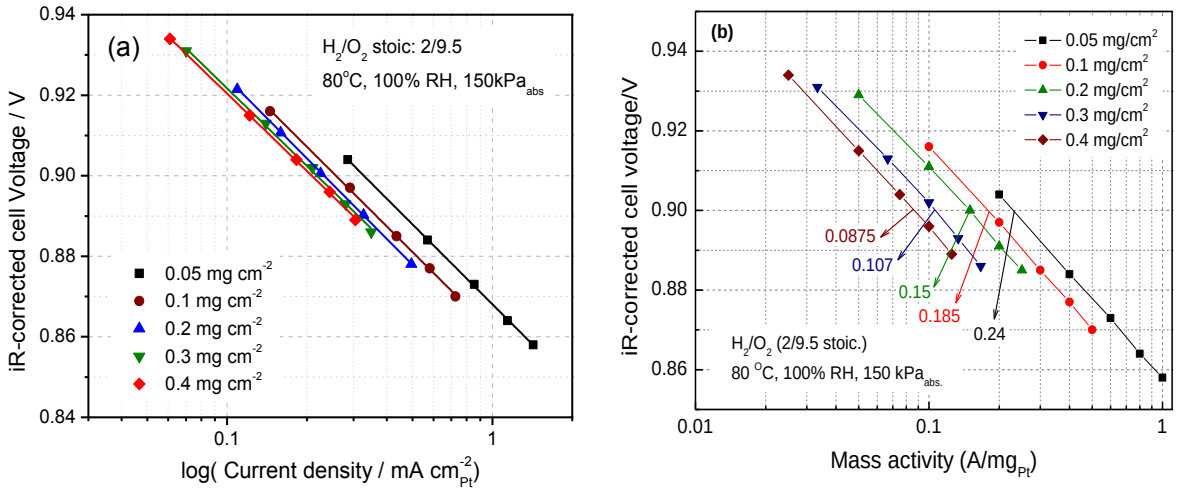

Figure 2. Effect of Pt loading on the (a) specific and (b) mass activity of MEAs under DOE fuel cell operating conditions.

Table 2. Physical characterization and pore structure of the catalyst layer at different Pt loadings

Loading	Specific surface area (m^2/g)	Agglomerate radius (cm)	Pore diameter (μm)	Porosity (%)	Surface Fractal dimension
0.05	754	$3.97\ 10^{-6}$	0.012	39	2.937
0.1	557	$5.83\ 10^{-6}$	0.011	31	2.898
0.3	244	$1.02\ 10^{-5}$	0.044	34	2.763
0.4	212	$1.35\ 10^{-5}$	0.0391	43	2.722

4.1.5. Validity of Tafel approximation for the calculation of mass and specific activity

While the catalyst layer is not a planar surface, a simple Tafel relationship cannot be applied, therefore a spherical agglomerate model was used and analyzed by analytical and numerical models [9-11]. The dimensionless penetration depth was identified as the main factor which controls the validity of the application of the kinetic Tafel-equation, i.e. when the mass activity is independent of catalyst loading. The penetration depth however depends on the loading. Consequently, mass and specific activities are independent of the loading in a certain region only as it is shown in Fig. 3.

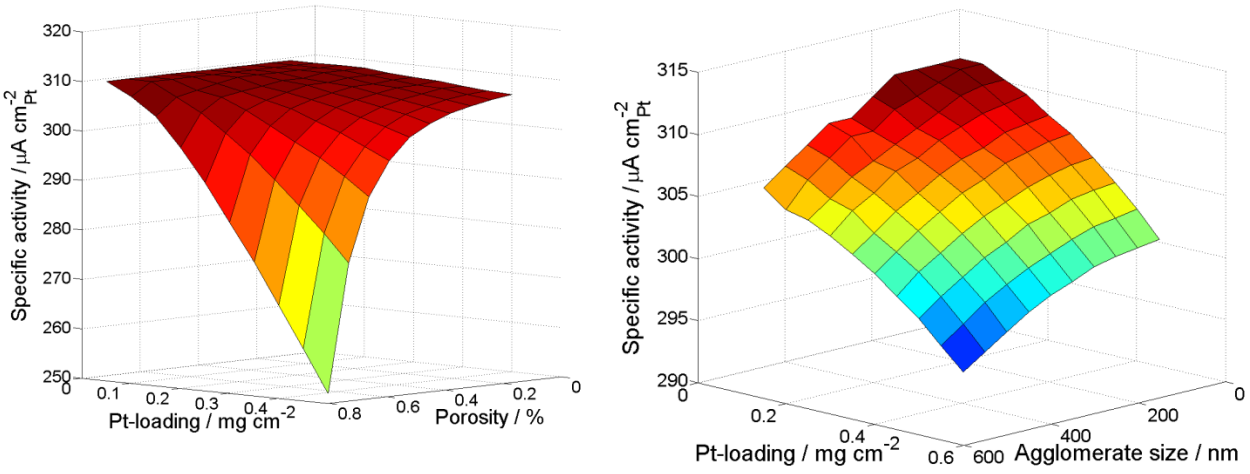

Figure 3. (a) Calculated specific activity at different loadings and porosities and 50 nm constant agglomerate size, and (b) at different agglomerate sizes and 54% porosity. The plots were calculated according to the uncorrected spherical agglomerate model at 0.9 $V_{iR\text{-}free}$ cell potential.

A non-uniform reaction profile may be formed even at small currents which affects the apparent value of mass and specific activities. When the exchange current density is high (for highly active catalysts of the future or at the anode), mass and specific activity depend on the loading, therefore they are not a good measure of catalytic activity in the MEA. The porosity, agglomerate size, and Nafion® layer thickness influence the mass and specific activities by shifting the double Tafel-slope asymptotic solutions to more positive potentials and consequently the mass and specific activities slightly decrease even at 0.9 $V_{iR\text{-}free}$. However, the loss of the validity of the Tafel-approximation is clearly indicated by the increased Tafel-slope from the theoretical value (0.07 V/decade) as it is shown in Fig. 4.

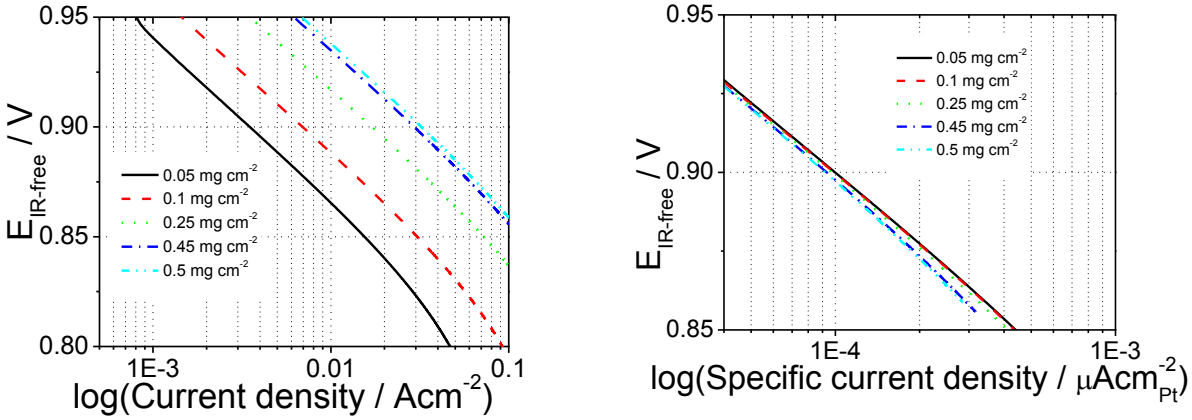

Figure 4. Calculated current densities (a) and the specific current densities (b) at different catalysts loadings and at 73% porosity in Tafel representation.

4.1.6. Non-linear scaling and the microstructure dependent mass and specific activity

A detailed and more precise definition of mass activity (MA) and specific activity (SA) was given to elucidate the variation of MA and SA with catalyst loading. The asymptotic solution of the agglomerate macro homogenous model has been applied in order to elucidate the dependence of MA and SA on catalyst loading. In the spherical agglomerate model, the surface area per unit volume is regarded as independent of the loading. However, as in the case of the ECSA, it may also depend on the loading and the thickness of the CL. A new non-linear scaling factor has been introduced which considers the effect of the loading on the volumetric agglomerate density. The parameters of the semi-empirical function have been determined by non-linear fitting. The scaling factor was found to be exponentially dependent on the loading. Finally, the loading dependent Tafel equation has been derived. This model contains both the utilization and the non-linear scaling factor.

Specific surface area should be precisely calculated as the quotient of the total surface area of the catalyst (A_{tot}) and the total volume of the catalyst layer (V_{tot}).

$$a_{\mathrm{Pt}} = \frac{A_{tot}}{V_{tot}} = \frac{ECSA \cdot M_{\mathrm{Pt}}}{V_{tot}} = ECSA(M_{\mathrm{Pt}})\rho_{\mathrm{Pt}}(M_{\mathrm{Pt}}) \qquad (11)$$

where M_{Pt} (mg) is the total Pt loading and $\rho_{Pt}(M_{Pt})$ (mg/cm^3) is the loading dependent Pt density in the agglomerates or in the CL. Eq. (11) is valid only if the ECSA and the ρ_{Pt} are to be independent of the loading. However, the measured data shown in Table 1 indicate that the

ECSA depends on the loading. The catalyst density may also depend on the loading which were summarized previously according to [137]. Introducing a non-linear scaling factor, similar to the utilization of the ECSA (Table 1) Eq. (11) can be rewritten into the following form

$$a_{\mathrm{Pt}} = ECSA \cdot \nu_{MEA} \rho_{\mathrm{Pt}} P_{MEA} \tag{12}$$

where ν_{MEA} is the catalyst utilization (%) of the MEA at different loadings and P_{MEA} is the non-linear scaling factor (%). While ρ_{Pt} now does not depend on the loading, it can be calculated by dividing it with the geometrical surface area:

$$\rho_{\mathrm{Pt}} = \frac{M_{\mathrm{Pt}}}{V_{CL}} = \frac{m_{\mathrm{Pt}}}{W_{CL}} \tag{13}$$

and Eq. (11) becomes

$$a_{\mathrm{Pt}} = ECSA \cdot \nu_{MEA} \frac{m_{\mathrm{Pt}}}{W_{CL}} P_{MEA} \tag{14}$$

The combination of the asymptotic solutions of the macro homogeneous and agglomerate models with the new form of the surface area per unit volume of the cathode CL renders the log *i*-V relationship with the following general form:

$$\eta_0 = TS \ln\left[\frac{j_{cell}}{\mathrm{ECSA} \cdot \nu_{\mathrm{MEA}} i_0 P_{MEA} m_{\mathrm{Pt}}} \left(\frac{c_{REF}^{O_2}}{c_{GDL}^{O_2}} \right)^{\gamma} \right] \tag{15}$$

Substituting $\frac{j_{cell}}{m_{\mathrm{Pt}}} = i_m$ with the mass specific current and using the log identities we reach

$$\eta = TS \ln(i_m) - TS \ln\left(\mathrm{ECSA} \cdot \nu_{\mathrm{MEA}} i_0 P_{MEA} \left(\frac{c_{GDL}^{O_2}}{c_{REF}^{O_2}} \right)^{\gamma} \right) \tag{16}$$

Also including $\frac{j_{cell}}{ECSA \cdot \nu_{MEA} m_{Pt}} = i_{Pt}$ we reach

$$\eta = TS \ln(i_{Pt}) - TS \ln\left(i_0 P_{MEA} \left(\frac{c_{GDL}^{O_2}}{c_{REF}^{O_2}} \right)^{\gamma} \right) \tag{17}$$

which are both Tafel-type equations, however the constants are different from the original Tafel equation. In the later work the effect of the non-linear scaling factor was investigated on the

mass activity and mass transport losses by using combined experimental and simulation techniques.

4.1.7. Detailed model of effect of Pt loading on mass activity and mass transport

The complex experimental and numerical analysis revealed that a decrease of 46% Pt/C catalyst loading results in a substantial change in the catalyst layer structure and the mass transport processes. The reduction of the complexity of the numerical model was achieved by applying such experimental conditions where flooding and water management are less influential (neither hysteresis nor negative spikes was found on the polarization curves). It was revealed that the diffusion resistances increased at lower loadings, which should have been decreased for thinner layers and smaller agglomerates. It justifies that the effect of the gas diffusion layer was not limited under the applied experimental conditions and MEAs. The result also implies that the effect of loading cannot be modeled by simply varying the thickness of the catalyst layer because it does not consist of randomly distributed particles. It can be characterized more sufficiently with a self-similar structure and the fractal dimension. For low loading (thin layer) where the fractal dimension is close to 3, the particles form a smooth layer with small agglomerate size and small void spaces. This structure more or less corresponds to the assumption of the spherical agglomerate model. This kind of layer forms during the spraying of first few layers directly to the Nafion® membrane. The volumetric agglomerate density is the highest because of the closely packed non-agglomerated particles. The addition of more and more catalyst enhances the agglomeration. The agglomerates, of course, do not stick together randomly, but through deterministic processes which are currently not known. The effect of these processes can be characterized by the fractal dimension. During the layer formation, the fractal dimension decreases, i.e. the catalyst fills the layer less effectively. This decreases the volumetric density of the agglomerates and consequently the mass activity.

At low loadings the inner surface area of the agglomerates/particles is high, which results a very thin covering Nafion® film. A linear relationship was found between the inner surface area of the agglomerate and the diffusion limiting current. This indicates that $A_{agg}D_{Film}$ are constant or that the diffusion coefficient is inversely proportional with the effective surface area of the ionomer. For the same system, it may imply that the diffusion resistance of the covering Nafion® film cannot be improved by increasing the effective surface area of the agglomerate, since in the case of rougher surface the diffusion path (via tortuosity) also increases.

Inside the agglomerate smaller effectiveness factor was found for lower loadings, even if the agglomerates are smaller at lower loadings. This is partially caused by the increased kinetic current caused by the higher ECSA at low loading and an increased mass transport resistance. The mass transport resistance inside the agglomerate can be affected by the variation of the agglomerate density or the effective diffusion coefficient in the agglomerate, though we propose to use a fractal dimension dependent Thiele modulus:

$$\text{Thiele modulus} \approx \left(\sqrt{\frac{I_{Kin}}{D_{eff}}} \right)^{2-D_f} \tag{18}$$

Eq. (18) shows that an increase of the fractal dimension increases the Thiele modulus**,** thus decreasing the effectiveness factor. In the gas phase**,** the very small void spaces increase the effective diffusion coefficient probably because of the increased tortuosity and the its cross correlation with flooding.

4.1.8. Effect of microstructure of mass and specific activity

A novel approach for the integration of pore-scale models with macroscopic models has been suggested. Different full layers at pore-scale level have been reconstructed by varying the interparticle interaction between the particles during the coating process. Instead of adding more and more specific structural input parameters to the macroscopic model, the characteristic properties of the layers have been collapsed into one line by using scaling analysis (Fig. 5). The model has been successfully applied for the elaboration of the effect of loading on the electrochemical properties of various systems, such as interpretation of mass activity of fuel cells and active carbon loading of supercapacitors (Fig. 6). It was shown by simulation and by experimental data, that the commonly applied approach for the calculation of the surface area per unit volume is not generally applicable. Although thickness is linearly dependent on loading the particle density and consequently the surface area per unit volume significantly decrease until saturation at a certain loading is reached. The following simple scaling function has been introduced for the correction of surface area per unit volume, which can be easily incorporated into existing fuel cell, battery, and supercapacitor models. The average surface area per unit volume can be calculated according to:

$$a_{real} = \overline{N}(m_{real})\frac{\pi}{d} \quad \text{or} \quad a_{real} = \overline{N}(m_{real})a_m \tag{19}$$

where d is the diameter of a particle, a_m is the surface area per unit volume of a closely packed layer, m_{real} is the active material loading and

$$\overline{N} = 1 + \frac{a_{sat}(p) - 1}{1 + \left(\frac{3 \cdot m_{real}}{m_0(p) \cdot d \cdot \rho \cdot \pi} \right)^y} \tag{20}$$

where ρ is the particle density, $m_0(p) = 73 \cdot p^{-0.78}$, $a_{sat}(p) = p^{-0.18}$, y=0.95 and p is the sticking probability (0-100%), i.e. interaction between the particles.

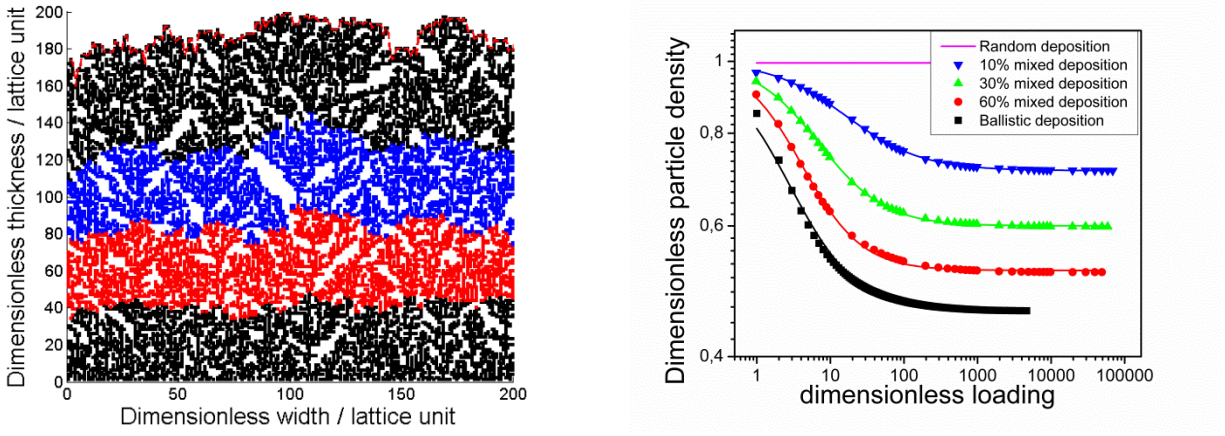

a) b)

Figure 5. (a) The layer formed during the deposition of an active material. The different colors correspond to different loadings (deposition of 1000 particles). (b) The volumetric particle's density (scatter) with the fitting of the particle density function (line) calculated from the Monte-Carlo simulation.

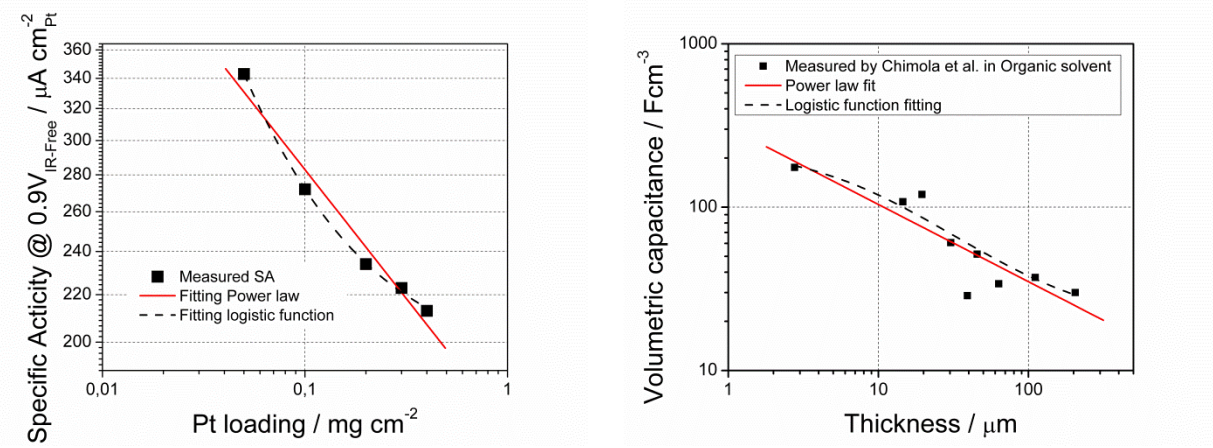

a) b)

Figure 6. Measured values and fitted power law and logistic function (Eq. 16) of (a) apparent specific activity of spray deposited fuel cell electrode and (b) of volumetric capacitance of monolithic carbide-derived carbon film in organic electrolyte from ref. [139].

4.2. Highly Active and Durable Pt*/CCCS (Pt* = Compressive Pt lattice) Cathode Catalyst for Polymer Electrolyte Membrane Fuel Cells

4.2.1. Preparation of carbon composite catalyst support

The CCCS was prepared using the procedure developed at University of South Carolina [140-147]. In brief, as-received carbon (Ketjen Black EC-300J) was oxidized with 9.8 M HNO_3 solution at 85 °C for 9 h under refluxing conditions. After filtering, the oxidized carbon black was washed with DI water several times and dried under vacuum at 80 °C for 12 h. A desired amount of $Co(NO_3)_2$ and ethylene diamine, used as Co and N precursors, respectively, were mixed with the oxidized carbon black in 200 ml isopropyl alcohol. The mol ratio of Co and N precursors was maintained at 1:9. The mixture was reflexed for 3 h at 85 °C under vigorous stirring, followed by drying under vacuum at 80 °C. The resultant powder was subjected to heat-treatment under inert atmosphere at 800 °C for 1 h followed by leaching in 0.5 M H_2SO_4 at 80 °C for 3 h to remove excess Co. The final product is denoted as CCCS. A schematic of CCCS synthesis is shown in Fig. 7.

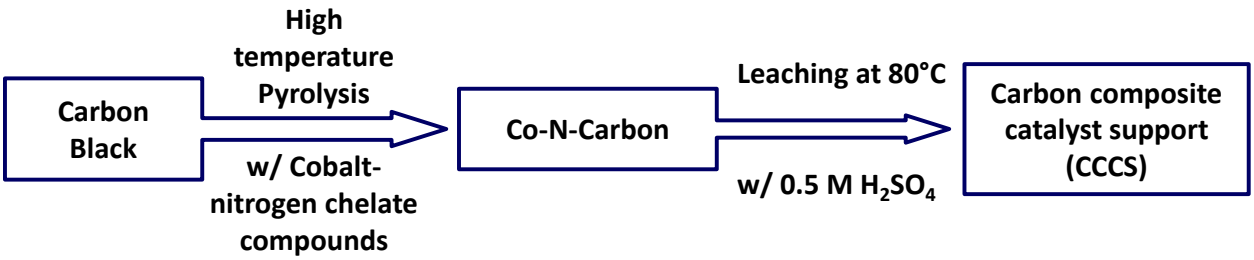

Figure 7. Schematic of CCCS synthesis.

Figure 8 (a) and (b) show the nitrogen adsorption-desorption isotherms and BJH PSD curves of CCCS and Ketjen black (KB). The specific surface area of CCCS and KB are 398, and 826.4 $m^{2/}g$, respectively. The CCCS exhibits characteristic Type IV adsorption/desorption isotherm behavior according to IUPAC classification indicating its mesoporous nature [148]. The isotherms show hysteresis loop with sharp adsorption and desorption branches over a relative pressure range of 0.4-0.8. The nitrogen uptake is observed when (P/P0) ratio is 0.94-1.0, which indicates the presence of mesopores [148]. The total pore volume was reduced from 0.846 to 0.688 ml/g. As shown in Figure 2(c), after the metal-catalyzed pyrolysis the peak pore diameter is ca. 4 nm. The effect of temperature on the BET surface area of various CCCS is compared in Table 3. As shown in Table 3, BET analysis of various carbon supports indicated surface area

values of 800, 400, 250, 190, and 160 m^2/g for Ketjen black, CCCS-800 °C, CCCS-1100 °C, CCCS-1300 °C, and CCCS-1500 °C, respectively. The BET surface area decreased for different CCCS as the heat treatment temperature increased due to the removal of micropores and high degree of graphitization occurred at temperatures >1000 °C.

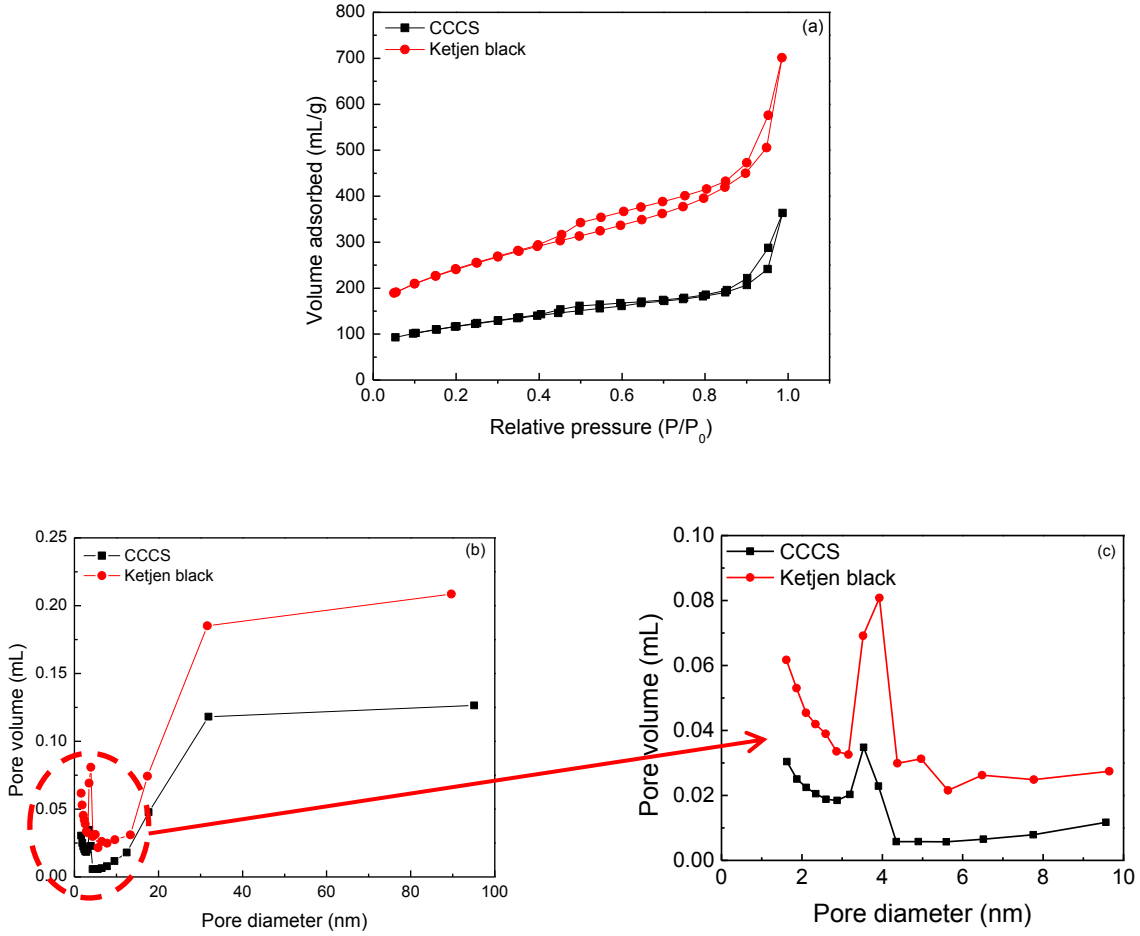

Figure 8. (a) N_2 adsorption/desorption isotherms and (b) BJH pore-size distribution curves obtained from the adsorption branch of CCCS and Ketjen Black. Pore diameter in the range 0-10 nm is shown in (c).

Figure 9 (a) presents XRD patterns of the CCCS and KB and Fi. 9 (b) presents the effect of heat treatment on the crystallinity and graphitic property of CCCS. Generally the characteristic diffraction peaks of (002) and (101) planes for carbon are found at ca. 26 and 43°. The diffraction peaks of CCCS are sharper with increased intensity and shift to more positive

angles. Consequently, the interlayer spacing of CCCS based on (002) plane decreases to 0.3456 nm, while that of KB is 0.3615 nm. The results indicated that the carbon surface of CCCS has been partially graphitized during metal-catalyzed pyrolysis. Furthermore, the CCCS shows characteristic diffraction peaks at 44.2, 51.5, and 75.8° which correspond to the (111), (200), and (220) planes of face centered cubic (fcc) structure of Co metal particle (PDF#97-007-6632), respectively. The XRD results confirm the presence of Co metal after acid-leaching at 80 °C.

Table 3. Comparison of physical properties of various CCCS, 30% Pt/CCCS catalysts, and commercial 46.7% Pt/C catalyst.

Supports	BET surface area of the support (m^2/g)
Ketjen black	800 [74]
CCCS-800 °C	400
CCCS-1100 °C	250
CCCS-1300 °C	190
CCCS-1500 °C	160

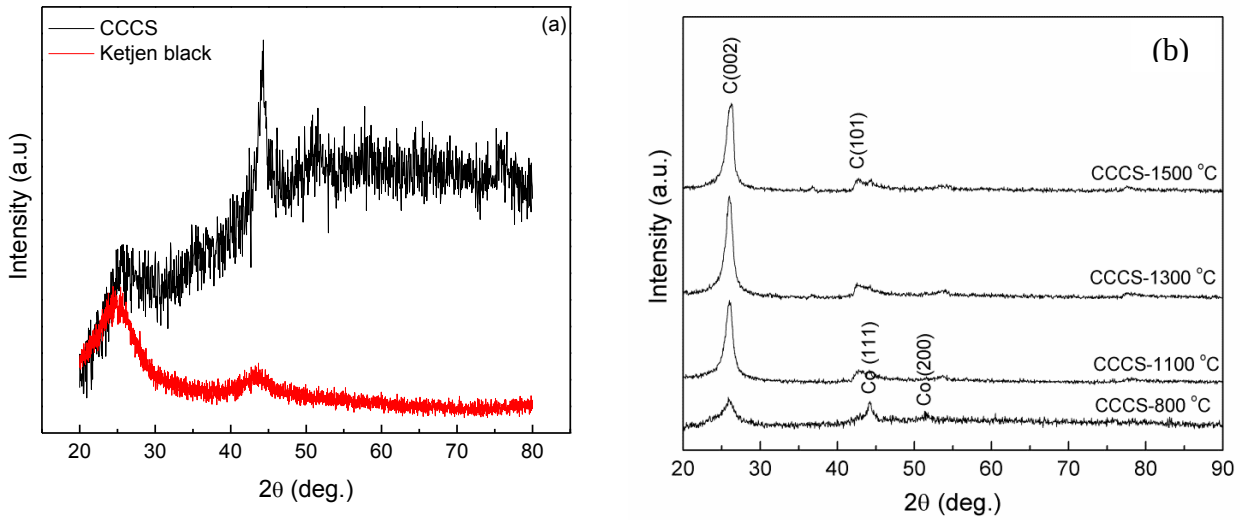

Figure 9. (a) Comparison of X-ray diffraction patterns of CCCS and Ketjen Black and (b) effect of temperature on the XRD of CCCS.

The effect of temperature on the supports' crystallinity was studied by heat treating the CCCS support from 800 to 1500 °C and the results are shown in Fig. 9 (b). In the case of CCCS, the degree of graphitization increases with pyrolysis temperature. The crystallite thickness (L_c) calculated by Scherrer's formula and the interlayer spacing (d_{002}) obtained from Bragg's law, are

given in Table 4. It has been reported that higher L_c values of the (002) peak and lower d002 numbers imply higher degree of graphitization [149, 150]. The ratio between the D and G peaks (I_D/I_G) obtained from Raman spectroscopy along with values for L_c and d002 for various CCCS are given in Table 4. For the CCCS, the L_c value increased and both d_{002} and the Id/IG ratio decreased as a function of pyrolysis temperature indicating the increased degree of graphitization.

Table 4. The degree of graphitization for different CCCS.

Sample	Pyrolysis temperature (°C)	L_c (nm) (XRD)	d_{002} (nm) (XRD)	I_D/I_G (Raman)
Ketjen black	-	1.1	0.3613	1.60
CCCS-800 °C	800	3.6	0.3440	1.43
CCCS-1100 °C	1100	7.3	0.3431	1.25
CCCS-1300 °C	1300	7.8	0.3430	1.07
CCCS-1500 °C	1500	7.9	0.3416	0.83

Figure 10 shows the Raman spectra for CCCS and KB. Both CCCS and KB show the D band and G band at approximately 1350 and 1580 cm^{-1}, respectively. The D band originates from structural defects and disorder-induced features on carbon, while the G band corresponds to the stretching vibration mode of graphite crystals [151, 152]. Relative ratio of D band to the G band (I_D/I_G) for CCCS and KB is estimated to be 2.42 and 2.60, respectively, indicating that CCCS is more graphitized than KB. The effect of heat treatment temperature on the I_D/I_G ratios of various CCCS is compared in Table 4.

The HRTEM images of various CCCS (after acid leaching) and KB are shown in Fig. 11(a-e). The apparent difference between them is the presence of Co particles encapsulated by carbon shells in the CCCS since the Co particles present on the surface are removed during acid leaching. Nanostructured fibers or tubes of graphitic carbon are also formed as a result of pyrolysis in the presence of Co metal [153, 154] while KB showed amorphous morphology as shown in Figure 11 (a). The CCCS synthesized at high temperatures show graphitic carbon tubes and carbon fiber structure formation during metal-catalyzed pyrolysis. Highly graphitized crystalline carbon structures are formed in CCCS synthesized at temperatures above 1000 °C.

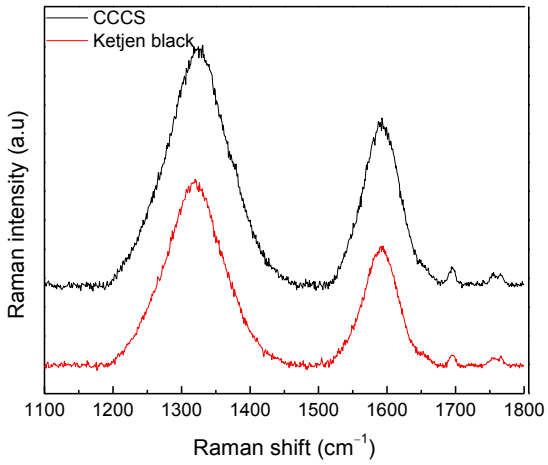

Figure 10. Comparison of Raman spectra of CCCS and Ketjen Black.

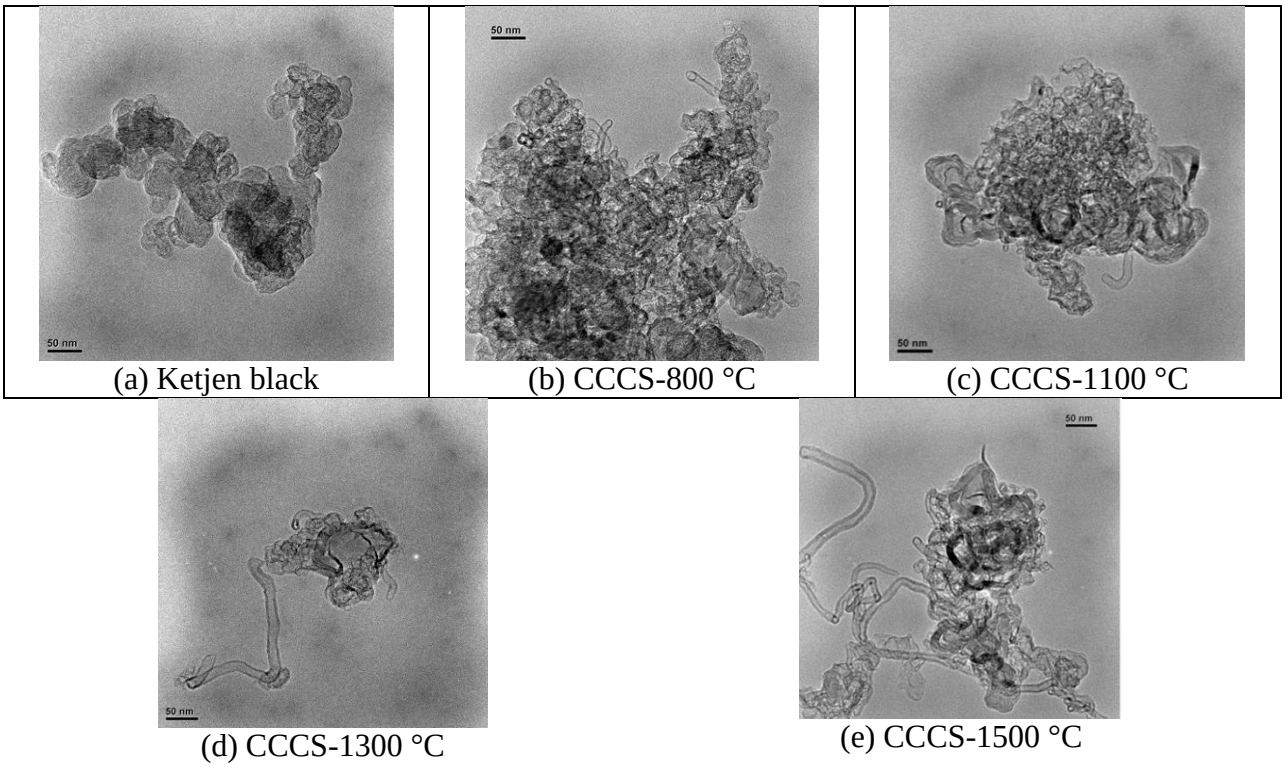

Figure 11. HRTEM images of (a) Ketjen black, (b) CCCS-800 °C, (c) CCCS-1100 °C, (d) CCCS-1300 °C, and (e) CCCS-1500 °C. The scale bar is 50 nm.

The results of XPS analysis performed on CCCS and KB supports are presented in Figure 12(a) and (b), respectively. Figure 12 (a) shows the survey scans for CCCS and KB. Only XPS spectrum of CCCS, as shown in Figure 12(b), exhibits a broad peak around 398.9 eV which corresponds to the nitrogen atom. The nitrogen peak shown in Figure 12 (b) for CCCS can be

deconvoluted into four major peaks corresponding to pyridinic, pyrrolic and/or pyridone, quaternary, and pyridinic-N^+-O^- (oxidized nitrogen). The peak at 398.4 eV accounts for the presence of pyridinic-N whereas the peak at 400.3 eV corresponds to the pyrrolic-N and/or pyridine-N. The peaks at 401.1 and 403.4 eV are ascribed to the presence of quaternary-N and pyridinic-N^+-O^-, respectively. Relative percentages of pyridinic-N and pyrrolic-N and/or pyridine-N are 41 and 38.5 % of total nitrogen, respectively. Quaternary-N accounts for 6.6 % while pyridinic-N^+-O^- occupies 13.9 %. It is well-known that pyridinic-N situated on the edge of the graphite planes promotes ORR by donating one p-electron to the aromatic π system [154-156]. Moreover, previous studies report that the quaternary-N plays a role as stable ORR active sites [144, 157-159].

Comparison of ORR kinetics of Ketjen black and CCCS-800 °C and hydrogen peroxide formation on CCCS-800 °C are shown in Figures 13 (a) and 13 (b), respectively. Ketjen black shows no activity in terms of onset potential for ORR and diffusion current when compared to CCCS-800 °C which shows onset potentials of ~0.86 V vs. RHE and well-defined kinetic and mass-transfer regions in 0.1 M $HClO_4$ electrolyte at room temperature.

Koutecky–Levich analysis resulted in slopes close to that for the theoretical four-electron transfer reaction with the calculated number of transferred electrons of about 3.6 for CCCS. The RRDE studies also indicated that the H_2O_2 production on CCCS-800 °C is only 2.5% (Figure 13 (b)). The formation of H_2O_2 is detrimental to the Nafion® membrane and the ionomer in PEM fuel cells [160]. Studies carried out by Sethuraman et al. [161] and Stamenkovic et al. [162] correlate the % H_2O_2 production to the number of electron transferred during ORR in acid electrolytes. Stamenkovic et al. [162] reported that the kinetics/reaction pathways of the oxygen reduction reaction on Pt-poly and Pt (110) are almost identical, i.e., the 4 e^- reduction (with ca. 5-10% of H_2O_2 production at 0.1 V) is operative on Pt-poly in acid solutions. Since the H_2O_2 production is less than 5% on CCCS-800 °C, the ORR kinetics follows the 4 e^- reduction pathways and is similar to that on Pt catalysts. Similar results have been reported in our previous studies for various non-precious metal catalysts [140-144, 159].

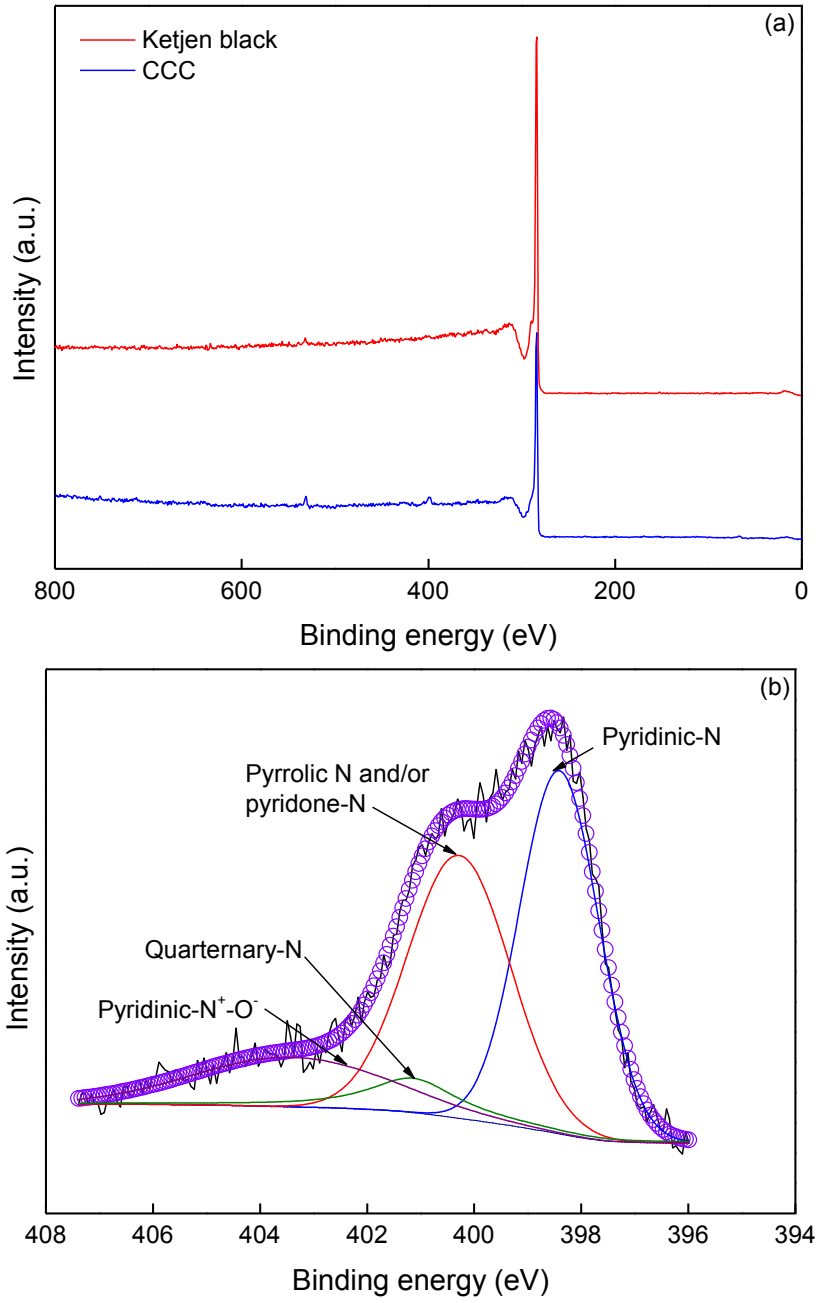

Figure 12. (a) XPS survey scans of CCCS and Ketjen Black and (b) deconvoluted N1s XPS spectra of CCCS.

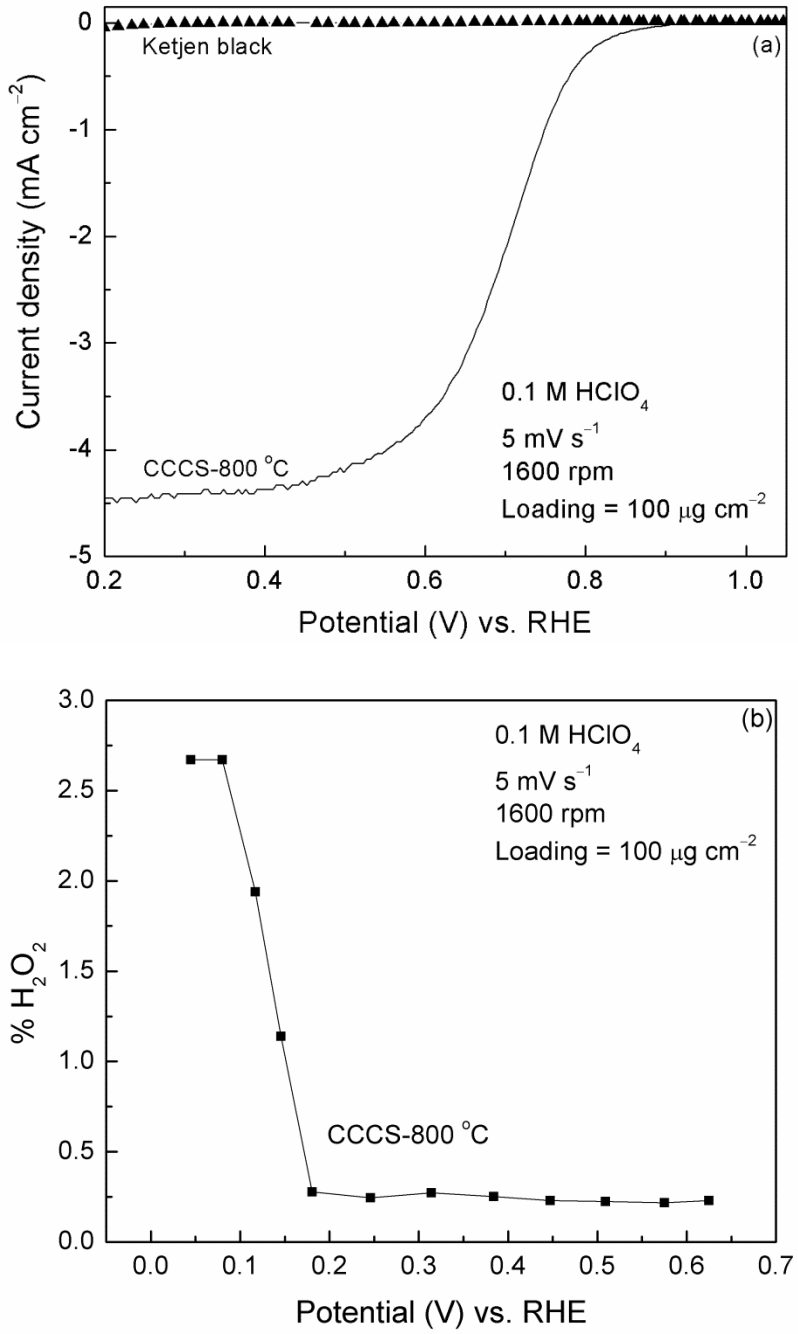

Figure 13. Linear sweep voltammetry of Ketjen black and CCCS-800 °C. (a) Comparison of ORR kinetics of Ketjen black and CCCS-800 °C and (b) H_2O_2 production on CCCS-800 °C.

Our previous studies on various non-precious metal catalysts showed that high temperature pyrolysis produces pyridinic and graphitic-type nitrogen on the surface of CCCS and the pyridinic-nitrogen groups act as catalytic sites for the oxygen reduction reaction [140-144, 159]. Maldonado et al. [153] have reported that a strong Lewis basicity of such nitrogen-modified sites facilitates the reductive adsorption of oxygen without the irreversible formation of oxygen functionalities, due to an increase in the electron-donor property of carbon. The surface analysis using X-ray photoelectron spectroscopy did not show the presence of cobalt and indicated the presence of only carbon, nitrogen, and oxygen on the CCCS surface (Table 5). It is important to note that Co is present only in the bulk as indicated by the ICP-AES analysis. The Co content determined using ICP-AES indicate that the CCCS-800 °C supports have ~10 wt% Co after 8 h leaching in 0.5 M H_2SO_4 (Figure 14). Thus, the ORR catalytic activity of CCCS is due to the presence of pyridinic-nitrogen groups and addition of Co for metal-catalyzed pyrolysis helps the inclusion of nitrogen into the CCCS [140-144, 153].

Table 5. XPS analysis of CCCS-800 °C.

Surface concentration determined by XPS (wt%)				
C	O	N	Co	Fe
94.86	1.26	3.88	-	-

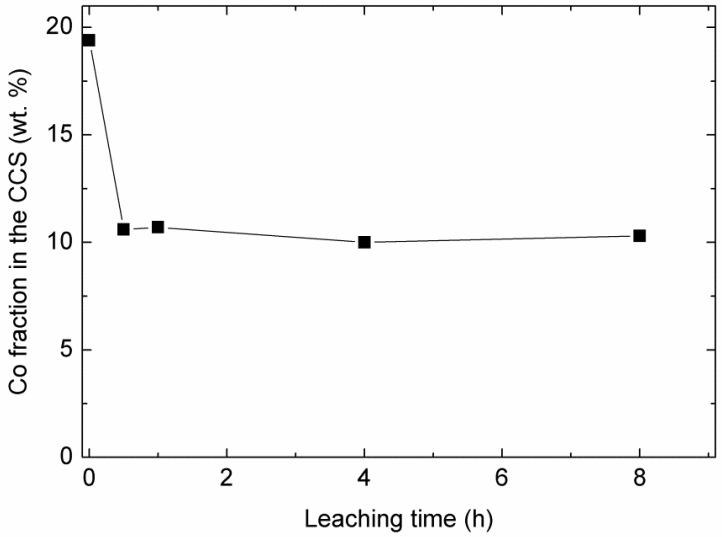

Figure 14. Effect of leaching time on the Co content in CCCS-800 °C support determined by ICP-AES.

4.2.2. Support Surface Functionalization and Platinum Deposition

A surface functionalization process to increase the hydrophilic property of CCCS was developed using a bifunctional organic molecule containing aromatic hydrocarbon and acid groups. A surface modification process is necessary in order to obtain a uniform Pt particle size distribution on the CCCS. Ketjen black and CCCS-800 °C were used for the synthesis of 5% Pt/C and 5% Pt/CCCS-800 °C catalysts, respectively.

It is generally accepted that oxygen functional groups transform carbon surfaces from hydrobobic to hydrophilic. The hydrophilicity of as-synthesized CCCS and surface-modified CCCS is evaluated by observing dispersions of CCCS in de-ionized water. Initially, the CCCS samples are uniformly dispersed in water using an ultrasonic bath. After 1 h, the as-synthesized CCCS that did not undergo functionalization formed large aggregates and settled down completely. The functionalized CCCS remained a stable dispersion for at least 60 h in aqueous media (Fig. 15). The stability of surface functionalized CCCS in water is attributed to the grafting of oxygen-containing groups onto the support surface which endows it with negative charges and provides the electrostatic stability required for a colloidal dispersion.

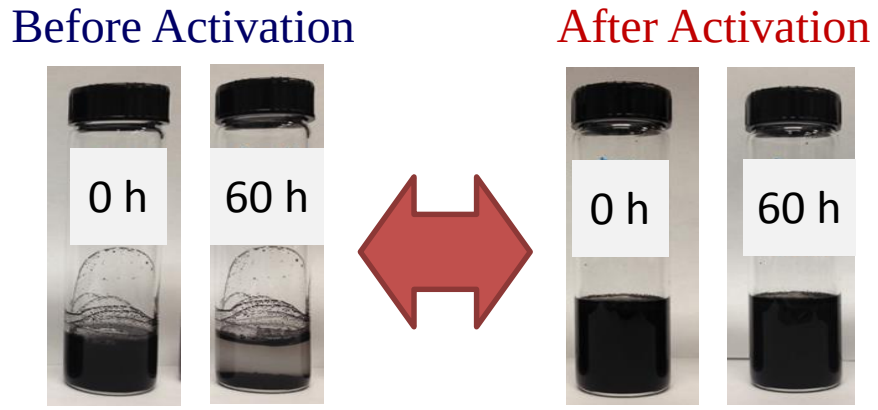

Figure 15. Photographs of CCCS supports before and after surface functionalization.

Platinum nanoparticle deposition with an initial loading of 1, 5 and 30 wt% Pt was carried out using a modified polyol process, which uses additives to control the particle size and enhance the catalyst-support interaction. In brief, a measured amount of $PtCl_4$ was dissolved in an appropriate volume of ethylene glycol under vigorous stirring for 30 min. 0.1M NaOH was introduced into the solution to adjust the pH. The pH of the reaction mixture was precisely controlled at every step of the process in order to obtain a uniform Pt deposition. Then,

calculated amounts of CCCS were added to the solution so that the desired initial Pt loading was achieved in the final Pt/CCCS catalyst. The resulting suspension was stirred for 1 h at room temperature followed by refluxing at 160 °C for 3 h. The solution was allowed to cool down to room temperature and kept for 12 h under continuous stirring. 0.1M H_2SO_4 was then added to the cooled mixture and the solution pH was adjusted to 3. The mixture was kept stirred for 24 h. The Pt/CCCS catalyst in the solution were filtered and thoroughly washed with de-ionized water. The resulting carbon-supported Pt catalysts were dried in air for 1h at 160 °C and stored for further studies. The effectiveness of surface activation on CCCS is clearly seen in Figure 16.

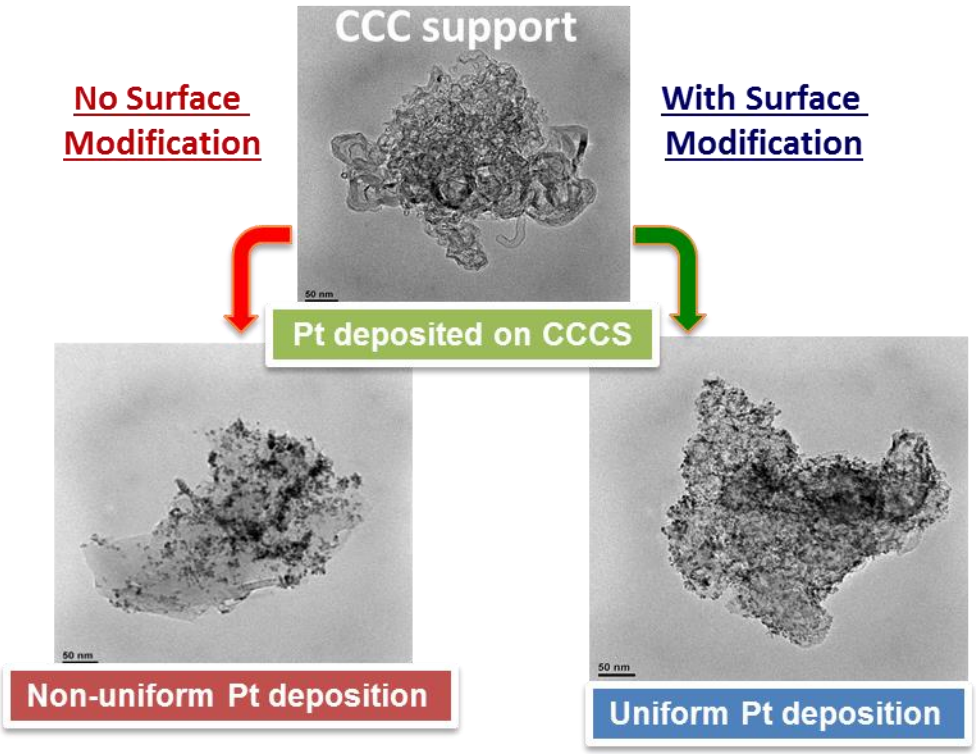

Figure 16. Comparison of Pt deposition on CCCS support with and without surface activation.

Figure 16 shows the HRTEM images of CCCS and Pt/CCCS catalysts prepared with and without surface modification. The effectiveness of surface functionalization of CCCS to obtain uniform Pt deposition is clearly shown in the figure while the supports without surface activation non-uniform Pt deposition. The non-modified CCCS shows partial Pt deposition due to the hydrophobic nature of the CCCS surface. The surface-modified CCCS promotes uniform Pt deposition which is essential for achieving high catalyst utilization and durability in PEM fuel

cells. The Pt deposition process parameters have been optimized to obtain uniform Pt deposition with an average Pt particle size, d_{Pt}, of 2-4 nm on various supports developed at USC.

The XRD patterns of 30% Pt/CCCS-800 °C and 30% Pt/CCCS-1100 °C catalysts are compared in Figure 17. The diffraction patterns represent all the reflections corresponding to the face centered cubic (fcc) lattice of Pt supported on various CCCS. The diffraction peak appearing at 26° for the Pt/CCCS-1100 °C catalyst can be attributed to C(002) of the supports. Table 3 compares the BET surface area of the supports used for different Pt/CCCS catalyst preparation. Scherrer's equation was used for calculating the Pt crystallite size using the Pt(220) peak appearing at 67.5° [18, 60]. The d_{Pt} values calculated from the XRD analysis are 2.2, 2.5, for 30% Pt/CCCS-800 °C and 30% Pt/CCCS-1100 °C catalysts, respectively, which are confirmed by the HRTEM and corresponding particle size distribution shown in Figure 18.

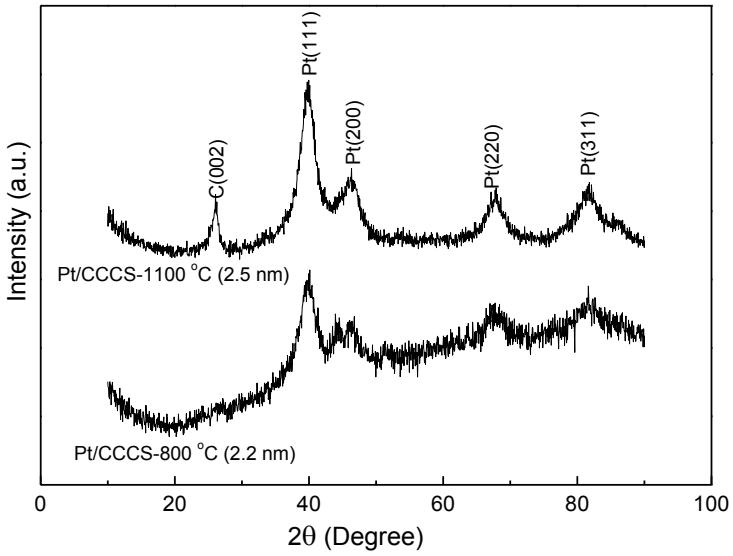

Figure 17. XRD patterns of 30% Pt/CCCS-800 °C and 30% Pt/CCCS-1100 °C catalysts.

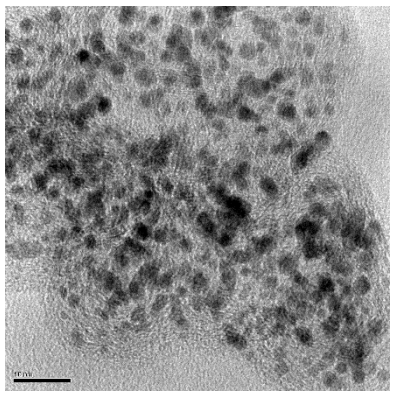

Commercial 46.7% Pt/C

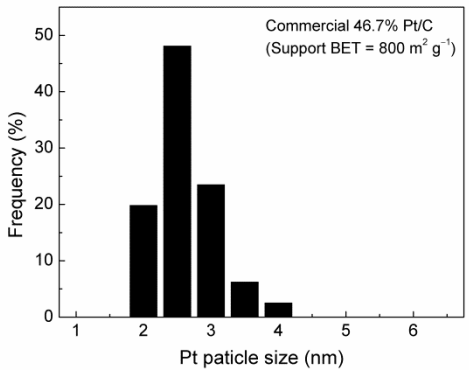

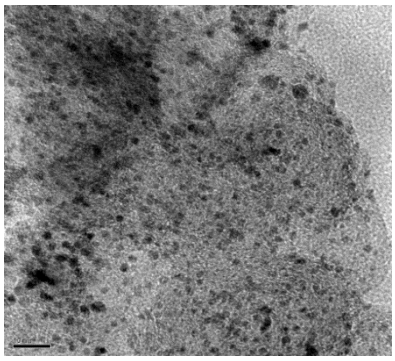

30% Pt/CCCS-800 °C

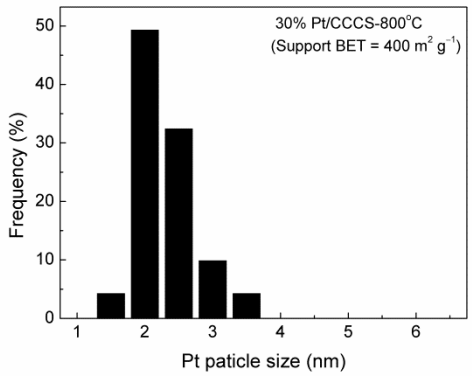

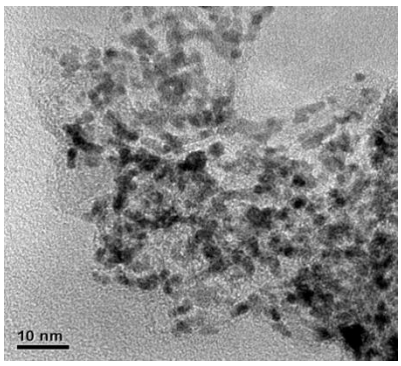

30% Pt/CCCS-1100 °C

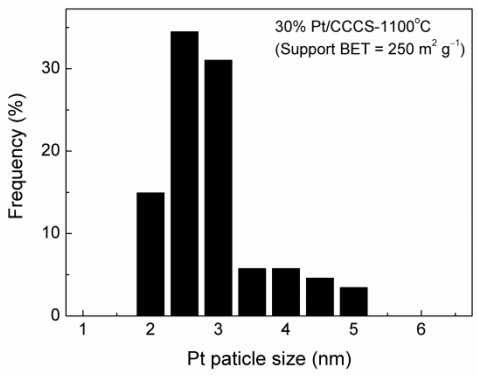

Figure 18. HRTEM images and particle size distribution of commercial 46.7% Pt/C, 30% Pt/CCCS-800 °C, and 30% Pt/CCCS-1100 °C catalysts. The scale bar is 10 nm.

4.2.3. Evaluation of Synergistic Effect of Pt/CCCS Catalyst

One of the objectives of this study is to combine the catalytic activity of CCCS and Pt and to show that the synergistic effect of the resulting Pt/CCCS catalyst results in enhanced ORR activity. For this purpose, 5% Pt supported catalysts are synthesized using CCCS-800 °C and Ketjen black and their ORR activities are compared. Figure 19 shows the comparison of ORR activities of CCCS-800 °C, 5% Pt/C, and 5% Pt/CCCS-800 °C catalysts. The catalyst loadings in the glassy carbon disk are 100 μg/cm^2 for the CCCS-800 °C and 20 μg/cm^2 for the Pt/CCCS-800 °C and Pt/C catalysts. The catalyst loadings of CCCS-800 °C and Pt catalysts were chosen based on the loading effect studies which indicated mass transfer-controlled reaction kinetics for these catalysts. The onset potentials for ORR for CCCS-800 °C, 5% Pt/C, and 5% Pt/CCCS-800 °C catalysts are 0.86, 0.97, and 1.01 V, respectively. The current density values at 0.8 V (vs. RHE) for the CCCS-800 °C, 5% Pt/C, and 5% Pt/CCCS-800 °C catalysts are 0.3, 1.9, and 3.9 mA/cm^2, respectively. Furthermore, the diffusion currents of CCCS-800 °C, 5% Pt/C, and 5% Pt/CCCS-800 °C catalysts are 4.5, 4.9, and 5.6 mA/cm^2, respectively. For 5% Pt, with Pt loading of 20 μg/cm^2, the carbon loading is 380 μg/cm^2, which may result in thicker catalyst layer. Thus, the higher limiting current density (i_L) for 5% Pt/CCCS-800 °C than that for 5% Pt/C may be attributed to the difference in the catalyst layer thickness on the glassy carbon electrode according to the following equation [163]:

$$i_L = -\frac{DnFC_b}{\delta} \tag{21}$$

where D is the diffusion coefficient of the reacting species, n is the number of electrons participating in the reaction, F is Faraday's constant, C_b is the concentration of the electroactive species in the bulk of the electrolyte, and δ is the diffusion layer thickness. In the case of the 5% Pt/CCCS-800 °C catalyst, the BET surface area of the CCCS-800 °C support is much smaller (400 m^2/g) than that of the Ketjen black support (800 m^2/g) which was used to synthesize 5% Pt/C. Therefore, the 5% Pt/CCCS-800 °C catalyst shows larger limiting current density due to a much thinner catalyst layer than the 5% Pt/C catalyst. Since the experimental conditions are identical for the 5% Pt/C and 5% Pt/CCCS-800 °C catalysts, the enhanced activity as evidenced by the increase of 40 mV in the ORR onset potential and the doubling of the currents in the kinetic region can be attributed to the synergistic effect on activity of the CCCS-800 °C and Pt catalyst.

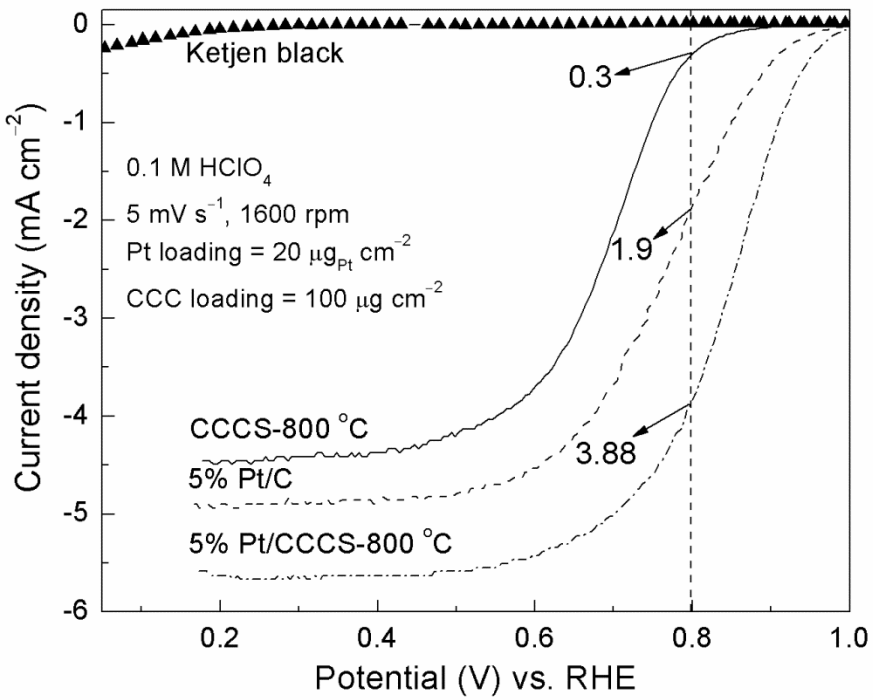

Figure 19. Comparison of ORR activities of Ketjen black, CCCS-800 °C, 5% Pt/C and 5% Pt/CCCS-800 °C catalysts in rotating disk electrodes.

4.2.4. Performance evaluation of 30% Pt/CCCS Catalyst

The H_2-air fuel cell polarization performances of the 30% Pt/CCCS-800 °C and commercial 46.7% Pt/C catalysts are compared in Figure 20. The Pt loading on the anode and cathode electrodes are 0.1 mg/cm^2 as measured by the XRF. Comparison of H_2 air fuel cell performance at 0.6 $V_{iR\text{-}free}$ showed current density values of 1350, and 1260 mA/cm^2 for 30% Pt/CCCS-800 °C and commercial 46.7% Pt/C catalysts, respectively. The power densities (rated) are 0.23 g_{Pt}/kW and 0.25 g_{Pt}/kW for 30% Pt/CCCS-800 °C and commercial Pt/C catalysts, respectively.

Corrosion of high surface area carbon in the presence of Pt is inevitable at high potentials under PEM fuel cell operating conditions such as high oxygen concentration, high water content, and low pH which favor carbon oxidation [14, 80]. During operation, the cathodes of automotive fuel cells often experience very high potentials due to startup/shutdown cycles or due to local fuel starvation at the anode [2, 41, 165]. Reiser et al. [41] have shown that the cathode interfacial potential difference can reach as high as 1.5 V due to the H_2/air front in the anode compartment during shutdown/startup. Carbon corrosion occurs at 0.207 V vs. RHE; however, it is not

detected during fuel cell operation due to its sluggish reaction kinetics [166]. In general, carbon corrosion is estimated by measuring the amount of CO_2 produced [27, 29, 167, 168] or the corrosion current [166] at high applied potentials in a PEM fuel cell by supplying pure H_2 to the anode and pure N_2 to the cathode. However, the measured current is always coupled with the H_2-oxidation current at the cathode due to H_2 cross-over from the anode through the Nafion® membrane [166]. In the present investigation, the cathode is subjected to 1.2 V constant potential for 400 h to study the support stability by measuring H_2-air polarization performance at regular intervals. The cell potential loss at 800 mA/cm^2 current density is used as a metric to evaluate the support stability in commercial Pt/C, Pt/CCCS-800 °C, and Pt/CCCS-1100 °C catalysts.

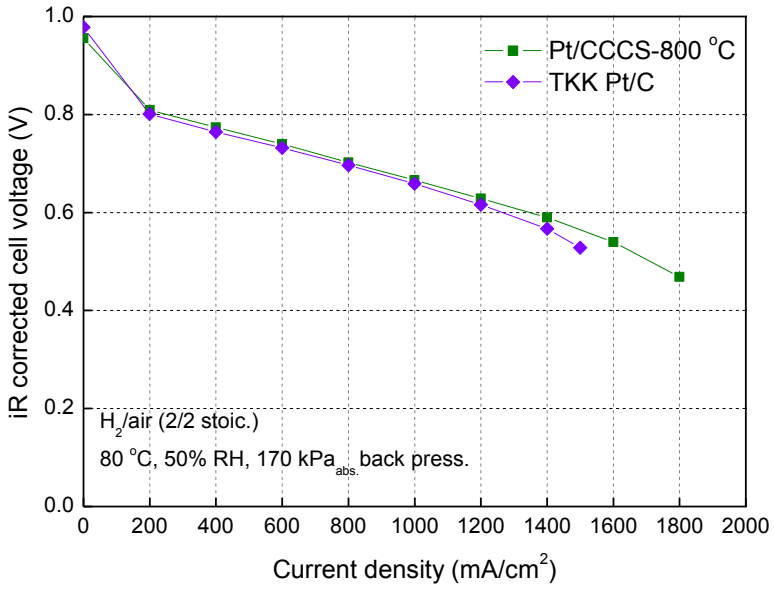

Figure 20. Comparison of H_2-air polarization performances of 30% Pt/CCCS-800 °C and commercial 46.7% Pt/C catalysts.

4.2.5. Synthesis of Pt*/CCCS Catalyst

Pt*/CCCS catalyst was synthesized by annealing the Pt/CCCS sample with polyaniline as the protective coating. Oxidative polymerization of aniline sulfate was performed at room temperature using ammonium peroxysulfate as the oxidizing agent [169, 170]. The polyaniline coated Pt/CCCS was then subjected to heat-treatment at 800 °C for 0.5 to 4 h under reducing/inert atmosphere. During the controlled heating process, the Co which is incorporated in to the CCCS diffuses to the surface and forms Pt*/CCCS catalyst. The heat-treatment process

was optimized to control the particle size between 3-5 nm, resulting in compressive Pt-lattice catalyst having Pt-shell/doped metal core structure. A schematic of Pt*/CCCS catalyst synthesis is shown in Fig. 21.

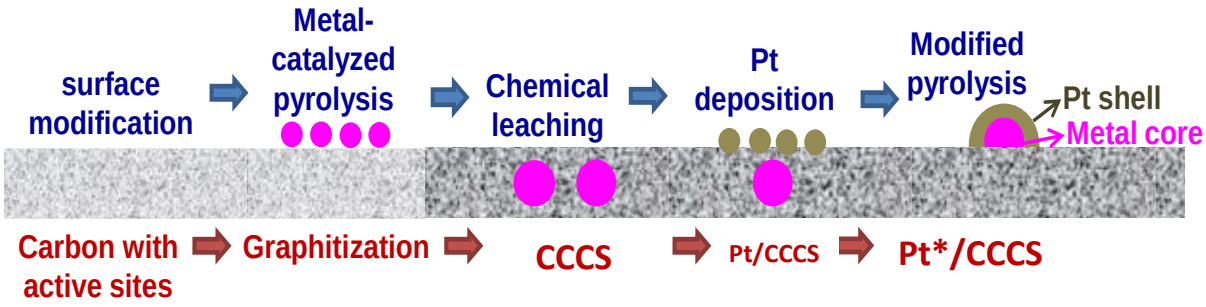

Figure 21. Schematic diagram of synthesize Pt*/CCCS.

It has been reported that the Pt-alloy particle size can increase as high as 20 nm after heat-treatment at 800 °C [171]. In order to control the particle-size growth and inhibit particle agglomeration, a novel protective-coating methodology with polyaniline was developed for the synthesis of Pt*/CCCS during high temperature pyrolysis process. In order to study the effectiveness of the polyaniline protective coating, the Pt/CCCS catalyst was pyrolyzed at 800 °C for 60 min in the presence of protective coating and at 800 °C for 30 min without protective coating. The HRTEM images of these two catalysts are compared in Figure 22. It is important to note that the Pt/CCCS catalyst heated for 30 min. in the absence of polyaniline protective coating resulted in particle agglomeration and Pt particle size growth (5-8 nm). On the other hand, the catalyst obtained after pyrolysis at 800 °C for 60 min. with the polyaniline protective coating showed very uniform particle distribution with an average particle size of ~3.5 nm.

The novelty of the catalyst synthesis is to diffuse Co, which is already incorporated in to the graphitic carbon matrix (CCCS), into Pt to form Pt* catalyst during heat-treatment as reported in our previous studies [93, 172]. This procedure is much simpler than the conventionally used impregnation method which uses excess amount of transition metal salts for impregnating Pt/C catalyst followed by heat-treatment to make PtM_3 (M = Cu, Co, Ni) catalyst [58, 82, 83, 103, 173, 174]. The unreacted transition metals are then leached out in strong acids for longer duration [58, 103, 173, 174].

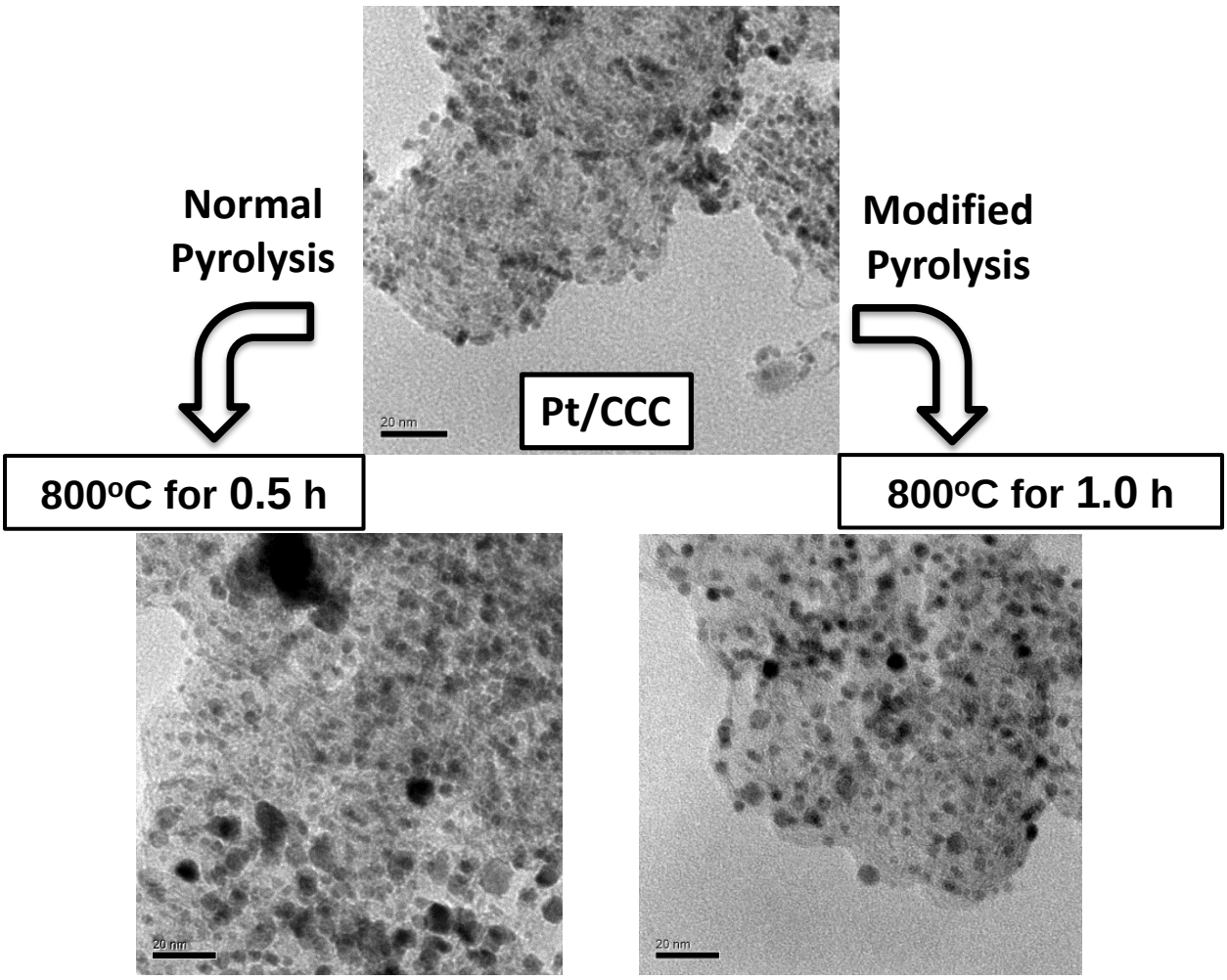

Figure 22. TEM images of Pt/CCCS pyrolyzed with and without protective coating.

The HRTEM images of Pt/CCCS, Pt*/CCCS, commercial Pt-Co/C, and commercial Pt/C are shown in Figure 23 (a), (b), (c), and (d), respectively. The average particle sizes and the particle size distribution were measured using an average of 100 nanoparticles. The Pt nanoparticles are deposited with uniform size and distribution on the CCCS. The mean particle size is approximately 2.5, 5.4, 6, and 2.4 nm for the Pt/CCCS, Pt*/CCCS, commercial Pt-Co/C, and commercial Pt/C, respectively. For the Pt/CCCS catalyst, Pt nanoparticles uniformly deposit on the support and 2-3 nm-sized particles are dominant. Most of the particles in Pt*/CCCS catalyst are in the range of 4-7 nm while a few large particles are shown due to the high temperature treatment, but well-distributed on the support. However, the commercial Pt-Co/C showed majority of the particles in the range 5-6 nm with considerable number of particles that are above 10 nm and as high as 20 nm.

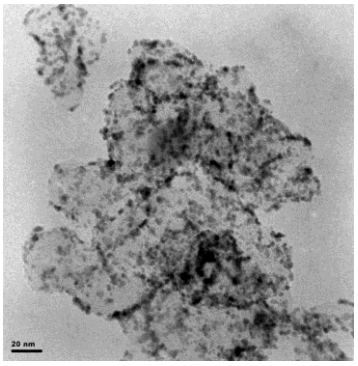

(a) Pt/CCCS

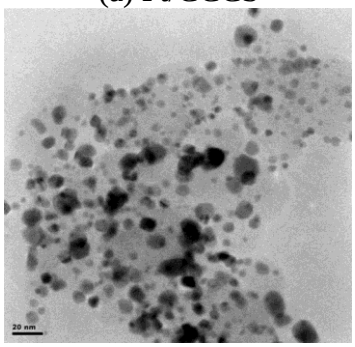

(b) Pt*/CCCS

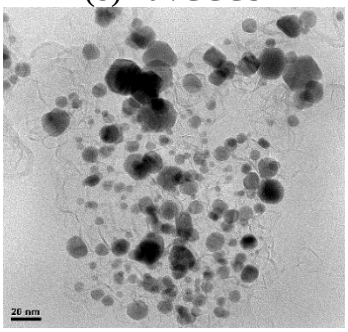

(c) Commercial Pt/Co/C

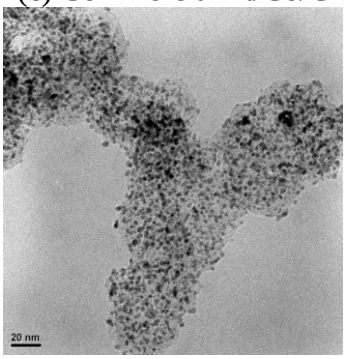

(d) Commercial Pt/C

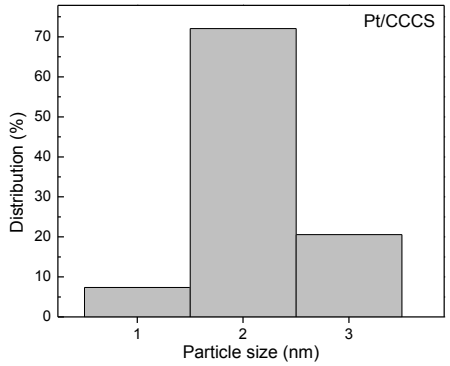

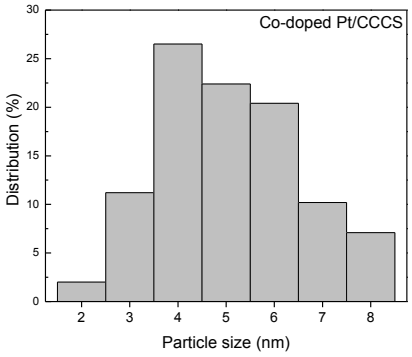

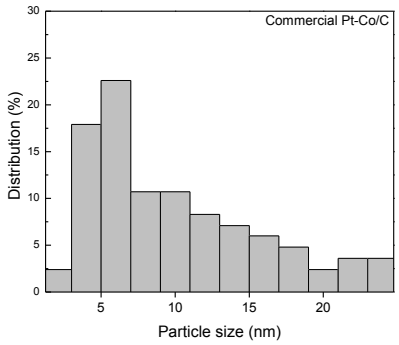

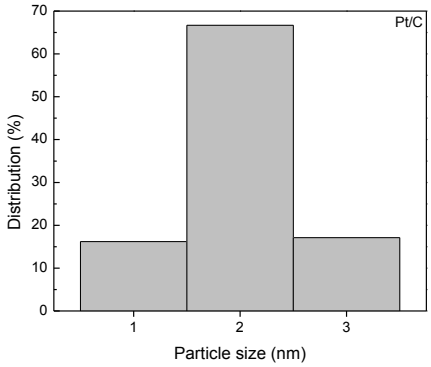

Figure 23. HRTEM images of fresh (a) Pt/CCCS and (b) Pt*/CCCS catalysts. Scale bar is 20 nm.

To study the effect of heat-treatment time on the Co doping, the Pt/CCCS catalyst was heat treated at 800 °C for different time and the catalysts were characterized by XRD (Figure 24). With the inclusion of Co into the fcc structure of Pt, the reflections for Pt shifts to a higher 2θ values which indicates the contraction of Pt lattice [175]. The degree of doping increases as the heat- treatment time increases as seen from the shift in the 2θ to higher values (Figure 24a). Two peaks can be observed in Pt (2 2 0) which appears at 66-70° for the 30 (circled in Figure 24a) and 60 min. heat-treated samples. The de-convoluted XRD peak (2 2 0) for 30 minutes heat-treated sample is shown in Figure 24b. The first peak that appears at 67.8° corresponds to pure Pt, while the other peak at 69.5° results from Pt* catalyst. The de-convolution results indicate that Co starts to diffuse into the Pt particle from the Co-doped CCCS. Co-doping increases with the increase of the heat-treatment duration. Complete Co diffusion into Pt particles resulting in Pt* catalyst is completed after heat-treatment duration of 2 h.

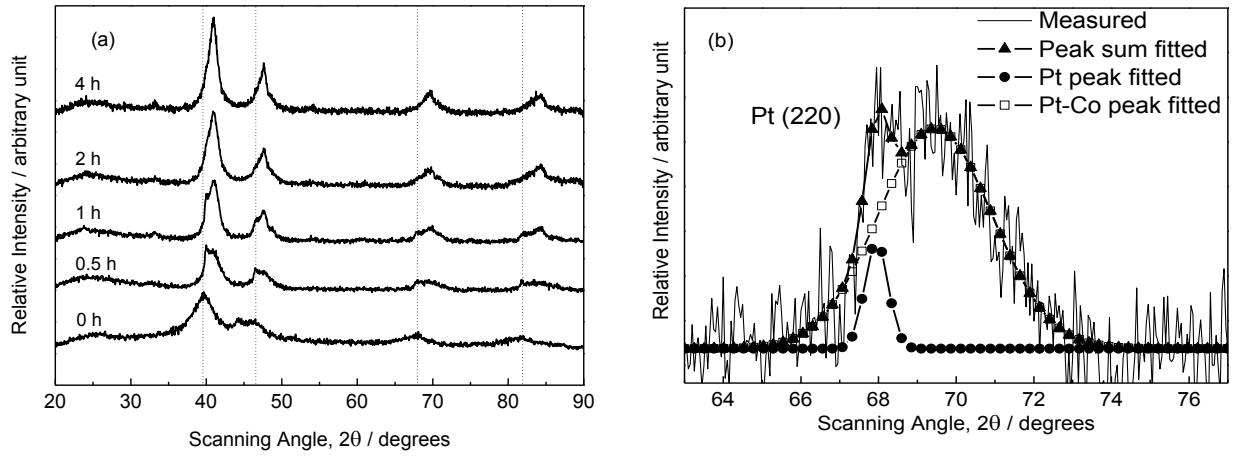

Figure 24. (a) XRD patterns of Pt/CCCS catalyst annealing from 0.5 hour to 4 hours, (b) de-convoluted XRD peak <2 2 0> for 0.5-hour heat-treated Pt*/CCCS catalyst.

The line-scan of XEDS results for Pt*/CCCS (fresh) is shown in Figure 25. The fresh Pt*/CCCS shows an initial Pt-rich layer thickness of ~0.75 nm. From density functional theory simulations, it has been postulated that the optimized Pt skin thickness is 2 to 3 monolayers which is equal to 0.50 - 0.75 nm [176, 177]. It has also been reported that the ligand effects are only effective up to 1-3 atomic layers [178] and the geometric effects can modify the Pt-Pt interatomic distances up to 7 atomic layers [179]. Since the Pt-shell thickness in Pt*/CCCS is ~3

atomic layers, the increased ORR activity can be attributed to the combination of ligand and geometric effects resulted from Co doping in the Pt lattice.

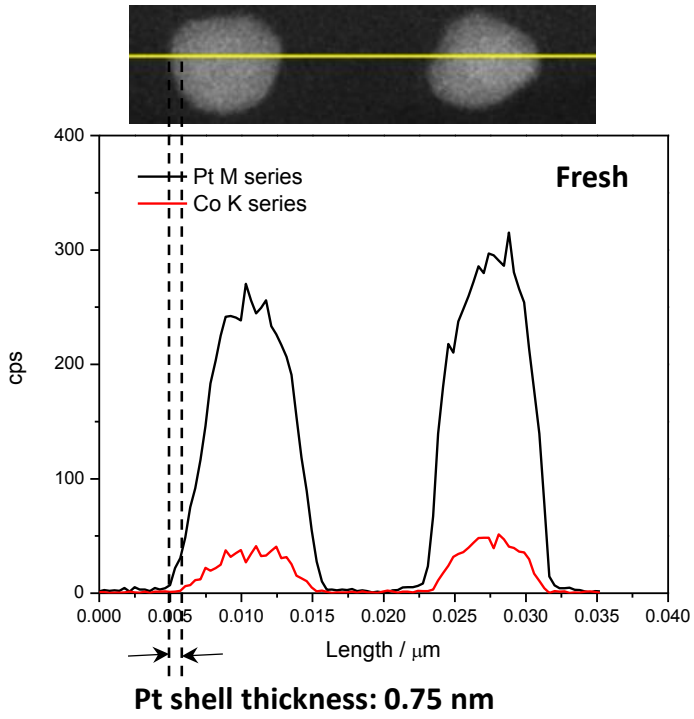

Figure 25. XEDS particle line-scan of Pt*/CCCS catalyst (fresh).

4.2.6. Evaluation of catalyst durability under 0.6-1.0 potential cycling conditions

The initial mass activities and stability of mass activities of Pt*/CCCS in three 25 cm^2 MEAs are shown in Figure 26 (a-c). The stability of mass activity of commercial Pt_3Co/C, and commercial Pt/C catalysts at 0.9 ViR-free are shown in Figure 27 (a & b) for comparison. The mass activity is defined as the ORR rate per gram of Pt measured at 0.9 $V_{iR\text{-}free}$. The mass activity measurements were performed using the AST protocol suggested by U.S DRIVE Fuel Cell Tech Team [45]. The Pt*/CCCS shows much higher kinetic activity (0.4~0.44 A/mg_{Pt}) at 0.9 $V_{iR\text{-}free}$ than the commercial Pt_3Co (0.38 A/mg_{Pt}) and commercial Pt/C (0.15 A/mg_{Pt}) catalysts due to the formation of Pt* core and Pt-rich shell type catalyst particles with compressive Pt lattice during annealing [56, 180-182]. The high kinetic activity can be attributed to the formation of Pt* core and Pt-rich shell type catalyst particles during annealing. When transition metals such as Co are used to modify Pt, two major electronic effects namely, strain effect and ligand effect, are induced within the Pt host lattice [181, 183-185]. The strain effect leads to a decrease in the Pt-Pt

interatomic distance when compared to pure Pt while the ligand effect results in the modification of the surface electronic structure due to hetero-metallic bonding interactions [184].

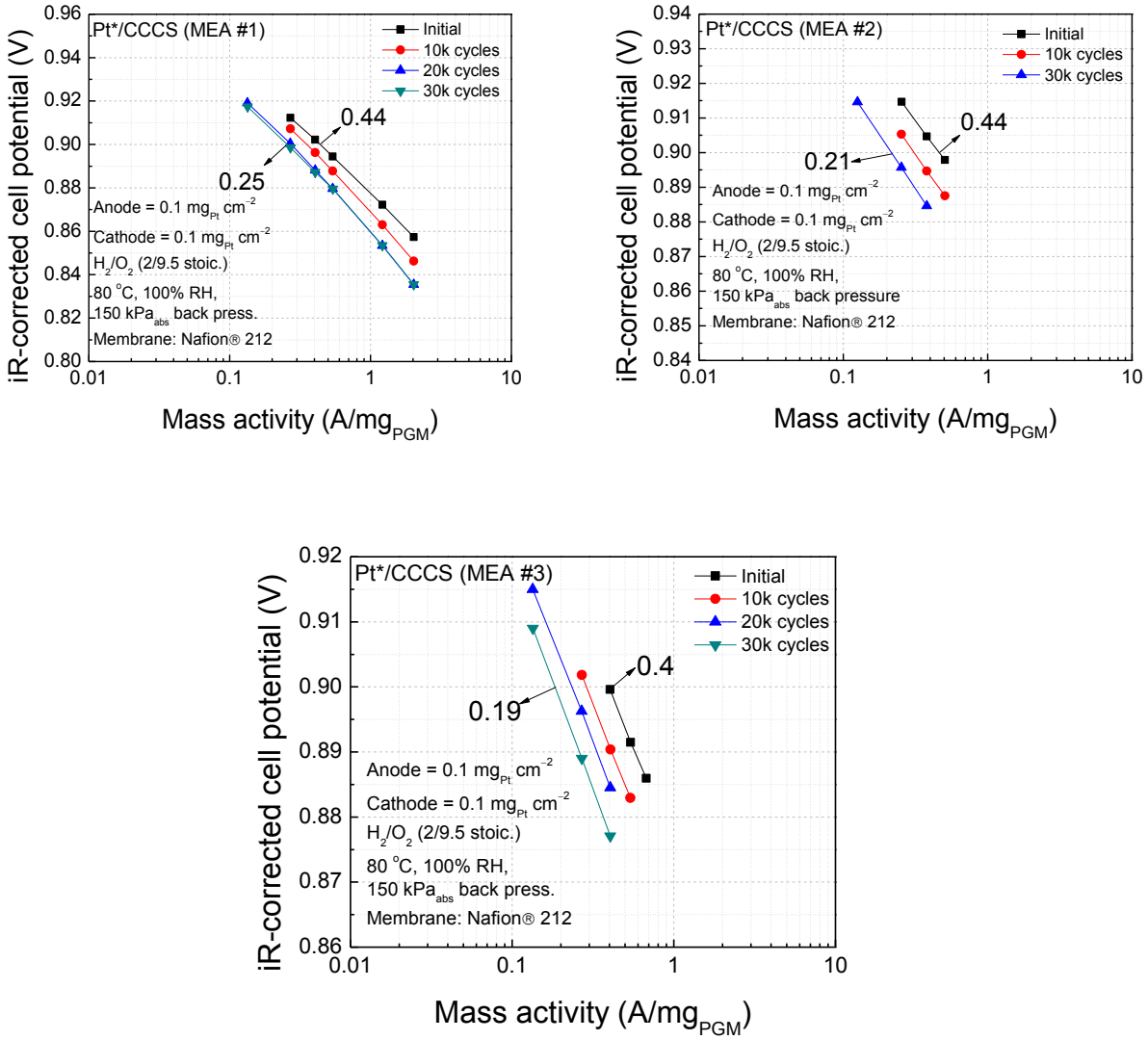

Figure 26. Reproducibility of initial and stability of mass activities of Pt*/CCCS in three 25 cm^2 MEAs. H_2/O_2 (2/9.5 stoic.), 80 °C, 100% RH, and 150 kPa_{abs}. back pressure.

As indicated in Figure 28 (a-c), the Pt*/CCCS tested in three 25 cm^2 MEAs shows a stable H_2-air fuel cell performance with only 40~46 mV loss after 30,000 cycles between 0.6 and 1.0 V. On the other hand the performance of commercial Pt_3Co/C and commercial Pt/C catalysts drastically decreased due to Ostwald ripening, Pt dissolution and re-deposition as shown in Figure 29(a) and Figure 29(b), respectively.

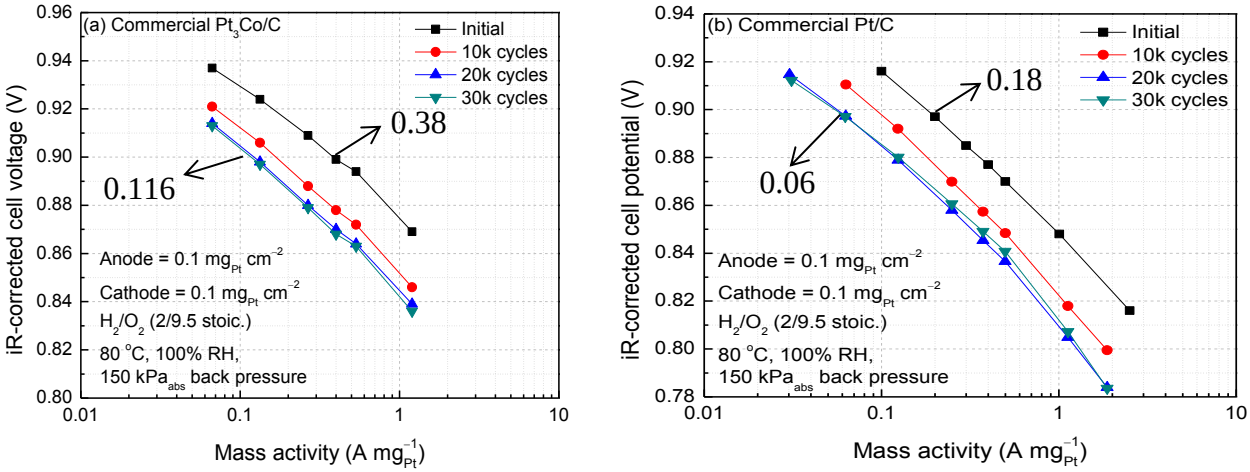

Figure 27. Initial and stability of mass activity of (a) commercial Pt_3Co/C and (b) commercial Pt/C catalysts as a function of cycle number. H_2/O_2 (2/9.5 stoic.), 80 °C, 100% RH, and 150 $kPa_{abs.}$ back pressure.

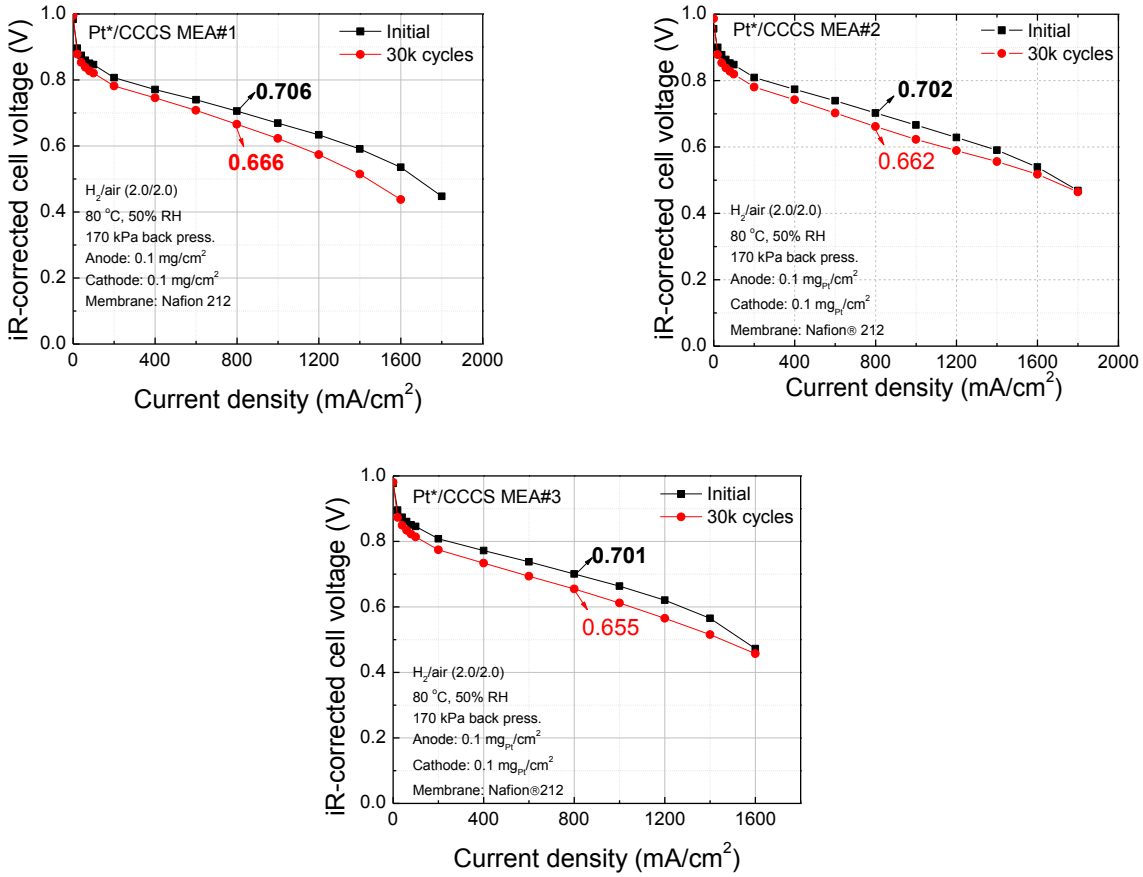

Figure 28. Reproducibility of stability of H_2-air polarization performance of Pt*/CCCS in three 25 cm^2 MEAs. The fuel cell operating conditions are: H_2/air (2.0/2.0), 80 °C, 50% RH, 170 kPa back pressure.

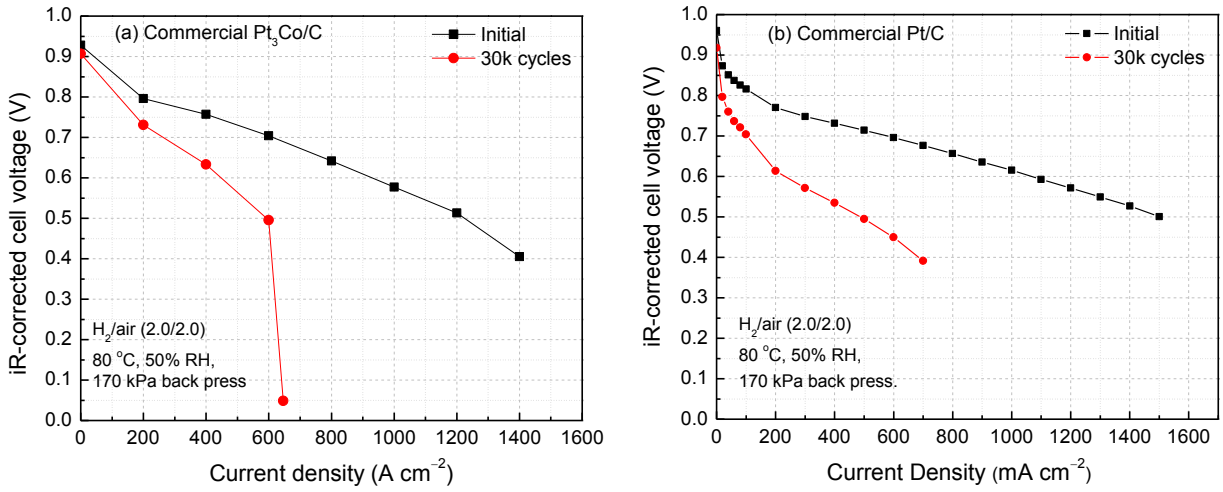

Figure 29. H_2-air polarization curves and the corresponding power density of the PEM fuel cells prepared with (a) commercial Pt_3Co/C and (b) commercial 46% Pt/C catalysts before and after 30,000 cycles. The fuel cell operating conditions are: H_2/air (2.0/2.0), 80 °C, 50% RH, 170 kPa back pressure.

The mass activity degradation tendencies of Pt*/CCCS, commercial Pt-Co/C, and Pt/C catalysts are summarized in Fig. 30. The figure shows a linear decrease until 20,000 cycles and stabilized after 20,000 cycles for all the three catalysts. The initial mass activity and mass activity after 30,000 cycles and H_2-air fuel cell performance of Pt*/CCCS (in three MEAs), commercial Pt-Co/C, and Pt/C catalysts are summarized in Table 6. After 30,000 cycles, the overall mass activity losses are ca. 43%, 69%, and 64% for Pt*/CCCS, commercial Pt-Co/C, and commercial Pt/C, respectively. Furthermore, the Pt*/CCCS still retained a significant amount of mass activity (0.24 A/ mg_{Pt}) after 30,000 cycles which is much higher than that of initial mass activity of Pt/C catalysts reported in literature [90, 186]. This may be due to the fact Co doping has increased the durability of Pt*/CCCS catalyst under potential cycling conditions. After potential cycling between 0.6 and 1.0 V, thick Pt skin (~1.8 nm) is formed on the catalyst due to Pt dissolution/re-deposition (Figure 31), which is still active for the ORR as indicated by the high mass activity even after 30,000 cycles. The thick Pt skin reduces the electronic effect in Pt* [176] which may be one of the reasons for the mass activity loss besides the well-explained Pt particle agglomeration effect [20]. On the other hand, Co from commercial Pt-Co/C catalyst is rapidly dissolved after 10,000 cycles and the mass activity reached a value which is close to that of initial value for the Pt/C catalyst. Thus, after 10,000 cycles, the commercial Pt-Co/C catalyst

performs like a pure Pt/C catalyst and further performance degradation is caused by the Pt dissolution and redeposition mechanism which occurs at higher rate than the one observed for Pt*/CCCS.

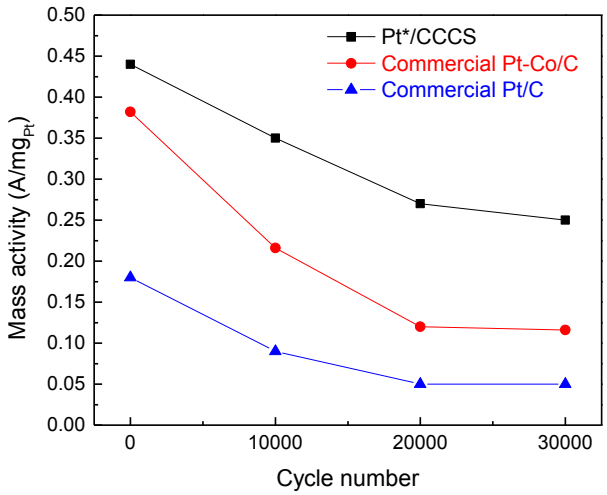

Figure 30. Summary of mass activity degradation of Pt*/CCCS, commercial Pt-Co/C, and commercial Pt/C catalysts as a function of cycle number.

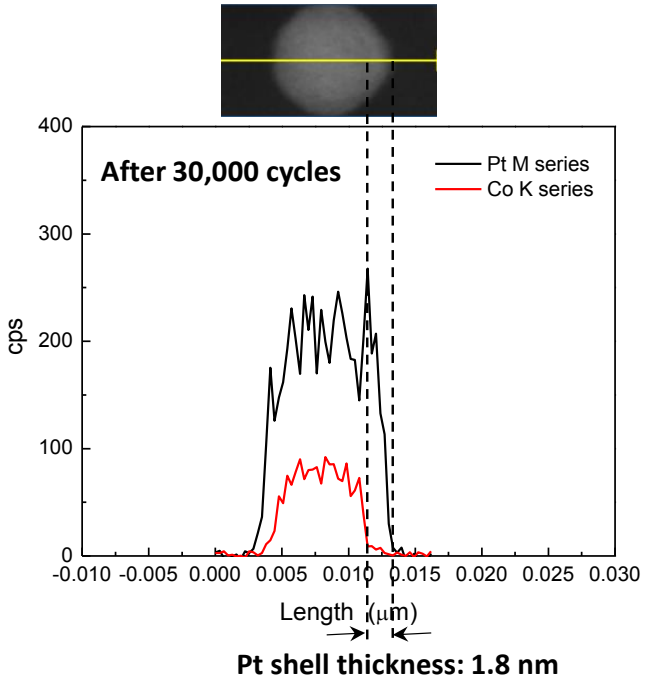

Figure 31. XEDS particle line-scan of Pt*/CCCS catalyst (after 30,000 cycles).

Table 6. Comparison of measured activities in H_2-O_2 at 0.9 $V_{iR\text{-}free}$, open circuit potentials in H_2-air, and maximum power density for Pt*/CCCS, commercial Pt-Co/C, and commercial Pt/C catalysts.

Catalyst	Mass activity at 0.9 $V_{iR\text{-}free}$ (A/mg_{Pt})*			iR-corrected potential at 0.8 A/cm^2 (V)**			Maximum power density (mW/cm^2)**		
	Initial	30k	Loss (%)	0	30k	Loss (mV)	0	30k	Loss (%)
Pt*/CCCS									
MEA#1	0.44	0.25	43	0.706	0.666	40	857	721	16
MEA#2	0.44	0.21	52	0.702	0.662	40	863	779	8
MEA#3	0.40	0.19	53	0.701	0.655	46	791	732	8
Commercial Pt_3Co/C	0.38	0.116	69	0.640	-	-	482	251	48
Commercial Pt/C	0.18	0.06	67	0.656	-	-	746	274	63

* H_2/O_2 (2/9.5 stoic.), 80 °C, 100% RH, 150 $kPa_{abs.}$ back pressure.

** H_2/air (2/2 stoic.), 80 °C, 50% RH, 170 $kPa_{abs.}$ back pressure.

To further understand the loss in measured activity and H_2-air fuel cell performance, the normalized ECSAs calculated for Pt*/CCCS, commercial Pt-Co/C, and Pt/C catalysts as a function of cycle number are shown in Figure 32. Initial ECSA values of 75, 68, and 75 m^2/g_{Pt} were obtained for Pt*/CCCS, commercial Pt-Co/C, and commercial Pt/C catalysts, respectively. Lower degradation rate for Pt*/CCCS is observed in Figure 32 after 10,000 cycles when compared to commercial Pt Co/C and Pt/C catalysts. After 30,000 cycles, 64%, 21%, and 18% of initial ECSA are retained for Pt*/CCCS, commercial Pt-Co/C, and commercial Pt/C catalysts, respectively, which indicate that the Pt*/CCCS is remarkably stable when compared to commercial Pt-Co/C and Pt/C catalysts.

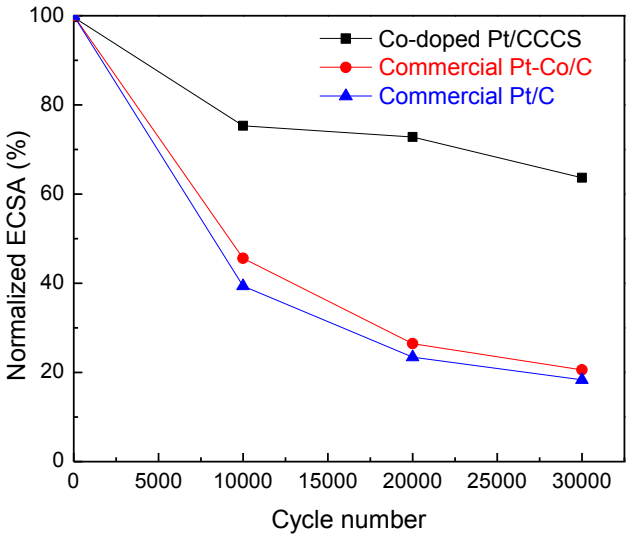

Figure 32. Normalized ECSA plot of Pt*/CCCS, commercial Pt-Co/C, and commercial Pt/C catalysts as a function of cycle number. ECSAs were calculated from cyclic voltammograms obtained between 0.05 and 0.6 V (vs. RHE) at 80 °C. Fully humidified H_2 (75 sccm) and N_2 (200 sccm) were supplied to the anode and the cathode, respectively.

The HRTEM images of Pt*/CCCS and commercial Pt/C after AST are shown in Figure 33 (a) and (b), respectively. After AST, the mean particle size of Pt*/CCCS and Pt/C increased to 6.2 nm 7.3 nm, respectively and the particle size distribution based on the histograms represents that the particle size of Pt*/CCCS still exhibits good catalyst dispersion and no extensive agglomeration is observed. On the other hand, the Pt/C shows large particles (> 10 nm)

and significant catalyst agglomeration indicating poor particle distribution. Since the ECSA and particle agglomeration are related to the catalyst activity, the measured activity of Pt*/CCCS is more stable than that of commercial Pt-Co and Pt/C catalysts.

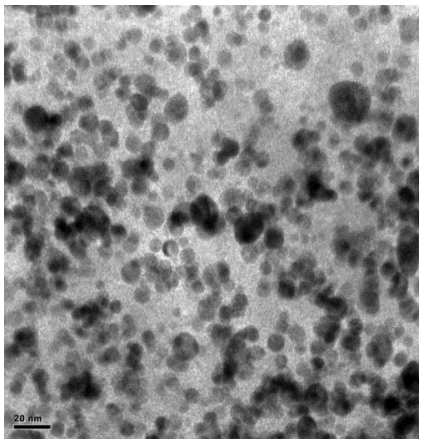

(a) Pt*/CCCS (after 30,000 cycles)

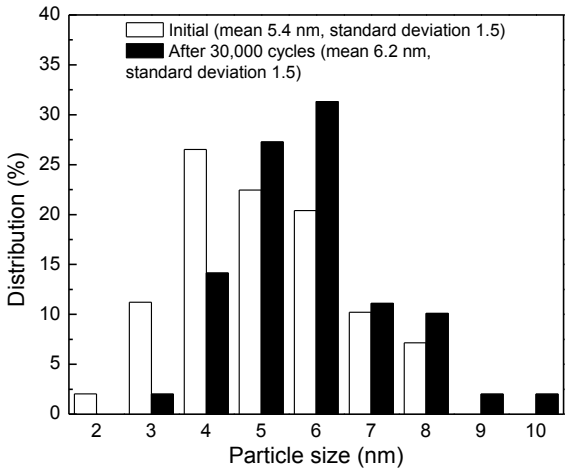

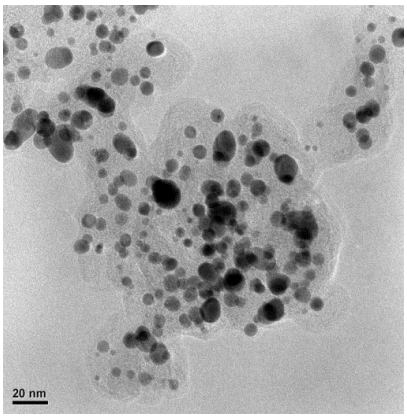

(b) Commercial Pt/C (after 30,000 cycles)

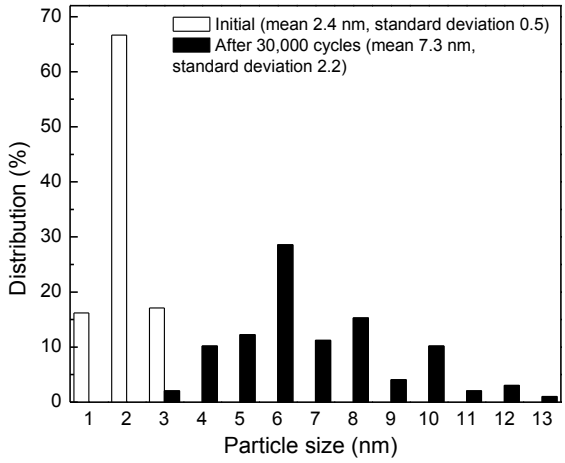

Figure 33. HRTEM images and particle size distribution for (a) Pt*/CCCS and (b) commercial Pt/C catalysts before and after 30,000 cycles. Scale bar is 20 nm.

XRD studies were performed to investigate the structural changes in Pt*/CCCS catalyst before and after AST as shown in Figure 34. After the AST, the Pt*/CCCS shows obvious Bragg angle shift to lower angles. The lattice parameter for the Pt*/CCCS catalyst increased from 3.8006 to 3.9082 Å. The increased lattice parameter after AST is similar to that of pure Pt which indicates that the catalyst surface is modified with thick Pt-rich layer during potential cycling experiment. The Co on the catalyst surface is removed electrochemically during potential cycling between 0.6 and 1.0 V, and the dissolution/redeposition of Pt occurs on the catalyst particles. As

a result, thick Pt-enriched layer is formed on the catalyst particles. Recent reports attributed the structural and compositional changes to the degradation of Pt-Co catalyst stability [187]. Furthermore, the peak shift of Pt-Co catalyst toward lower angle was ascribed to the formation of Pt-rich shell due to Co dissolution [188]. Hidai et al., using Co 2p soft X-ray photoemission spectroscopy (SXPES) spectra of the cycle-tested Pt-Co catalyst, showed absence of cobalt on the surface of catalyst particles and the presence of thick Pt skin layer (>1.4 nm) on the catalyst surface [189].

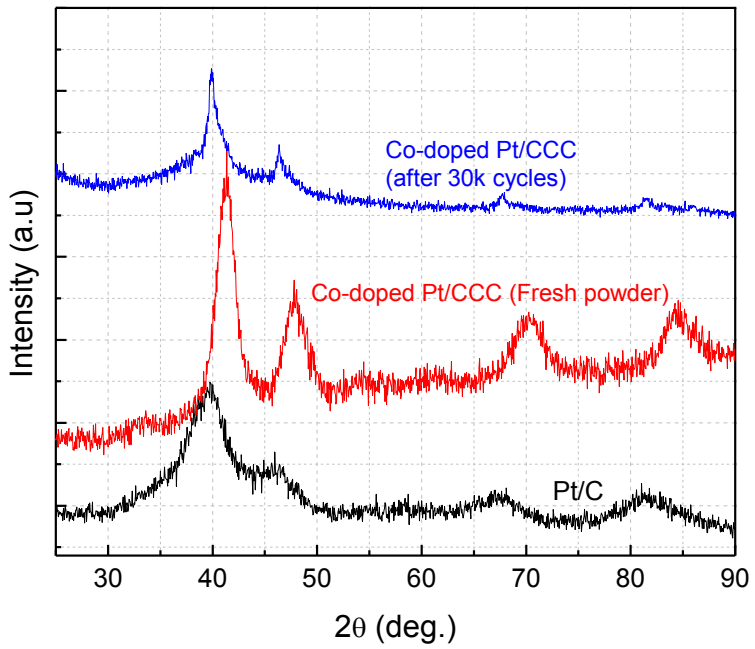

Figure 34. Comparison of X-ray diffraction patterns of Pt/C, Pt*/CCCS (fresh powder), and Pt*/CCCS (after 30,000 cycles).

The elemental composition of Pt*/CCCS catalyst before and after AST was examined using XRF (Table 7). The results indicated that the initial Pt:Co atomic ratio (1.1:1) for the fresh Pt*/CCCS increased to 2.3:1 after 30,000 cycles due to the dissolution of Co from the catalyst during potential cycling. Previous studies have also showed Pt-Co catalyst degradation under fuel cell operating conditions due to rapid leaching of Co and formation of a "Pt skeleton" structure at the topmost surface layer within the first few hours of operation [79, 80]. Further degradation makes a Pt-enriched shell/Pt-Co core structure due to Co surface segregation/leaching and Ostwald ripening of Pt [189, 190]. It has been found that the Co content

in the bulk Pt-Co decreased and Co concentration of near-surface Pt-Co was lower than the bulk concentration after degradation [189].

Table 7. Pt:Co atomic compositions of Pt/CCCS and Pt*/CCCS given by ICP-AES, XPS, and XRF.

	ICP	XPS	XRF	
			Initial	After AST
Pt/CCCS	1:1	-		
Pt*/CCCS	1.1:1	1.2:1	1.1:1	2.3:1

Table 8 compares measured activities in H_2-O_2 at 0.9 $V_{iR\text{-}free}$, open circuit potentials (OCP) in H_2-air, and maximum power density in H_2-air fuel cell for Pt*/CCCS, commercial Pt-Co/C, and commercial Pt/C catalysts. The OCP measurements indicated stable and very high values for the Pt*/CCCS during the entire potential cycling period. Specifically, the OCP after 10,000 cycles is close to 1.0 V which may be attributed to the Co dissolution and formation of Pt-rich surface layer during potential cycling.

Table 8. Comparison of open circuit potentials in H_2-air for Pt*/CCCS, commercial Pt-Co/C, and commercial Pt/C catalysts.

Catalyst	Open circuit potential (V)**			
	Initial	10,000 cycles	20,000 cycles	30,000 cycles
Pt*/CCCS	0.984	0.998	0.997	0.995
Commercial Pt-Co/C	0.922	0.918	0.906	0.907
Commercial Pt/C	0.960	0.949	0.940	0.917

Furthermore, as indicated in Table 6, the Pt*/CCCS showed initial power density of 857 mW/cm^2 with a loss of only 16% after 30,000 cycles under H_2-air fuel cell operating conditions. On the other hand, the commercial Pt-Co/C and Pt/C catalysts showed initial power densities of 482 and 746 mW/cm^2, respectively and very high power density losses of 48 and 63%, respectively after 30,000 cycles. The drastic performance degradation for the commercial Pt-

Co/C and Pt/C catalysts can be attributed to Ostwald ripening, Pt dissolution and redeposition [3-9, 145, 185].

The H_2-O_2 fuel cell polarization under constant flow of 750/750 sccm shown in Figure 35 indicates no performance degradation when the cathode reactant is sufficiently supplied for ORR at 100% RH since the Pt*/CCCS catalyst maintains the catalytic activity before and after 30,000 cycles. However, our previous study indicated a significant performance loss for the commercial Pt/C catalyst under the same operating conditions [145].

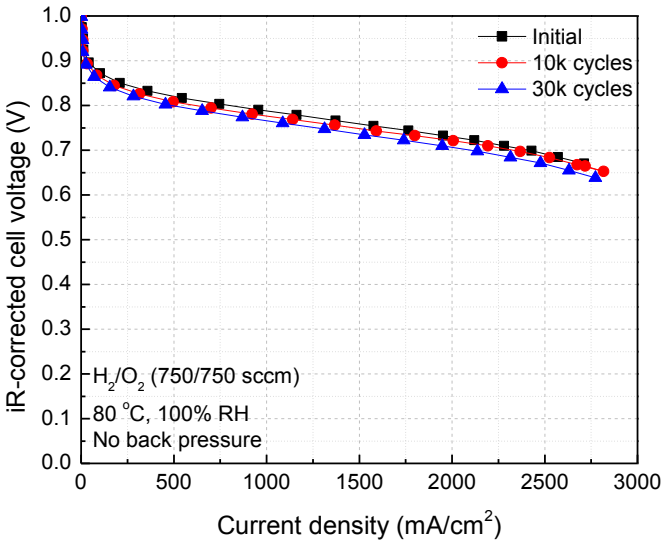

Figure 35. H_2-O_2 fuel cell polarization curves of Pt*/CCCS catalyst (initial and after 10,000 and 30,000 cycles). The cell was operated at 80 °C, 100% RH with a constant flow of H_2/O_2 (750/750 sccm). No back pressure was applied during the measurement.

It has been reported that water activation and Pt-OH formation on Pt-Co catalyst surface is shifted to higher potentials when compared to pure Pt [54, 191, 192]. The cyclic voltammograms recorded in rotating ring disk electrode (RRDE) for Pt*/CCCS and Pt/CCCS catalysts shown in Figure 36 indicate a shift in Pt-OH formation by ~40 mV for the Pt*/CCCS when compared to Pt/CCCS. Figure 37 also shows two regions namely, H adsorption/desorption below 0.4 V and oxygen-related reactions (Pt oxidation/reduction) between 0.6 and 1.0 V. During potential cycling from 0.6 to 1.0 V, Pt oxides are formed according to the following reactions [44]:

$$Pt + H_2O \rightarrow PtO + 2H^+ + 2e^- \quad (22)$$

$$Pt + 2H_2O \rightarrow PtO_2 + 4H^+ + 4e^- \quad (23)$$

At high potentials, adsorbed oxygen (Pt-O_{ad}) is formed due to water oxidation:

$$Pt + H_2O \rightarrow Pt - O_{ad} + 2H^+ + 2e^- \quad (24)$$

In the reverse scan from 1.0 to 0.6 V, platinum oxides are reduced to Pt according to the following reactions:

$$PtO + 2H^+ + 2e^- \rightarrow Pt + H_2O \quad (25)$$

$$PtO_2 + 4H^+ + 4e^- \rightarrow Pt + 2H_2O \quad (26)$$

$$Pt - O_{ad} + 2H^+ + 2e^- \rightarrow Pt + H_2O \quad (27)$$

The potential shift for Pt oxidation to higher values, as indicated by the higher OCP observed in H_2-air polarization curve, increases the mass activity (from 0.15 to >0.4 A/mg_{Pt}) due to the suppression of Pt oxide formation which has much lower exchange current density for ORR (i^o =1.7×10^{-10} A/cm^2) when compared to pure Pt (i^o = 2.8×10^{-7} A/cm^2) [193]. Besides the effect of higher mass activity, Pt* catalyst also illustrates improved stability when compared to pure Pt catalyst. Since Pt oxide dissolves during potential cycling conditions according to Eq. (28), less PtO_2 formation in the forward scan due to higher Pt oxidation potential in the case of Pt*/CCCS catalyst alleviates Pt dissolution in the reverse scan and enhances the catalyst stability.

$$PtO_2 + 4H^+ + 2e^- \rightarrow Pt^{2+} + 2H_2O \quad (28)$$

However, in automotive applications at applied potentials of ~0.6-0.7 V, only pure Pt catalytic sites will be present on the catalyst surface for ORR at high current regions due to electrochemical reduction of Pt oxides formed when the cathode catalyst is subjected to high potentials during startup/shutdown cycles and/or fuel starvation. Thus, the H_2/air performance at low potentials will not be greatly affected as much as in the case of mass activity which is measured at 0.9 $V_{iR\text{-}free}$.

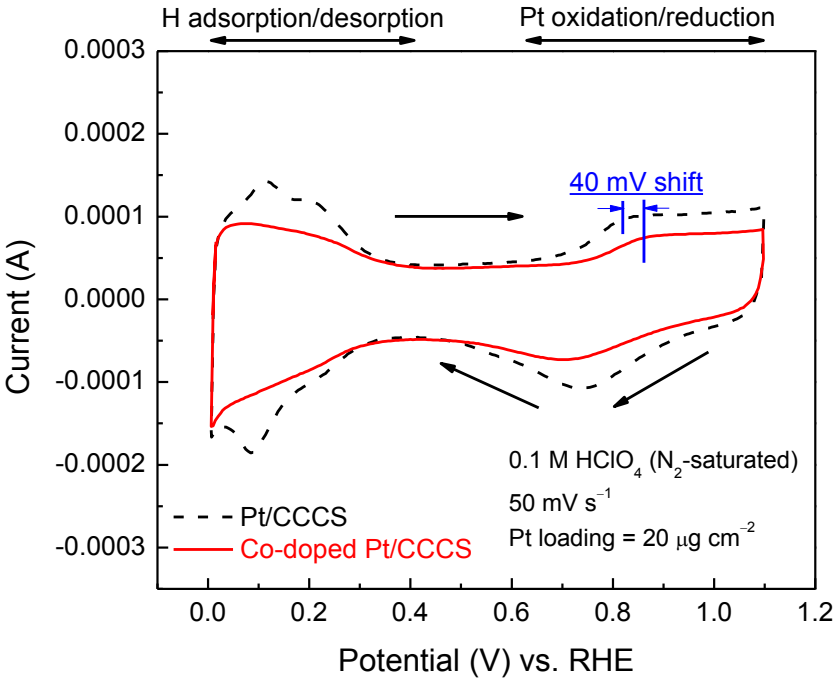

Figure 36. Cyclic voltammograms of Pt/CCCS and Pt*/CCCS. The measurements were carried out at room temperature by sweeping the potential from 0.05-1.1 V vs. RHE at 50 mV/ s in nitrogen-purged 0.1 M $HClO_4$.

4.3. Development of Pt and Pt* Catalysts Supported on Activated Carbon Composite Support (ACCS-1)

4.3.1. Synthesis of Activated Carbon Composite Support (ACCS-1)

In order to further improve the support stability at high potentials (1.0-1.5 V) the ACCS-1 was synthesized using a purification and stabilization process as shown in Fig. 37.

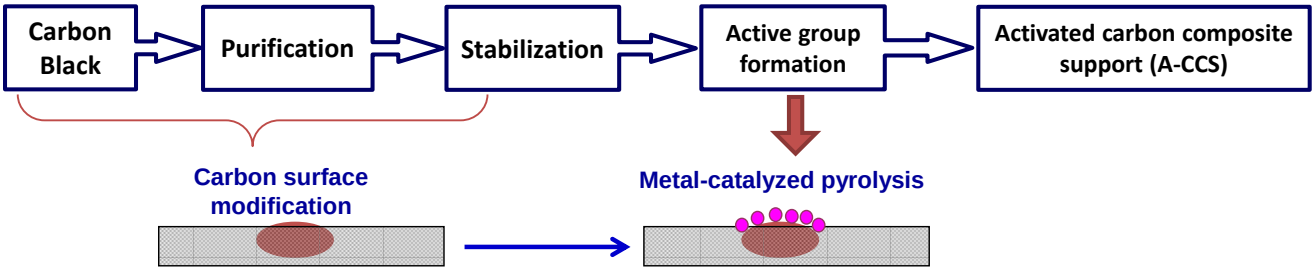

Figure 37. Schematic of ACCS-1 synthesis.

The ACCS-1 was used to synthesize 30% Pt/ACCS-1 catalyst. The HRTEM images shown in Fig. 38 indicate that the Pt particles are uniformly distributed over the ACCS-1 support with an average particle size of ~3.1 nm.

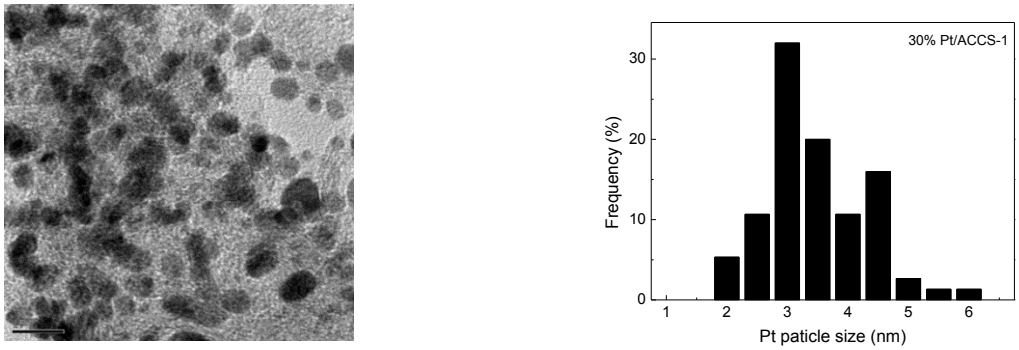

Figure 38. Transmission electron microscopy image of Pt/A-CCS-1 catalyst (The scale bar is 10 nm).

Figure 39 exhibits the XRD patterns of ACCS-1 and Pt/ACCS-1. It has been reported that higher L_c value of (002) peak at 26^o implies higher degree of graphitization, which can be calculated by Scherrer formula [194, 195]. The L_c value for A-CCS-1 is only 2.8 while that for Ketjen black is 1.1. Compared to CCCS, ACCS-1 did not show significant graphitic structures. However, due to difference in the carbon precursors' nature, ACCS-1 exhibits improved hydrophobicity.

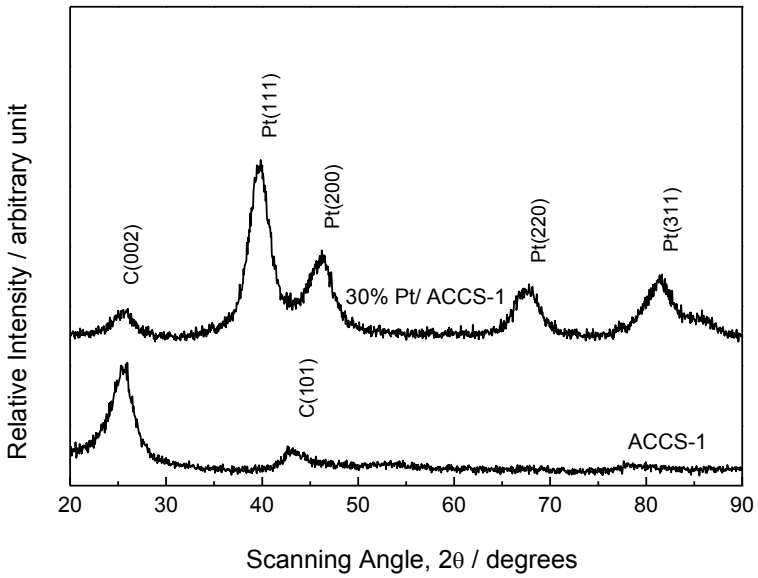

Figure 39. X-ray diffraction patterns of ACCS-1 support and 30% Pt/ACCS-1 catalyst.

Our previous studies on graphitic carbon supports indicated highly graphitic carbon is not friendly for Pt anchorage due to its small BET surface area and smooth surface. The catalyst after 30,000 potential cycles between 0.6 and 1.0V exhibits poor catalytic performance. Thus, it was very important to study the Pt-C interaction on ACCS-1 to improve the catalyst-support interaction and further enhance the catalyst durability.

4.3.2. Catalyst Stability of 30% Pt/ACCS-1 under 0.6-1.0 Potential Cycling Conditions

To investigate the Pt catalyst stability in PEM fuel cells under 100% RH and 80 °C cell temperature, potential cycling experiment (0.6-1.0 V for 30,000 cycles) was performed on the Pt/ACCS-1 and Pt/C catalysts. Figures 40, 41, and 42 present the polarization curves of 30% Pt/ACCS-1 and commercial Pt/C catalysts before and after 30,000 cycles under constant flow of H_2-O_2 (750/750 mL/min) (Fig. 40), stability of mass activity under H_2-O_2 (stoic 2.0/9.5) (Fig. 41), and H_2-air (2.0/2.0 stoic.) (Fig. 42) operating conditions, respectively. As shown in Figure 40(a), when the cathode reactant is sufficiently supplied for ORR at 100% RH, the Pt/ACCS-1 catalyst maintains the activity before and after 30,000 cycles. However, the performance loss of the commercial Pt/C catalyst is much more significant after 30,000 cycles (Figure 40 b).

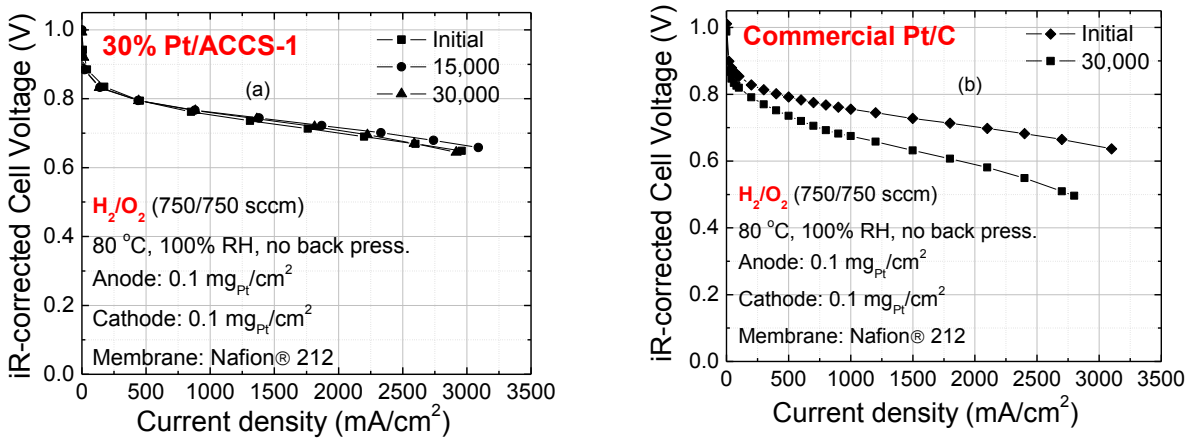

Figure 40. H_2-O_2 polarization curves of the PEM fuel cells prepared with (a) Pt/ACCS-1 and (b) commercial Pt/C catalysts before and after 30,000 cycles. The fuel cell operating conditions are: H_2/O_2 (750/750 sccm), 80 ^oC, 100% RH, no back pressure.

At kinetic region shown in Figure 41, when fuel supply is limited, mass activity losses of 50 and 61% are noticed for Pt/ACCS-1 and Pt/C, respectively. In the case of air with reduced humidity (50% RH), the performance decrease is observed in both the catalysts. In the case of Pt/ACCS-1 catalyst (Figure 42 a), the $V_{iR\text{-}free}$ loss is 72 mV (cell voltage decreased from 715 to 643 mV after 30,000 cycles between 0.6 and 1.0 V) at 800 mA/cm^2. Furthermore, the Pt/ACCS-1 catalyst showed initial maximum power density of 944 mW/cm^2 and 703 mW/cm^2 after 30,000 cycles (26% loss). The Pt/C (Figure 42 b) showed no activity at that current density and the maximum power density drops from 746 mW/cm^2 to 274 mW/cm^2 (63% loss). The increased stability can be attributed to strong π-bond in the ACCS-1 due to enhanced graphitic nature, which acts as anchoring sites (sp^2-hybridized carbon) for Pt [196, 197].

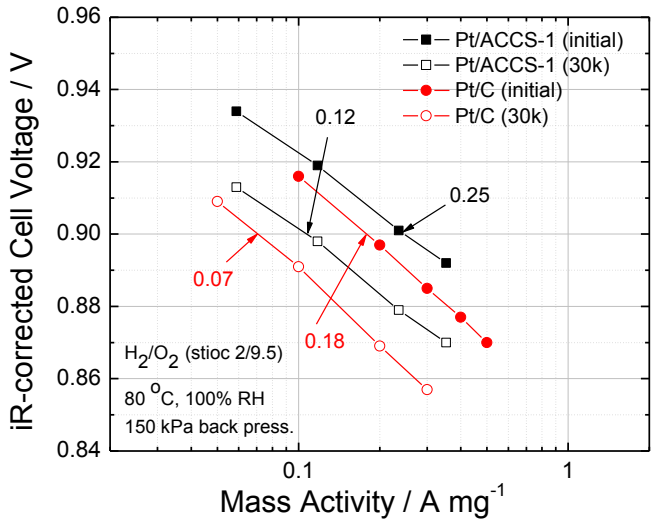

Figure 41. Mass Activity of Pt/ACCS-1 and Pt/C catalysts before and after 30,000 potential cycling between 0.6 and 1.0V (iR-corrected cell voltage vs. current density). The fuel cell operating conditions are: H_2/O_2 (2.0/9.5), 80 ^oC, 100% RH, 150kPa back pressure.

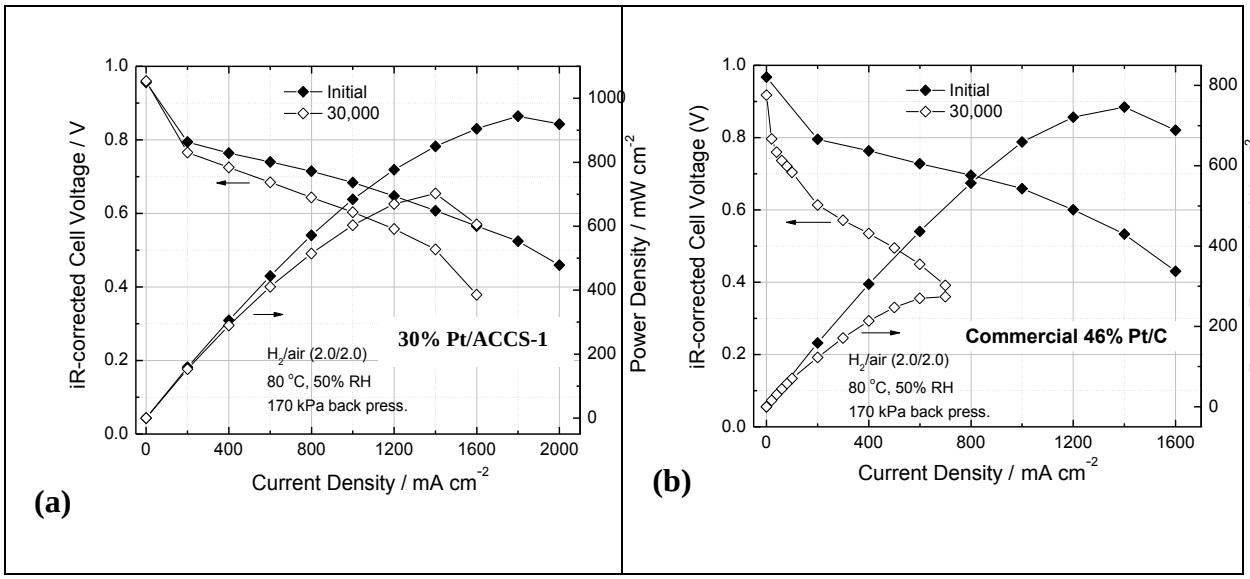

Figure 42. H_2-air polarization curves and the corresponding power density of the PEM fuel cells prepared with (a) 30% Pt/ACCS-1 and (b) commercial Pt/C catalysts before and after 30,000 cycles. The fuel cell operating conditions are: H_2/air (2.0/2.0), 80 ^oC, 50% RH, 170 kPa back pressure.

The ECSA change during potential cycling shown in Figure 43 also supports the above explanation. The ECSA of commercial catalyst experienced significant loss from 65 to 13 m^2/g while that of Pt/ACCS-1 is much more stable during the cycling test with only 41% loss (from 39 to 23 m^2/g). As shown in Figure 43(c), the normalized ECSA remained at around 60% of its initial value for the Pt/ACCS-1 catalyst when compared to 80% ECSA loss for the commercial Pt/C catalyst which is consistent with the results obtained from the polarization curves. With improved catalyst durability, it is also crucial to investigate the support stability at high potentials in order to be a promising candidate for automotive applications.

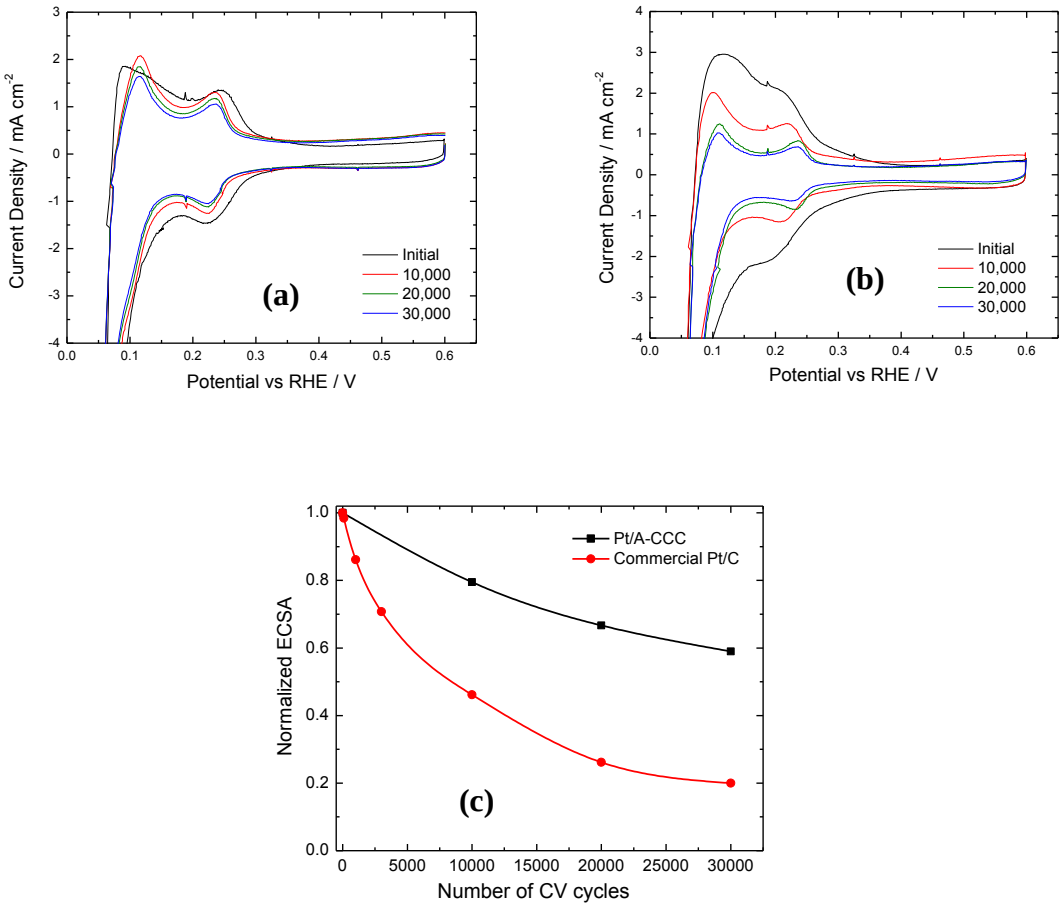

Figure 43. Cyclic voltammetry curves of (a) 30% Pt/ACCS-1 and (b) commercial Pt/C catalysts during 30,000 cycles; (c) normalized ECSA change as a function of potential cycles.

4.3.3. Support Stability of 30% Pt/ACCS-1 under 1.2 V Potential Holding Conditions

Corrosion of high surface area carbon in the presence of Pt is inevitable at high potentials under PEM fuel cell operating conditions such as high oxygen concentration, high water content, and low pH which favor carbon oxidation [164, 198]. During operation, the cathodes of automotive fuel cells often experience very high potentials due to startup/shutdown cycles or due to local fuel starvation at the anode [2, 41, 165]. Reiser et al. [41] have shown that the cathode interfacial potential difference can reach as high as 1.5 V due to the H_2/air front in the anode compartment during shutdown/startup. Carbon corrosion occurs at 0.207 V vs. RHE; however, it is not detected during fuel cell operation due to its sluggish reaction kinetics [2]. In general, carbon corrosion is estimated by measuring the amount of CO_2 produced [27, 29, 167, 168] or the corrosion current [2] at high applied potentials in a PEM fuel cell by supplying pure H_2 to the anode and pure N_2 to the cathode. However, the measured current is always coupled with the H_2-oxidation current at the cathode due to H_2 cross over from the anode through the Nafion® membrane [2]. In the present investigation, the cathode is subjected to 1.2 V constant potential for 400 h to study the support stability by measuring H_2-air polarization performance at regular intervals. The cell potential loss at 800 mA/cm^2 current density is used as a metric to evaluate the support stability in commercial Pt/C, and Pt/ACCS-1 catalysts.

The initial H_2-air polarization curve and polarization curves obtained after 100 h, 200 h, and 400 h potential holding at 1.2 V for the 30% Pt/ACCS-1 catalyst are compared in Figure 44. The 30% Pt/ACCS-1 catalyst showed an initial potential of 689 mV and 662 mV after 400 h potential holding with a potential loss of 27 mV. The initial peak power density is 1098 mW/ cm^2 which decreased to 958 mW/cm^2 after 400 h stability tests corresponding to a loss of only 13%. Besides, there is a mass activity loss of only 32% as shown in Fig. 45. Figure 46 (a) and Figure 46 (b) compare the ECSA loss in the fuel cell for the commercial 46.7% Pt/C and 30% Pt/ACCS-1 catalysts, respectively. The commercial Pt/C showed an initial ECSA of 52 m^2/g_{Pt} which drastically decreased to 15 m^2/g_{Pt} (71% loss) after 25 h due to severe carbon corrosion. Conversely, the 30% Pt/ACCS-1 showed much lower ECSA loss of only 30% with initial and final ECSA values of 40 and 28 m^2/g_{Pt}, respectively (Fig. 47).

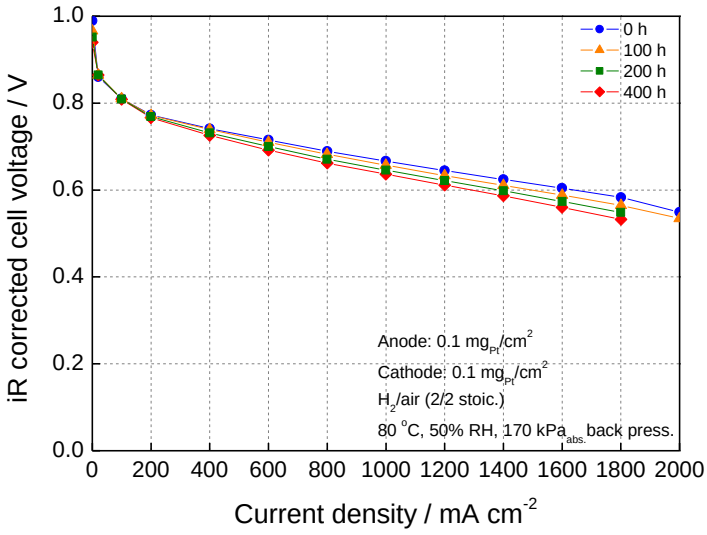

Figure 44. H_2-air polarization curves and the corresponding power density of the PEM fuel cells prepared with Pt/ACCS-1 catalyst before and after 400 hours potential holding at 1.2 V. The fuel cell operating conditions are: H_2/air (2.0/2.0), 80 °C, 50% RH, 170 kPa back pressure.

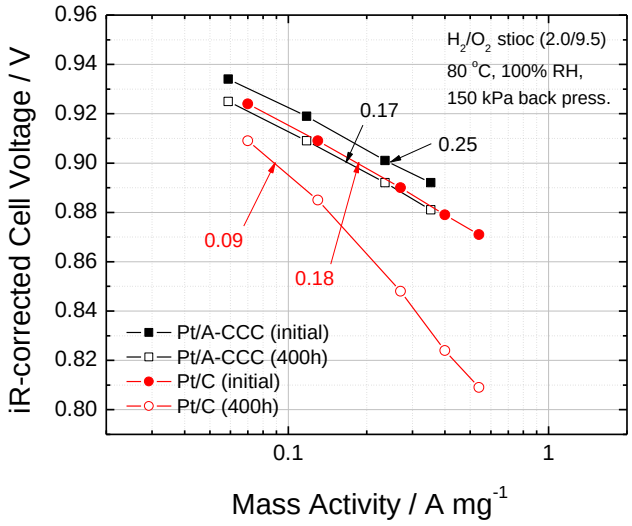

Figure 45. Mass activity of 30% Pt/ACCS-1 and Pt/C catalysts before and after 400h potential holding at 1.2 V (iR-corrected cell voltage vs. current density). The fuel cell operating conditions are: H_2/O_2 (2.0/9.5), 80 °C, 100% RH, 150kPa back pressure.

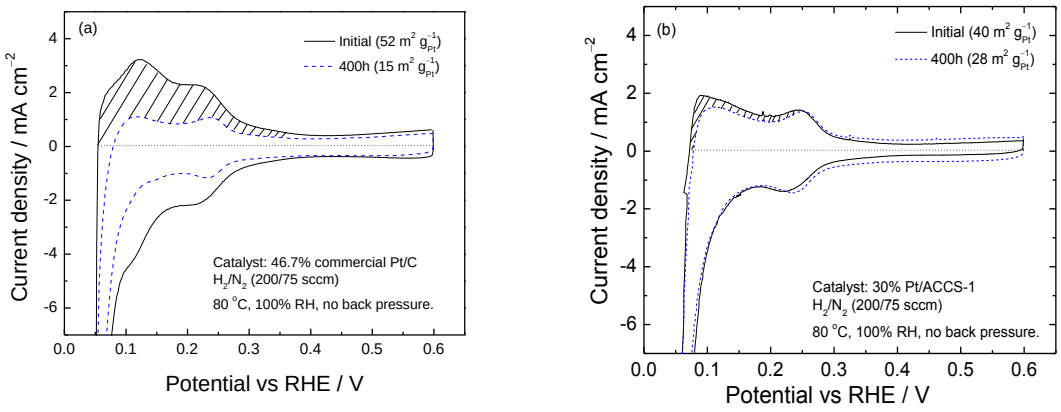

Figure 46. Cyclic voltammetry curves of (a) commercial Pt/C and (b) 30% Pt/ACCS-1 catalysts before and after 400 hours potential holding at 1.2 V.

All the fuel cell polarization results together with kinetic activity loss and ECSA loss data clearly indicate that graphitic carbon-support offers better corrosion resistance during potential holding. Furthermore, significantly low potential loss of 27 mV at 800 mA/cm^2 after 400 h potential holding experiment obtained for the 30% Pt/ACCS-1 catalyst is also attributed to the increased hydrophobicity of the support [167] and a relatively stronger catalyst-support interaction [197] when compared to other Pt catalysts investigated in this study.

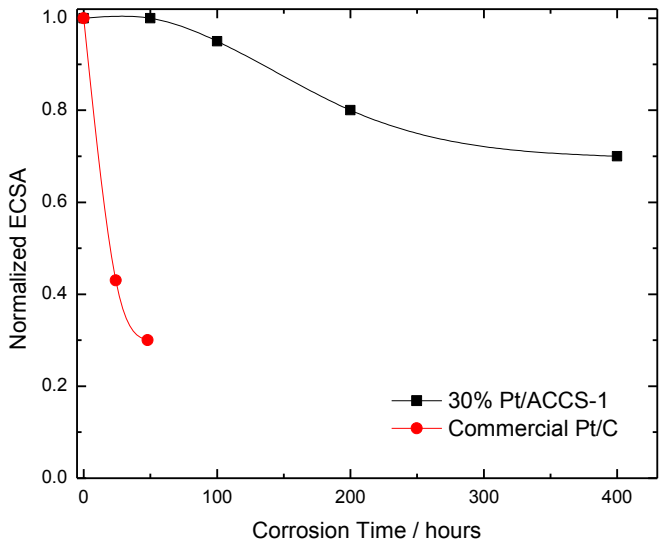

Figure 47. Normalized ECSA change as a function of potential holding time for commercial Pt/C and 30% Pt/ACCS-1 catalysts.

4.3.4. Support Stability of 30% Pt/ACCS-1 under 1.0-1.5 V Potential Cycling Conditions

In order to further evaluate the support stability of Pt/ACCS-1 under very severe corroding conditions, AST [199] between 1.0 and 1.5 V for 5,000 cycles at 500 mV/s sweep rate was performed under H_2/N_2 at 80 °C and 100% RH and the results are compared with that of commercial Pt/C catalyst in Figure 48 (a and b). The 30% Pt/ACCS-1 catalyst showed no potential loss up to 2,000 cycles and only 24 mV loss cycles at 1500 mA/cm^2 after 5,000 which satisfy the DOE targets for support stability [199]. The maximum initial power density is 970 mW/cm^2 and the loss is only 3% after 5,000 cycles which shows that the ACCS-1 support in 30% Pt/ACCS-1 catalyst is highly stable under severe corroding conditions. However, the commercial Pt/C catalyst showed drastic performance degradation after only 500 cycles and showed poor activity after 2,000 cycles due to severe carbon support corrosion at high potentials. These results clearly indicate that the ACCS-1 support offers better resistance to corrosion at high potentials between 1.0 and 1.5 V, which may be attributed to the increased hydrophobicity when compared to commercial high surface area supported Pt catalyst.

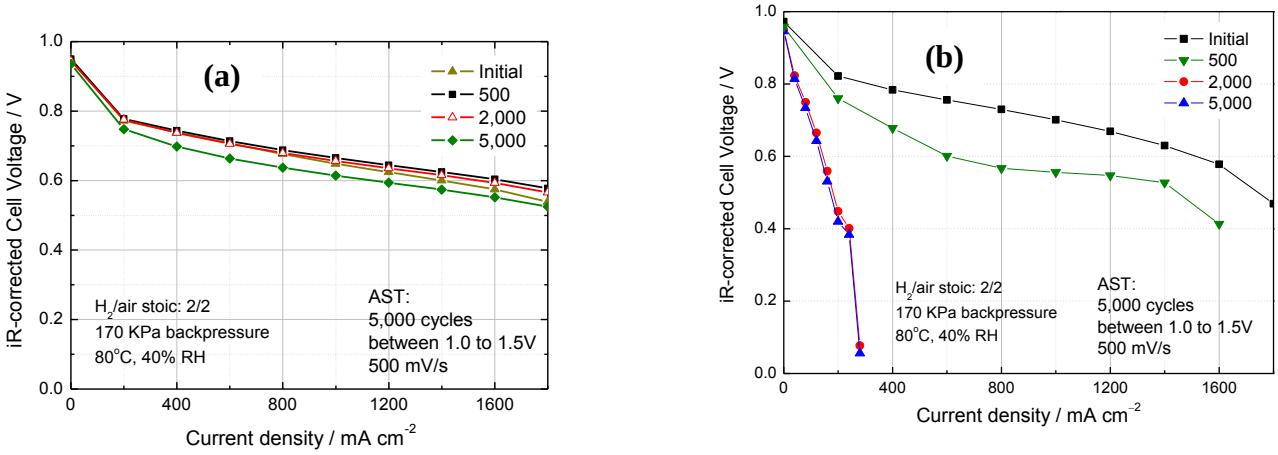

Figure 48. H_2-air polarization curves and the corresponding power density of the PEM fuel cells prepared with (a) 30% Pt/ACCS-1 and (b) commercial Pt/C catalysts before and after 5,000 cycles between 1.0 and 1.5 V. The fuel cell operating conditions are: H_2/air (2.0/2.0), 80 °C, 50% RH, 170 kPa back pressure.

4.3.5. Development of Pt*/ACCS-1 Catalyst

As discussed in section 4.4.4, pure Pt supported on ACCS-1 presents high support stability and enhanced catalyst durability when compared to commercial Pt/C catalyst. In order to further improve the durability, Pt should be doped with Co to induce Pt-lattice contraction which decreases Pt dissolution during potential cycling (0.6-1.0 V). However, doping Pt with excess of Co decreases the ORR activity due to Co coverage on the Pt active sites. On the other hand, our results indicated that smaller Co to Pt ratio may not be effective to provide the compressed Pt strain. Therefore, Pt to Co ratio plays a significant role in catalyst development and needs to be optimized to synthesize a highly active and durable catalyst.

4.3.5.1. Effect of Pt to Co Ratio on ORR Catalytic Activity

Initially Co-doped ACCS-1 was synthesized by mixing ACCS-1 with Co precursor and nitrogen containing organic compound followed by annealing at 800 ^{o}C for 1 hour in inert atmosphere. The final product, which is leached in 0.5M H_2SO_4 for 4 hours to remove the excess of Co on the surface, is named as ACCS-1. Table 10 summarizes the ACCS-1 composition for the starting materials of carbon, Co and ligand compound and the final Co weight percentage in the support and Pt to Co ratio after 30% Pt deposition. From the Table, one can see that the Co amount included in the support can be varied by modifying the cobalt to ligand ratio. The role of ligand is to form Co-N chelate compound. Therefore, the amount of Co incorporated into ACCS-1 is only related to carbon to Co ratio. XRD patterns of ACCS with different Co concentration are compared in Figure 49. The presence of Co metal is confirmed by the peak appearing at 44^{o}. The Co peak intensity increases as the Co concentration in the support increases. The graphitic (002) peak at 26^{o} for the sample with less Co is higher due to less ligand inclusion, which may be attributed to formation of more amorphous carbon.

30% Pt was deposited on the supports with different Co concentrations and PtCo alloy catalysts with the Pt to Co ratio between 1:1 and 3:1 are formed. The heat-treated catalysts are named as Pt*/ACCS-1. The XRD of this catalyst is shown in Figure 50. After annealing at 800 ^{o}C, all the Pt peaks shift to higher angle indicating a lattice contraction caused by the substitution of the smaller Co metal atoms for the larger Pt atoms. The higher the amount of Co doping into Pt, the higher the peak shift observed in XRD. Among various PtCo catalysts, Pt_1Co_1 exhibits clear ordered fct structure with extra peak formation by show additional super lattice reflections such as (100) reflection at 33^{o}. The effect of Pt to Co ratio on ORR catalytic activity are

compared in PEMFC with Pt loadings of 0.1 mg/cm^2 on both anode and cathode in a single PEM fuel cell (25 cm^2 MEA).

Table 9. Pt to Co ratio prepared by different Co to ligand amount.

C : Co : ligand / wt. ratio	Co wt. percentage in ACCS-1 %	Pt to Co / wt. ratio	Pt to Co / atomic ratio
4 : 1 : 20	13%	77:23	1:1
4 : 1 : 10	14%	75:25	1:1.1
4 : 1 : 5	13%	77:23	1:1
4 : 0.5 : 5	6.4%	87:13	1:0.50
4 : 0.5 : 2.5	6.4%	87:13	1:0.50
4 : 0.33 : 3.33	4.3%	91:9	1:0.33

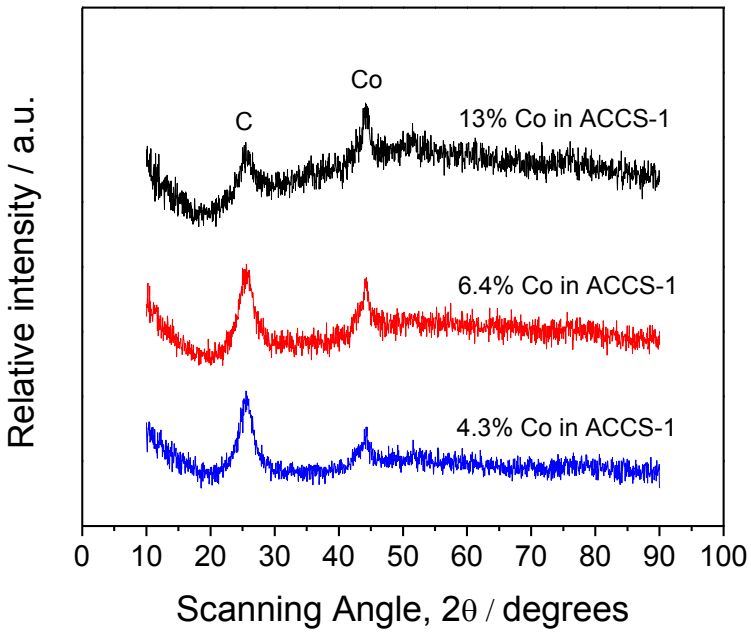

Figure 49. XRD patterns of various ACCS-1 with different Co concentrations.

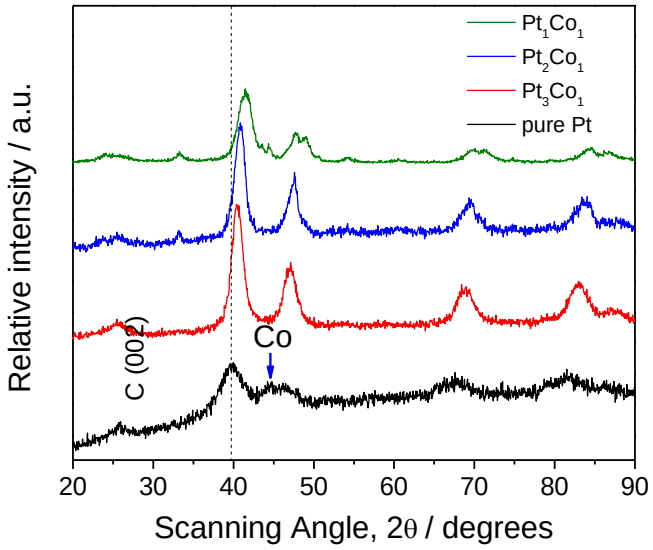

Figure 50. XRD patterns of Pt*/ACCS-1 with different Pt to Co ratios.

The mass activity is measured at high potential region under the condition: H_2/O_2 (2.0/9.5 stoic.), 100% RH and 150 kPa_{abs} back pressure, 80°C cell temperature. As shown in Figure 51, at 0.9V, the mass activities are 0.220, 0.298, 0.311, 0.356, 0.420 and 0.383A/mg for pure Pt, Pt_3Co_1, $Pt_{2.5}Co_1$, Pt_2Co_1, $Pt_{1.5}Co_1$ and Pt_1Co_1 catalysts, respectively. From Figure 51 b, one can see that the mass activity increases as the Co to Pt ratio increases, following a linear fit, except for Pt_1Co_1. The lower mass activity achieved with Pt_1Co_1 is due to the formation of ordered fct structure. It has been reported by Koh [200] that ordered PtCo fct structure is more corrosion resistant but less active for ORR.

The polarization curves shown in Fig. 52 are obtained under H_2/air (2.0/2.0 stoic.), 50% RH and 170 kPa_{abs} back pressure, 80°C cell temperature. According to our studies higher mass activity at high potentials does not always translate to a high performance in high current regions. Due to more surface coverage of Pt with excess Co in the case of catalysts with high Co to Pt ratio, the current density decreases as the Co amount increases. The best performance is achieved with Pt to Co ratio of 3:1.

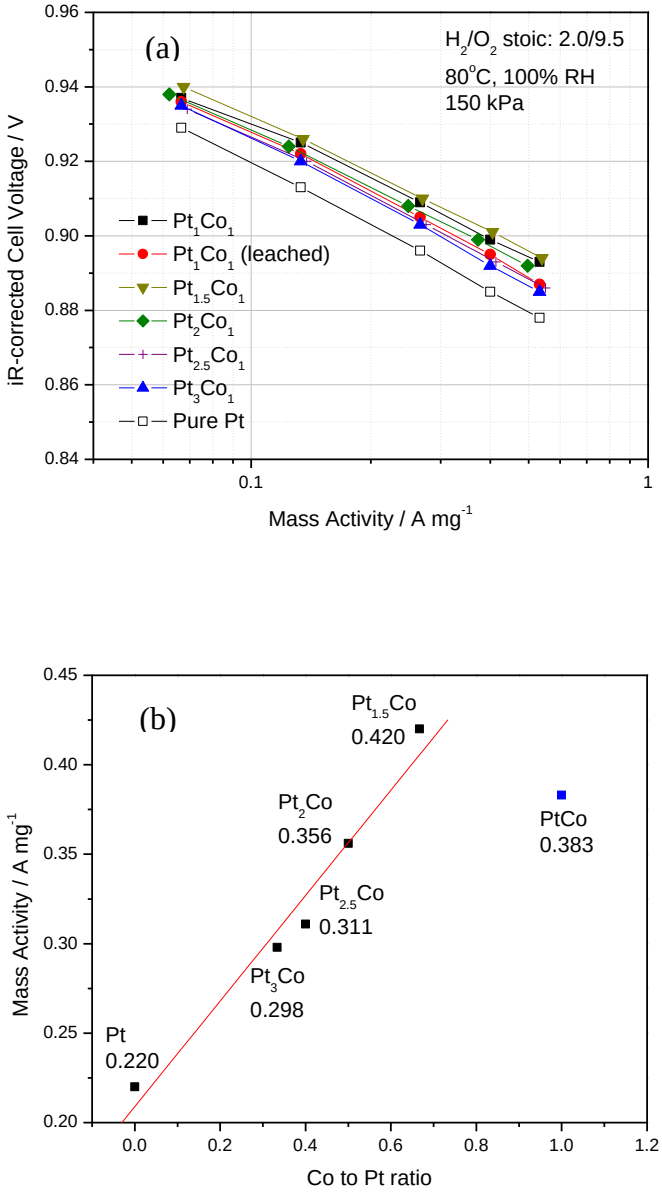

Figure 51. (a) Mass Activity Tafel plot of Pt*/ACCS-1 catalysts with different Co to Pt ratio (iR-corrected cell voltage vs. mass activity) (b) mass activity at 0.9V as a function of Co to Pt ratio. The fuel cell operating conditions are: H_2/O_2 (2.0/9.5), 80 ^oC, 100% RH, 150kPa back pressure.

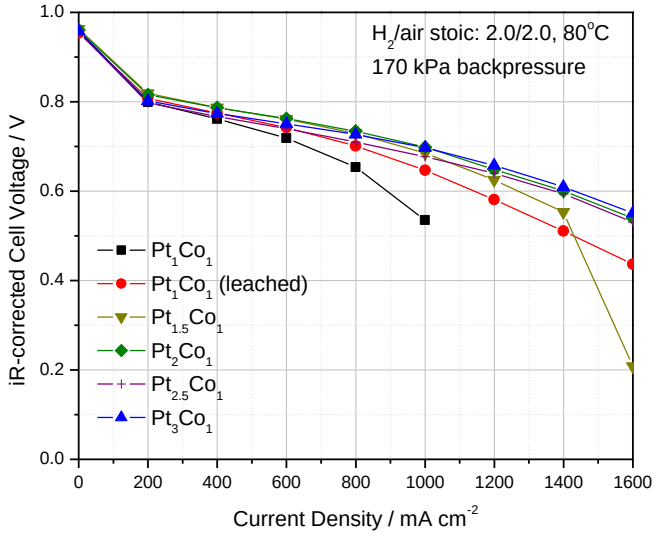

Figure 52. H_2-air polarization curves of the PEM fuel cells prepared with Pt*/ACCS-1 catalysts with different Co to Pt ratio (iR-corrected cell voltage vs. current density). The fuel cell operating conditions are: H_2/air (2.0/2.0), 80 °C, 50% RH, 170 kPa back pressure.

4.3.5.3. Effect of Annealing Temperature on ORR Catalytic Activity

Since Co is chemically and electrochemically not stable in acidic media especially in the presence of Pt, it is important to have maximum amount of Co in the Pt structure to keep the compressive lattice strain as long as possible during potential cycling between 0.6 and 1.0 V. The purpose of studying the effect of Pt to Co ratio is to include maximum possible Co in the structure without decreasing the performance. Pt to Co ratios between 2:1 and 3:1 give higher activity than pure Pt at 0.6 V.

As reported in the literature, when the annealing temperature is increased, more ordered PtCo structure with lower activity is form [200]. At 650 °C, most of the catalyst shows disordered structure. In this study, 700 °C is chosen to be the lowest annealing temperature. All the catalysts show peak shift in XRD after subjected to annealing (Figure 53). Furthermore, the catalyst annealed at higher temperature exhibits higher shift in 2θ angle indicating more compressive Pt lattice formation.

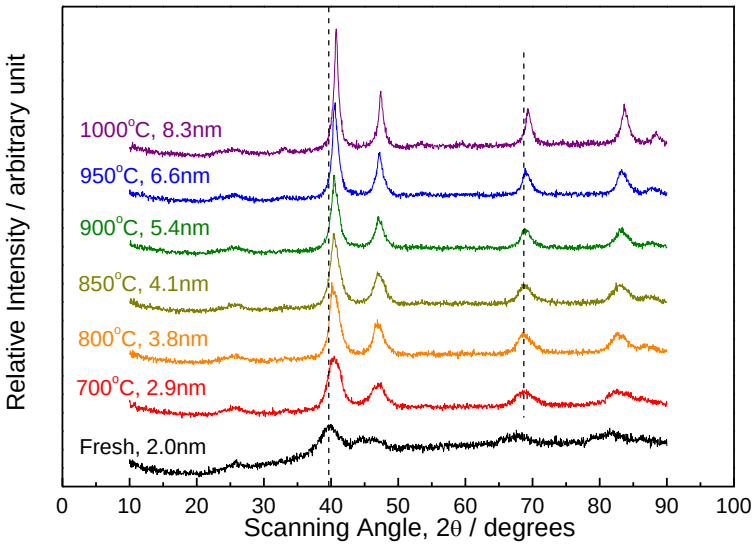

Figure 53. XRD patterns of Pt_2Co_1 annealed at different temperatures.

The effect of annealing temperature on ORR catalytic activity is compared using PEMFC prepared with Pt loadings of 0.1 mg/cm^2 on both anode and cathode in a single PEM fuel cell (25 cm^2 MEA). The mass activity results are shown in Figure 54 (a & b), at 0.9 $V_{iR\text{-}free}$. The highest mass activity of 0.356 A/mg is obtained for the Pt_2Co catalyst heat-treated at 800 ^oC. Figure 54(b) shows that above 800^oC, the mass activity decreases as temperature increases. The H_2/air polarization curves shown in Figure 55 (a & b) present a similar tendency as in the mass activity study. The observed phenomenon is due to more ordered structure formation at high temperature which decreases the activity due to Pt particles growth and agglomeration. Therefore, the compressive Pt-lattice catalyst development is a trade-off between the catalyst activity and durability. As shown in Fig. 55 (b) At 0.6 V, the catalysts pyrolyzed between 700 and 850 ^oC show better ORR activity than pure Pt. Based on these studies, the catalysts annealed at 800 and 850 ^oC are chosen for catalyst durability studies.

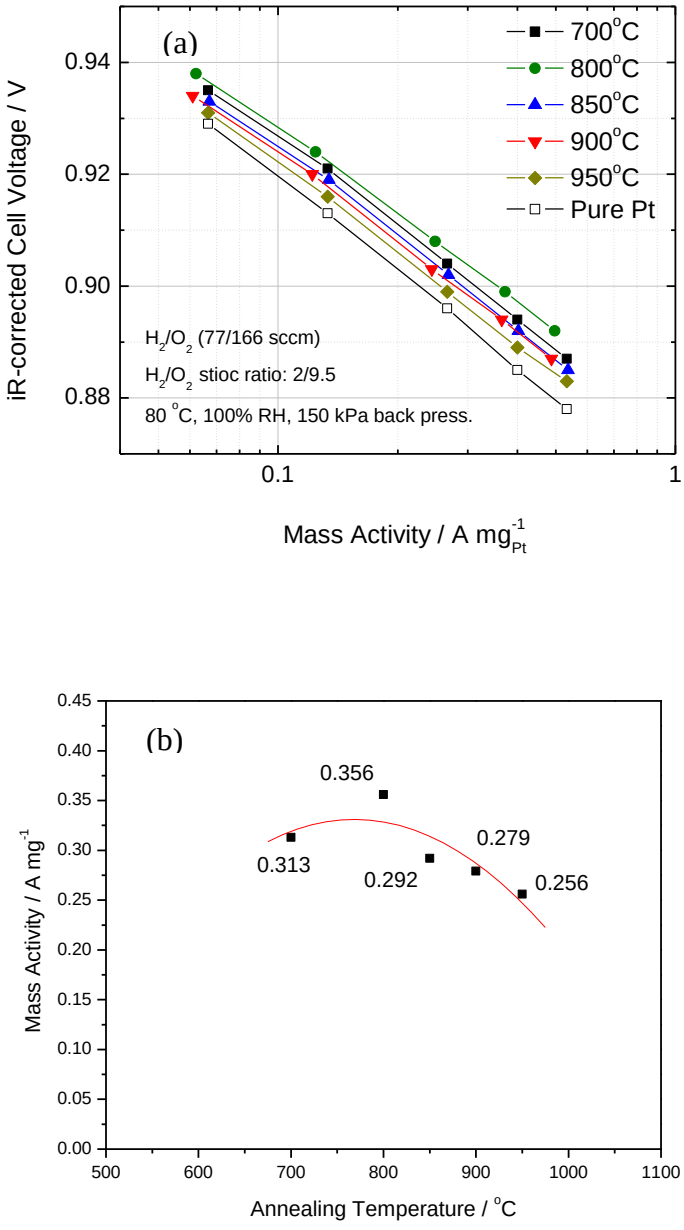

Figure 54. (a) Mass Activity Tafel plot of Pt*/ACCS-1 catalysts with Pt to Co ratio of 2:1 at different annealing temperature (iR-corrected cell voltage vs. mass activity) (b) Mass activity at 0.9V as a function of annealing temperature. The fuel cell operating conditions are: H_2/O_2 (2.0/9.5), 80 °C, 100% RH, 150kPa back pressure.

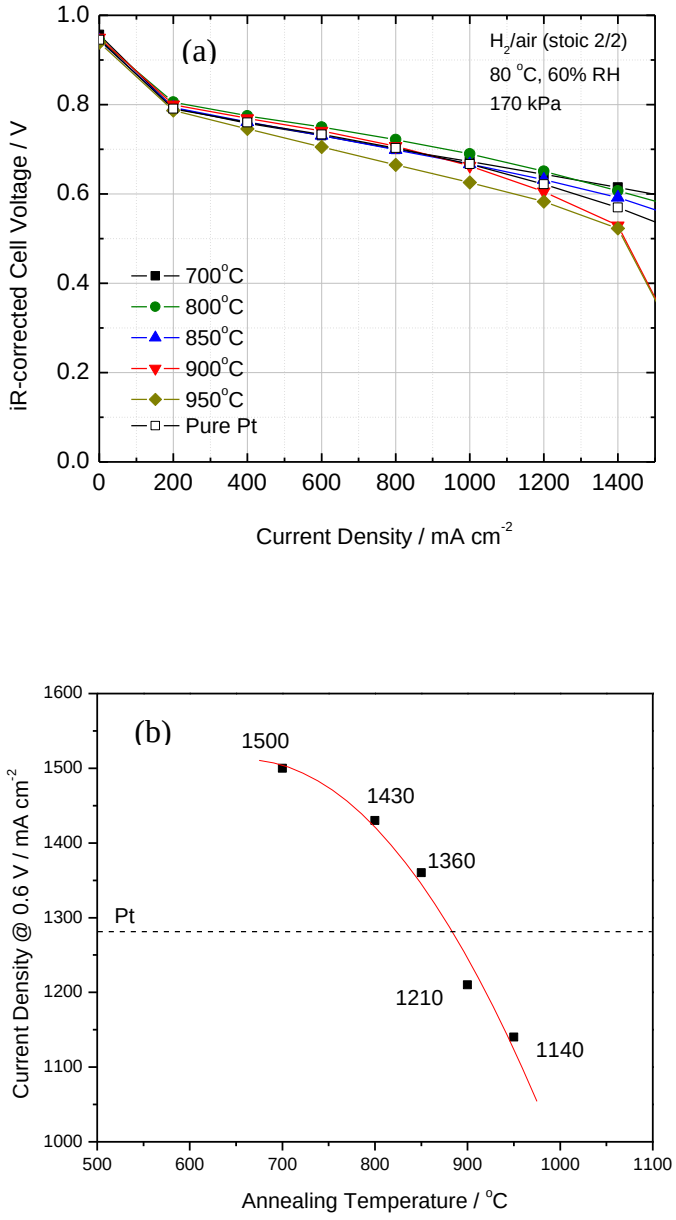

Figure 55. (a) H_2-air polarization curves of the PEM fuel cells prepared with Pt*/ACCS-1 having Pt to Co ratio of 2:1 at different annealing temperature (iR-corrected cell voltage vs. current density) and (b) current density at 0.6 V as a function of annealing temperature. The fuel cell operating conditions are: H_2/air (2.0/2.0), 80 ^oC, 50% RH, 170 kPa back pressure.

4.3.5.4. Support Stability Studies of Pt/ACCS-1 Catalysts*

To determine if the support stability is affected by Co doping, the Pt_2Co_1 cathode catalyst was cycled between 1.0 and 1.5 V for 5,000 times under the AST conditions: the anode and cathode were under H_2 and N_2 atmosphere at 80 °C and 100% inlet RH. The polarization curve measured in H_2-air shows no decrease of ORR activity after 5,000 cycles (Fig. 56). Instead, there is a 10 mV gain at 1500 mA/cm^2. This is because Co is leached out from the structure both chemically (due to low pH at the cathode/electrolyte interface) and electrochemically (due to high overpotential during 1.0-1.5V cycling) and expose more Pt surface active sites. However, at moderate cycling condition such as the one between 0.6 and 1.0 V, Pt dissolution occurs through Pt oxidation and Pt-oxide reduction process and the activity increase is not observed. But during high potential cycling, Pt is passivated by Pt oxide film, so the activity increase shows up.

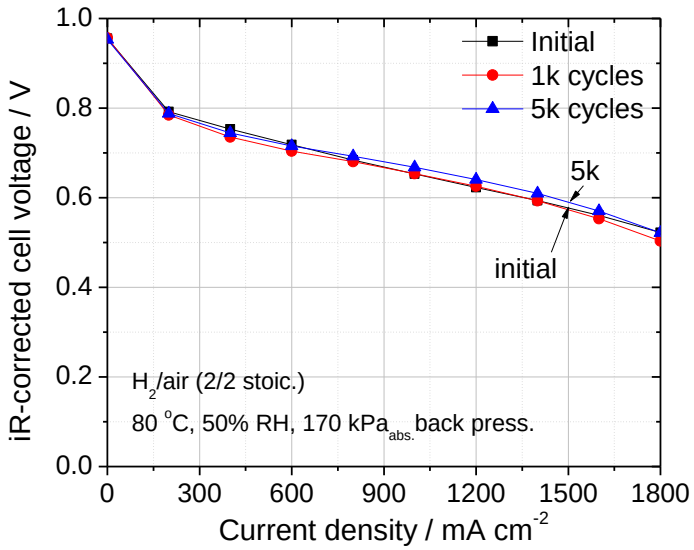

Figure 56. H_2-air polarization curves of the PEM fuel cells prepared with Pt*/ACCS-1 catalyst before and after 5,000 cycles between 1.0 and 1.5 V. The fuel cell operating conditions are: H_2/air (2.0/2.0), 80 °C, 50% RH, 170 kPa back pressure.

4.4. Development of Pt and Pt* Catalysts Supported on Activated Carbon Composite Support – 2 (ACCS-2)

4.4.1. Synthesis of Activated Carbon Composite Support – 2 (ACCS-2)

The ACCS-2 was synthesized by two-step process - purification and stabilization – from a carbon black as a starting material. The carbon black was heat treated to remove the electrochemically unstable amorphous carbon. Next, the sample was heat treated at elevated temperatures under N_2 or Ar flow. With this step, surface functional groups could be removed from the carbon surface thus making the ACCS-2 support more corrosion resistant.

4.4.2. Characterization of ACCS-2

A variety of carbon supports such as Ketjen black EC-300J (Akzo Nobel), Vulcan XC-72 (Cabot), Ensaco 290G (Timcal), ACCS-2, and CNF (Sigma-Aldrich) were selected and their thermal stability was measured by heat treatment at 600 °C for 1 h with 10 °C/min ramping time in a tube furnace with constant air flow (150 ml/min). The weights before and after heat treatment were measured using a digital balance to calculate the weight loss of each carbon. Complete thermal decomposition of carbons was studied by thermogravimetric analysis (TGA) (Q5000IR, TA Instruments). The experiments were conducted under mixed gas of 10 ml/min of nitrogen and 25 ml/min of air. The temperature was increased up to 1000 °C at 10 °C/min ramping time.

The thermal stability of various carbons was examined by heat treatment under air flow at 600 °C for 1 h. Fig. 57 shows the weight retentions after thermal stability test for various carbons. The Ketjen black EC-300J, Vulcan XC-72, Ensaco 290G, CNF, and ACCS-2 developed at USC were compared. While two commonly used carbon supports such as Ketjen black EC-300J and Vulcan XC-72 show low weight retention after thermal stability test (1.0% for Ketjen black EC-300J and 13.4% for Vulcan XC-72), ACCS shows 90.7% retention which is similar to that of CNF (91.4%). The thermal stability results indicate that ACCS is more stable than Ketjen black EC-300J and Vulcan XC-72 carbons. S.M. Andersen et al. [32] claimed that CNF and CNT supports for Pt cathode catalyst showed higher thermal stability as well as higher electrochemical stability in MEA test (0 – 1.6 V, 15000 cycling) than those of carbon black support. From the thermal stability test results, it is expected that the ACCS-2 which showed similar thermal stability as the CNF would show good electrochemical stability in MEA tests.

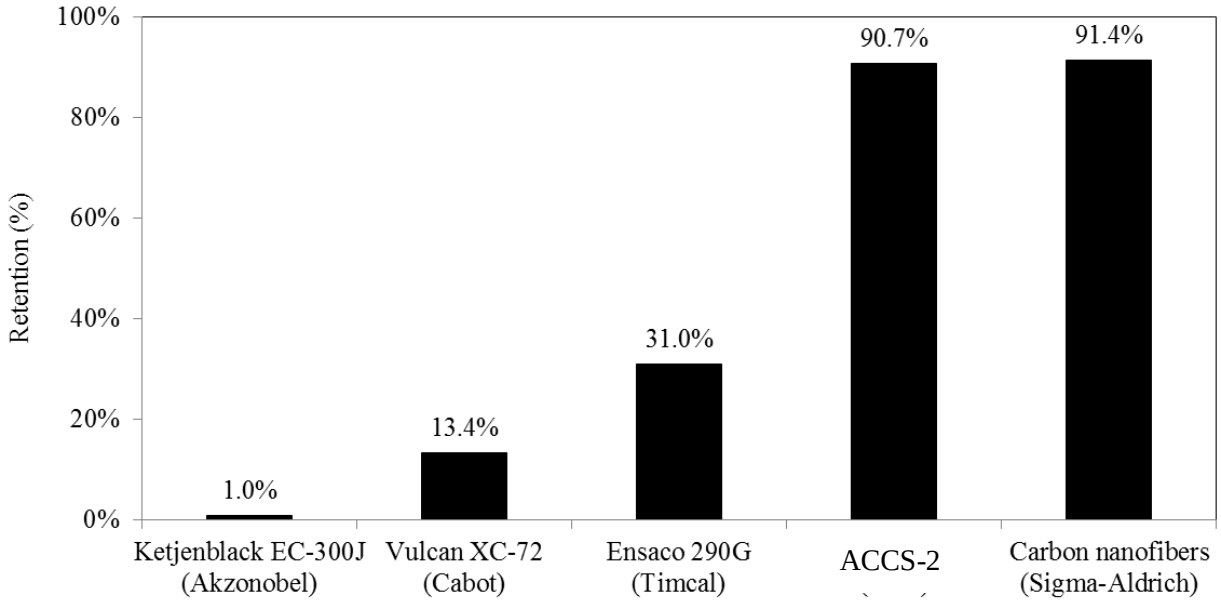

Figure 57. Thermal stability results at 600 °C for 1 h of Ketjen black EC-300J, Vulcan XC-72, Ensaco 290G, ACCS-2, and carbon nanofibers.

Among various carbons, Ketjen black EC-300J, Ensaco 290G and ACCS-2 were selected for more detailed thermal decomposition analysis using TGA. Fig. 58 shows the result of TGA for the three selected carbons. The ACCS shows the highest thermal stability by showing highest on-set temperature for decomposition. The Ensaco 290G shows intermediate thermal stability and Ketjen black EC-300J shows the lowest thermal stability which agrees well with the thermal stability study results presented in Fig. 57. The temperatures at a maximum derivation of weight loss are 705, 740, and 781 °C for Ketjen black EC-300J, Ensaco 290G, and ACCS, respectively.

The XRD patterns of Ketjen black EC-300J, Ensaco 290G and ACCS-2 are shown in Fig. 59. The crystallite thickness (L_c) calculated by Scherrer's formula and the interlayer spacing (d_{002}) obtained from Bragg's law are used as the factors to determine the degree of graphitization of carbons. It has been reported that higher L_c value of the (002) peak and lower d_{002} number imply a higher degree of graphitization [17, 38, 39]. The ACCS-2 shows L_c value which is almost twice higher than that of Ketjen black EC-300J and Enasco 290G, and the lowest d_{002} of 0.349 when compared to the other two carbons. From the XRD analysis, a higher degree of graphitization of ACCS-2 compared with the Ketjen black EC-300J and Ensaco 290G was observed and it could be attributed to the higher thermal stability of ACCS-2 than Ketjen black

EC-300J and Ensaco 290G. The BET surface area, maximum derivation of weight loss on TGA, Lc values, and d002 values obtained from XRD analysis are summarized in Table 10.

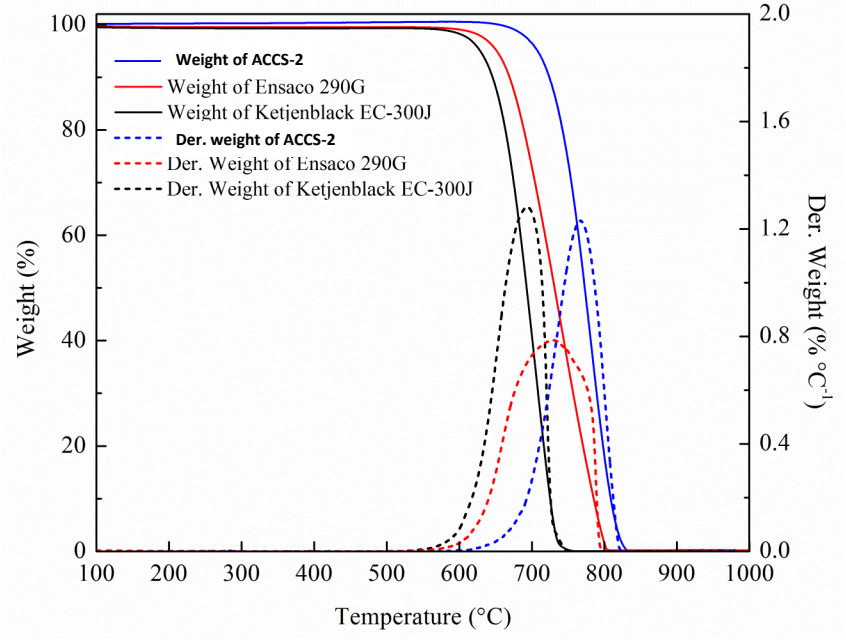

Figure 58. Comparison of TGA profiles for Ketjen black EC-300J, Ensaco 290G, and ACCS-2.

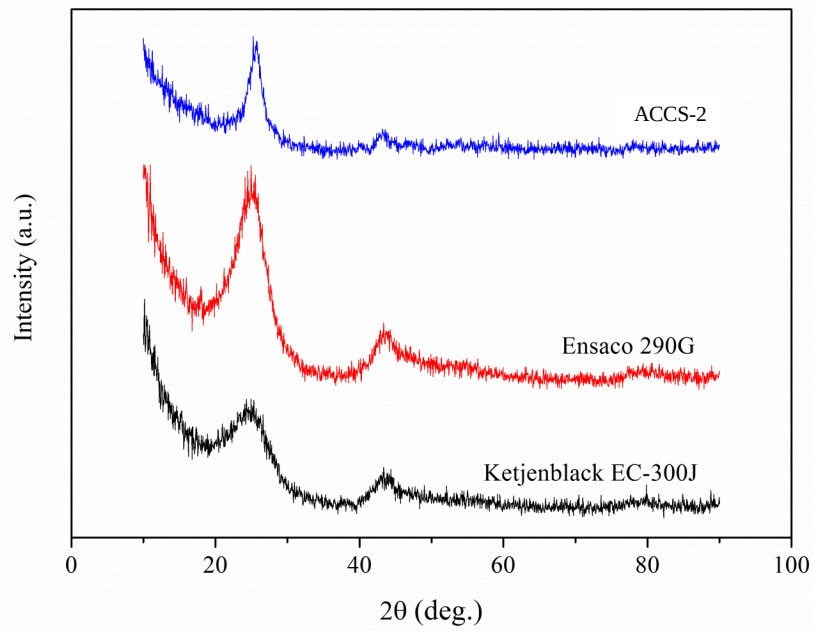

Figure 59. Comparison of XRD patterns for Ketjen black EC-300J, Ensaco 290G, and ACCS-2.

Table 10. List of carbons and carbon properties.

Sample	Surface area (m^2/g) (BET)	L_c (nm) (XRD)	d_{002} (nm) (XRD)	Max der. temp. (°C) (TGA)
Ketjen black EC-300J	800	1.8	0.361	705
Ensaco 290G	220	2.0	0.358	740
ACCS-2	200	4.0	0.349	781

4.4.3. Platinum Deposition

The 30 wt. % Pt on Ensaco 290G carbon support (Pt/290G) and 30 wt. % Pt on ACCS-2 support (Pt/ACCS-2) catalysts were synthesized using a modified polyol reduction process. Commercially available Pt/C (TEC10E30E, 28.2% Pt on Ketjen black EC-300J) was compared with Pt/290G and Pt/ACCS-2 as a cathode catalyst to represent the Pt catalyst on Ketjen black EC-300J support since Ketjenblack-EC300J was used as a support material for this commercial catalyst [161]. The XRD patterns of commercial Pt/C, Pt/290G, and Pt/ACCS catalysts are compared in Fig. 60. The diffraction patterns represent all the reflections corresponding to the face centered cubic (fcc) lattice of Pt supported on various carbon supports. Scherrer's equation was used for calculating the Pt crystallite size using the Pt(220) peak appearing at 67.5° [194]. The d_{Pt} values calculated from the XRD analysis are 1.6, 3.2, and 2.1 nm for the commercial Pt/C, Pt/290G, and Pt/ACCS catalysts, respectively, which are confirmed by the HRTEM images and corresponding particle size distribution shown in Fig. 61.

4.4.4. MEA performance evaluation and support stability test under 1.0-1.5 V cycling

The support stability tests were carried out by subjecting the MEAs to a potential cycling test (1.0-1.5 V, 5000 cycles) to simulate the start-up/shut-down conditions of an automotive PEMFC. The corrosion rate of carbon increases drastically at high electrode potentials, and can result in severe degradation of the carbon support via the following reaction [201]:

$$C + 2H_2O \rightarrow CO_2 + 4H^+ + 4e^- \qquad E^\circ = 0.207 \text{ V vs. RHE} \qquad (29)$$

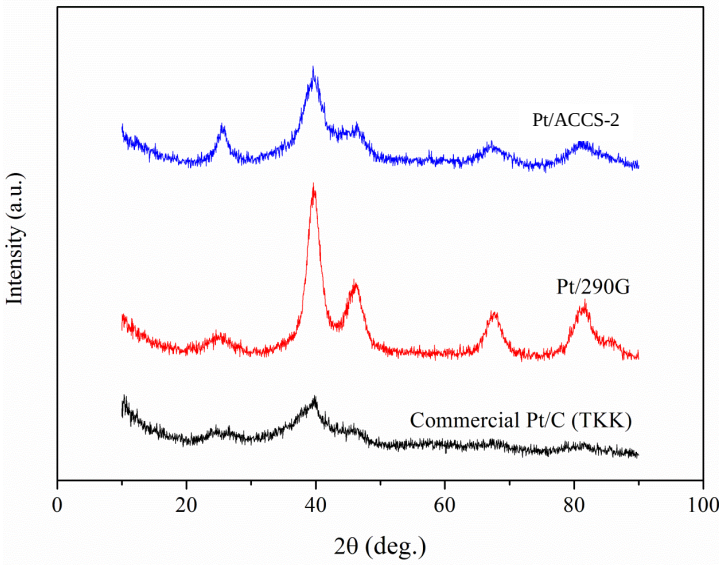

Figure 60. Comparison XRD patterns for commercial Pt/C, Pt/290G, and Pt/ACCS-2.

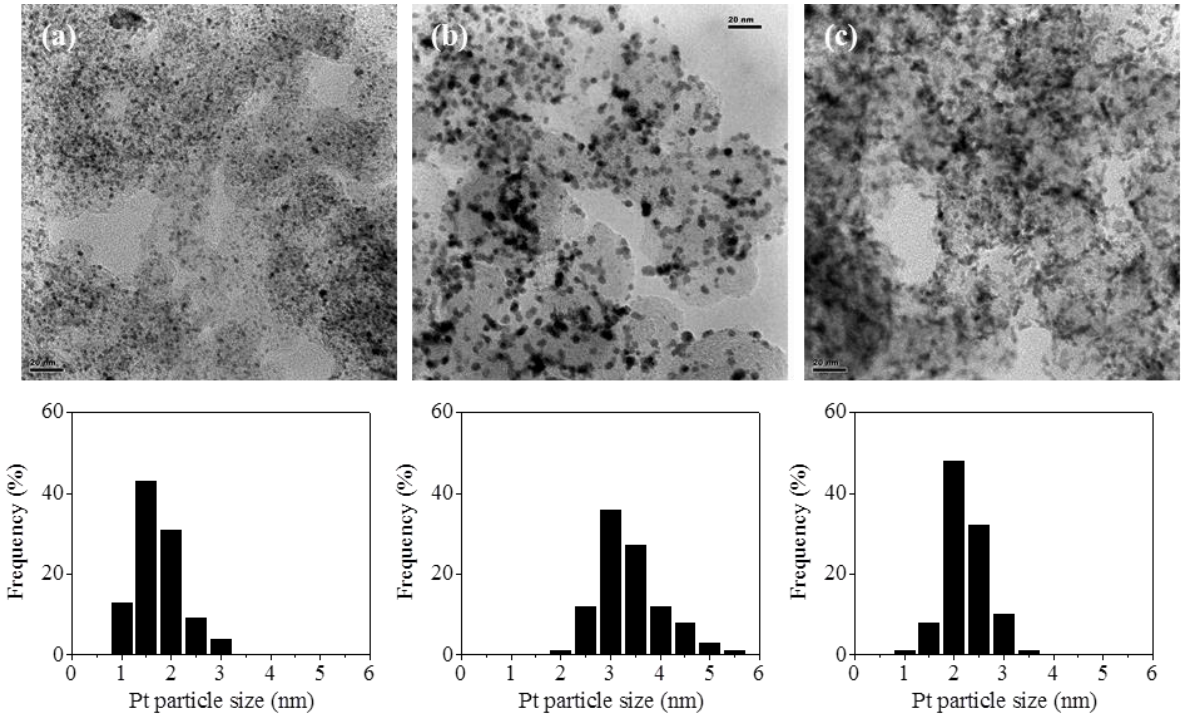

Figure 61. HRTEM images and Pt particle size distributions of (a) commercial Pt/C, (b) Pt/290G, and (c) Pt/ACCS-2. The scale bar is 20 nm.

Oxidation of the carbon surface increases its hydrophilicity and affects water removal, resulting in an increased mass-transfer resistance. In addition, oxidation of carbon increases the electrical resistance of the catalysts [202, 203], which leads to the detachment or aggregation of catalyst particles, and damages the cathode catalyst layer structure. Furthermore, platinum increases the corrosion rate by catalyzing the carbon oxidation [32].

Figure 62 shows H_2-air fuel cell polarization curves for the three different cathode catalysts. After 5000 cycles, the Pt/ACCS-2 shows no loss in H_2-air performance indicating good support stability under high potentials (Fig. 62(c)). On the other hand, commercial Pt/C catalyst shows 69.5% power density loss only after 1000 cycles and a further decrease to 88.7% after 5000 cycles (Fig. 62(a)). The Pt/290G catalyst shows moderate stability with 22.5% power density loss until 2000 cycles and a rapid decay between 2000 and 5000 cycles resulting in overall power density loss of 84.0% (Fig. 63(b)). Mass activities under H_2-O_2 operating conditions at 0.9 $V_{iR\text{-}free}$ were measured before and after support stability test to examine the kinetic performance changes of these three catalysts (Fig. 63). The Pt/ACCS-2 catalyst shows no loss after the support stability test while commercial Pt/C and Pt/290G catalysts show 57.5% and 66.2% losses, respectively. Similar trends were observed in EIS analysis (Fig. 64). Commercial Pt/C and Pt/290G catalysts show an increase of charge-transfer resistance after the support stability test, but Pt/ACCS-2 shows a small decrease of resistance. The maximum power densities and mass activities before and after the stability test for commercial Pt/C, Pt/290G, and Pt/ACCS catalysts are summarized in Table 11.

The good support stability of ACCS-2 was attributed to the higher degree of graphitization of ACCS than Ketjen black EC-300J and Ensaco 290G supports which was confirmed by XRD analysis. Also, it could be elucidated by the hydrophobic character of ACCS-2 since carbon corrosion occurs in the presence of water [167]. In order to determine the hydrophilic/hydrophobic nature, the carbon supports were dispersed in water/hexane mixture and the results are shown in Fig. 65. The Ketjen black EC-300J and Ensaco 290G carbon supports are mainly dispersed in the water phase which indicates the hydrophilicity of these carbons. On the other hand, ACCS-2 shows dispersion mainly in the hexane phase while only a small amount of carbon is dispersed in the water phase which shows good hydrophobic property for ACCS-2 when compared with the other two carbons.

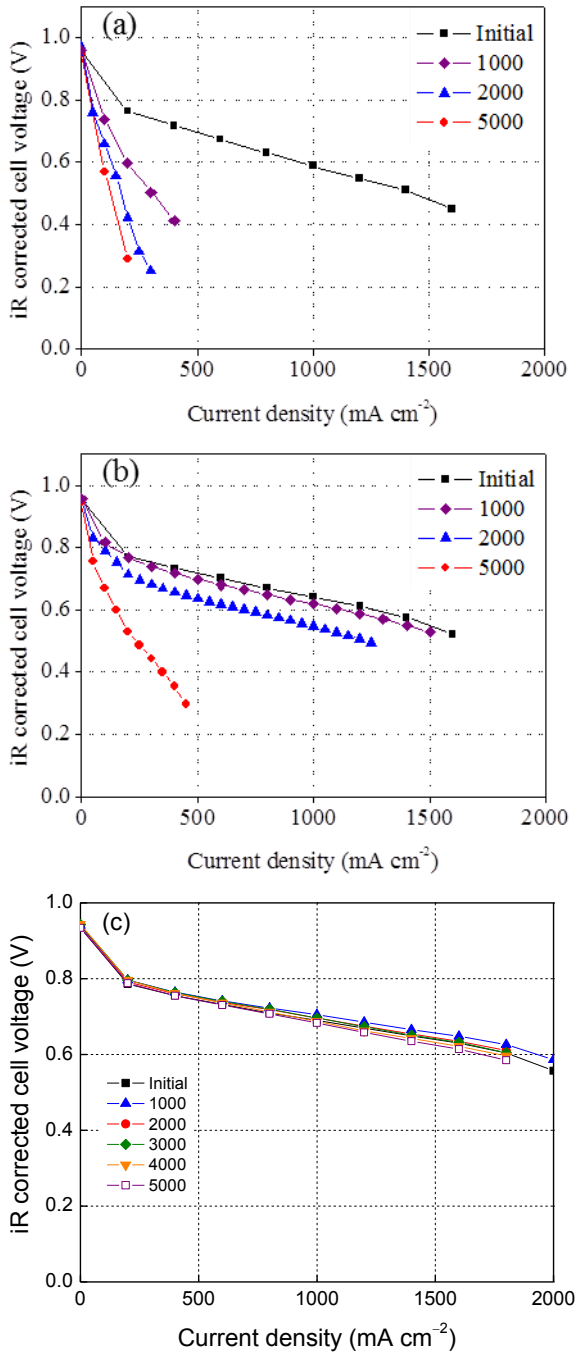

Figure 62. H_2-air PEMFC polarization curves of (a) commercial Pt/C, (b) Pt/290G, and (c) Pt/ACCS-2 cathode catalysts before and after the support stability test (1.0-1.5 V potential cycling for 5000 cycles). The H_2-air polarization performances were measured under H_2/air (2/2 stoic.), 80 °C, 40% RH, and 170 kPa_{abs}.

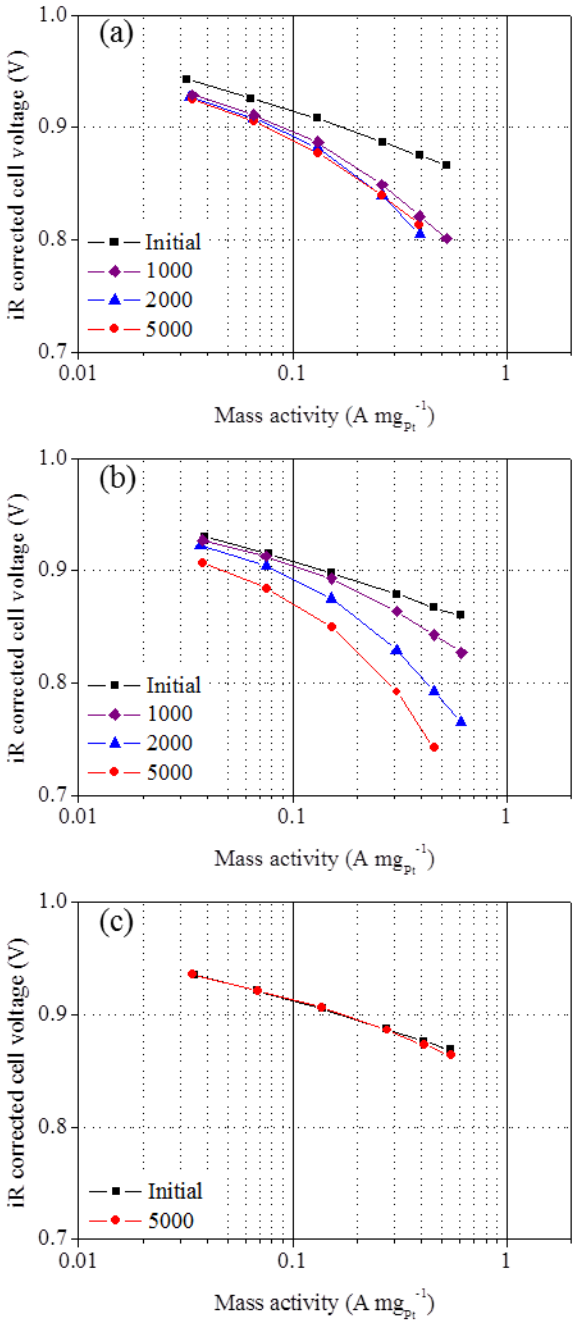

Figure 63. Mass activities under the H_2-O_2 condition of (a) commercial Pt/C, (b) Pt/290G, and (c) Pt/ACCS-2 cathode catalysts before and after the support stability test (1.0-1.5 V potential cycling for 5000 cycles). The mass activities were measured at 0.9 $V_{iR\text{-}free}$ under H_2/O_2 (2.0/9.5 stoic.), 80 °C, 100% RH, and 150 kPa_{abs}.

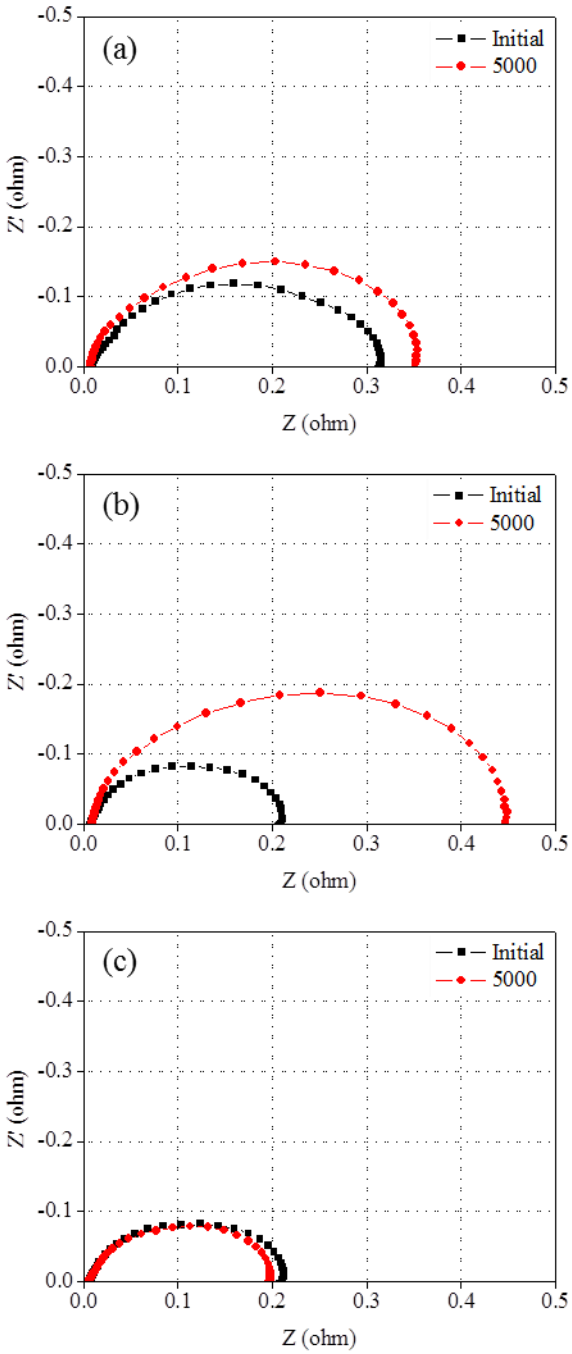

Figure 64. EIS plots under the H_2-air condition of (a) commercial Pt/C, (b) Pt/290G, and (c) Pt/ACCS-2 cathode catalysts before and after the support stability test (1.0-1.5 V potential cycling for 5000 cycles).

Table 11. Comparison of maximum power density and mass activity changes after stability test for commercial Pt/C, Pt/290G, and Pt/ACCS-2 catalysts.

Sample	Maximum power density (mW/cm^2)			Mass activity (A/mg_{Pt})		
	Initial	After 5000 cycles	Change (%)	Initial	After 5000 cycles	Change (%)
Commercial Pt/C	495	56	−88.7	0.167	0.071	−57.5
Pt/290G	530	85	−84.0	0.139	0.047	−66.2
Pt/ACCS-2	722	793	+9.8	0.165	0.167	+1.0

The enhanced hydrophobic property of ACCS-2 is also confirmed by the contact angle measurement. As shown in Fig. 66, ACCS showed a contact angle of 132° which is much greater than that for Ketjen black EC-300J (38°) and Ensaco 290G (32°) carbons. The enhanced hydrophobic property of ACCS-2 can minimize water adsorption on the carbon surface resulting in less carbon corrosion. Furthermore, the difference in hydrophobicity affects the H_2-air fuel cell performance in the mass-transport region. While commercial Pt/C and Pt/290G show current densities of 950 mA/cm^2 and 1250 mA/cm^2 at 0.6 $V_{iR\text{-}free}$, respectively, Pt/ACCS-2 shows 1700 mA/cm^2 at 0.6 $V_{iR\text{-}corr}$. The higher H_2-air fuel cell performance of Pt/ACCS-2 is due to (i) optimized support properties such as BET surface area which resulted in thin catalyst layer thus favoring effective mass-transfer to the Pt catalytic sites and (ii) hydrophobicity of the ACCS-2 support which results in better water removal during high current operation.

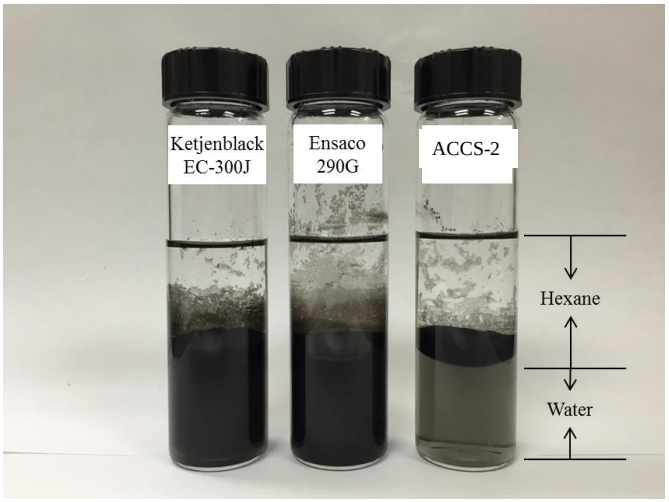

Figure 65. Dispersion of Ketjen black EC-300J, Ensaco 290G, and ACCS-2 in water/hexane mixture.

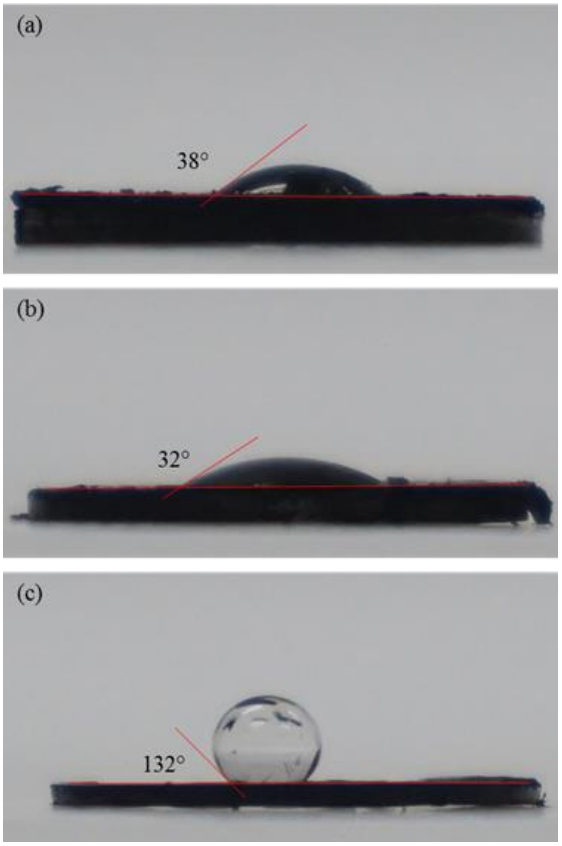

Figure 66. Contact angle measurements on (a) Ketjen black EC-300J, (b) Ensaco 290G, and (c) ACCS-2.

4.4.5. Evaluation of catalyst stability under 0.6-1.0 V cycling

Figure 67 shows the H_2-Air fuel cell performance of Pt/A-CCS catalyst tested in 25-cm^2 MEA subjected to 0.6-1.0 V potential cycling test. The Pt/A-CCS catalyst showed an initial current density of 1.88 A/cm^2 at 0.6 $V_{iR\text{-}free}$ with a potential loss of 73 mV (iR-free) at 0.8 A/cm^2 after 30,000 potential cycles between 0.6 and 1.0 V. As shown in Table 12, the commercial 46% Pt/C showed no activity after 30,000 cycles.

Figure 68 shows initial mass activity of 0.193 A/mg_{Pt} and the stability of mass activity for the Pt/ACCS-2 catalyst subjected to potential cycling between 0.6 and 1.0 V. The catalyst durability test resulted in 52% mass activity loss after 30,000 cycles. The commercial 46% Pt/C catalyst showed 0.18 A/mg_{Pt} initial mass activity and 58% loss after 30,000 cycles (Table 12).

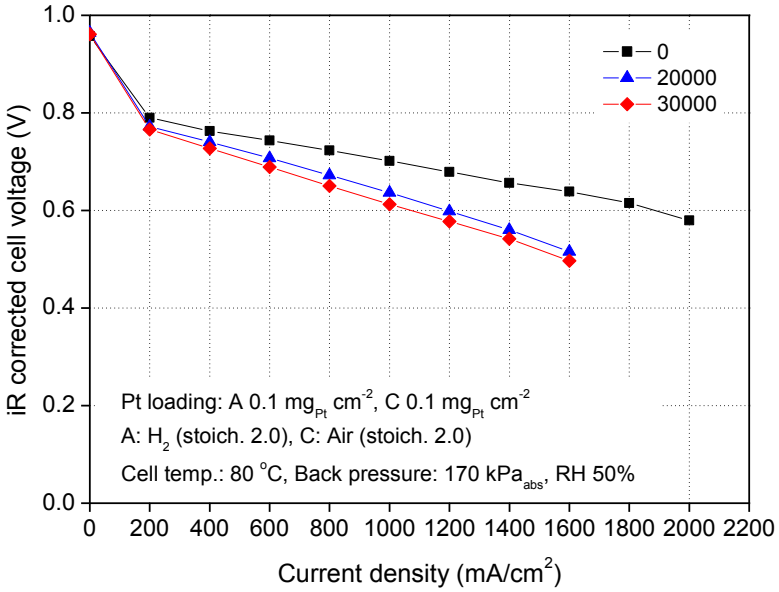

Figure 67. Comparison of H_2/air fuel cell performance of 30% Pt/ACCS-2 catalyst subjected to 30,000 potential cycles between 0.6 and 1.0 V at 50 mV/s. Catalyst loading is 0.1 mg_{PGM}/cm^2 on both the anode and cathode electrodes. The fuel cell operating conditions are: H_2/air (2/2 stoic.), 80 °C, 50% RH, 170 kPa_{abs} back pressure. Nafion® NRE 212 membrane is used as the electrolyte.

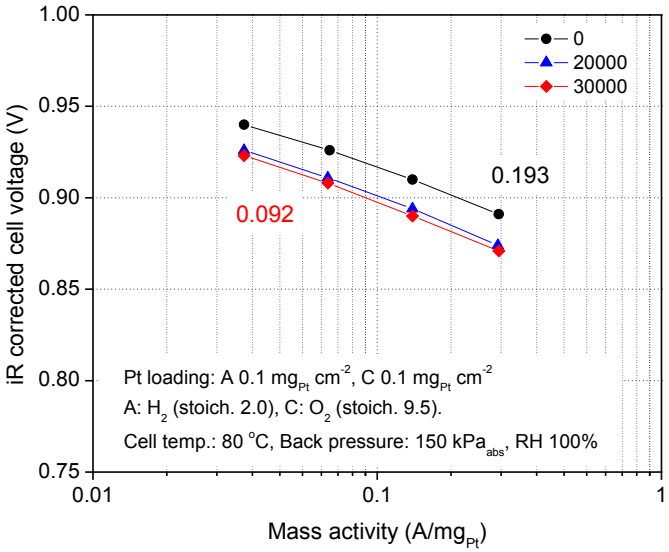

Figure 68. Stability of mass activity of Pt/ACCS-2 catalyst subjected to 30,000 potential cycles between 0.6 and 1.0 V at 50 mV/s. The fuel cell operating conditions are: H_2/O_2 (2/9.5 stoic.), 80°C, 100% RH, 150 kPa_{abs} back pressure. Nafion® NRE 212 membrane is used as the electrolyte.

Table 12. Summary of Support Stability Test (5,000 Potential Cycles between 1.0 and 1.5 V) and Catalyst Durability Test (30,000 Potential Cycles between 0.6 and 1.0 V) for Pt/ACCS-2 and Commercial Pt/C catalysts.

Catalyst/Test	Particle size (nm)	Mass activity loss (%)		ECSA (m^2/g_{Pt})		Cell voltage loss (mV)
		Initial	Final	Initial	Final	$\Delta V_{iR\text{-}free}$
Pt/ACCS-2 Support Stability	2.9	**0.215**	**0.14 (35% loss)** (5k cycles)	**50.0**	**27.5 (45% loss)** (5k cycles)	**15 mV loss** at 1.5 A/cm^2 (5k cycles)
Catalyst Durability	2.9	**0.193**	**0.092 (52% loss)** (30k cycles)	**41.0**	**14 (66% loss)** (30k cycles)	**73 mV loss** at 0.8 A/cm^2 (30k cycles)
Commercial Pt/C Support Stability	2.2	**0.18**	**0.047** (**74% loss**) (5k cycles)	**59.8**	**11.0 (82% loss)** (5k cycles)	No activity (5k cycles)
Catalyst Durability	2.2	**0.18**	**0.075** (**58% loss**) (30k cycles)	**62**	**13.6 (78% loss)** (30k cycles)	No activity (30k cycles)

4.4.6. Development of Pt*/ACCS-2 Catalyst

4.4.6.1. Effect of protective coating and cobalt

Pt*/ACCS-2 catalyst was prepared using a methodology developed at USC. Figure 78 shows the effect of protective coating and cobalt presence on the peak shift and particle size of Pt*/ACCS-2 catalyst and the results are summarized in Table 13. As shown in Fig. 69 and Table 13, the peak shift increased from 39.81° to 40.92 and the particle size decreased from 6.7 to 3.2 nm in the presence of both protective coating and cobalt.

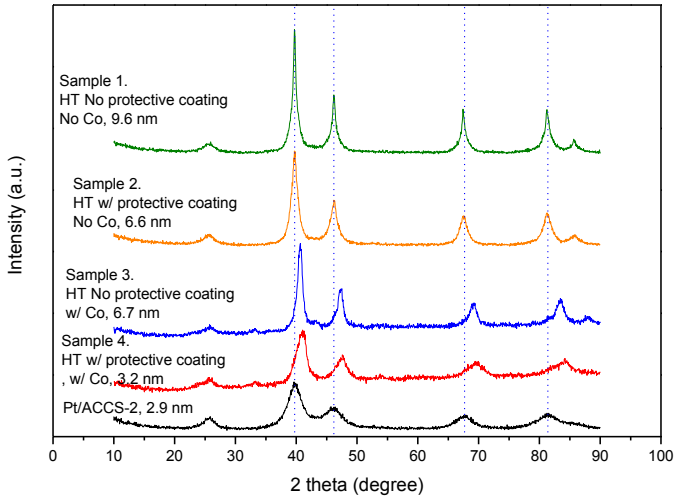

Figure 69. XRD of Pt*/ACCS-2 formed with and without protective coating and cobalt.

Table 13. Effect of protective coating and cobalt presence on particle size of Pt*/ACCS-2.

Sample	Protective coating	Co	d_{Pt} from Pt (220) peak (nm)	2θ for Pt (111) or PtCo (111) (°)
Pt/ACCS-2	N/A	N/A	2.9	39.81
Sample 1	N	No	9.6	39.73
Sample 2	Y	No	6.6	39.74
Sample 3	N	Yes	6.7	40.64
Sample 4	Y	Yes	3.2	40.92

The effect of protective coating and cobalt presence on the particle size and particle size distribution of Pt*/ACCS-2 is shown in Figure 70. The pristine Pt/ACCS-2 shows uniform Pt dispersion on the ACCS-2 support. Without protective coating, large particles are seen in the range between 8 and 12 nm. However, when both protective coating and cobalt are present, uniform particle distribution is seen with particle size in the range between 3 and 5 nm.

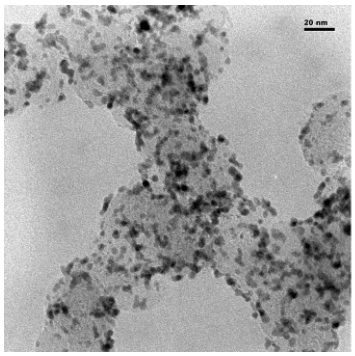

Pt/ACCS-2

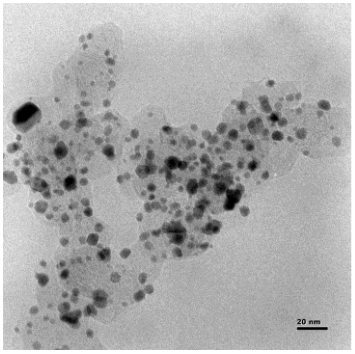

Sample 2: HT 800 °C 4 h, No protective coating and No Co

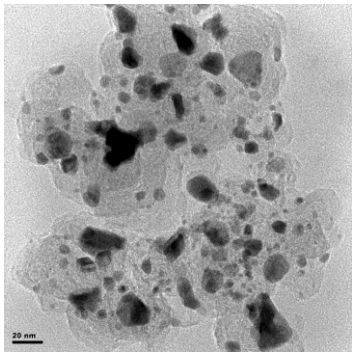

Sample 3: HT 800 °C 4 h, No protective coating and with Co

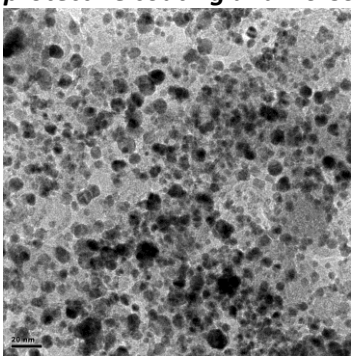

Sample 4: HT 800 °C 4 h, with protective coating and Co

Figure 70. Effect of protective coating and cobalt presence on the particle size of Pt*/ACCS-2.

4.4.6.2. Effect of annealing temperature

The effect of annealing temperature on the particle sizes of Pt*/ACCS-2 was studied in the temperature range from 300 to 900 °C and the corresponding XRD patterns are shown in Fig. 71. The Pt(1 1 1) peak is shifted to a higher 2θ value as the annealing temperature is increased. The effect of annealing temperature on the particle size is shown in the HRTEM images (Fig. 72). Particle agglomeration and particle size growth is observed with an increase in the annealing temperature.

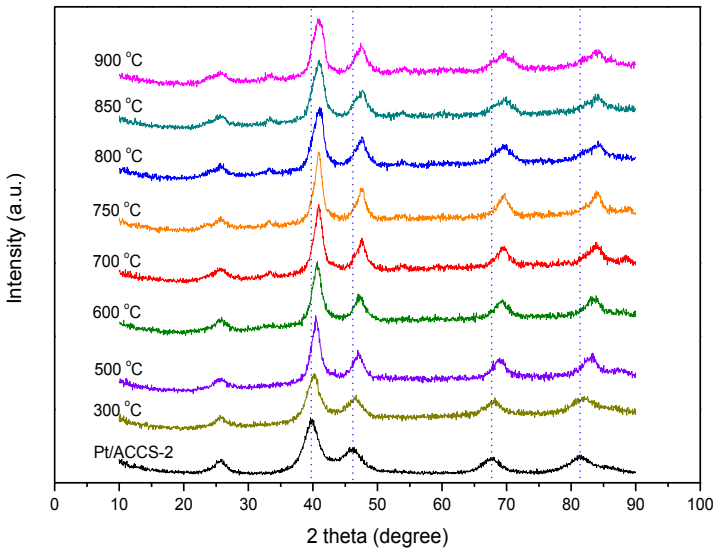

Figure 71. Effect of annealing temperature on the particle size of Pt*/ACCS-2.

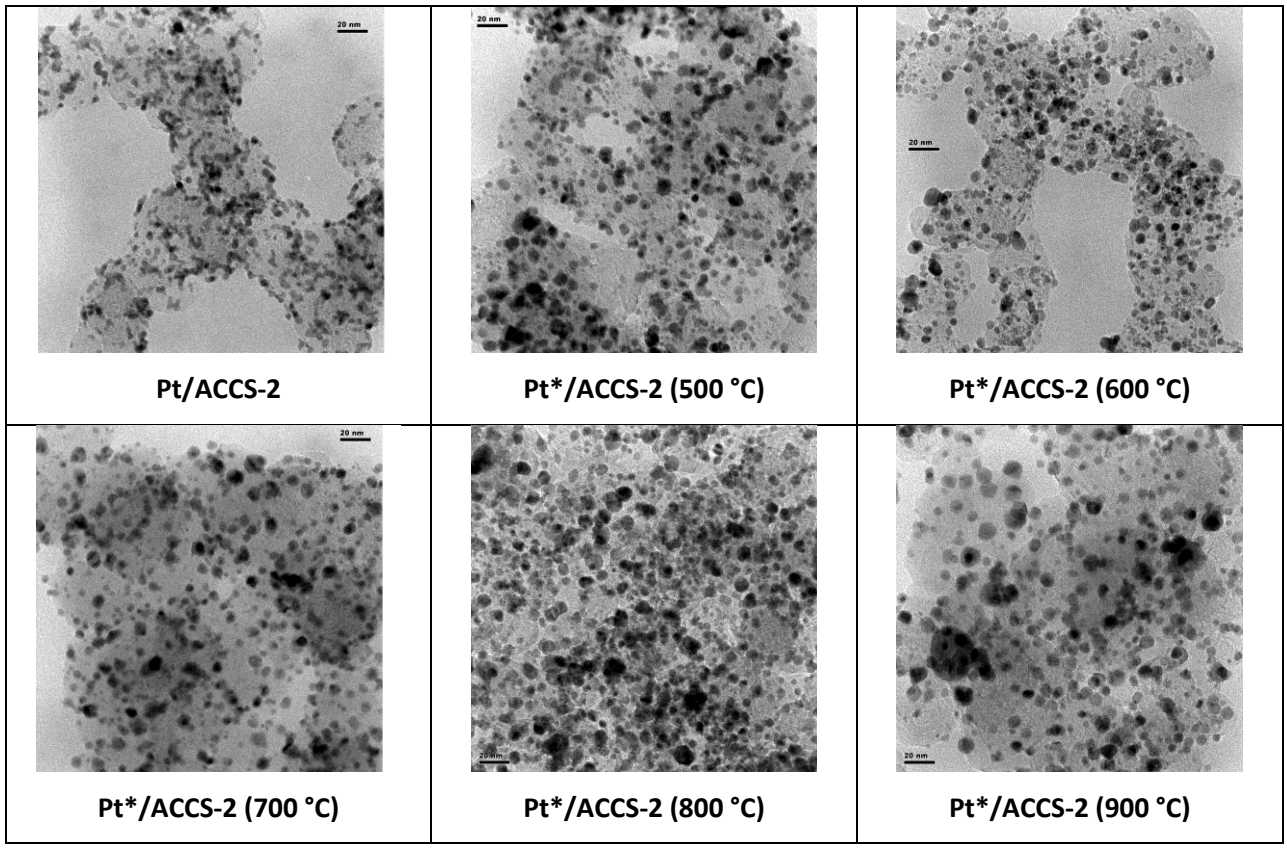

Figure 72. HRTEM images of Pt*/ACCS-2 showing the effect of annealing temperature on the particle size. The scale bar is 20 nm.

The effect of annealing temperature on the catalyst mass activity and H_2-air polarization performance of Pt*/ACCS-2 with a composition of Pt_2Co_1 is shown in Fig. 73 and Fig. 74, respectively. The mass activity at 0.9 $V_{iR\text{-}free}$ gradually increased until 700 °C and starts to decrease. The increase in mass activity can be attributed to unreacted cobalt present when subjected to annealing at lower temperatures which predominantly dissolves during electrochemical measurement and contributes to the mass activity. On the other hand, the gradual decrease in mass activity beyond 700 °C is due to the formation of stable PtCo phase with mass activity >0.4 A/mg_{Pt}. The effect of annealing temperature on the mass activity at 0.9 $V_{iR\text{-}free}$ current density at 0.6 $V_{iR\text{-}free}$ under H_2-air operating condition is summarized in Table 14.

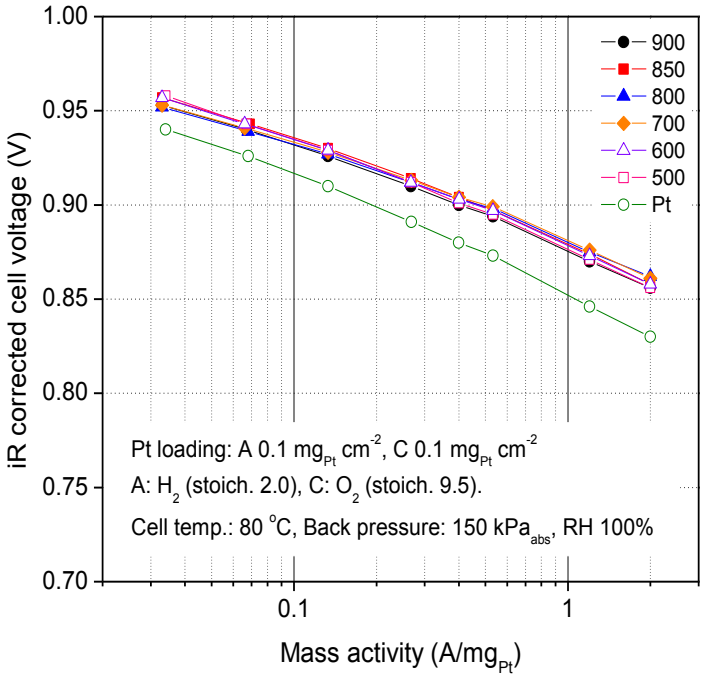

Figure 73. Effect of annealing temperature on the catalyst mass activity of Pt*/ACCS-2.

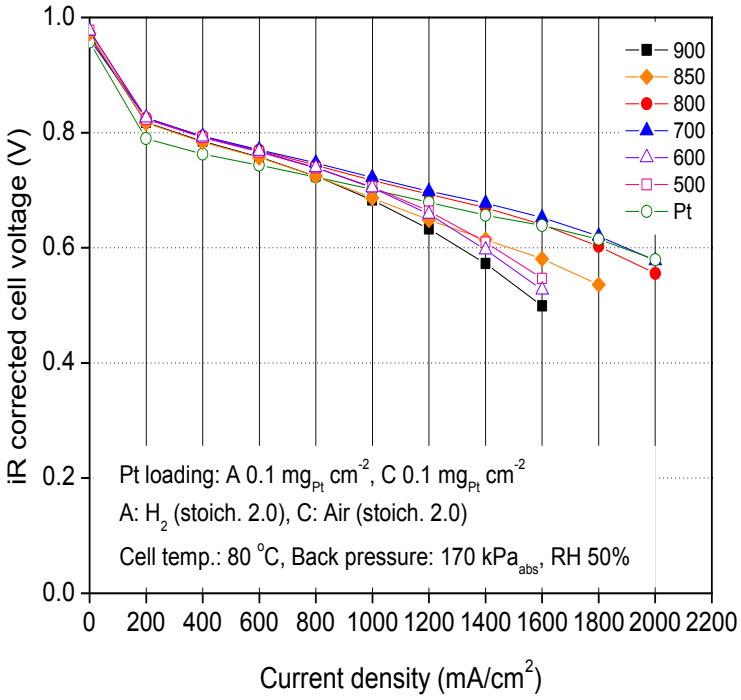

Figure 74. Effect of annealing temperature on the catalyst mass activity of Pt*/ACCS-2.

Table 14. Effect of annealing temperature on the mass activity (at 0.9 $V_{iR\text{-}free}$), current density at 0.6 $V_{iR\text{-}free}$ under H_2-air, open circuit potential, and ECSA of Pt*/ACCS-2.

Annealing temp. (°C)	**Mass activity (A/mg_{Pt})**	**Current density at 0.6 $V_{iR\text{-}free}$ (mA/cm^2)**	**OCV (V)**	**ECSA (m^2/g_{Pt})**
Pt	0.193	1884	0.958	41.0
500	0.425	1418	0.978	34.2
600	0.458	1395	0.977	30.5
700	0.492	1889	0.962	30.4
800	0.474	1800	0.966	26.1
850	0.471	1488	0.973	28.4
900	0.408	1308	0.968	26.6

4.4.6.3. Effect of Pt/Co ratio

The effect of Pt/Co ratio on the particle size, mass activity, and H_2-air fuel cell performance is shown in Fig. 75, Fig. 76, and Fig. 77, respectively and the results are summarized in Table 15. As shown in Fig. 75 and Fig. 76, the particle size increased and the mass activity decreased as the Pt/Co ratio decreased.

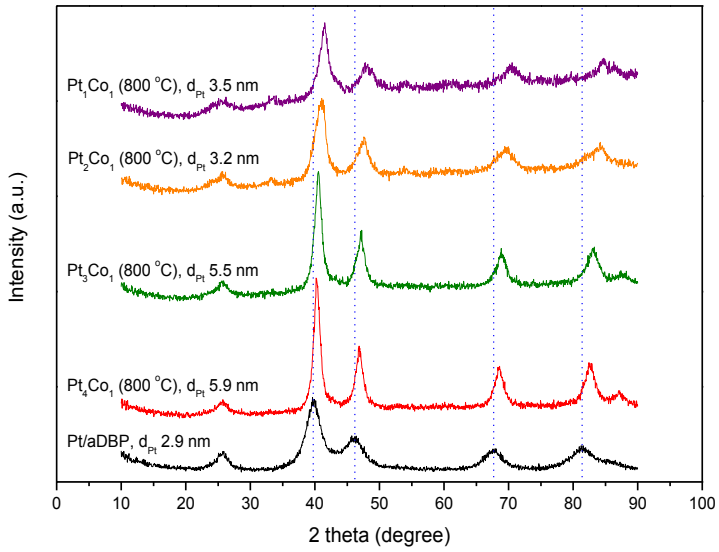

Figure 75. Effect of Pt/Co ratio on the XRD patterns of Pt*/ACCS-2.

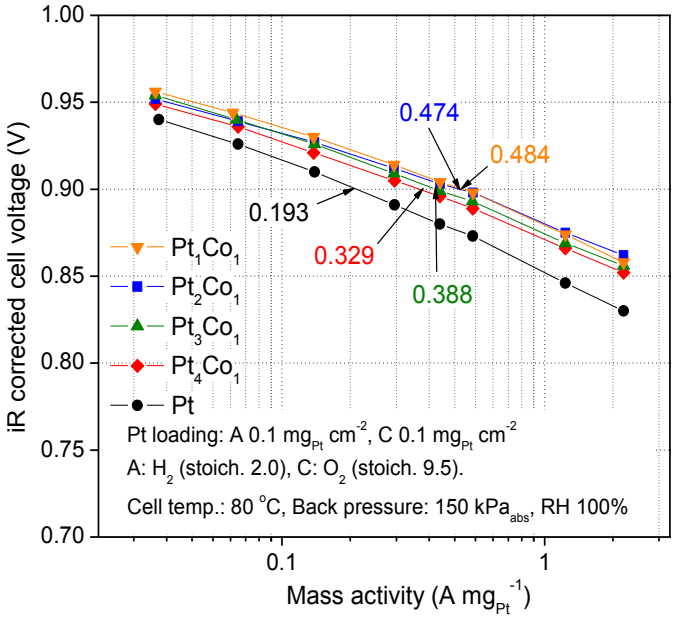

Figure 76. Effect of Pt/Co ratio on the mass activity of Pt*/ACCS-2.

The H_2-air fuel cell performance of Pt*/ACCS-2 catalysts is lower when compared to that of pristine Pt/ACCS-2 catalyst. However, the catalyst stability under 0.6-1.0 V potential cycling experiment is significantly enhanced as will be discussed in the following section.

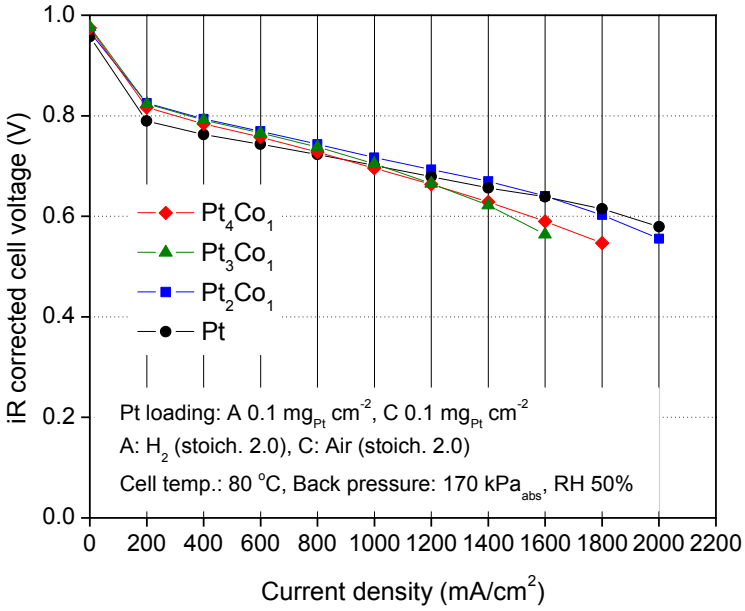

Figure 77. Effect of Pt/Co ratio on the mass activity of Pt*/ACCS-2.

Table 15. Summary of effect of Pt/Co ratio on particle size, mass activity, and H_2-air fuel cell performance of Pt*/ACCS-2.

Pt/Co ratio	**d_{Pt} (nm)**	**Mass activity (A/mg_{Pt})**	**Current density at 0.6 $V_{iR\text{-}corr}$ (mA/cm^2)**
Pt	2.9	0.193	1884
Pt_2Co_1	3.2	0.474	1800
Pt_3Co_1	3.7	0.388	1477
Pt_4Co_1	3.7	0.329	1545

Based on the physical properties and electrochemical properties of various Pt*/ACCS-2 catalysts with different Pt/Co ratios, a catalyst with a composition of Pt_3Co was selected and subjected to catalyst durability and support stability studies under 0.6-1.0 V and 1.0-1.5 V potential cycling conditions, respectively.

4.4.6.4. Support Stability under 1.0-1.5 V Cycling

H_2-Air fuel cell performance of Pt^*/ACCS-2 catalyst tested in 25-cm^2 MEA subjected to 1.0-1.5 V potential cycling test is shown in Fig. 78. The Pt^*/ACCS-2 catalyst showed an initial current density of 1.74 A/cm^2 at 0.6 $V_{iR\text{-}free}$. The high H_2/air fuel cell performance is due to the optimized catalyst layer thickness used for the USC-made catalysts. The catalyst showed a potential loss of only 8 mV (iR-free) at 1.5 A/cm^2 after 5,000 potential cycles between 1.0 and 1.5 V. The support stability of commercial Pt/C is shown in Fig. 79. The commercial catalyst showed initial current density of 1.54 A/cm^2 at 0.6 $V_{iR\text{-}free.}$ At 1.5 A/cm^2, the iR-corrected cell voltage is 0.609 V for initial polarization and no activity is observed after 1,000 cycles between 1.0-1.5 V.

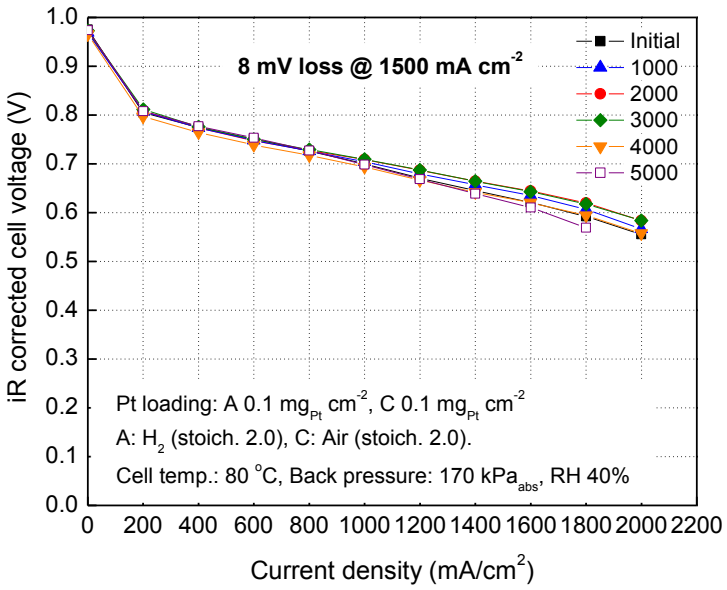

Figure 78. Comparison of H_2/air fuel cell performance of 30% Pt^*/ACCS-2 catalyst subjected to 5,000 potential cycles between 1.0 and 1.5 V at 500 mV/s. Catalyst loading is 0.1 mg_{Pt}/cm^2 on both the anode and cathode electrodes. The fuel cell operating conditions are: H_2/air (2/2 stoic.), 80 °C, 40% relative humidity (RH), 170 kPa_{abs} back pressure. Nafion® NRE 212 membrane is used as the electrolyte.

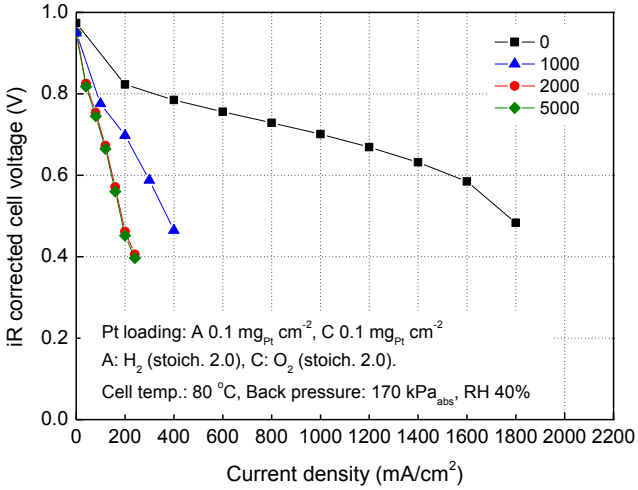

Figure 79. Comparison of H_2/air fuel cell performance of commercial 46% Pt/C catalyst subjected to 5,000 potential cycles between 1.0 and 1.5 V at 500 mV/s. Catalyst loading is 0.1 mg_{PGM}/cm^2 on both the anode and cathode electrodes. The fuel cell operating conditions are: H_2/air (2/2 stoic.), 80 °C, 40% RH, 170 kPa_{abs} back pressure. Nafion® NRE 212 membrane is used as the electrolyte.

Figure 80 shows the stability of mass activity for the Pt*/ACCS-2 catalyst. Potential cycling between 1.0 and 1.5 V resulted in 50% mass activity loss after 5,000 cycles. The commercial 46% Pt/C catalyst showed mass activity loss of 74% after 5,000 cycles (Table 16).

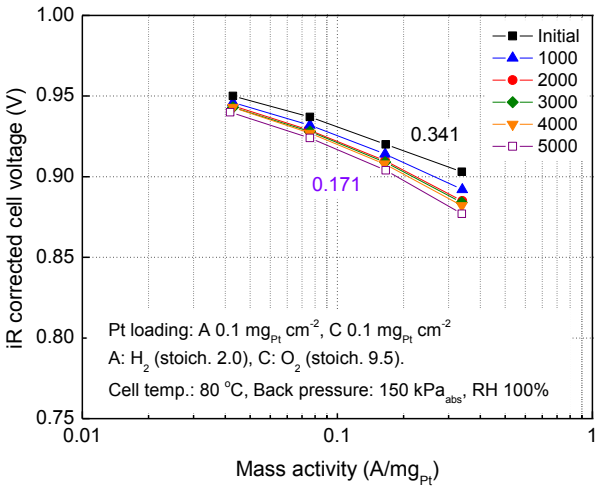

Figure 80. Stability of mass activity of Pt*/ACCS-2 catalyst subjected to 5,000 potential cycles between 1.0 and 1.5 V at 500 mV/s. The catalyst loading is 0.1 mg_{PGM}/cm^2 on both the anode and cathode electrodes. The fuel cell operating conditions are: H_2/O_2 (2/9.5 stoic.), 80°C, 100% RH, 150 kPa_{abs} back pressure. Nafion® NRE 212 membrane is used as the electrolyte.

Table 16. Summary of support stability test (5,000 potential cycles between 1.0 and 1.5 V) and catalyst durability test (30,000 potential cycles between 0.6 and 1.0 V) for Pt*/ACCS-2 and commercial Pt/C catalysts. The catalyst durability of commercial PtCo/C catalyst is also shown for comparison.

Catalyst/Test	Particle size (nm)	Mass activity loss (%)		ECSA (m^2/g_{Pt})		Cell voltage loss (mV)
		Initial	Final	Initial	Final	$\Delta V_{iR\text{-}free}$
Pt*/ACCS-2 Support Stability	3.7	**0.341**	**0.171 (50% loss)** (5k cycles)	**30.5**	**23.9 (22% loss)** (5k cycles)	**8 mV loss** at 1.5 A/cm^2 (5k cycles)
Catalyst Durability	3.7	**0.344**	**0.189 (45% loss)** (30k cycles)	**30.1**	**17.4 (42% loss)** (30k cycles)	**24 mV loss** at 0.8 A/cm^2 (30k cycles)
Commercial Pt/C Support Stability	2.2	**0.18**	**0.047** (**74% loss**) (5k cycles)	**59.8**	**11.0 (82% loss)** (5k cycles)	No activity (5k cycles)
Catalyst Durability	2.2	**0.18**	**0.075** (**58% loss**) (30k cycles)	**62**	**13.6 (78% loss)** (30k cycles)	No activity (30k cycles)
Commercial PtCo/C Support Stability	-	-	-	-	-	-
Catalyst Durability	4.5	**0.38**	**0.116 (69% loss)** (30k cycles)	**68**	**14.3 (79% loss)** (30k cycles)	No activity at 0.8 A/cm^2 (30k cycles)

4.4.6.5. Catalyst Stability under 0.6-1.0 V Cycling

Figure 81 shows the H_2-Air fuel cell performance of Pt*/ACCS-2 catalyst tested in 25-cm^2 MEA subjected to 0.6-1.0 V potential cycling test. The Pt*/ACCS-2 catalyst showed an initial current density of 1.85 A/cm^2 at 0.6 $V_{iR\text{-}free}$ with a potential loss of 24 $mV_{iR\text{-}free}$ at 0.8 A/cm^2 after 30,000 potential cycles between 0.6 and 1.0 V. As shown in Table 16, the commercial 46% Pt/C showed no activity after 30,000 cycles. For comparison, the H_2-air fuel

cell performance of commercial 46% PtCo/C catalyst is shown in Fig. 82. The commercial 46% PtCo/C catalyst showed an initial current density of 936 mA/cm^2 at 0.6 $V_{iR\text{-}free}$ and no activity after 30,000 potential cycles (0.6-1.0 V).

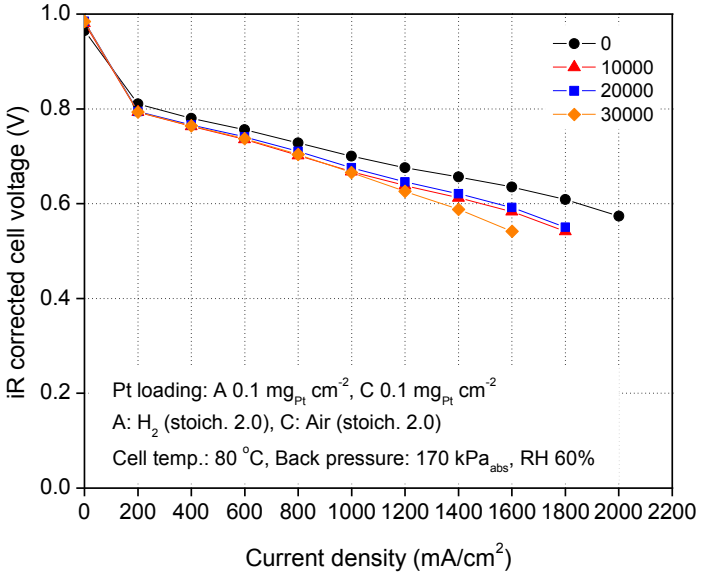

Figure 81. Comparison of H_2/air fuel cell performance of 30% Pt*/ACCS-2 catalyst subjected to 30,000 potential cycles between 0.6 and 1.0 V at 50 mV/s. Catalyst loading is 0.1 mg_{Pt}/cm^2 on both the anode and cathode electrodes. The fuel cell operating conditions are: H_2/air (2/2 stoic.), 80 °C, 60% RH, 170 kPa_{abs} back pressure. Nafion® NRE 212 membrane is used as the electrolyte.

Figure 83 shows initial mass activity of 0.344 A/mg_{Pt} and the stability of mass activity for the Pt*/ACCS-2 catalyst subjected to potential cycling between 0.6 and 1.0 V. The catalyst durability test resulted in 45% mass activity loss after 30,000 cycles. The commercial 46% Pt/C and 46% PtCo/C catalysts showed initial mass activities of 0.18 and 0.38 A/mg_{Pt} and loss of 58% and 69% after 30,000 cycles (Table 16).

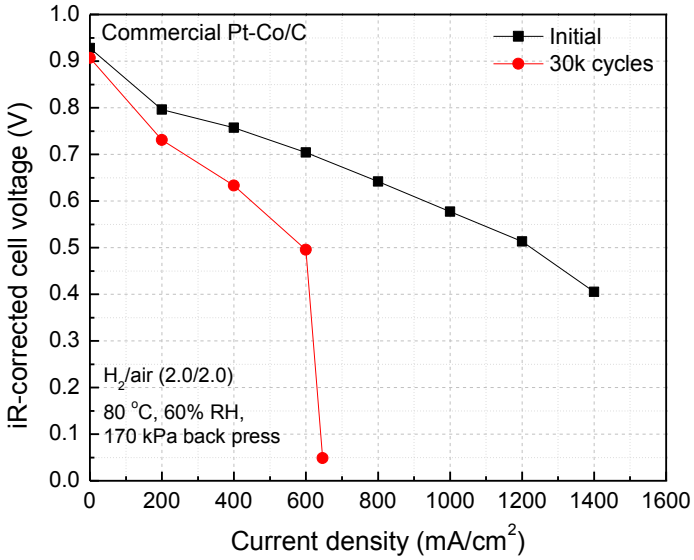

Figure 82. Comparison of H_2/air fuel cell performance of commercial 46% PtCo/C catalyst subjected to 30,000 potential cycles between 0.6 and 1.0 V at 50 mV/s. Catalyst loading is 0.1 mg_{Pt}/cm^2 on both the anode and cathode electrodes. The fuel cell operating conditions are: H_2/air (2/2 stoic.), 80 °C, 50% RH, 170 kPa_{abs} back pressure. Nafion® NRE 212 membrane is used as the electrolyte.

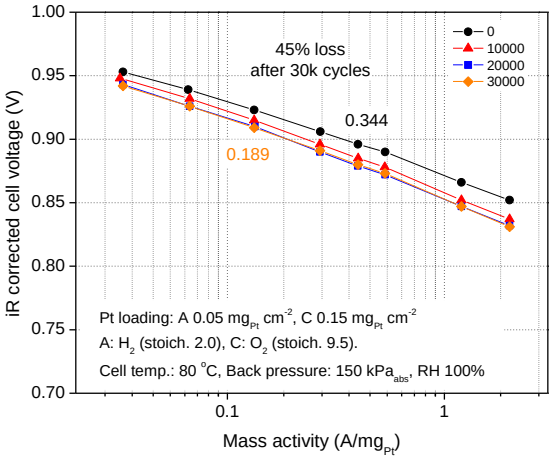

Figure 83. Stability of mass activity of Pt^*/ACCS-2 catalyst subjected to 30,000 potential cycles between 0.6 and 1.0 V at 50 mV/s. The catalyst loading is 0.1 mg_{Pt}/cm^2 on both the anode and cathode electrodes. The fuel cell operating conditions are: H_2/O_2 (2/9.5 stoic.), 80°C, 100% RH, 150 kPa_{abs} back pressure. Nafion® NRE 212 membrane is used as the electrolyte.

The effect of relative humidity on the catalyst stability in H_2-air fuel cell under 0.6-1.0 V potential cycling is shown in Fig. 84 (a & b) and the potential losses with respect to cycle number is summarized in Table 17. From Fig. 82 and 84 (a & b), the potential loss at 800 mA/cm^2 increases as the applied RH value decreased. At 40% and 50% RH values, the Pt*/ACCS-2 catalyst showed 47 mV and 35 mV potential loss at 800 mA/cm^2 after 30,000 cycles which are higher than the one observed when 60% RH is used (24 mV, Fig. 82).

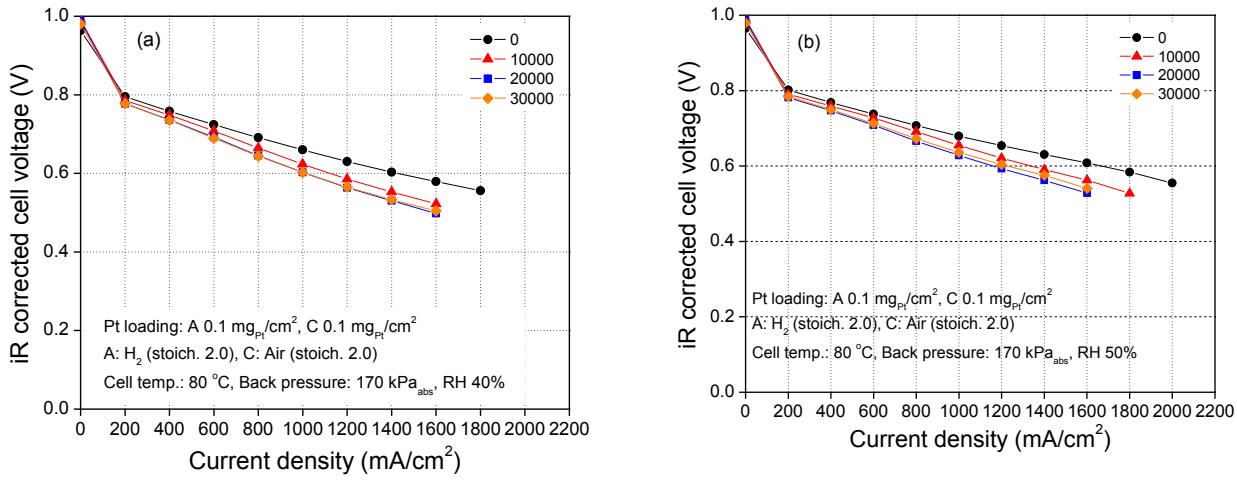

Figure 84. Comparison of H_2/air fuel cell performance of 30% Pt*/ACCS-2 catalyst subjected to 30,000 potential cycles between 0.6 and 1.0 V at 50 mV/s. (a) Relative humidity 40% and (b) Relative humidity 50%. Catalyst loading is 0.1 mg$_{Pt}$/cm^2 on both the anode and cathode electrodes. The fuel cell operating conditions are: H_2/air (2/2 stoic.), 80 °C, 60% RH, 170 kPa$_{abs}$ back pressure. Nafion® NRE 212 membrane is used as the electrolyte.

4.5. Performance Evaluation of Pt/ACCS-2 Catalyst in 50-cm^2 MEAs

For initial performance evaluation in 50-cm^2 MEAs, Pt/ACCS-2 catalyst was employed as the cathode catalyst while commercial 46% Pt/C was used as a catalyst for the anode. Catalyst inks were prepared by ultrasonically mixing the respective catalysts (32 mg), isopropyl alcohol (IPA, 1.8 ml), Nafion® ionomer (5% solution, Alfa Aesar), and DI water (0.2 ml). The ionomer content was 30% and 20% in the anode and cathode inks, respectively. The catalyst inks were sprayed directly on the Nafion® 212 membrane covering an active area of 50-cm^2. The Pt loading on the anode and cathode electrodes is kept at 0.1 mg/cm^2 and the Pt loading was measured using X-ray Fluorescence Spectrometer. The catalyst coated membrane was then hot

pressed at 140 °C using a pressure of 20 kg/cm^2 for 6 min. in between the gas diffusion layers (Sigracet GDL 10BC, SGL) and Teflon gaskets to prepare the membrane electrode assembly (MEA) for the performance evaluation studies in fuel cell. The 50-cm^2 single cell hardware and 50-cm^2 MEAs are shown in Fig. 85.

Table 17. Comparison of cell potential (iR-free) at 800 mA/cm^2 and corresponding potential losses with respect to cycle number at different relative humidity values for Pt*/ACCS-2 catalyst subjected to 0.6-1.0 V potential cycling.

Cycle #	$V_{iR\text{-}free}$ @ 800 mA/cm^2 (mV) RH 40%	Loss (mV)	$V_{iR\text{-}free}$ @ 800 mA/cm^2 (mV) RH 50%	Loss (mV)	$V_{iR\text{-}free}$ @ 800 mA/cm^2 (mV) RH 60%	Loss (mV)
0	690.9	-	707.2	-	728.3	-
10000	664.6	26.3	690.9	16.3	702.0	26.3
20000	645.4	45.5	666.2	41.0	710.4	17.9
30000	643.9	47.0	672.5	34.7	704.0	24.4

(a)

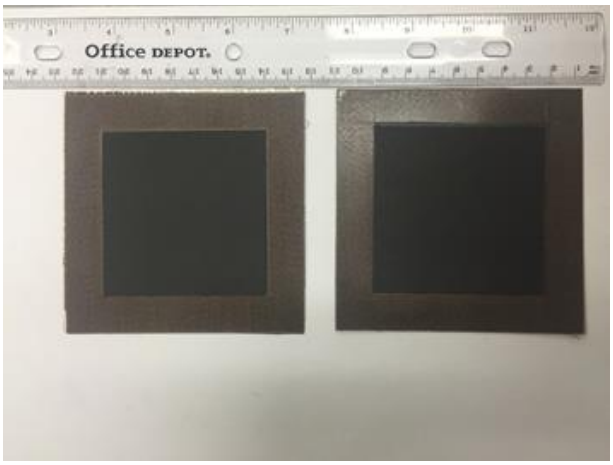

(b)

Figure 85. Photographs of (a) 50-cm^2 single cell hardware and fuel cell station and (b) 50-cm^2 MEAs employing 30% Pt/ACCS-2 as cathode catalyst.

Initially, the MEA was activated under a supply of H_2 and O_2 at 80 °C to the anode and cathode compartments, respectively with a flow rate of 1.5 L/min and 100% relative humidity (RH). After MEA activation, the initial mass activity at 0.9 $V_{iR\text{-}free}$ was evaluated under H_2/O_2 (2/9.5 stoic.) at 80 °C, 100% RH, and 150 kPa_{abs}. back pressure. The electrochemical surface area (ECSA) was estimated using cyclic voltammetry experiments carried out between 0.05 and 0.6 V (vs. RHE) at 80 °C under fully humidified H_2 and N_2 supply to the anode and the cathode, respectively. The H_2-air polarization curves were recorded at 2/2 stoic. and 80 °C, 40%, 50% and 60% RH, and an applied back pressure of 170 kPa_{abs}.

Figure 86 shows the H_2-O_2 fuel cell polarization obtained at a constant reactant flow of 1.5L/1.5 L/min. Figure 87 shows the initial mass activity of 0.185 A/mg_{Pt} for the Pt/ACCS-2 at 0.9 $V_{iR\text{-}free}$. Figure 88 shows the initial H_2-air fuel cell polarization obtained at various relative humidities (40, 50, and 50% RH). At 0.6 $V_{iR\text{-}free}$ the Pt/ACCS-2 catalyst showed ~2.0 A/cm^2 at all relative humidities.

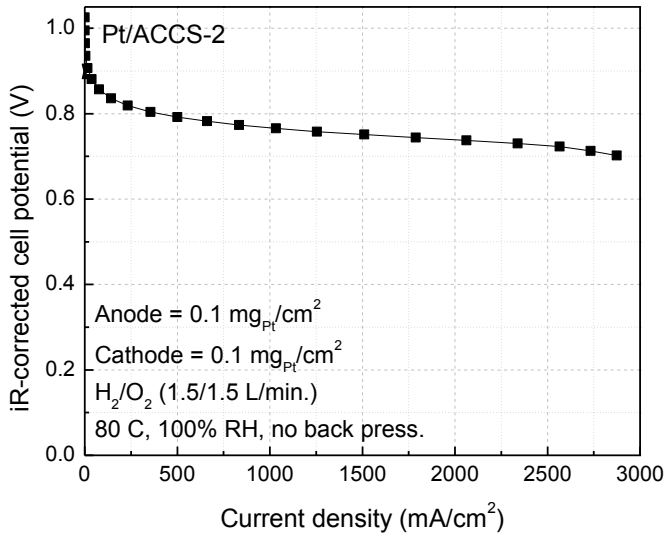

Figure 86. Comparison of H_2/O_2 fuel cell performance of 30% Pt/ACCS-2 catalyst. Catalyst loading is 0.1 mg_{Pt}/cm^2 on both the anode and cathode electrodes. The fuel cell operating conditions are: H_2/O_2 (1.5/1.5 L/min stoic.), 80 °C, 100% RH, no back pressure. Nafion® NRE 212 membrane is used as the electrolyte.

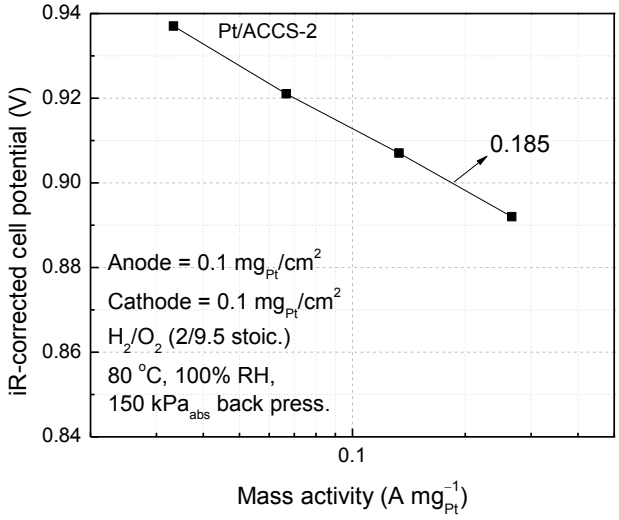

Figure 87. Initial mass activity of Pt/ACCS-2 catalyst. The catalyst loading is 0.1 mg_{Pt}/cm^2 on both the anode and cathode electrodes. The fuel cell operating conditions are: H_2/O_2 (2/9.5 stoic.), 80°C, 100% RH, 150 kPa_{abs} back pressure. Nafion® NRE 212 membrane is used as the electrolyte.

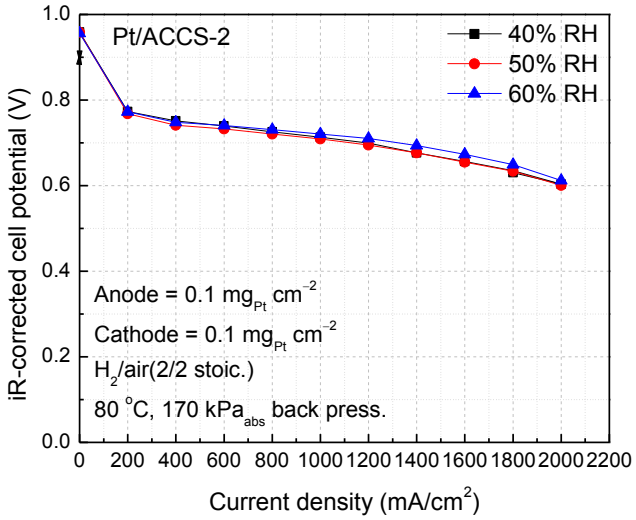

Figure 88. Comparison of H_2/air fuel cell performance of 30% Pt/ACCS-2 catalyst at different relative humidity values (40%, 50%, and 60%). Catalyst loading is 0.1 mg_{Pt}/cm^2 on both the anode and cathode electrodes. The fuel cell operating conditions are: H_2/air (2/2 stoic.), 80 °C, 170 kPa_{abs} back pressure. Nafion® NRE 212 membrane is used as the electrolyte.

4.6. MEA Fabrication using Pt/ACCS-2 and Pt*/ACCS-2 Cathode Catalysts for Independent Evaluation at NREL

4.6.1. Preparation of 25-cm^2 MEAs with Pt/ACCS-2 as cathode catalyst

Based on the reproducibility results, two 25 cm^2 MEAs were fabricated and assembled in fuel cell hardware for independent evaluation at NREL. These two MEAs were activated and their initial H_2-air fuel cell performances (1.85 and 1.83 A/cm^2 at 0.6 $V_{iR\text{-}free}$ for MEA#1 and MEA#2, respectively) and mass activities (0.181 and 0.207 A/mg_{Pt} for MEA#1 and MEA#2, respectively) were measured as shown in Fig. 89 and Fig. 90, respectively.

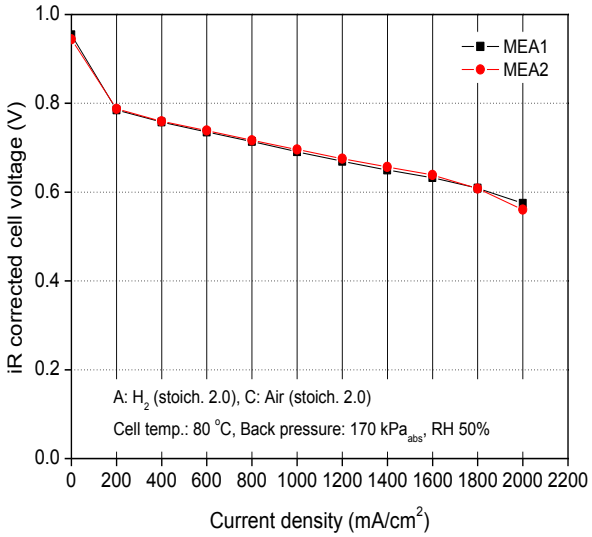

Figure 89. Comparison of initial H_2/air fuel cell performances of 30% Pt/A-CCS catalyst in two MEAs assembled in fuel cell hardware for further evaluation at NREL. Catalyst loading is 0.1 mg_{PGM}/cm^2 on both the anode and cathode electrodes. The fuel cell operating conditions are: H_2/air (2/2 stoic.), 80 °C, 50% RH, 170 kPa_{abs} back pressure. Nafion® NRE 212 membrane is used as the electrolyte.

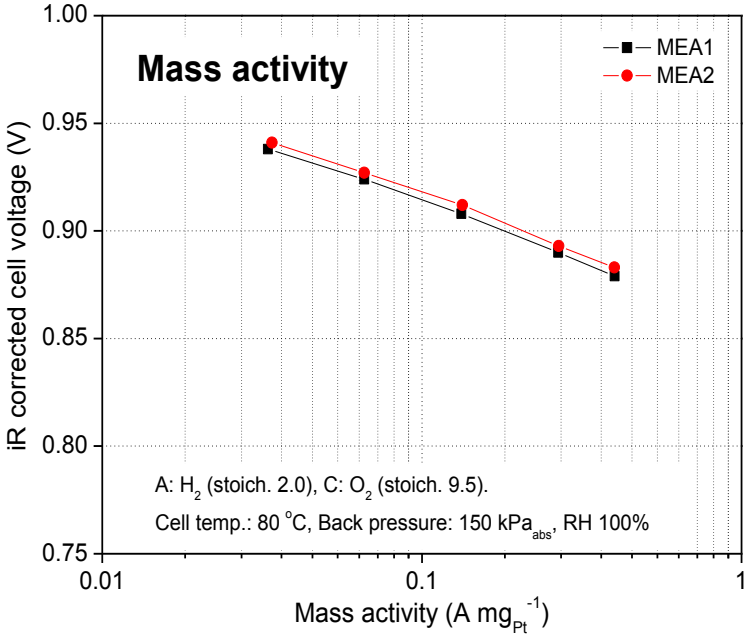

Figure 90. Comparison of initial mass activities of 30% Pt/A-CCS catalyst in two MEAs assembled in fuel cell hardware for further evaluation at NREL. Catalyst loading is 0.1 mg_{PGM}/cm^2 on both the anode and cathode electrodes. The fuel cell operating conditions are: H_2/O_2 (2/9.5 stoic.), 80°C, 100% RH, 150 kPa_{abs} back pressure. Nafion® NRE 212 membrane is used as the electrolyte.

4.6.2. Preparation of 25-cm2 MEAs with Pt/ACCS-2 as cathode catalyst*

Based on the reproducibility results, five 25 cm^2 MEAs were fabricated using Pt*/ACCS-2 as cathode catalyst for independent evaluation at NREL. These five MEAs were activated and their initial H_2-air fuel cell performances (1.76, 1.72, 1.66, 1.66, and 1.69 A/cm^2 at 0.6 $V_{iR\text{-}free}$ for MEA#1, #2, #3, #4, and #5 respectively) and mass activities (0.334, 0.341, 0.348, 0.331, and 0.349 A/mgPt for MEA#1, #2, #3, #4, and #5 respectively) were measured as shown in Fig. 91 and Fig. 92 respectively.

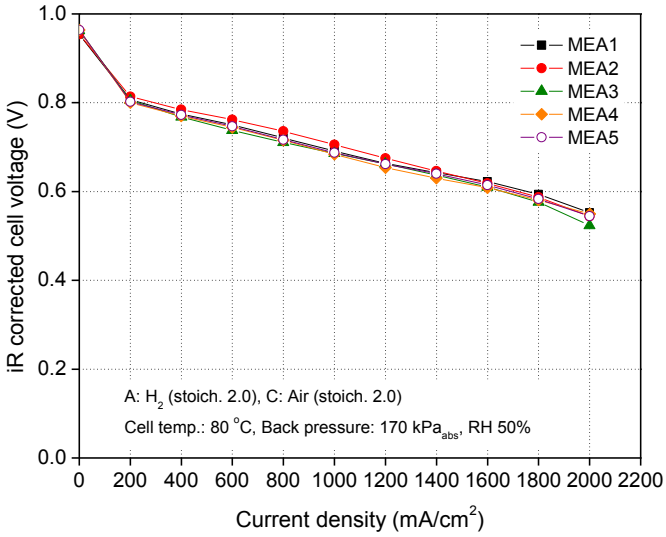

Figure 91. Comparison of initial H_2/air fuel cell performances of 30% Pt*/ACCS-2 catalyst in five MEAs assembled in fuel cell hardware for further evaluation at NREL. Catalyst loading is 0.1 mg_{Pt}/cm^2 on both the anode and cathode electrodes. The fuel cell operating conditions are: H_2/air (2/2 stoic.), 80 °C, 50% RH, 170 kPa_{abs} back pressure. Nafion® NRE 212 membrane is used as the electrolyte.

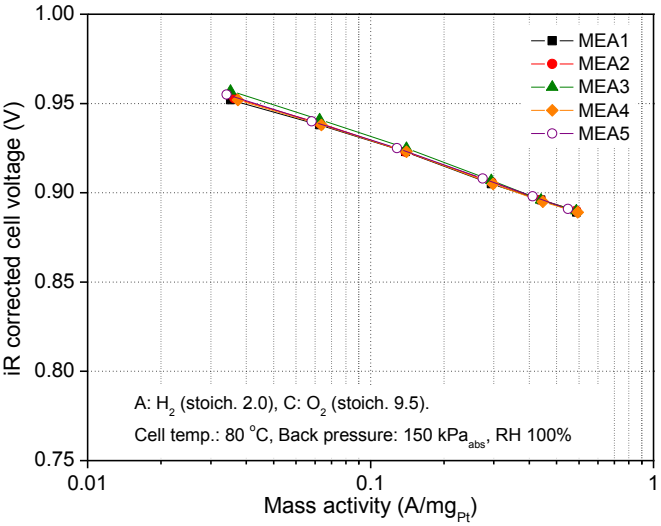

Figure 92. Comparison of initial mass activities of 30% Pt*/ACCS-2 catalyst in five MEAs assembled in fuel cell hardware for further evaluation at NREL. Catalyst loading is 0.1 mg_{PGM}/cm^2 on both the anode and cathode electrodes. The fuel cell operating conditions are: H_2/O_2 (2/9.5 stoic.), 80°C, 100% RH, 150 kPa_{abs} back pressure. Nafion® NRE 212 membrane is used as the electrolyte.

5.0. Summary

Combined experimental and simulation techniques were applied to evaluate the validity of the commonly applied Tafel-approximation for the calculation of the mass and specific activities. A one dimensional agglomerate-based macro-homogeneous model was developed and solved analytically and numerically to understand the effects of exchange current density, porosity, agglomerate size, Nafion® film thickness and Pt loading on the mass activity.

A comprehensive experimental characterization of MEAs at different Pt loadings implied, that the mass activity (MA) is controlled not only by and the ORR kinetics, but also by the utilization of the Pt surface area which in turn depends on the cathode Pt loading. The MA is also controlled by the morphology of the catalyst layer which depends on the self-assembled nature of the catalyst and how effectively it fills out the volume. Therefore a detailed and more precise definition of MA is given to elucidate the variation of MA with catalyst loading.

A combined experimental and numerical model based parameter estimation technique has been applied for the separation of the kinetic and mass transport resistances. A new parameter has been proposed for the characterization of the layer growth process. The fractal dimension was measured by Hg porosimetry and was found to decrease as the loading increased, which is an indication of a higher degree of agglomeration. The theoretically predicted variation showed that the decrease of the fractal dimension decreases the mass activity, while increasing the mass transport resistances.

A general pore-scale model was developed which mimics the electro-active layer formation process. The model was used to simulate the active material loading on battery, fuel cell and supercapacitor electrodes. The active layer was reconstructed by coating 108 particles with different inter-particle interactions onto a smooth surface. The analysis of experimental data and modeling results revealed that (measurable) specific activity and volumetric capacitance increase at ultra-low loading, because the surface area in unit volume (or porosity) and the thickness scale differently with loading. Finally a general relationship was proposed, which describes the evolution of volumetric surface area density of fuel cells, batteries and supercapacitor with loading, and can be used to build a bridge between mesoscale morphology and macroscopic simulation.

Cathode catalyst based on Pt* (Pt* = compressive Pt lattice catalyst) deposited on carbon composite catalyst support (CCCS) with high measured activity and stability under potential

cycling conditions for polymer electrolyte membrane (PEM) fuel cells was developed in this study. The catalyst was synthesized through platinum deposition on Co-doped CCCS support containing pyridinic-nitrogen active sites followed by controlled heat-treatment. High resolution transmission electron microscopy (HRTEM) and X-ray diffraction (XRD) studies confirmed uniform Pt deposition (Pt/CCCS catalyst, d_{Pt} = 2 nm) and formation of Pt*/CCCS catalyst (d_{Pt} = 5.4 nm) respectively. X-ray energy dispersive spectrometry (XEDS) line-scan studies showed the formation of Co-core Pt-shell type catalyst with a Pt-shell thickness of ~0.75 nm. At 0.9 ViR-free, the Pt*/CCCS catalyst showed initial mass activity of 0.44 A/mg_{Pt} and 0.25 A/mg_{Pt} after 30,000 potential cycles between 0.6 and 1.0 V corresponding to an overall measured activity loss of 42.8%. The enhanced catalytic activity at high potentials and stability of mass activity for the Pt*/CCCS catalyst are attributed to the formation of compressive Pt lattice catalyst due to Co doping. The Pt*/CCCS showed stable open circuit potential close to 1.0 V under H2-air with an initial power density of 857 mW/cm^2 and only 16% loss after 30,000 cycles. Catalyst durability studies performed between 0.6 and 1.0 V indicated that Co doping increased the onset potential for PtO_2 formation close to 1.0 V vs. reversible hydrogen electrode (RHE). The enhanced catalytic activity and stability of Pt*/CCCS catalyst are attributed to (i) higher onset potential for PtO_2 formation resulting in less PtO_2 formation during potential cycling which alleviates Pt dissolution in the reverse scan (ii) higher stability of CCCS used as a support compared with commercially used supports, and (iii) optimized electrochemical properties of the catalyst and the support which results in the synergistic effect between pyridinic nitrogen catalytic sites from the Co-doped CCCS and compressive Pt-lattice catalyst.

Activated carbon composite support-1 (ACCS-1) was synthesized using purification and stabilization process with a different carbon precursor as a starting material. The Pt on ACCS-1 support exhibits improved Pt catalyst stability due to modified pore size distribution and graphitization of the support. On the other hand, the Pt/ACCS-1 catalyst exhibited only 27 mV loss at 800 mA/cm^2 after 400-hour potential holding at 1.2 V and 35 mV loss at 1500 mA/cm^2 after 5,000 potential cycles between 1.0 and 1.5 V. The enhanced support stability is attributed to high surface hydrophobicity which repels water that is produced during high current operation and slows down carbon corrosion.

Pt*/ACCS-1 catalyst was synthesized according to the methodology developed at USC and its catalyst durability under 0.6-1.0 V potential cycling and support stability under 1.0-1.5 V

potential cycling was evaluated. To avoid the leaching step during Pt* catalyst synthesis, the effect of Pt to Co ratio on the ORR activity in PEMFC was investigated. With the increase of Co to Pt ratio from 0 to 0.67:1, the mass activity at high potential (0.9 $V_{iR\text{-}free}$) increases while the H_2-air performance at low potential decreases. Co to Pt ratio of 0.5:1 was selected to further analyze the annealing temperature effect on the activity and stability of the catalyst. Low temperature treated catalyst exhibits better activity while high temperature treated catalyst shows higher catalyst stability under moderate potential cycling conditions. Therefore, it is a trade-off between the catalyst activity and durability. The final optimized Pt* catalyst is achieved with Pt2Co1 ratio annealed at 850 °C. The ACCS-1 support also shows high corrosion-resistance in the presence of Pt* during potential cycling between 1.0 and 1.5V.

Activated carbon composite support-2 (ACCS-2) was synthesized using a novel methodology developed at USC. The ACCS-2 showed good thermal stability similar to that of carbon nanofibers (CNFs). Pt/ACCS-2 catalyst showed excellent support stability under simulated start-up/shut-down operating conditions (1.0-1.5 V, 5000 cycles). The Pt/ACCS-2 catalyst showed an initial mass activity of 0.215 A/mgPt and a loss of 52% after 30,000 cycles between 0.6 and 1.0 V. The catalyst showed 73 mV loss at 800 mA/cm^2 with an ECSA loss of 66% after 30,000 cycles. Furthermore, Pt/ACCS-2 showed 35% loss of mass activity and 15 mV potential loss at 1.5 A/cm^2 after 5000 cycles (1.0-1.5 V). The good activity and excellent stability of Pt/ACCS-2 is attributed to the higher degree of graphitization and enhanced hydrophobicity of ACCS-2.

Pt*/ACCS-2 catalyst was synthesized according to the methodology developed at USC and its catalyst durability under 0.6-1.0 V potential cycling and support stability under 1.0-1.5 V potential cycling was evaluated. The Pt*/ACCS-2 catalyst showed an initial mass activity of 0.34 A/mg_{PGM} at 0.9 $V_{iR\text{-}free}$ and loss of mass activity of 45% after 30,000 cycles (0.6-1.0 V). The catalyst performance under H_2-air fuel cell operating conditions showed only 24 mV (iR-free) loss at 0.8 A/cm^2 with an ECSA loss of 42% after 30,000 cycles (0.6-1.0 V). The support stability under 1.0-1.5 V potential cycling showed mass activity loss of 50%, potential loss of 8 mV (iR-free) at 1.5 A/cm^2, and ECSA loss of 22% after 5,000 cycles. Furthermore, the Pt*/ACCS-2 catalyst showed an initial power density (rated) of 0.174 g_{PGM}/kW.

The performance and durability results of 30%Pt*/CCCS, 30%Pt*/ACCS-2, and 30%Pt*/ACCS-2 are summarized below:

Catalyst: 30% Pt*/CCCS (Table A)

- Accomplished initial mass activity of 0.44 A/mg_{PGM} and loss of mass activity of **43% after 30k cycles** (0.6-1.0 V).
- Accomplished **potential loss of 40 mV after 30k cycles** (0.6-1.0 V) at 0.8 A/cm^2.
- Accomplished **32% ECSA loss** after 30k cycles.
- Accomplished (rated) initial power density of **0.23 g_{PGM}/kW.**

Catalyst: 30% Pt/ACCS -2 (Table B)

- Accomplished initial mass activity of 0.215 A/mg_{PGM} and loss of mass activity of 52% after 30k cycles (0.6-1.0 V).
- Accomplished potential loss of 73 mV after 30k cycles (0.6-1.0 V) at 0.8 A/cm^2.
- Accomplished 66% ECSA loss after 30k (0.6-1.0 V) cycles.
- Accomplished initial mass activity of 0.215 A/mg_{PGM} and loss of mass activity of 35% after 5k cycles (1.0-1.5 V).
- Accomplished **15 mV loss** at 1.5 A/cm^2 after 5k cycles (1.0-1.5 V).
- Accomplished (rated) initial power density of 0.18 g_{PGM}/kW.

Catalyst: 30% Pt*/ACCS-2 (Table C)

- Accomplished initial mass activity of **0.34 A/mg_{PGM}** and **45% loss** after 30k cycles (0.6-1.0 V).
- Accomplished **24 mV potential loss** (iR-free) after 30k cycles (0.6-1.0 V) at 0.8 A/cm^2.
- Accomplished **42% ECSA loss** after 30k (0.6-1.0 V) cycles.
- Accomplished initial mass activity of **0.34 A/mg_{PGM}** and **50% loss** after 5k cycles (1.0-1.5 V).
- Accomplished **8 mV (iR-free) loss** at 1.5 A/cm after 1.0-1.5 V potential cycling.
- Accomplished **22% ECSA loss** after 5k (1.0-1.5 V) cycles.
- Accomplished (rated) initial power density of **0.174 g_{PGM}/kW**.

Table A. Summary of accomplishments obtained with 30% Pt*/CCCS catalyst

Metric	Units	*Status Sep 30, 2015*	Commercial Pt/C	2017 DOE target
Initial Mass Activity				
Initial Mass activity	A/mg_{PGM} @ 900 $mV_{iR\text{-}free}$	***0.44***	0.18	≥0.44
Catalyst Stability (0.6-1.0 V cycling)				
Loss in catalyst activity	% loss after 30k cycles	***43%***	58%	≤40%
Loss in ECSA	% loss after 30k cycles	***32%***	78%	≤40%
Potential loss @ 800 mA/cm^2	mV loss after 30k cycles	***40 mV***	No Activity	≤30 mV
PGM Content and PGM Loading				
PGM total content (Power Density)	g_{PGM}/kW (rated)	***0.23***	0.3	≤0.125
PGM total loading	mg_{PGM}/cm^2_{geo}	***0.2***	0.2	≤0.125

Table B. Summary of accomplishments obtained with 30% Pt/A-CCS-2

Metric	Units	*Status (Sep 30, 2015)*	Commercial Pt/C	2017 DOE target
Initial Mass Activity				
Initial Mass activity	A/mg_{PGM} @ 900 $mV_{iR\text{-}free}$	***0.215***	0.18	≥0.44
Catalyst Stability (0.6-1.0 V cycling)				
Loss in catalyst activity	% loss after 30k cycles	***52%***	58%	≤40%
Loss in ECSA	% loss after 30k cycles	***66%***	78%	≤40%
Potential loss @ 800 mA/cm^2	mV loss after 30k cycles	***73 mV***	No Activity	≤30 mV
Support Stability (1.0-1.5 V cycling)				
Loss in catalyst activity	% loss after 400 h	***35%***	74%	≤40%
Loss in ECSA	% loss after 400 h	***45%***	82%	≤40%
Potential loss @ 1500 mA/cm^2	mV loss after 400 h	***15 mV***	No Activity	≤30 mV
PGM Content and PGM Loading				
PGM total content (Power Density)	g_{PGM}/kW (rated)	***0.18***	0.3	≤0.125
PGM total loading	mg_{PGM}/cm^2_{geo}	***0.2***	0.2	≤0.125

Table C. Summary of accomplishments obtained with 30% Pt*/ACCS-2 catalyst

Characteristic	Units	2017 DOE Targets	Status (Dec 31, 2015) (Pt*/ACCS-2)
PGM total content	g/kW (rated)	0.125	0.174
PGM total loading	mg_{PGM}/cm^2	0.125	0.2
Mass activity (H_2/O_2 (2/9.5 stoic.) 80 °C, 100% RH, 150 kPa_{abs}.)	A/mg_{Pt} @ 0.9 $V_{iR\text{-}free}$	0.44	0.344
Catalyst durability (30,000 cycles, 0.6-1.0 V, 50 mV/s, 80°C, H_2/N_2, 100% RH, No back press.)	% Mass activity (MA) loss % ECSA loss mV loss @ 0.8 A/cm^2	≤40% ≤40% ≤30 mV @ 0.8 A/cm^2	45% loss (MA) 42% loss (ECSA) 24 mV loss (H_2-air)
Support stability (5,000 cycles, 1.0-1.5 V, 500 mV/s, 80°C, H_2/N_2, 100% RH, No back press.)	% Mass activity (MA) loss % ECSA loss mV loss @ 1.5 A/cm^2	≤40% ≤40% ≤30 mV @ 1.5 A/cm^2	50% loss (MA) 22% loss (ECSA) 8 mV loss (H_2-air)

6.0. Accomplishments against the milestones described in "Statement of Project Objectives" dated 01/23/2014

Quarterly Milestones (Starting 1/1/14)

Q1: Determination of structure and composition of the Pt*/A-CCS catalyst prepared by the USC methodology which will have a mass activity of at least 0.3 A/mg_{PGM}.

Q2: Stability of the mass activity of the Pt*/A-CCS catalyst as measured by ≤40% loss of the initial value and at least 0.26 A/mg_{PGM} after 30k cycles (0.6-1.0 V).

Q3: Demonstration of an optimized A-CCS support with improved surface properties, facilitating uniform Pt deposition (2.5 to 3.5 nm) and homogeneous distribution of Pt* (3-5 nm), resulting in achieving a mass activity of at least 0.26 A/mg_{PGM} and only 30-50 mV loss at 0.8 A/cm^2 after 400 h of potential holding at 1.2 V.

Q4: Demonstration of MEA performance in H_2/air with an initial high current density performance of at least 1.5 A/cm^2 at 0.6 $V_{iR\text{-}free}$ and power density ≤0.24 g_{PGM}/kW (rated).

Q5: Demonstration of stable MEA high current density performance (0.8 A/cm^2) in H_2/air by achieving only 30-60 mV loss after potential cycling for 30k cycles (0.6 and 1.0 V) and only 30-50 mV loss after potential holding (1.2 V) for 400 h.

Q6: Demonstration of a most promising catalyst in a 50 cm^2 single cell with the following characteristics: (i) initial mass activity of 0.3 A/mg_{PGM} and stability of mass activity of at least 0.26 A/mg_{PGM} after 30k cycles, (ii) initial high current density performance of at least 1.5 A/cm^2 at 0.6 $V_{iR\text{-}free}$, and (iii) stability of high current density of only 30-60 mV loss at 0.8 A/cm^2 following accelerated stress testing.

Status against Quarterly Milestone as of 12/31/2015

Catalyst: 30% Pt*/A-CCS-2

Metric	Units	*Status (June 30, 2015)*	Commercial Pt/C	SOPO Quarterly Milestones
Initial Mass Activity (Q1)				
Initial Mass activity	A/mg_{PGM} @ 900 $mV_{iR\text{-}free}$	***0.34***	0.18	At least 0.3
Stability of Mass Activity (0.6-1.0 V cycling) (Q2)				
Stability of Mass activity (30k cycles)	A/mg_{PGM} @ 900 $mV_{iR\text{-}free}$	**0.187 (45% loss)**	0.06 (66% loss)	At least 0.26
Support Stability (1.0-1.5V Cycling) (Q3) Additional Test Performed Instead of 1.2 V Holding				
Stability of Mass activity (1.0-1.5V Cycling)	A/mg_{PGM} @ 900 $mV_{iR\text{-}free}$	**0.17 (50% loss)**	0.07 (61% loss)	Not defined in SOPO
Potential loss @ 1500 mA/cm^2 (1.0-1.5V Cycling)	mV loss after 5k cycles	***8 mV loss***	No Activity	Not defined in SOPO
Rated Power Density (Q4)				
PGM total content (Power Density)	g_{PGM}/kW (rated)	***0.174***	0.3	≤0.24
Catalyst Durability (0.6-1.0 V Cycling) (Q5)				
Potential loss @ 800 mA/cm^2	mV loss after 30k cycles	***24***	No Activity	30-60 mV

Abbreviations Used in the Report

ACCS-1 – Activated Carbon Composite Support-1

ACCS-2 – Activated Carbon Composite Support-2

BET Surface Area – Brunauer-Emmett-Teller Surface Area

BJH – Barrett-Joyner-Halenda

CCCS – Carbon Composite Catalyst Support

HRTEM – High-Resolution Transmission Electron Microscopy

MEA – Membrane Electrode Assembly

NRE 212 – Trade name for Nafion® 212 membrane purchased from DuPont

NREL – National Renewable Energy Laboratory

ORR - Oxygen Reduction Reaction

PEMFC - Polymer Electrolyte Membrane Fuel Cell

PGM - Platinum Group Metal

Pt – Platinum

Pt* – Compressive Platinum Lattice Catalyst

Pt*/A-CCS – Compressive platinum lattice catalyst deposited on carbon composite catalyst support

Pt/ACCS-1 – Platinum Deposited on Activated Carbon Composite Support-1

Pt/A-CCS-2 – Platinum Deposited on Activated Carbon Composite Support-2

Pt*/ACCS-1 – Compressive platinum lattice catalyst deposited on activated carbon composite support-1

Pt*/ACCS-2 – Compressive platinum lattice catalyst deposited on activated carbon composite support-2

RH - Relative Humidity

SXPES - X-ray photoemission spectroscopy

USC - University of South Carolina

XEDS - X-ray energy-dispersive spectrometry

XRF – X-ray fluorescence

XRD - X-ray Diffraction

Publications (2009-2015)

1. Taekeun Kim and Branko N. Popov, Enhanced activity and stability for oxygen reduction reaction on Pt-Co electrocatalysts in polymer electrolyte membrane fuel cells by optimizing synthesis parameters, **Submitted to** *Electrochim. Acta*, Dec 2015.
2. Tianyuan Xie and B.N. Popov, Effect of carbon graphitization degree on catalyst support stability at high potentials in polymer electrolyte membrane fuel cells, **Under Preparation** for submission in *J. Electrochem. Soc.* Dec 2015.
3. Wonsuk Jung and Branko N. Popov, Development of hybrid cathode catalyst for PEMFCs: synergistic effect of Pt and carbon composite catalyst, **Under Preparation** for submission in *Int. J. Hyd. Energy*, Dec 2015.
4. Taekeun Kim, Tianyuan Xie, and Branko N. Popov, Development of highly-active and stable Pt/C catalyst for polymer electrolyte membrane fuel cells under simulated start-up/shut-down cycling, **Accepted for publication in** , *Int. J. Hyd. Energy*, October 2015.
5. Wonsuk Jung, Tianyuan Xie, Taekeun Kim, Prabhu Ganesan, Branko N. Popov, Highly Active and Durable Co-Doped Pt/CCC Cathode Catalyst for Polymer Electrolyte Membrane Fuel Cells, *Electrochim. Acta*, **167**, (2015) 1-12.
6. T. Kim, T. Xie, W.S. Jung, F. Gadala-Maria, P. Ganesan, B.N. Popov, Development of Catalytically Active and Highly Stable Catalyst Supports for Polymer Electrolyte Membrane Fuel Cells, *J. Power Sources*, **273**, (2015) 761-774.
7. T. Xie, W.S. Jung, T. Kim, P. Ganesan, B.N. Popov, Development of Highly Active and Durable Hybrid Cathode Catalysts or Polymer Electrolyte Membrane Fuel Cells, *J. Electrochem. Soc*., **161** (2014) F1489-F1501.
8. Branko N. Popov, Tianyuan Xie, Taekeun Kim, Won Suk Jung, and Prabhu Ganesan, Development of Ultra-Low Loading Pt Alloy Cathode Catalyst for PEM Fuel Cells, *ECS Transactions*, **58** (2013) 761-778.
9. Ákos Kriston, Tianyuan Xie and Branko N. Popov, Impact of Ultra-low Platinum loading on Mass Activity and Mass Transport in H_2-Oxygen and H_2-Air PEM Fuel Cells, *Electrochim. Acta*, **121** (2014) 116-127.
10. Ákos Kriston, Tianyuan Xie, David Gamliel, Prabhu Ganesan, Branko N. Popov, Effect of Ultra-Low Pt Loading on Mass Activity of PEM Fuel Cells, *J. Power Sources*, **243** (2013) 958-963.
11. Akos Kriston, Tianyuan Xie, Prabhu Ganesan, Branko N. Popov, Analysis of the Effect of Pt Loading on Mass and Specific Activity in PEM Fuel Cells, *J. Electrochem. Soc*., **160** (2013) F406-F412.
12. Branko N. Popov, Tianyuan Xie, Taekeun Kim, Won-suk Jung, Akos Kriston Brian Murphy and Prabhu Ganesan, Development of Ultra-Low Pt Alloy Cathode Catalyst for PEM Fuel Cells, *ECS Transactions*, **50** (2013) 773-785.
13. Tianyuan Xie, Taekeun Kim, Won Suk Jung, Kriston Akos Prabhu Ganesan and Branko N. Popov, Development of Highly Active Pt_2Ni/C Catalyst for PEM Fuel Cell, *ECS Transactions*, **50** (2013) 1615-1626.
14. Taekeun Kim, Won Suk Jung, Tianyuan Xie, Akos Kriston, Prabhu Ganesan, David Gamliel, Brian Murphy and Branko N. Popov, "Development of Hybrid Cathode Catalyst for PEM Fuel Cells," *ECS Transactions*, **50** (2013) 1875-1885.
15. Akos Kriston, Tianyuan Xie, Taekeun Kim, Won Suk Jung, David Gamliel, Brian Murphy Prabhu Ganesan, Branko N. Popov, Analyzing the effect of Ultra-Low Pt

Loading on Mass and Specific Activity of PEM Fuel Cells, *ECS Transactions*, **50**, (2013) 1427-1438.
16. Sheng-Yang Huang, Prabhu Ganesan, and Branko N. Popov, Electrocatalytic Activity and Stability of Titania Supported Platinum-Palladium Catalysts for Polymer Electrolyte Membrane Fuel Cell, *ACS Catalysis*, **2** (2012) 825-831.
17. Sheng-Yang Huang, Prabhu Ganesan, Ho-Young Jung and Branko N. Popov, Development of supported bifunctional oxygen electrocatalysts and corrosion-resistant gas diffusion layer for unitized regenerative fuel cell applications, *J. Power Sources*, **198** (2012) 23-29.
18. Sehkyu Park, Branko N. Popov, Effect of a GDL based on carbon paper or carbon cloth on PEM fuel cell performance, *Fuel*, **90** (2011) 436-440.
19. Xuguang Li, Branko N. Popov, Takeo Kawahara, Hiroyuki Yanagi, Non-precious metal catalysts synthesized from precursors of carbon, nitrogen, and transition metal for oxygen reduction in alkaline fuel cells, *J Power Sources*, **196** (2011) 1717-1722.
20. Gang Liu, Xuguang Li, Jong-Won Lee and Branko Popov, A Review of the Development of Nitrogen Modified Carbon-based catalyst for Oxygen Reduction at USC, *Catalysis Science & Technology*, **1** (2011) 207-217.
21. Sheng-Yang Huang, Prabhu Ganesan, Branko N. Popov, Titania supported platinum catalyst with high electrocatalytic activity and stability for polymer electrolyte membrane fuel cell, *Appl. Catal. B: Environmental*, **102** (2011) 71-77.
22. Xuguang Li, Gang Liu, Prabhu Ganesan, Hansung Kim, Bumwook Roh, and Inchul Hwang, Development of Ultra-Low Pt Alloy Cathode Catalyst for PEM Fuel Cells, Branko N. Popov, *ECS Transactions*, **41** (2011) 955-969.
23. S. Y. Huang, P. Ganesan, and B. N. Popov, Titanium dioxide-supported platinum catalysts, *ECS Transactions*, **41** (2011) 2255-2268.
24. B. N. Popov, X. Li and J. W. Lee, Power source research at USC: Development of advanced electrocatalysts for polymer electrolyte membrane fuel cells, *Int. J. Hyd. Energy*, **36** (2011) 1794-1802.
25. Li Xuguang, Park Sehkyu, Branko N. Popov, Highly stable Pt and PtPd hybrid catalysts supported on a nitrogen-modified carbon composite for fuel cell application, *J Power Sources*, **195** (2010) 445-452.
26. Liu Gang, Li Xuguang, Ganesan Prabhu, Branko N. Popov, Studies of oxygen reduction reaction active sites and stability of nitrogen-modified carbon composite catalysts for PEM fuel cells, *Electrochim. Acta*, **55** (2010) 2853-2858.
27. Xuguang Li, Gang Liu, Branko N. Popov, Activity and stability of non-precious metal catalysts for oxygen reduction in acid and alkaline electrolytes, *J. Power Sources*, **195** (2010) 6373-6378.
28. Peng Zhang, Shengyang Huang and B. N. Popov, Mesoporous Tin Oxide as an Oxidation-Resistant Catalyst Support for Proton Exchange Membrane Fuel Cells, *J. Electrochem. Soc*., **157** (2010) B1163-B1172.
29. Huang Sheng-Yang, Ganesan Prabhu, Popov Branko N, Electrocatalytic activity and stability of niobium-doped titanium oxide supported platinum catalyst for polymer electrolyte membrane fuel cells, *Appl. Catal. B: Environmental*, **96** (2010) 224-231.
30. X. Li, B.N. Popov, T. Kawahara, H. Yanagi, Recent Advances in Non-Precious Metal Catalyst for Oxygen Reduction Reaction in Fuel Cells, *ECS Transactions*, **33** (2010) 1769-1776.

31. X. Li, S. Huang, B.N. Popov, Development of Low Platinum Loading Cathode Catalysts for Polymer Electrolyte Membrane Fuel Cells, *ECS Transactions*, **33** (2010) 239-246.
32. S. Huang, P. Ganesan, W. Jung, N. Cadirov, B.N. Popov, Development of Supported Bifunctional Oxygen Electrocatalysts with High Performance for Unitized Regenerative Fuel Cell Applications, *ECS Transactions*, **33** (2010) 1979-1987.
33. S. Huang, P. Ganesan, W. Jung, N. Cadirov, B.N. Popov, Titania Supported Platinum Catalyst with High Electrocatalytic Activity and Stability for Polymer Electrolyte Membrane Fuel Cell, *ECS Transactions*, **33** (2010) 483-491.
34. Huang Sheng-Yang, Ganesan Prabhu, Popov Branko N, Development of conducting polypyrrole as corrosion-resistant catalyst support for polymer electrolyte membrane fuel cell (PEMFC) application, *Appl. Catal. B: Environmental*, **93** (2009) 75-81.
35. Liu Gang, Li Xuguang, Ganesan Prabhu, Popov Branko N, Development of non-precious metal oxygen-reduction catalysts for PEM fuel cells based on N-doped ordered porous carbon,, *Appl. Catal. B: Environmental,* **93** (2009) 156-165.
36. Subramanian Nalini P, Li Xuguang, Nallathambi Vijayadurda, Kumaraguru Swaminatha P, colon-Mercado Hector, Wu Gang, Lee Jong-Won, Popov Branko N, Nitrogen-modified carbon-based catalysts for oxygen reduction reaction in polymer electrolyte membrane fuel cells, *J Power Sources*, **188** (2009) 38-44.
37. Huang Sheng-Yang, Ganesan Prabhu, Park Sehkyu, Popov Branko N, Development of a Titanium Dioxide-Supported Platinum Catalyst with Ultrahigh Stability for Polymer Electrolyte Membrane Fuel Cell Applications, *J. Am. Chem. Soc.*, **131** (2009) 13898-13899.

Presentations (2009-2013)

1. Tianyuan Xie, Taekeun Kim, Won Suk Jung, Prabhu Ganesan, and Branko N. Popov, Development of Ultra-Low Loading Pt Hybrid Catalyst for PEM Fuel Cells, *224th ECS Meeting*, San Francisco, CA, October 27-November 01, 2013.
2. Branko N. Popov, Tianyuan Xie, Taekeun Kim, Won Suk Jung, and Prabhu Ganesan, Development of Ultra-Low Loading Pt Alloy Cathode Catalyst for PEM Fuel Cells, *224th ECS Meeting*, San Francisco, CA, October 27-November 01, 2013.
3. Taekeun Kim, Won Suk Jung, and Prabhu Ganesan, Tianyuan Xie, and Branko N. Popov, Development of Ultra-Low Loading Pt/AGC Catalyst for PEM Fuel Cells, *224th ECS Meeting*, San Francisco, CA, October 27-November 01, 2013.
4. Akos Kriston, Tianyuan Xie, Taekeun Kim, Won Suk Jung, David Gamliel, Brian Murphy Prabhu Ganesan, Branko N. Popov, Analyzing the effect of Ultra-Low Pt Loading on Mass and Specific Activity of PEM Fuel Cells, *222nd ECS Meeting*, Honolulu, HI, October 7-12, 2012.
5. Branko N. Popov, Tianyuan Xie, Taekeun Kim, Won-suk Jung, Akos Kriston Brian Murphy, David Gamliel and Prabhu Ganesan, Development of Ultra-Low Pt Alloy Cathode Catalyst for PEM Fuel Cells, *222nd ECS Meeting*, Honolulu, HI, October 7-12, 2012.
6. Tianyuan Xie, Won Suk Jung, Taekeun Kim, Kriston Akos Prabhu Ganesan and Branko N. Popov, Development of Highly Active Pt_2Ni/CCC Catalyst for PEM Fuel Cell, *222nd ECS Meeting*, Honolulu, HI, October 7-12, 2012.

7. Taekeun Kim, Won Suk Jung, Tianyuan Xie, Akos Kriston, Prabhu Ganesan, David Gamliel, Brian Murphy and Branko N. Popov, Development of Hybrid Cathode Catalyst for PEM Fuel Cells, *222nd ECS Meeting*, Honolulu, HI, October 7-12, 2012.
8. Branko N. Popov, Tae-keun Kim, Xie Tianyuan, Prabhu Ganesan, and Hansung Kim, Development of ultra-low platinum alloy cathode catalyst for PEM fuel cells, *220th ECS Meeting*, Boston, MA, October 9-14, 2011.
9. S. Huang, P. Ganesan, and B. N. Popov, Titanium Dioxide-Supported Platinum Catalysts, *220th ECS Meeting*, Boston, MA, October 9-14, 2011.
10. X. Li, G. Liu, T. Kim, S. Ganesan, P. Ganesan, and B. N. Popov, Development of Non-Precious Metal Catalysts for Oxygen Reduction Reaction in Fuel Cells with High Activity and Stability, *220th ECS Meeting*, Boston, MA, October 9-14, 2011.
11. X. Li, S. Huang, B.N. Popov, Development of Low Platinum Loading Cathode Catalysts for Polymer Electrolyte Membrane Fuel Cells, *218th Meeting of the Electrochem. Soc*., Las Vegas, Nevada, October 13, 2010.
12. X. Li, B.N. Popov, T. Kawahara, H. Yanagi, Recent Advances in Non-Precious Metal Catalyst for Oxygen Reduction Reaction in Fuel Cells, *218th Meeting of the Electrochem. Soc*., Nevada, October 13, 2010.
13. S. Huang, P. Ganesan, W. S. Jung, N. Cardirov and B. N. Popov, Titania Supported Platinum Catalyst with High Electrocatalytic Activity and Stability for Polymer Electrolyte Membrane Fuel Cell, *218th Meeting of the Electrochem. Soc*., Las Vegas, Nevada, October 13, 2010.
14. G. Liu, X. Li,, B. Popov, Stability Study of Carbon-Based Catalysts for Oxygen Reduction Reaction in Polymer Electrolyte Membrane Fuel Cells, *216th Meeting of the Electrochem. Soc*., Vienna, Austria, October 2009.
15. H. Jung, P. Ganesan, B.N. Popov, Development of High Durability Bifunctional Oxygen Electrode for Unitized Regenerative Fuel Cell, *216th Meeting of the Electrochem. Soc*., Vienna, Austria, October 2009.
16. S. Huang, P. Ganesan, B.N. Popov, Development of Novel Metal Oxide Supported Pt Catalysts for Proton Exchange Membrane and Unitized Regenerative Fuel Cells Applications, *216th Meeting of the Electrochem. Soc*., Vienna, Austria, October 2009.
17. Branko N. Popov, Development of Durable Cathode Catalysts for Polymer Electrolyte Membrane Fuel Cells at University of South Carolina, Fuel Cell Durability and Performance, 5th Annual conference, Alexandria, VA, December 2009.

Task Schedule

Task Number	Project Milestones	Task Completion Data				Progress Notes
		Original Plan	Revised Plan	Actual	Percent Complete	
1	Ultra-low Pt loading catalyst synthesis using carbon supports.	11/30/12	12/31/15		100%	On-Track
2	Ultra-low Pt loading catalyst synthesis using activated graphitic carbon.	11/30/12	12/31/15		100%	On-Track
3	ORR kinetics studies	11/30/12	12/31/15		100%	On-Track
4	Structure-property relationship studies	11/30/12	12/31/15		100%	On-Track
5	(a) Durability studies and (b) Evaluation of Corrosion mechanism in single cell configuration	(a) 11/30/12 (b) 05/31/14	12/31/15		100%	On-Track
6	Durability analysis in 25-cm^2 cells	05/31/14	12/31/15		100%	On-Track

Project Spending and Estimate of Future Spending (through May 31, 2015)

Quarter	From	To	Estimated Federal Share of Outlays*	Actual Federal Share of Outlays	Estimated Recipient Share of Outlays*	Actual Recipient Share of Outlays	Cumulative
3Q10	Start	9/30/2010	$12,649	$2,607	$0	$0	$2,607
4Q10	10/1/2010	12/31/2010	$323,233	$212,430	$91,667	$0	$215,037
1Q11	1/1/2011	3/31/2011	$406,153	$311,266	$91,667	$46,709	$573,012
2Q11	4/1/2011	6/30/2011	$357,965	$204,641	$91,667	$25,232	$802,885
3Q11	7/1/2011	9/30/2011	$306,856	$216,895	$68,750	$21,875	$1,041,655
4Q11	10/1/2011	12/31/2011	$238,768	$153,905	$68,750	$49,383	$1,244,943
1Q12	1/1/2012	3/31/2012	$290,469	$129,225	$68,750	$152,559	$1,526,727
2Q12	4/1/2012	6/30/2012	$290,445	$293,589	$68,750	$109,906	$1,930,221
3Q12	7/1/2012	9/30/2012	$359,672	$150,202	$68,750	$1,415	$2,081,838
4Q12	10/1/2012	11/30/2012	$163,790	$159,034	$6,249	$99,948	$2,340,820
1Q13	12/1/2012	12/31/2012	0	$198,584	0	$69,816	$2,609,220
2Q13			0	$90,801	0	$ 19,813	$2,719,835
3Q13			0	$207,050	0	0	$2,926,884
			0	$134,347	0	$34,919	$3,096,150
	1/1/2014	3/31/2014	$170,000	$165,872	0	0	$3,262,022
	4/1/2014	6/30/2014	0	$198,963	0	($6,575)	$3,454,410
	7/1/2014	9/30/2014	$780,000	$124,023	$115,000	$6,574	$3,585,000
	10/1/2014	12/31/2014	0	$224,115	0	0	$3,685,100
	01/1/2015	03/31/2015	0	$167,867	0	0	$3,852,967
	04/1/2015	5/31/2015	0	$91,778			$3,944,745
Totals			**$3,700,000**	**$3,313,170**	**$740,000**	**$631,574**	

References

1. H.A. Gasteiger, S.S. Kocha, B. Sompalli, F.T. Wagner, Activity benchmarks and requirements for Pt, Pt-alloy, and non-Pt oxygen reduction catalysts for PEMFCs, Appl. Catal. B: Environ. 56 (2005) 9-35.
2. R. Makharia, S.S. Kocha, P.T. Yu, M.A. Sweikart, W. Gu, F.T. Wagner, H.A. Gasteiger, Durable PEM fuel cell electrode materials: Requirements and benchmarking methodologies, ECS Trans., 1 (2006) 3-18.
3. X. Li, H.R. Colón-Mercado, G. Wu, J.-W. Lee, B.N. Popov, Development of method for synthesis of Pt-Co cathode catalysts for PEM fuel cells, Electrochemical and Solid-State Lett., 10 (2007) B201-B205.
4. J. Wu, X.Z. Yuan, J.J. Martin, H. Wang, J. Zhang, J. Shen, S. Wu, W. Merida, A review of PEM fuel cell durability: Degradation mechanisms and mitigation strategies, J. Power Sources, 184 (2008) 104-119.
5. Y. Sugawara, A.P. Yadav, A. Nishikata, T. Tsuru, EQCM Study on anodic dissolution of platinum in acid solutions, Electrochemistry, 75 (2007) 359-365.
6. P.J. Ferreira, G.J. la O', Y. Shao-Horn, D. Morgan, R. Makharia, S. Kocha, H.A. Gasteiger, Instability of Pt/C electrocatalysts in proton exchange membrane fuel cells: A mechanistic investigation, J. Electrochem. Soc., 152 (2005) A2256-A2271.
7. S. Mitsushima, S. Kawahara, K.-i. Ota, N. Kamiya, Consumption rate of Pt under potential cycling, J. Electrochem. Soc., 154 (2007) B153-B158.
8. F. Kodera, Y. Kuwahara, A. Nakazawa, M. Umeda, Electrochemical corrosion of platinum electrode in concentrated sulfuric acid, J. Power Sources, 172 (2007) 698-703.
9. R. Borup, J. Davey, F. Garzon, D. Wood, P. Welch, K. More, PEM fuel cell durability with transportation transient operation, ECS Trans., 3 (2006) 879-886.
10. V.A. Sethuraman, J.W. Weidner, A.T. Haug, L.V. Protsailo, Durability of perfluorosulfonic acid and hydrocarbon membranes: Effect of humidity and temperature, J. Electrochem. Soc., 155 (2008) B119-B124.
11. M. Crum, W. Liu, Effective testing matrix for studying membrane durability in PEM fuel cells: Part 2. Mechanical durability and combined mechanical and chemical durability, ECS Trans., 3 (2006) 541-550.

12. A. Laconti, H. Liu, C. Mittelsteadt, R. McDonald, Polymer electrolyte membrane degradation mechanisms in fuel cells - Findings over the past 30 years and comparison with electrolyzers, ECS Trans., 1 (2006) 199-219.
13. S.-Y. Huang, P. Ganesan, S. Park, B.N. Popov, Development of a titanium dioxide-supported platinum catalyst with ultrahigh stability for polymer electrolyte membrane fuel cell applications, J. Am. Chem. Soc., 131 (2009) 13898-13899.
14. S.D. Knights, K.M. Colbow, J. St-Pierre, D.P. Wilkinson, Aging mechanisms and lifetime of PEFC and DMFC, J. Power Sources, 127 (2004) 127-134.
15. L.M. Roen, C.H. Paik, T.D. Jarvi, Electrocatalytic corrosion of carbon support in PEMFC cathodes, Electrochem. Solid-State Lett., 7 (2004) A19-A22.
16. Y. Shao, G. Yin, J. Zhang, Y. Gao, Comparative investigation of the resistance to electrochemical oxidation of carbon black and carbon nanotubes in aqueous sulfuric acid solution, Electrochim. Acta, 51 (2006) 5853-5857.
17. B. Avasarala, R. Moore, P. Haldar, Surface oxidation of carbon supports due to potential cycling under PEM fuel cell conditions, Electrochim. Acta, 55 (2010) 4765-4771.
18. Kim M, Park J, Kim H, Song S, Lee W. The preparation of Pt/C catalysts using various carbon materials for the cathode of PEMFC. J Power Sources 2006; 163: 93-7.
19. Dicks AL. The role of carbon in fuel cells. J Power Sources 2006; 156: 128-41.
20. Y. Shao, G. Yin, and Y. Gao, Understanding and approaches for the durability issues of Pt-based catalysts for PEM fuel cell, J. Power Sources, 171, 558 (2007).
21. Honda K, Yoshimura M, Rao TN, Tryk DA, Fujishima A, Yasui K, Sakamoto Y, Nishio K, Masuda H. Electrochemical properties of Pt-modified nano-honeycomb diamond electrodes. J Electroanal Chem 2001; 514: 35-50.
22. Montilla F, Morallon E, Duo I, Comninellis Ch, Vazquez JL. Platinum particles deposited on synthetic boron-doped diamond surfaces. Application to methanol oxidation. Electrochim Acta 2003; 48: 3891-7.
23. Spătaru N, Zhang X, Spătaru T, Tryk DA, Fujishima A. Platinum electrodeposition on conductive diamond powder and its application to methanol oxidation in acidic media. J Electrochem Soc 2008; 155: B264-9.
24. Han KI, Lee JS, Park SO, Lee SW, Park YW, Kim H. Studies on the anode catalysts of carbon nanotube for DMFC. Electrochim Acta 2004; 50: 791-4.

25. Lee K, Zhang J, Wang H, Wilkinson DP. Progress in the synthesis of carbon nanotube- and nanofiber-supported Pt electrocatalysts for PEM fuel cell catalysis. J Appl Electrochem 2006; 36: 507-22.
26. Wang C, Waje M, Wang X, Tang JM, Haddon RC, Yan Y. Proton exchange membrane fuel cells with carbon nanotube based electrodes. Nano Lett 2004; 4: 345-8.
27. Oh HS, Lim KH, Roh B, Hwang I, Kim H. Corrosion resistance and sintering effect of carbon supports in polymer electrolyte membrane fuel cells. Electrochim Acta 2009; 54: 6515-21.
28. Oh HS, Kim K, Ko YJ, Kim H. Effect of chemical oxidation of CNFs on the electrochemical carbon corrosion in polymer electrolyte membrane fuel cells. Int J Hydrogen Energy, 2010; 35: 701-8.
29. Lim KH, Oh HS, Kim H. Use of a carbon nanocage as a catalyst support in polymer electrolyte membrane fuel cells. Electrochem Commun 2009; 11: 1131-4.
30. Rao CV, Reddy ALM, Ishikawa Y, Ajayan PM. Synthesis and electrocatalytic oxygen reduction activity of graphene-supported Pt3Co and Pt3Cr alloy nanoparticles. Carbon 2011; 49: 931-6.
31. Shao Y, Zhang S, Wang C, Nie Z, Liu J, Wang Y, Lin Y. Highly durable graphene nanoplatelets supported Pt nanocatalysts for oxygen reduction. J Power Sources 2010; 195: 4600-5.
32. Anderson SM, Borghei M, Lund P, Elina Y, Pasanen A, Kauppinen E, Ruiz V, Kauranen P, Skou EM. Durability of carbon nanofiber (CNF) & carbon nanotube (CNT) as catalyst support for Proton Exchange Membrane Fuel Cells. Solid State Ionics 2013; 231: 94-101.
33. Ma PC, Liu MY, Zhang H, Wang SQ, Wang R, Wang K, Wong YK, Tang BZ, Hong SH, Paik KW, Kim JK. Enhanced electrical conductivity of nanocomposites containing hybrid fillers of carbon nanotubes and carbon black. ACS Appl Mater Interfaces 2009; 1: 1090-6.
34. Antolini E. Carbon supports for low-temperature fuel cell catalysts. Appl Catal B-Environ 2009; 88: 1-24.
35. Knights SD, Colbow KM, St-Pierre J, Wilkinson DP. Aging mechanisms and lifetime of PEFC and DMFC. J Power Sources 2004; 127: 127-34.

36. DOE cell component accelerated stress test protocols for PEM fuel cells. March 2007. http://www1.eere.energy.gov/hydrogenandfuelcells/fuelcells/pdfs/component_durability_profile.pdf, p4. Accessed October 30, 2015.
37. Iiyama A, Iguchi S, Daimaru A, Shinohara K. Objectives, R&D challenge topics and proposed evaluation methods for polymer electrolyte fuel cells. 2007. Fuel Cell Commercialization Conference of Japan.
38. Iiyama A, Shinohara K, Ohma A, Yoshida T, Daimaru A. Objectives, R&D challenge topics and proposed evaluation methods for polymer electrolyte fuel cells. 2011. Fuel Cell Commercialization Conference of Japan.
39. Ohma A, Shinohara K, Iiyama A, Yoshida T, Daimaru A. Membrane and catalyst performance targets for automotive fuel cells by FCCJ membrane, catalyst, MEA WG. ECS Trans 2011; 41: 775-84.
40. Hashimasa Y, Matsuda Y, Shimizu T. Comparison of carbon corrosion test methods for polymer electrolyte fuel cell. Electrochim Acta 2015; 179: 119-25.
41. Reiser CA, Bregolia L, Patterson TW, Yi JS, Yang JD, Perry ML, Jarvi TD. A reverse-current decay mechanism for fuel cells. Electrochem Solid St 2005; 8: A273-6.
42. Patterson TW, Darling RM. Damage to the cathode catalyst of a PEM fuel cell caused by localized fuel starvation. Electrochem Solid St 2006; 9: A183-5.
43. Park YC, Kakinuma K, Uchida M, Tryk DA, Kamino T, Uchida H, Watanabe M. Investigation of the corrosion of carbon supports in polymer electrolyte fuel cells using simulated start-up/shutdown cycling. Electrochim Acta 2013; 91: 195-207.
44. Sugawara Y, Okayasu T, Yadav AP, Nishikata A, Tsuru T. Dissolution mechanism of platinum in sulfuric acid solution. J Electrochem Soc 2012; 159: F779-86.
45. U.S. DRIVE. Fuel cell technical team roadmap. June 2013. http://energy.gov/sites/prod/files/2014/02/f8/fctt_roadmap_june2013.pdf, p8. Accessed October 30, 2015.
46. Mukundan R. Accelerated testing validation. June 2014. http://www.hydrogen.energy.gov/pdfs/review14/fc016_mukundan_2014_o.pdf, p. 11. Accessed October 30, 2015.
47. B. C. H. Steele and A. Heinzel, Materials for fuel cell technologies, *Nature*, **415**, 345 (2001).

48. C.J. Tseng, S.T. Lo, S.C. Lo, and P.P. Chu, Characterization of Pt-Cu binary catalysts for oxygen reduction for fuel cell applications, *Mater. Chem. Phys*., **100**, 385 (2006).
49. E. Antolini, J.R.C. Salgado, and E.R. Gonzales, The stability of Pt–M (M = first row transition metal) alloy catalysts and its effect on the activity in low temperature fuel cells: A literature review and tests on a Pt-Co catalyst, *J. Power Sources*, **160**, 957 (2006).
50. L. Xiong, A.M. Kannan, and A. Manthiram, Pt–M (M=Fe, Co, Ni and Cu) electrocatalysts synthesized by an aqueous route for proton exchange membrane fuel cells, *Electrochem. Commun*., **4**, 898 (2002).
51. F.H.B. Lima, M.J. Giz, and E.A. Ticianelli, Electrochemical Performance of Dispersed Pt-M (M =V, Cr and Co) Nanoparticles for the Oxygen Reduction Electrocatalysis*J. Braz. Chem. Soc*. **16**, 328 (2005).
52. N. Travitsky, T. Ripenbein, N. Golodnitsky, Y. Rosenberg, L. Burshtein, and L. Peled, Pt-, PtNi- and PtCo-supported catalysts for oxygen reduction in PEM fuel cells, *J. Power Sources*, **161**, 782 (2006).
53. M.-k. Min, J. Cho, K. Cho, H. Kim, Particle size and alloying effects of Pt-based alloy catalysts for fuel cell applications, Electrochim. Acta, 45 (2000) 4211-4217.
54. U.A. Paulus, A. Wokaun, G.G. Scherer, T.J. Schmidt, V. Stamenkovic, V. Radmilovic, N.M. Markovic, P.N. Ross, Oxygen reduction on carbon-supported Pt-Ni and Pt-Co alloy catalysts, J. Phys. Chem. B, 106 (2002) 4181-4191.
55. V.R. Stamenkovic, B.S. Mun, M. Arenz, K.J.J. Mayrhofer, C.A. Lucas, G. Wang, P.N. Ross, N.M. Markovic, Trends in electrocatalysis on extended and nanoscale Pt-bimetallic alloy surfaces, Nat. Mater., 6 (2007) 241-247.
56. V. Stamenkovic, B.S. Mun, K.J.J. Mayrhofer, P.N. Ross, N.M. Markovic, J. Rossmeisl, J. Greeley, J.K. Nørskov, Changing the activity of electrocatalysts for oxygen reduction by tuning the surface electronic structure, Angew. Chem. Int. Ed., 45 (2006) 2897-2901.
57. K. Jayasayee, J.A.R.V. Veen, T.G. Manivasagam, S. Celebi, E.J.M. Hensen, F.A. de Bruijn, Oxygen reduction reaction (ORR) activity and durability of carbon supported PtM (Co, Ni, Cu) alloys: Influence of particle size and non-noble metals, Appl. Catal. B-Environ., 111–112 (2012) 515-526.
58. P. Mani, R. Srivastava, P. Strasser, Dealloyed binary PtM_3 (M = Cu, Co, Ni) and ternary $PtNi_3M$ (M = Cu, Co, Fe, Cr) electrocatalysts for the oxygen reduction reaction:

Performance in polymer electrolyte membrane fuel cells, J. Power Sources, 196 (2011) 666-673.

59. A.S. Aricò, A.K. Shukla, H. Kim, S. Park, M. Min, V. Antonucci, An XPS study on oxidation states of Pt and its alloys with Co and Cr and its relevance to electroreduction of oxygen, Appl. Surf. Sci., 172 (2001) 33-40.
60. A.K. Shukla, M. Neergat, P. Bera, V. Jayaram, M.S. Hegde, An XPS study on binary and ternary alloys of transition metals with platinized carbon and its bearing upon oxygen electroreduction in direct methanol fuel cells, J. Electroanal. Chem., 504 (2001) 111-119.
61. T. Toda, H. Igarashi, H. Uchida, M. Watanabe, Enhancement of the electroreduction of oxygen on Pt alloys with Fe, Ni, and Co, J. Electrochem. Soc., 146 (1999) 3750-3756.
62. T. Toda, H. Igarashi, M. Watanabe, Role of electronic property of Pt and Pt alloys on electrocatalytic reduction of oxygen, J. Electrochem. Soc., 145 (1998) 4185-4188.
63. V. Stamenković, T.J. Schmidt, P.N. Ross, N.M. Marković, Surface composition effects in electrocatalysis: Kinetics of oxygen reduction on well-defined Pt_3Ni and Pt_3Co alloy surfaces, J. Phys. Chem. B, 106 (2002) 11970-11979.
64. V.R. Stamenkovic, B. Fowler, B.S. Mun, G. Wang, P.N. Ross, C.A. Lucas, N.M. Marković, Improved oxygen reduction activity on $Pt_3Ni(111)$ via increased surface site availability, Science, 315 (2007) 493-497.
65. Y. Hoshi, T. Yoshida, A. Nishikata, T. Tsuru, Dissolution of Pt–M (M: Cu, Co, Ni, Fe) binary alloys in sulfuric acid solution, Electrochim. Acta, 56 (2011) 5302-5309.
66. U.A. Paulus, A. Wokaun, G.G. Scherer, T.J. Schmidt, V. Stamenkovic, N.M. Markovic, P.N. Ross, Oxygen reduction on high surface area Pt-based alloy catalysts in comparison to well defined smooth bulk alloy electrodes, Electrochim. Acta, 47 (2002) 3787-3798.
67. Q. Huang, H. Yang, Y. Tang, T. Lu, D.L. Akins, Carbon-supported Pt-Co alloy nanoparticles for oxygen reduction reaction, Electrochem. Commun., 8 (2006) 1220-1224.
68. M. Pourbaix. Atlas of Electrochemical Equilibria in Aqueous Solutions, Pergamon Press, Oxford (1966).
69. M. Uchimura and S. Kocha, The Impact of Cycle Profile on PEMFC Durability, *ECS Trans.*, **11** (1) 1215 (2007).

70. R. M. Darling and J. M. Meyers, Kinetic Model of Platinum Dissolution in PEMFCs, *J. Electrochem. Soc*., **150**, A1523 (2003).
71. D. C. Johnson, D. T. Napp, and S. Bruckenstein, A ring-disk electrode study of the current/potential behaviour of platinum in 1.0 M sulphuric and 0.1 M perchloric acids, *Electrochim. Acta*, **15**, 1493 (1970).
72. K. Kinoshita, J. T. Lundquist, and P. Stonehart, Potential cycling effects on platinum electrocatalyst surfaces, *J. Electroanal. Chem*., **48**, 157 **(**1973).
73. K.I. Ota, S. Nishigori, and N. Kamiya, Dissolution of platinum anodes in sulfuric acid solution, *J. Electroanal. Chem*., **257**, 205 **(**1988).
74. G. Zhang, S. Sun, M. Cai, Y. Zhang, R. Li, and X. Sun, Porous Dendritic Platinum Nanotubes with Extremely High Activity and Stability for Oxygen Reduction Reaction *Scientific Reports*, **3**, 1526 (2013).
75. M. Inaba, Durability of Electrocatalysts in Polymer Electrolyte Fuel Cells, *ECS Trans*., **25** (1) 573 (2009).
76. J. Wang, G. Yin, Y. Shao, S. Zhang, Z. Wang, and Y. Gao, Effect of carbon black support corrosion on the durability of Pt/C catalyst, *J. Power Sources*, **171**, 331 (2007).
77. A. Marcu, G. Toth, and P. Pietrasz, Cathode Catalysts Degradation Mechanism from Liquid Electrolyte to Polymer Electrolyte Membrane Fuel Cells, *ECS Trans*., **50** (2) 1523 (2012).
78. C. Grolleau, C. Coutanceau, F. Pierre, and J. M. Leger, Effect of potential cycling on structure and activity of Pt nanoparticles dispersed on different carbon supports, *Electrochim. Acta*, **53**, 7157 (2008).
79. H. R. Colon-Mercado, H. Kim, and B. N. Popov, Durability study of Pt_3Ni_1 catalysts as cathode in PEM fuel cells, *Electrochem. Commun*., **6**, 795 (2004).
80. S. C. Zignani, E. Antolini, and E. R. Ginzalez,
81. Evaluation of the stability and durability of Pt and Pt–Co/C catalysts for polymer electrolyte membrane fuel cells, *J. Power Sources*, **182**, 83 (2008).
82. L. Gan, M. Haggen, R. O'Malley, B. Theobald, and P. Strasser, Understanding and Controlling Nanoporosity Formation for Improving the Stability of Bimetallic Fuel Cell Catalysts, *Nano Lett*., **13**, 1131 (2013).

83. L. Gan, C. Cui, S. Rudi, and P. Strasser, Core–Shell and Nanoporous Particle Architectures and Their Effect on the Activity and Stability of Pt ORR Electrocatalysts, *Top. Catal*., **57**, 236 (2014).
84. R. Choi, S. Choi, C. H. Choi, K. M. Nam, S. I. Woo, J. T. Park, and S. W. Han, Designed Synthesis of Well-Defined Pd@Pt Core–Shell Nanoparticles with Controlled Shell Thickness as Efficient Oxygen Reduction Electrocatalysts, *Chem. Eur. J*., **19**, 8190 (2013).
85. S. T. Bliznakov, M. B. Vukmirovic, L. Yang, E. A. Sutter, and R. R. Adzic, Pt Monolayer on Electrodeposited Pd Nanostructures: Advanced Cathode Catalysts for PEM Fuel Cells, *J. Electrochem. Soc*., **159**, F501 (2012).
86. S. K. Mason, K. C. Neyerlin, M. Kuo, K. C. Horning, K. L. More, and A. M. Herring, Investigation of a Silicotungstic Acid Functionalized Carbon on Pt Activity and Durability for the Oxygen Reduction Reaction, *J. Electrochem. Soc*., **159**, F871 (2012).
87. J. Y. Kim, S. Lee, T. Y. Kim, and H. T. Kim, A Simple Diazonium Coupling Reaction Enhances Durability of Modified Graphitic Carbons Used as Catalyst Supports for Polymer Electrolyte Membrane Fuel Cell, *Electrochim. Acta*, **134**, 418 (2014).
88. P. Yu, M. Pemberton, P. Plasse, PtCo/C cathode catalyst for improved durability in PEMFCs, J. Power Sources, 144 (2005) 11-20.
89. M. Uchimura, S. Sugawara, Y. Suzuki, J. Zhang, and S. S. Kocha, Electrocatalyst Durability under Simulated Automotive Drive Cycles, *ECS Trans*., **16** (2) 225 (2008).
90. Z. Yang, S. Ball, D. Condit, and M. Gummalla, Systematic Study on the Impact of Pt Particle Size and Operating Conditions on PEMFC Cathode Catalyst Durability, *J. Electrochem. Soc*., **158**, B1439 (2011).
91. S. Arisetty, X. Wang, R. K. Ahluwalia, R. Mukundan, R. Borup, J. Davey, D. Langlois, F. Gambini, O. Polevaya, and S. Blanchet, Catalyst Durability in PEM Fuel Cells with Low Platinum Loading, *J. Electrochem. Soc*., **159**, B455 (2012).
92. Y. S. Kim, C. F. Wetch, N. H. Mack, R. P. Hjelm, E. B. Orler, M. E. Hawley, K. S. Lee, S. D. Yim, and C. M. Johnston, Highly durable fuel cell electrodes based on ionomers dispersed in glycerol, *Phys. Chem. Chem. Phys*., **16**, 5927 (2014).

93. X. Li, S. Park, and B. N. Popov, Highly stable Pt and PtPd hybrid catalysts supported on a nitrogen-modified carbon composite for fuel cell application, *J. Power Sources*, **195**, 445 (2010).
94. S. R. Dhanushkodi, S. Kundu, M. W. Fowler, and M. D. Pritzker, Study of the effect of temperature on Pt dissolution in polymer electrolyte membrane fuel cells via accelerated stress tests, *J. Power Sources*, **245**, 1035 (2014).
95. W. H. Lee and H. Kim, Electrocatalytic activity and durability study of carbon supported Pt nanodendrites in polymer electrolyte membrane fuel cells, *Int. J. Hyd. Energy*, **38**, 7126 (2013).
96. S. Ohyagi, T. Matsuda, Y. Iseki, T. Sasaki, and C. Kaito, Effects of operating conditions on durability of polymer electrolyte membrane fuel cell Pt cathode catalyst layer, *J. Power Sources*, **196**, 3743 (2011).
97. F. T. Wagner, H. A. Gasteiger, R. Makharia, K. C. Neyerlin, E. L. Thompson, and S. G. Yan, Catalyst Development Needs and Pathways for Automotive PEM Fuel Cells, *ECS Trans.*, **3** (1) 19 (2006).
98. A. Salvatore Aricò, A. Stassi, I. Gatto, G. Monforte, E. Passalacqua, V. Antonucci, Surface properties of Pt and PtCo electrocatalysts and their influence on the performance and degradation of high-temperature polymer electrolyte fuel cells, J. Phys. Chem. C, 114 (2010) 15823-15836.
99. A. Stassi, I. Gatto, G. Monforte, V. Baglio, E. Passalacqua, V. Antonucci, A.S. Aricò, The effect of thermal treatment on structure and surface composition of PtCo electro-catalysts for application in PEMFCs operating under automotive conditions, J. Power Sources, 208 (2012) 35-45.
100. Z. Yu, J. Zhang, Z. Liu, J.M. Ziegelbauer, H. Xin, I. Dutta, D.A. Muller, F.T. Wagner, Comparison between dealloyed $PtCo_3$ and $PtCu_3$ cathode catalysts for proton exchange membrane fuel cells, J. Phys. Chem. C, 116 (2012) 19877-19885.
101. Kim Kinsohita, Electrochemical oxygen technologies. New York : John Wiley & Sons, 1992.
102. Ákos Kriston, Tianyuan Xie, David Gamliel, Prabhu Ganesan, Branko N. Popov, Effect of Ultra-Low Pt Loading on Mass Activity of PEM Fuel Cells, J. Power Sources, 243 (2013) 958-963.

103. K.C. Neyerlin, R. Srivastava, C. Yu, P. Strasser, Electrochemical activity and stability of dealloyed Pt–Cu and Pt–Cu–Co electrocatalysts for the oxygen reduction reaction (ORR), J.Power Sources, 186, 261-267. (2009).

104. P. Mani, R. Srivastava, P. Strasser, Dealloyed Pt−Cu Core−Shell Nanoparticle Electrocatalysts for Use in PEM Fuel Cell Cathodes, J Phys. Chem. C, 112, 2770-2778. (2008).

105. F.T. Wagner, B. Lakshmanan, M. F. Mathias, Electrochemistry and the Future of the Automobile, J. Phys. Chem. Lett., Vol. 1, pp. 2204-2219. (2010).

106. K. F. Blurton, P. Greenberg, H. G. Oswin, D. R. Rutt. The Electrochemical Activity of Dispersed Platinum, J. Electrochem. Soc, 119, 559-564. (1972)

107. M. Peuckert, T. Yoneda, R. A. Dalla Betta, M. Boudart, Oxygen Reduction on Small Supported Platinum Particles, J. Electrochem. Soc., 133, 944-947 (1986).

108. I. E. L. Stephens, A. S. Bondarenko, U. Grønbjerg, J. Rossmeisl, I. Chorkendorff, Understanding the electrocatalysis of oxygen reduction on platinum and its alloys, Energy & Environmental Science, 5, 6744-6762. (2012).

109. M. Nesselberger, S. Ashton, J. C. Meier, I. Katsounaros, K. J. J. Mayrhofer, M. Arenz, The Particle Size Effect on the Oxygen Reduction Reaction Activity of Pt Catalysts: Influence of Electrolyte and Relation to Single Crystal Models, J. Am. Chem., 133, 17428–17433. (2011).

110. L. Gan, H. Du, B. Li, F. Kang, The effect of particle size on the interaction of Pt catalyst particles with a carbon black support, New Carbon Materials, 25, 53–59. (2010).

111. M. Inaba, H. Yamada, J. Tokunaga, A. Tasaka, Effect of Agglomeration of Pt/C Catalyst on Hydrogen Peroxide Formation, Electrochem. Solid-State Lett., 7, A474-A476. (2004).

112. A. Bonakdarpour, T. R. Dahn, R. T. Atanasoski, M. K. Debe, H2O2 Release During Oxygen Reduction Reaction on Pt Nano Particles, Electrochem. Solid-State Lett., 11, B208-211. (2008).

113. M. Watanabe, H. Sei, P. Stonehart., The influence of platinum crystallite size on the electroreduction of oxygen, J. Electroanal. Chem. Interfacial Electrochem., 261, 375–387. (1989).

114. M. K. Debe, Effect of Electrode Surface Area Distribution on High CurrentDensity Performance of PEM Fuel Cells, J. Electrochem. Soc., 159, B54-B67. (2012).

115. M. Lee, M. Uchida, D. A. Tryk, H. Uchida, M. Watanabe, The effectiveness of platinum/carbon electrocatalysts: Dependence on catalyst layer thickness and Pt alloy catalytic effects, Electrochimica Acta, 56, 4783–4790. (2011).

116. M. S. Saha, D. Malevich, E. Halliop, J. G. Pharoah, B. A. Peppley, K. Karan, Electrochemical Activity and Catalyst Utilization of Low Pt and Thickness Controlled Membrane Electrode Assemblies, J. Electrochem. Soc., 158, B562-B567. (2011).

117. N. Alonso-Vante, Platinum and Non-Platinum Nanomaterials for the Molecular Oxygen Reduction Reaction, ChemPhysChem, 11, 2732-2744. (2010).

118. A. Kucernak, S. Chen, Electrocatalysis under Conditions of High Mass Transport Rate: Oxygen Reduction on Single Submicrometer-Sized Pt Particles Supported on Carbon, J. Phys. Chem. B, 108, 3262-3276. (2004).

119. H.A. Gasteiger, J.E. Panels, S.G. Yan, Dependence of PEM fuel cell performance on catalyst loading, J. Power Sources, 127, 162-171. (2004).

120. W. Yoon, A. Weber, Modeling Low-Platinum-Loading Effects in Fuel-Cell Catalyst Layers, J. Electrochem. Soc., 158, B1007-B1018. (2011).

121. S. Kamarajugadda, S. Mazumder, Numerical investigation of the effect of cathode catalyst layer structure and composition on polymer electrolyte membrane fuel cell performance, J. Power Sources, 183, 629–642. (2008).

122. M. Perry, J. Newman, E. J. Cairns, Mass Transport in Gas- Diffusion Electrodes: A Diagnostic Tool for Fuel- Cell Cathodes, J. Electrochem. Soc., 145, 5-15. (1998).

123. E.L. Gyenge, Dimensionless numbers and correlating equations for the analysis of the membrane-gas diffusion electrode assembly in polymer electrolyte fuel cells, J. Power Sources, 152, 105-121. (2005).

124. M. Secanell, K. Karan, A. Suleman, N. Djilali, Multi-variable optimization of PEMFC cathodes using an agglomerate model, Electrochim. Acta, 52, 6318–6337. (2007).

125. W. Suna, B. A. Peppley, K. Karan, An improved two-dimensional agglomerate cathode model to study the influence of catalyst layer structural parameters, Electrochim. Acta, 50, 3359–3374. (2005).

126. K. Chan, M. Eikerling, A Pore-Scale Model of Oxygen Reduction in Ionomer-Free Catalyst Layers of PEFCs, J. Electrochem. Soc., 158, B18-B28. (2011).

127. J.P. James, H.-W. Choi, J.G. Pharoah, X-ray computed tomography reconstruction and analysis of polymer electrolyte membrane fuel cell porous transport layers, Int. J. Hydrogen Energy, 37 (23) 18216-18230 (2012).

128. N.A. Siddique, Fuqiang Liu, Process based reconstruction and simulation of a three-dimensional fuel cell catalyst layer, Electrochimica Acta, 55, 5357–5366. (2010).

129. S. Martin, P.L. Garcia-Ybarra, J.L. Castillo, High platinum utilization in ultra-low Pt loaded PEM fuel cell cathodes prepared by electrospraying, Int. J. Hydrogen Energy, 35, pp. 10446-10451. (2010).

130. Frederick T. Wagner, Balasubramanian Lakshmanan, and Mark F. Mathias. Electrochemistry and the Future of the Automobile, J. Phys. Chem. Lett., Vol. 1, pp. 2204-2219 (2010).

131. Thomas A. Greszler, David Caulk, Puneet Sinha, The Impact of Platinum Loading on Oxygen Transport Resistance. J. Electrochem. Soc., 159 (2012) F831-F840.

132. H. Angerstein-Kozlowska, in: E. Yeager, J.O.M. Bockris, B.E. Conway, S. Sarangapani (Eds.), Comprehensive Treatise of Electrochemistry, vol. 9, Plenum Press, New York, 1984. Pp 15-59. (Chapter 2).

133. A. J. Bard, L. R. Faulkner, Electrochemical methods. 2nd Ed., New York : John Wiley & Sons, 2001. pp. 156-226.

134. Havasi, Á., Horváth, R., Szabó, T, Comparison of Parameter Estimation Techniques Applied to Proton Exchange Membrane Fuel Cell Model, J. Fuel Cell Sci. Technol., 10 (2013) 051001 .

135. Qingzhi Guo, Vijay A. Sethuraman, Ralph E. White, Parameter Estimates for a PEMFC Cathode, J. Electrochem. Soc., 151 (2004) A983-A993.

136. Á. Havasi, R. Horváth, Á. Nemes, T. Szabó, Investigation of a Proton Exchange Membrane Fuel Cell Model by Parameter Fitting, Proceedings of Fifth Conference on

Finite Difference Methods, Lozenets, 2010: Theory and Applications, Vols. Rousse University press, 78-87.

137. Sheintuch, Moshe, Reaction engineering principles of process catalyzed fractal solids, Catalysis Reviews: Science and Engineering, 43 (2001) 233–289.

138. Hui Li, Yanghua Tang, Zhenwei Wang, Zheng Shi, Shaohong Wu, Datong Song, Jianlu Zhang, A review of water flooding issues in the proton exchange membrane fuel cell, J. Power Sources, 178 (2008) 103-117.

139. C. L. John Chmiola, Pierre-Louis Taberna, Patrice Simon, and Yury Gogotsi, S Monolithic Carbide-Derived Carbon Films for Micro-Supercapacitors, cience, 328 (2010) 480 (2010).

140. N.P. Subramanian, S.P. Kumaraguru, H. Colon-Mercado, H. Kim, B.N. Popov, T. Black, D.A. Chen, Studies on Co-based catalysts supported on modified carbon substrates for PEMFC cathodes, J. Power Sources, 157 (2006) 56-63.

141. V. Nallathambi, J.-W. Lee, S.P. Kumaraguru, G. Wu, B.N. Popov, Development of high performance carbon composite catalyst for oxygen reduction reaction in PEM Proton Exchange Membrane fuel cells, J. Power Sources, 183 (2008) 34-42.

142. N.P. Subramanian, X. Li, V. Nallathambi, S.P. Kumaraguru, H. Colon-Mercado, G. Wu, J.-W. Lee, B.N. Popov, Nitrogen-modified carbon-based catalysts for oxygen reduction reaction in polymer electrolyte membrane fuel cells, J. Power Sources, 188 (2009) 38-44.

143. X. Li, G. Liu, B.N. Popov, Activity and stability of non-precious metal catalysts for oxygen reduction in acid and alkaline electrolytes, J. Power Sources, 195 (2010) 6373-6378.

144. G. Liu, X. Li, P. Ganesan, B.N. Popov, Studies of oxygen reduction reaction active sites and stability of nitrogen-modified carbon composite catalysts for PEM fuel cells, Electrochim. Acta, 55 (2010) 2853-2858.

145. T. Xie, W.S. Jung, T. Kim, P. Ganesan, B.N. Popov, Development of highly active and durable hybrid cathode catalysts for polymer electrolyte membrane fuel cells, J. Electrochem. Soc., 161 (2014) F1489-F1501.

146. T. Kim, T. Xie, W.S. Jung, F. Gadala-Maria, P. Ganesan, B.N. Popov, Development of catalytically active and highly stable catalyst supports for polymer electrolyte membrane fuel cells, J. Power Sources, 273 (2015) 761-774.

147. W. S. Jung, T. Xie, T. Kim, P. Ganesan, B. N. Popov, Highly active and durable Co-doped Pt/CCC cathode catalyst for polymer electrolyte membrane fuel cells, Electrochim. Acta, 167 (2015) 1-12.

148. K.S.W. Sing, D.H. Everett, R.A.W. Haul, L. Moscou, R.A. Pierotti, J. Rouquerol, T. Siemieniewska, Reporting physisorption data for gas/solid systems with special reference to the determination of surface area and porosity (recommendations 1984), Pure and Appl. Chem., 57 (1985) 603-619.

149. T.H. Hyeon, S.J. Han, Y.E. Sung, K.W. Park, Y.W. Kim, Angew. Chem. Int. Ed. 42 (2003) 4352-4356.

150. 71. Y.A. Zhu, Z.J. Sui, T.J. Zhao, Y.C. Dai, Z.M. Cheng, W.K. Yuan, Carbon 43 (2005) 1694-1699.

151. C. Kim, S.-H. Park, J.-I. Cho, D.-Y. Lee, T.-J. Park, W.-J. Lee, K.-S. Yang, Raman spectroscopic evaluation of polyacrylonitrile-based carbon nanofibers prepared by electrospinning, J. Raman Spectrosc., 35 (2004) 928-933.

152. J. Tang, J. Yang, X. Zhou, Acetylene black derived hollow carbon nanostructure and its application in lithium-sulfur batteries, RSC Adv., 3 (2013) 16936-16939.

153. S. Maldonado, K.J. Stevenson, Influence of nitrogen doping on oxygen reduction electrocatalysis at carbon nanofiber electrodes, J. Phys. Chem. B, 109 (2005) 4707-4716.

154. P.H. Matter, L. Zhang, U.S. Ozkan, The role of nanostructure in nitrogen-containing carbon catalysts for the oxygen reduction reaction, J. Catal., 239 (2006) 83-96.

155. Y. Shao, J. Sui, G. Yin, Y. Gao, Nitrogen-doped carbon nanostructures and their composites as catalytic materials for proton exchange membrane fuel cell, Appl. Catal. B-Environ., 79 (2008) 89-99.

156. W.Y. Wong, W.R.W. Daud, A.B. Mohamad, A.A.H. Kadhum, E.H. Majlan, K.S. Loh, Nitrogen-containing carbon nanotubes as cathodic catalysts for proton exchange membrane fuel cells, Diam. Relat. Mater., 22 (2012) 12-22.

157. T. Ikeda, M. Boero, S.-F. Huang, K. Terakura, M. Oshima, J.-i. Ozaki, Carbon alloy catalysts: Active sites for oxygen reduction reaction, J. Phys. Chem. C, 112 (2008) 14706-14709.

158. H. Niwa, K. Horiba, Y. Harada, M. Oshima, T. Ikeda, K. Terakura, J.-i. Ozaki, S. Miyata, X-ray absorption analysis of nitrogen contribution to oxygen reduction reaction in carbon alloy cathode catalysts for polymer electrolyte fuel cells, Journal of Power Sources, 187 (2009) 93-97.

159. R.A. Sidik, A.B. Anderson, N.P. Subramanian, S.P. Kumaraguru, B.N. Popov, O2 Reduction on graphite and nitrogen-doped graphite: Experiment and theory, J. Phys. Chem. B, 110 (2006) 1787-1793.

160. X.G. Li, C.P. Liu, W. Xing, T.H. Lu, J. Power Sources 193 (2009) 470-476.

161. V.A. Sethuraman, J.W. Weidner, A.T. Haug, M. Pemberton, L.V. Protsailo, Electrochim. Acta 54 (2009) 5571-5582.

162. V. Stamenkovic, B.N. Grgur, P.N. Ross, N.M. Markovic, J. Electrochem. Soc. 152 (2005) A277-A282.

163. A.J. Bard, L.R. Faulkner, Electrochemical Methods: Fundamentals and Applications, 2nd ed., John Wiley & Sons, New York, 2001 (Chapters 3 and 9).

164. K.H. Kanagasniemi, D.A. Condit, T.D. Jarvi, J. Electrochem. Soc. 151 (2004) E125-E132.

165. A. Taniguchi, T. Skita, K. Yasuda, Y. Miyazaki, J. Power Sources 130 (2004) 42-49.

166. R. Makharia, S.S. Kocha, P.T. Yu, M.A. Sweikart, W. Gu, F.T. Wagner, H.A. Gasteiger, ECS Trans. 1 (2006) 3-18.

167. H.S. Oh, J.G. Oh, S. Haam, K. Arunabha, B. Roh, I. Hwang, H. Kim, Electrochem. Commun. 10 (2008) 1048-1051.

168. K.H. Lim, H.S. Oh, S.E. Jang, Y.J. Ko, H.J. Kim, H. Kim, J. Power Sources 193 (2009) 575-579.

169. G.A. Rimbu, I. Stamatin, C.L. Jackson, and K. Scott, J. Optoelectron. Adv. M, 8, 670 (2006).

170. J. Stejskal and R. G. Gilbert, Pure Appl. Chem. 74, 857 (2002).

171. C. Wang, G. Wang, D. van der Vliet, K. Chang, N.M. Markovica, and V.R. Stamenkovic, Phys. Chem. Chem. Phys., 12, 6933 (2010).

172. X. Li, H.R. Colon-Mercado, G. Wu, J.W. Lee, and B.N. Popov, Electrochem. Solid State Lett. 10, B201 (2007).

173. C. Chen, Y. Kang, Z. Huo, Z. Zhu, W. Huang, H. L. Xin, J. D. Snyder, D. Li, J. A. Herron, M. Mavrikakis, M. Chi, K. L. More, Y. Li, N. M. Markovic, G. A. Somorjai, P. Yang, and V. R. Stamenkovic, Science, 343, 1339 (2014).

174. R. Yang, J. Leisch, P. Strasser, and M. F. Toney, Chem. Mater., 22, 4712 (2010).

175. E. Antolini, J. R. C. Saldago, M. J. Giz, and E. R. Gonzalez, J. Power Sources, 30, 1213 (2005).

176. C. Wang, M. Chi, D. Li, D. Strmcnik, D. van der Vliet, G. Wang, V. Komanicky, K. C. Chang, A. P. Paulikas, D. Tripkovic, J. Pearson, K. L. More, N. M. Markovic, V. R. Stamenkovic, Design and synthesis of bimetallic electrocatalyst with multilayered Pt-skin surfaces, J. Am. Chem. Soc., 133 (2011) 14396-14403.

177. X. Tuaev, J.P. Paraknowitsch, R. Illgen, A. Thomas, and P. Strasser, Nitrogen-doped coatings on carbon nanotubes and their stabilizing effect on Pt nanoparticles, Phys. Chem. Chem. Phys., 14 (2012) 6444-6447.

178. A. Schlapka, M. Lischka, A. Groß, U. Kösberger, P. Jakob, P. Surface strain versus substrate interaction in heteroepitaxial metal layers: Pt on Ru(0001). Phys. Rev. Lett., 91 (2003) 016101.

179. J. Fusy, J. Meneaucourt, M. Alnot, C. Huguet, J.J. Ehrhardt, Growth and reactivity of evaporated platinum films on Cu(lll): a study by AES, RHEED and adsorption of carbon monoxide and xenon. Appl. Surf. Sci., 93 (1996) 211-220.

180. E. Antolini, J. R. C. Saldago, M. J. Giz, and E. R. Gonzalez, Effects of geometric and electronic factors on ORR activity of carbon supported Pt–Co electrocatalysts in PEM fuel cells, Int. J. Hyd. Energy, 30 (2005) 1213-1220.

181. V. R. Stamenkovic, B. S. Mun, K. J. J. Mayrhofer, P. N. Ross, and N. M. Markovic, Effect of surface composition on electronic structure, stability, and electrocatalytic properties of Pt-transition metal alloys: Pt-skin versus Pt-skeleton surfaces, J. Am. Chem. Soc., 128 (2006) 8813-8819.

182. L. A. Kibler, A.M. El-Aziz, R. Hoyer, D.M. Kolb, Tuning reaction rates by lateral strain in a palladium monolayer. Angew. Chem. Int. Ed. 44 (2005) 2080-2084.

183. A. Groβ, Reactivity of bimetallic systems studied from first principles, Top. Catal., 37 (2006) 29-39.

184. J. R. Kitchin, J. K. Nørskov, M. A. Barteau and J. G. Chen, Role of strain and ligand effects in the modification of the electronic and chemical properties of bimetallic surfaces, Phys. Rev. Lett., 93 (2004) 156801.

185. Y. Gauthier, M. Schmid, S. Padovani, E. Lundgren, V. Bus, G. Kresse, J. Redinger, P. Varga, Adsorption sites and ligand effect for co on an alloy surface: A direct view, Phys. Rev. Lett., 81 (2001) 036103.

186. B. Han, C.E. Carlton, A. Kongkanand, R.S. Kukreja, B.R. Theobald, L. Gan, R. O'Malley, P. Strasser, F.T. Wagner, Y. Shao-Horn, Record activity and stability of dealloyed bimetallic catalysts for proton exchange membrane fuel cells, Energ. Environ. Sci., 8 (2015) 258-266.

187. S. Ohyagi, T. Sasaki, Durability of a PEMFC Pt-Co cathode catalyst layer during voltage cycling tests under supersaturated humidity conditions, Electrochim. Acta, 102 (2013) 336-341.

188. L., M. Lopez-Haro, L. Castanheira, J. Durst, M. Chatenet, P. Bayle-Guillemaud, L. Guétaz, N. Caqué, E. Rossinot, F. Maillard, Probing the structure, the composition and the ORR activity of Pt3Co/C nanocrystallites during a 3422 h PEMFC ageing test, Appl. Catal. B-Environ., 142-143 (2013) 801-808.

189. S. Hidai, M. Kobayashi, H. Niwa, Y. Harada, M. Oshima, Y. Nakamori, T. Aoki, Changes in electronic states of platinum-cobalt alloy catalyst for polymer electrolyte fuel cells by potential cycling, J. Power Sources, 196 (2011) 8340-8345.

190. L. Dubau, F. Maillard, M. Chatenet, L. Guetaz, J. André, E. Rossinot, Durability of Pt3Co/C cathodes in a 16 cell PEMFC stack: Macro/microstructural changes and degradation mechanisms, J. Electrochem. Soc., 157 (2010) B1887-B1895.

191. S. Koh, M.F. Toney, P. Strasser, Activity-stability relationships of ordered and disordered alloy phases of Pt3Co electrocatalysts for the oxygen reduction (ORR), Electrochim. Acta, 52 (2007) 2765-2774.

192. M. Teliska, V.S. Murthi, S. Mukerjee, D.E. Ramaker, Correlation of water activation, surface properties, and oxygen reduction reactivity of supported Pt-M/C bimetallic electrocatalysts using XAS, J. Electrochem. Soc., 152 (2005) A2159-A2169.

193. A. Parthasarathy, S. Srinivasan , A.J. Appleby, C.R. Martin, Temperature dependence of the electrode kinetics of oxygen reduction at the platinum/Nafion interface - A microelectrode investigation. J Electrochem Soc 139 (1992) 2530-2537.

194. T. Hyeon, S. Han, Y.-E. Sung, K.-W. Park, Y.-W. Kim, High-Performance Direct Methanol Fuel Cell Electrodes using Solid-Phase-Synthesized Carbon Nanocoils, Angewandte Chemie International Edition, 42 (2003) 4352-4356.

195. Y.A. Zhu, Z.J. Sui, T.J. Zhao, Y.C. Dai, Z.M. Cheng, W.K. Yuan, Modeling of fishbone-type carbon nanofibers: A theoretical study, Carbon, 43 (2005) 1694-1699.

196. M. Cerro-Alarcón, A. Maroto-Valiente, I. Rodríguez-Ramos, A. Guerrero-Ruiz, Further insights into the Ru nanoparticles–carbon interactions and their role in the catalytic properties, Carbon, 43 (2005) 2711-2722.

197. S. Vinod Selvaganesh, G. Selvarani, P. Sridhar, S. Pitchumani, A.K. Shukla, Graphitic Carbon as Durable Cathode-Catalyst Support for PEFCs, Fuel Cells, 11 (2011) 372-384.

198. Z. Siroma, N. Fujiwara, T. Ioroi, S. Yamazaki, K. Yasuda, Y. Miyazaki, Dissolution of Nafion® membrane and recast Nafion® film in mixtures of methanol and water. J. Power Sources 126 (2004) 41-45.

199. Hydrogen, Fuel Cells & Infrastructure Technologies Program Multi-Year Research, Development and Demonstration Plan, 2010.

200. S. Koh, J. Leisch, M.F. Toney, P. Strasser, Structure-Activity-Stability Relationships of Pt−Co Alloy Electrocatalysts in Gas-Diffusion Electrode Layers, The Journal of Physical Chemistry C, 111 (2007) 3744-3752.

201. Y. Shao, G. Yin, Y. Gao, J. Power Sources 171 (2007) 558-566.

202. He C, Desai S, Brown G, Bollepalli S. PEM fuel cell catalysts: Cost, performance, and durability. Electrochem Soc Interface 2005; 14: 41-4.

203. Debe MK, Schmoeckel AK, Hendricks SM, Vernstrom GD, Haugen GM, Atanasoski RT. Durability aspects of nanostructured thin film catalysts for PEM fuel cells. ECS Trans 2006; 1: 51-66.

PROJECT
USC Pt*/ACCS-2 Catalyst Evaluation at NREL

Synthesis and Preparation of USC Membrane Electrode Assembly with Pt*/ACCS-2 for Cathode Catalyst and Support Evaluation Studies at NREL

Submitted to:

Dr. Shyam Kocha
National Renewable Energy Laboratory
15013 Denver West Parkway
Golden, CO 80401.
Dr. Shyam Kocha
Phone: (303) 275-3937
Email: Shyan.Kocha@nrel.gov

By

Dr. Branko N. Popov
University of South Carolina
301, Main Street, Dept. Chem. Eng. Room 2C02
Swearingen Engineering Center
Columbia, SC 29208
Phone (803) 777-7314
Fax: (803) 777-8265
Email: popov@cec.sc.edu

December 2015

Introduction

Three types of Pt and Pt* (Pt* = Compressive Pt-lattice catalyst) catalysts have been developed at USC using three different carbon-based supports namely, carbon composite catalyst support (CCCS) [1], activated carbon composite support-1 (ACCS-1) [2], and activated carbon composite support-2 (ACCS-2) [3-4]. These three supports are used for the synthesis of ultra-low loading Pt and Pt* catalysts using procedures developed at USC [1-4]. Furthermore, the effect of Pt loading on the catalyst mass activity and H_2-air fuel cell performance was evaluated using experimental studies and model development [5-7].

The research at USC was aimed at developing catalytically active and stable supports to sustain load cycling and startup/shutdown conditions. In the first step, the following major constraints directed our development of cathode catalyst supports: (1) the support should be chemically and electrochemically stable at high potentials, low pH, and high temperature; and (2) the support should have an onset potential and kinetic activity for ORR similar to that of the platinum catalyst. To accomplish these requirements, CCCS, ACCS-1, and ACCS-2 were synthesized with optimized (a) BET surface area, porosity, pore size, and pore size distribution; (b) hydrophilic/hydrophobic ratio; (c) structural properties (amorphous/crystalline ratio); (d) number of catalytic active sites through metal catalyzed pyrolysis; (e) Pt/Pt*-support interaction by inclusion of active surface functional groups; and (f) cobalt content incorporated into its structure, necessary for the formation of Pt*.

In the second step, a compressive Pt-lattice catalyst (Pt*) was synthesized through a USC-developed annealing procedure that controls the particle size during annealing. Monolayers of Pt* were formed by diffusing Co atoms present in the support into Pt which is deposited on the A-CCS. A mathematical model developed at USC was used to optimize the Co diffusion time, annealing temperature, and Pt/Co stoichiometric ratio. The final report will cover extensively the approach and the methodology used to optimize the catalyst and support performance and durability.

In this second report to NREL, detailed information is given for performance and durability Pt*/ACCS-2 catalyst. Five samples of this catalyst taken from two different batches were used (MEA# 1-4 were prepared from Batch 1 and MEA#5 was prepared from Batch 2) to to be analyzed at NREL for support and catalyst performance and durability.

The performance and durability results of Pt*/CCCS, Pt*/ACCS-1, Pt*/ACCS-2 are summarized below:

Catalyst 1: 30% Pt*/CCCS

- **Accomplished initial mass activity of 0.44 A/mg$_{PGM}$ and loss of mass activity of 43% after 30k cycles (0.6-1.0 V).**
- **Accomplished potential loss of 40 mV after 30k cycles (0.6-1.0 V) at 0.8 A/cm^2.**
- **Accomplished 32% ECSA loss after 30k cycles.**
- **Accomplished (rated) initial power density of 0.23 g$_{PGM}$/kW.**

Catalyst 2: 30% Pt*/ACCS-1

- **Accomplished initial mass activity of 0.292A/mg$_{PGM}$ and loss of mass activity of 50% after 30k cycles (0.6-1.0 V).**

- **Accomplished potential loss of 11 mV after 30k cycles (0.6-1.0 V) at 0.8 A/cm^2.**
- **Accomplished 40% ECSA loss after 30k (0.6-1.0 V) cycles.**
- **Accomplished 10 mV (at 1.5 A/cm^2) gain after 5k cycles (1.0-1.5 V) in H_2/air.**
- **Accomplished (rated) initial power density of 0.25 g_{PGM}/kW.**

Catalyst 3: 30% Pt*/ACCS-2

- **Accomplished initial mass activity of 0.34 A/mg_{PGM} and loss of mass activity of 45% after 30k cycles (0.6-1.0 V).**
- **Accomplished potential loss of 24 mV (iR-free) after 30k cycles (0.6-1.0 V) at 0.8 A/cm^2.**
- **Accomplished 42% ECSA loss after 30k (0.6-1.0 V) cycles.**
- **Accomplished initial mass activity of 0.34 A/mg_{PGM} and loss of mass activity of 50% after 5k cycles (1.0-1.5 V).**
- **Accomplished 8 mV (iR-free) loss at 1.5 A/cm after 1.0-1.5 V potential cycling.**
- **Accomplished 22% ECSA loss after 5k (1.0-1.5 V) cycles.**
- **Accomplished (rated) initial power density of 0.174 g_{PGM}/kW.**

In this report, the reproducibility of 30% Pt*/ACCS-2 catalyst obtained in 25-cm^2 MEAs are presented. The 30% Pt*/ACCS-2 catalyst was subjected to support stability (1.0-1.5 V cycling, 5,000 cycles) and catalyst durability (0.6-1.0 V, 30,000 cycles) tests according to U.S. DRIVE Fuel Cell Tech Team protocol. Commercial Pt/C catalyst 46% Pt/C, TEC10E50E, TKK, Japan) is used as the anode. Both the anode and the synthesized 30% Pt*/ACCS-2 cathode catalyst were sprayed on to a Nafion® 212 membrane to make catalyst coated membrane (CCM). The catalyst loading was measured at 25 points using X-ray fluorescence spectrometer. The catalyst loading on both sides are ~0.1 mg_{Pt}/cm^2 (±5% accuracy). The CCM was then hot pressed in between two gas diffusion layer (SGL 10 BC) at 140 °C for 3 min. (20 kg/cm^2 pressure). Based on the reproducibility results, five 25 cm^2 MEAs are fabricated for independent evaluation at NREL.

Reproducibility Studies of 30% Pt*/ACCS-2 catalyst

Support Stability (1.0-1.5 V Cycling)

H_2-Air fuel cell performance of Pt*/ACCS-2 catalyst tested in 25-cm^2 MEA subjected to 1.0-1.5 V potential cycling test is shown in Fig. 1. The Pt*/ACCS-2 catalyst showed an initial current density of 1.74 A/cm^2 at 0.6 $V_{iR\text{-}free}$. The high H_2/air fuel cell performance is due to the optimized catalyst layer thickness used for the USC-made catalysts. The catalyst showed a potential loss of **only 8 mV (iR-free)** at 1.5 A/cm^2 after 5,000 potential cycles between 1.0 and 1.5 V. The support stability of commercial Pt/C is shown in Fig. 2. The commercial catalyst showed initial current density of 1.54 A/cm^2 at 0.6 $_{ViR\text{-}free.}$ At 1.5 A/cm^2, the iR-corrected cell

voltage is 0.609 V for initial polarization and no activity is observed after 1,000 cycles between 1.0-1.5 V.

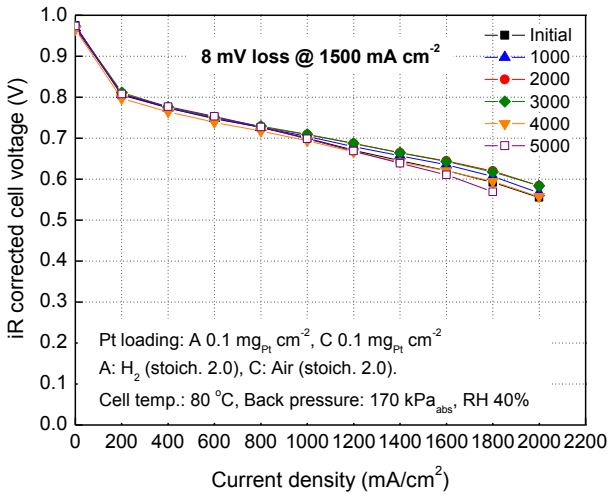

Figure 1. Comparison of H_2/air fuel cell performance of 30% Pt*/ACCS-2 catalyst subjected to 5,000 potential cycles between 1.0 and 1.5 V at 500 mV/s. Catalyst loading is 0.1 mg_{Pt}/cm^2 on both the anode and cathode electrodes. The fuel cell operating conditions are: H_2/air (2/2 stoic.), 80 °C, 40% relative humidity (RH), 170 kPa_{abs} back pressure. Nafion® NRE 212 membrane is used as the electrolyte.

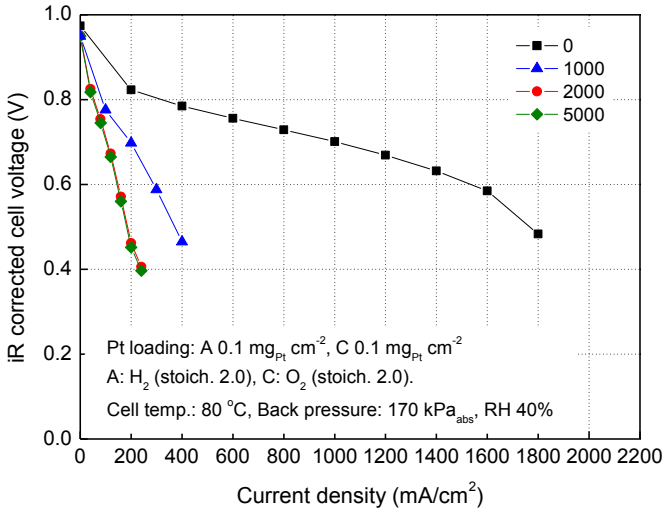

Figure 2. Comparison of H_2/air fuel cell performance of commercial 46% Pt/C catalyst subjected to 5,000 potential cycles between 1.0 and 1.5 V at 500 mV/s. Catalyst loading is 0.1 mg_{PGM}/cm^2 on both the anode and cathode electrodes. The fuel cell operating conditions are: H_2/air (2/2 stoic.), 80 °C, 40% RH, 170 kPa_{abs} back pressure. Nafion® NRE 212 membrane is used as the electrolyte.

Figure 3 shows the stability of mass activity for the Pt*/ACCS-2 catalyst. Potential cycling between 1.0 and 1.5 V resulted in **50% mass activity loss** after 5,000 cycles. The commercial 46% Pt/C catalyst showed mass activity loss of 74% after 5,000 cycles (Table 1).

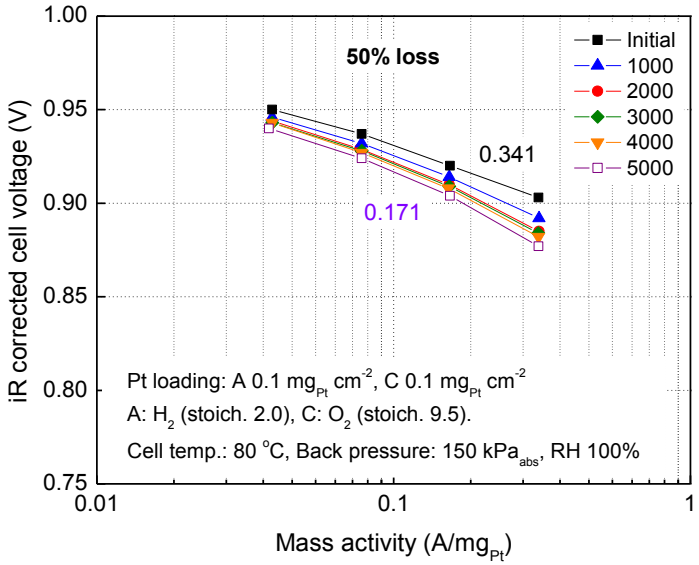

Figure 3. Stability of mass activity of Pt*/ACCS-2 catalyst subjected to 5,000 potential cycles between 1.0 and 1.5 V at 500 mV/s. The catalyst loading is 0.1 mg_{PGM}/cm^2 on both the anode and cathode electrodes. The fuel cell operating conditions are: H_2/O_2 (2/9.5 stoic.), 80°C, 100% RH, 150 kPa_{abs} back pressure. Nafion® NRE 212 membrane is used as the electrolyte.

Table 1. Summary of support stability test (5,000 potential cycles between 1.0 and 1.5 V) and catalyst durability test (30,000 potential cycles between 0.6 and 1.0 V) for Pt*/ACCS-2 and commercial Pt/C catalysts. The catalyst durability of commercial PtCo/C catalyst is also shown for comparison.

Catalyst/Test	Particle size (nm)	Mass activity loss (%)		ECSA (m^2/g_{Pt})		Cell voltage loss (mV)
		Initial	Final	Initial	Final	$\Delta V_{iR\text{-}free}$
Pt*/ACCS-2 Support Stability	3.7	**0.341**	**0.171 (50% loss)** (5k cycles)	**30.5**	**23.9 (22% loss)** (5k cycles)	**8 mV loss** at 1.5 A/cm^2 (5k cycles)
Catalyst Durability	3.7	**0.344**	**0.189 (45% loss)** (30k cycles)	**30.1**	**17.4 (42% loss)** (30k cycles)	**24 mV loss** at 0.8 A/cm^2 (30k cycles)
Commercial Pt/C Support Stability	2.2	**0.18**	**0.047** (**74% loss**) (5k cycles)	**59.8**	**11.0 (82% loss)** (5k cycles)	No activity (5k cycles)
Catalyst Durability	2.2	**0.18**	**0.075** (**58% loss**) (30k cycles)	**62**	**13.6 (78% loss)** (30k cycles)	No activity (30k cycles)
Commercial PtCo/C Support Stability	-	-	-	-	-	-
Catalyst Durability	4.5	**0.38**	**0.116 (69% loss)** (30k cycles)	**68**	**14.3 (79% loss)** (30k cycles)	No activity at 0.8 A/cm^2 (30k cycles)

Catalyst Durability (0.6-1.0 V Cycling)

Figure 4 shows the H_2-Air fuel cell performance of Pt*/ACCS-2 catalyst tested in 25-cm^2 MEA subjected to 0.6-1.0 V potential cycling test. The Pt*/ACCS-2 catalyst showed an initial current density of 1.85 A/cm^2 at 0.6 $V_{iR\text{-}free}$ with a potential loss **of 24 mV (iR-free) at 0.8 A/cm^2** after 30,000 potential cycles between 0.6 and 1.0 V. As shown in Table, the commercial 46% Pt/C showed no activity after 30,000 cycles. For comparison, the H_2-air fuel cell performance of commercial 46% PtCo/C catalyst is shown in Fig. 5. The commercial 46% PtCo/C catalyst showed an initial current density of 936 mA/cm^2 at 0.6 $V_{iR\text{-}free}$ and no activity after 30,000 potential cycles (0.6-1.0 V).

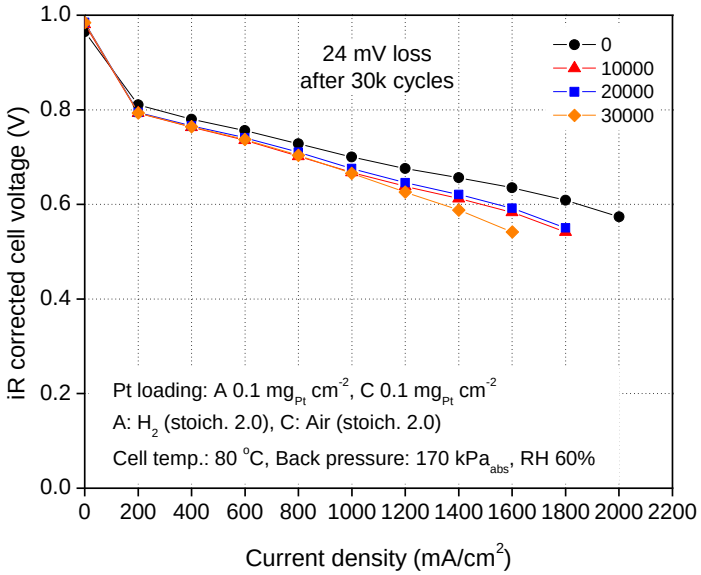

Figure 4. Comparison of H_2/air fuel cell performance of 30% Pt*/ACCS-2 catalyst subjected to 30,000 potential cycles between 0.6 and 1.0 V at 50 mV/s. Catalyst loading is 0.1 mg_{Pt}/cm^2 on both the anode and cathode electrodes. The fuel cell operating conditions are: H_2/air (2/2 stoic.), 80 °C, 60% RH, 170 kPa_{abs} back pressure. Nafion® NRE 212 membrane is used as the electrolyte.

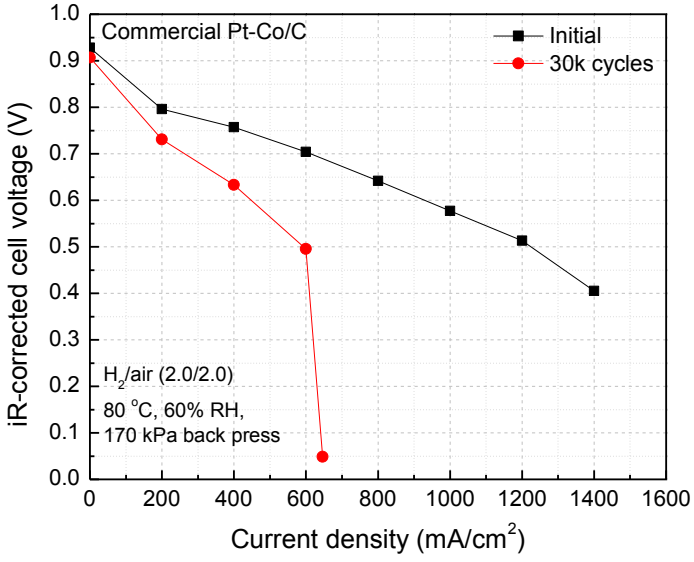

Figure 5. Comparison of H_2/air fuel cell performance of commercial 46% PtCo/C catalyst subjected to 30,000 potential cycles between 0.6 and 1.0 V at 50 mV/s. Catalyst loading is 0.1 mg_{Pt}/cm^2 on both the anode and cathode electrodes. The fuel cell operating conditions are: H_2/air (2/2 stoic.), 80 °C, 50% RH, 170 kPa_{abs} back pressure. Nafion® NRE 212 membrane is used as the electrolyte.

Figure 6 shows initial mass activity of 0.344 A/mg_{Pt} and the stability of mass activity for the Pt^*/ACCS-2 catalyst subjected to potential cycling between 0.6 and 1.0 V. The catalyst durability test resulted in **45% mass activity loss after 30,000 cycle**s. The commercial 46% Pt/C and 46% PtCo/C catalysts showed initial mass activities of 0.18 and 0.38 A/mg_{Pt} and loss of 58% and 69% after 30,000 cycles (Table 1).

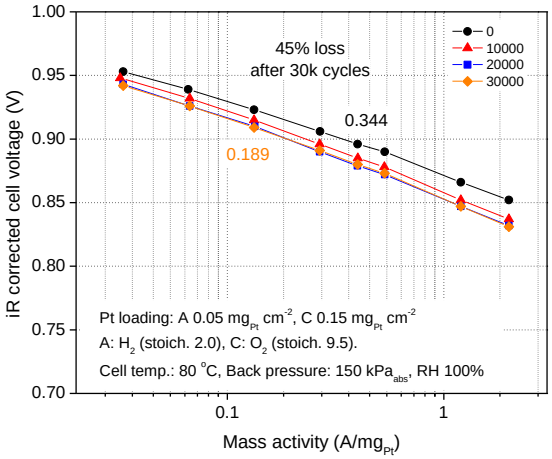

Figure 6. Stability of mass activity of Pt^*/ACCS-2 catalyst subjected to 30,000 potential cycles between 0.6 and 1.0 V at 50 mV/s. The catalyst loading is 0.1 mg_{Pt}/cm^2 on both the anode and cathode electrodes. The fuel cell operating conditions are: H_2/O_2 (2/9.5 stoic.), 80°C, 100% RH, 150 kPa_{abs} back pressure. Nafion® NRE 212 membrane is used as the electrolyte.

MEA Fabrication for Independent Evaluation at NREL

Based on the reproducibility results, five 25 cm^2 MEAs were fabricated using Pt*/ACCS-2 as cathode catalyst for independent evaluation at NREL. These four MEAs were activated and their initial H_2-air fuel cell performances (1.76, 1.72, 1.66, 1.66, and 1.69 A/cm^2 at 0.6 $V_{iR\text{-}free}$ for MEA#1, #2, #3, #4, and #5 respectively) and mass activities (0.334, 0.341, 0.348, 0.331, and 0.349 A/mg_{Pt} for MEA#1, #2, #3, #4, and #5 respectively) were measured as shown in Fig. 7 and Fig. 8, respectively.

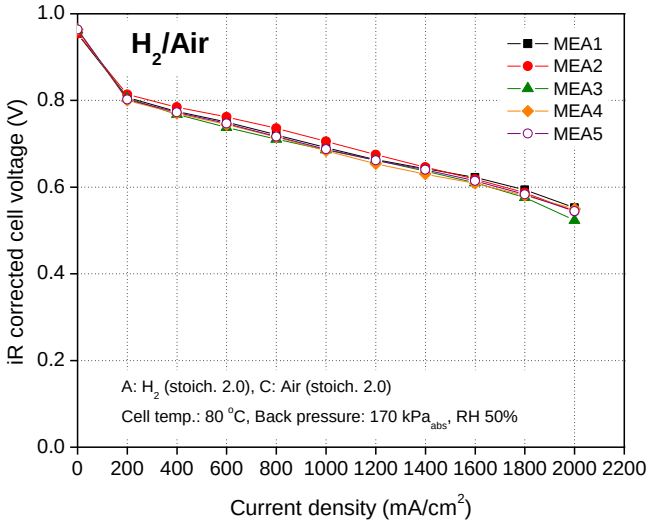

Figure 7. Comparison of initial H_2/air fuel cell performances of 30% Pt*/ACCS-2 catalyst in five MEAs assembled in fuel cell hardware for further evaluation at NREL. Catalyst loading is 0.1 mg_{Pt}/cm^2 on both the anode and cathode electrodes. The fuel cell operating conditions are: H_2/air (2/2 stoic.), 80 °C, 50% RH, 170 kPa_{abs} back pressure. Nafion® NRE 212 membrane is used as the electrolyte.

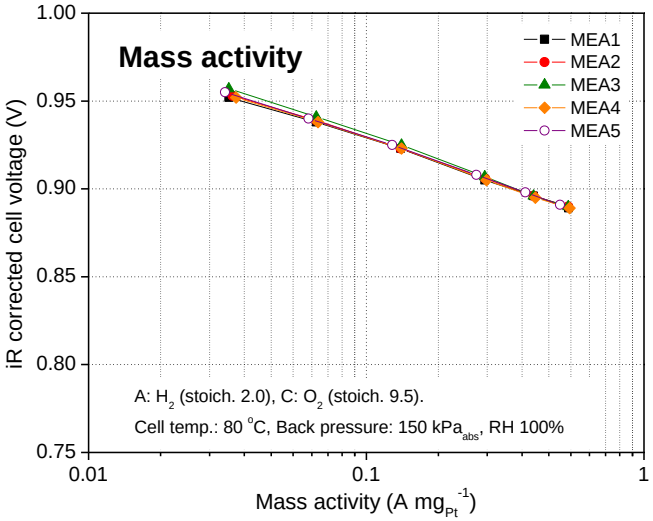

Figure 8. Comparison of initial mass activities of 30% Pt*/ACCS-2 catalyst in five MEAs assembled in fuel cell hardware for further evaluation at NREL. Catalyst loading is 0.1 mg_{PGM}/cm^2 on both the anode and cathode electrodes. The fuel cell operating conditions are: H_2/O_2 (2/9.5 stoic.), 80°C, 100% RH, 150 kPa_{abs} back pressure. Nafion® NRE 212 membrane is used as the electrolyte.

References

1. Wonsuk Jung, Tianyuan Xie, Taekeun Kim, Prabhu Ganesan, Branko N. Popov, Highly Active and Durable Co-Doped Pt/CCC Cathode Catalyst for Polymer Electrolyte Membrane Fuel Cells, *Electrochim. Acta*, **167**, (2015) 1-12.
2. T. Xie, W.S. Jung, T. Kim, P. Ganesan, B.N. Popov, Development of Highly Active and Durable Hybrid Cathode Catalysts or Polymer Electrolyte Membrane Fuel Cells, *J. Electrochem. Soc*., **161** (2014) F1489-F1501.
3. T. Kim, T. Xie, W.S. Jung, F. Gadala-Maria, P. Ganesan, B.N. Popov, Development of Catalytically Active and Highly Stable Catalyst Supports for Polymer Electrolyte Membrane Fuel Cells, *J. Power Sources*, **273**, (2015) 761-774.
4. Taekeun Kim and Branko N. Popov, Development of highly-active and stable Pt/C catalyst for polymer electrolyte membrane fuel cells under simulated start-up/shut-down cycling, **In Press**, *Int. J. Hyd. Energy*, Dec 2015.
5. Ákos Kriston, Tianyuan Xie, David Gamliel, Prabhu Ganesan, Branko N. Popov, "Effect of Ultra-Low Pt Loading on Mass Activity of PEM Fuel Cells," *J. Power Sources*, **243** (2013) 958-963.
6. Akos Kriston, Tianyuan Xie, Prabhu Ganesan, Branko N. Popov, "Effect of Pt Loading on Mass and Specific Activity in PEM Fuel Cells," *J. Electrochem. Soc*., **160** (2013) F406-F412.
7. Ákos Kriston, Tianyuan Xie and Branko N. Popov, "Impact of Ultra-low Platinum loading on Mass Activity and Mass Transport in H_2-Oxygen and H_2-Air PEM Fuel Cells," *Electrochim. Acta*, **121** (2014) 116-127.

FINAL NREL REPORT

USC Pt*/ACCS-2 Catalyst and Support Evaluation Studies at NREL

Submitted to

Dr. Branko N. Popov
University of South Carolina
301, Main Street, Dept. Chem. Eng. Room 2C02
Swearingen Engineering Center
Columbia, SC 29208
Phone (803) 777-7314
Fax: (803) 777-8265
Email: popov@cec.sc.edu

by

K.C Neyerlin, Jason Zack, Shyam Kocha
National Renewable Energy Laboratory
15013 Denver West Parkway
Golden, CO 80401.
Dr. Shyam Kocha
Phone: (303) 275-3937
Email: Shyan.Kocha@nrel.gov

October 2016

NREL
NATIONAL RENEWABLE ENERGY LABORATORY

NREL–USC
Active Durable Catalyst Project
(Pt*/ACCS-2 catalyst)

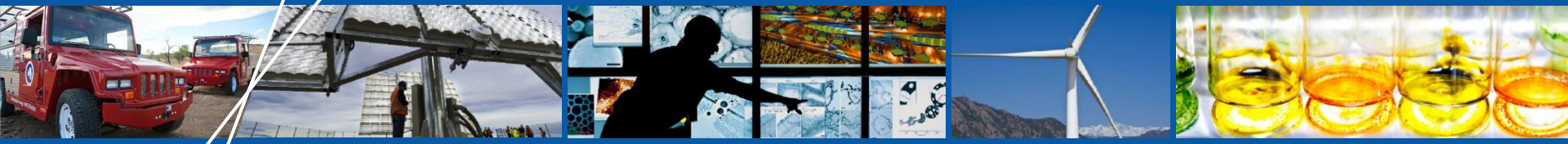

Report 2

KC Neyerlin, Jason Zack, Shyam Kocha

October 2016

NREL is a national laboratory of the U.S. Department of Energy, Office of Energy Efficiency and Renewable Energy, operated by the Alliance for Sustainable Energy, LLC.

NREL-USC Project Timeline

- SOW and TSA/Fund-in paperwork was commenced in January 2015.
- Contract was signed in October 2015
- NREL and USC compared their cell hardware, soft-goods and test protocols.
- First installment of funds arrived at NREL in the last week of December 2015
- After resolution of measurement differences between labs, USC submitted 2 subscale fuel cells completely assembled to NREL for evaluation
- NREL has completed the evaluation of the first catalyst and submitted Report-1
- USC provided NREL with MEAs with their second catalyst.
- NREL has evaluated the second set of MEAs with USC advanced catalyst for ORR activity and H_2-Air performance and durability. The results are presented in this final report.

Beginning of Life Performance (BOL)

30% Pt*/ACCS-2 catalyst
Pt* stands for suppressed platinum lattice catalyst synthesized with Co doped platinum

H_2-O_2 Curves and ORR Activity

USC ORR Activity Results from their Report

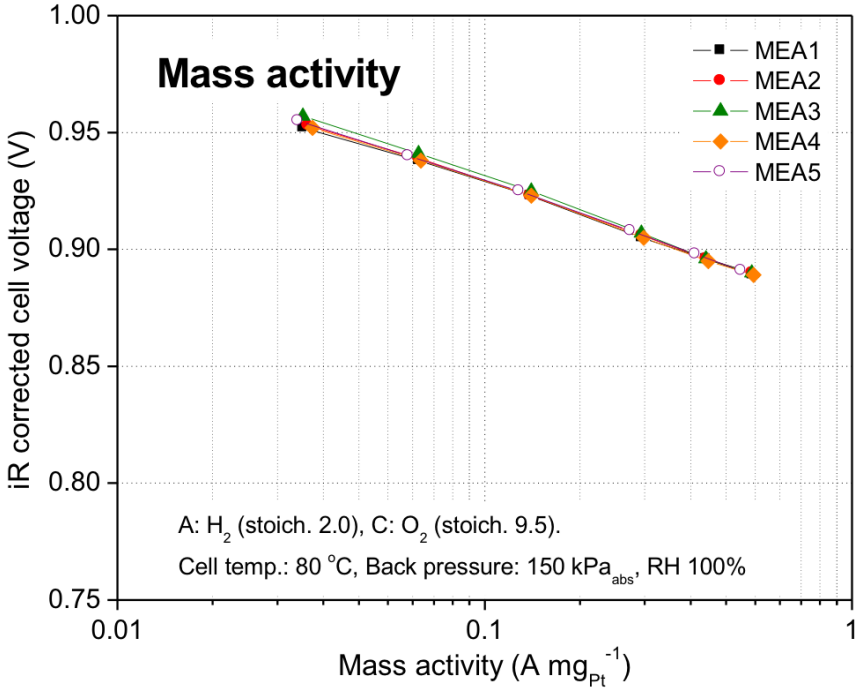

Figure 8. Comparison of initial mass activities of 30% Pt*/ACCS-2 catalyst in five MEAs assembled in fuel cell hardware for further evaluation at NREL. Catalyst loading is 0.1 mg_{PGM}/cm^2 on both the anode and cathode electrodes. The fuel cell operating conditions are: H_2/O_2 (2/9.5 stoic.), 80° C, 100% RH, 150 kPa_{abs} back pressure. Nafion® NRE 212 membrane is used as the electrolyte.

ORR Activity Results @NREL

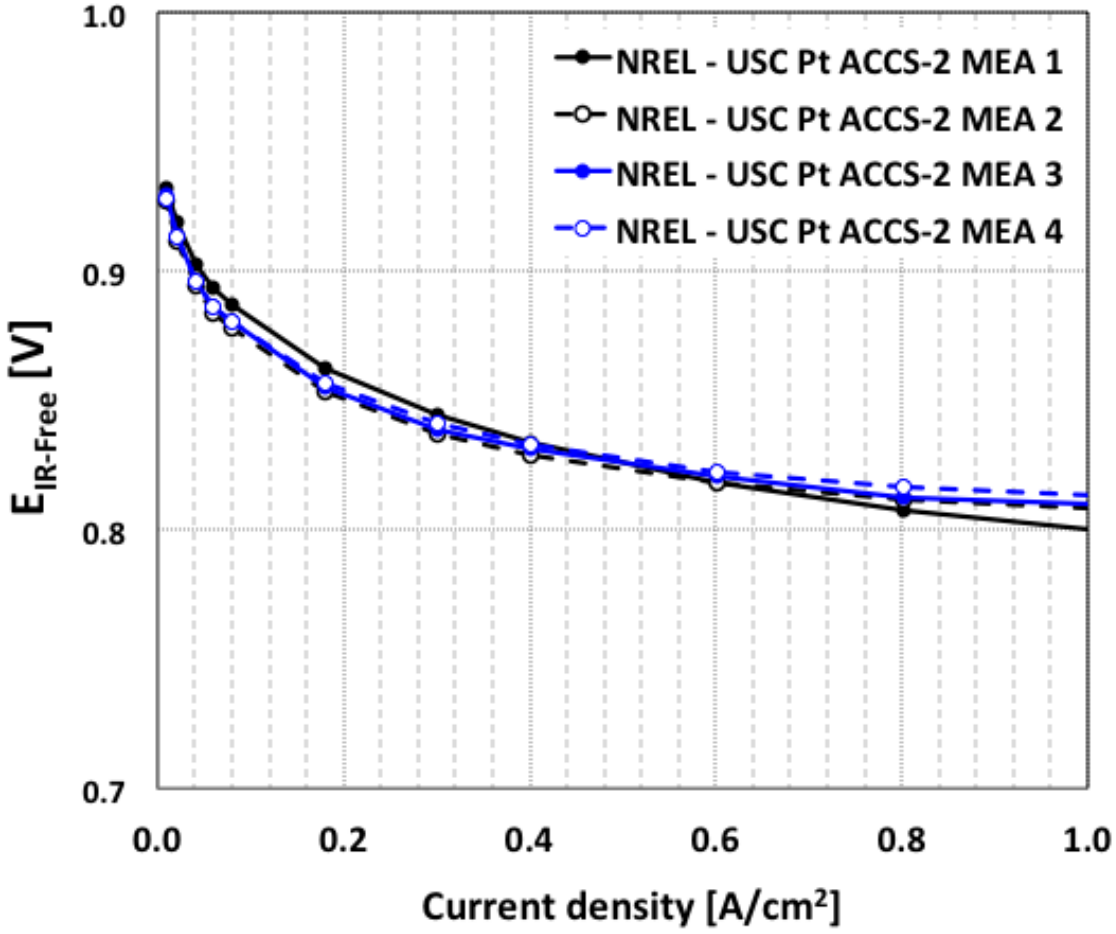

4 USC MEAs were tested at NREL referred to as: MEA1, MEA2, MEA3, MEA4.

ORR Activity of USC MEAs @ 0.90 V

#	MA NREL	MA USC	SA NREL	ECA NREL
MEA1	503	334	714	70.4
MEA2	364	341	707	51.4
MEA3	387	348	655	59
MEA4	389	331	552	70.4

MA= mA/mg_{Pt}; SA= $\mu A/cm^2Pt$; ECA= m^2/g_{Pt}

Results for ORR activity between labs are comparable. MA values measured at NREL are slightly higher.

Beginning of Life Performance (BOL)

30% Pt*/ACCS-2 catalyst
Pt* stands for suppressed platinum lattice catalyst synthesized with Co doped platinum

H_2-Air I-V Curves

USC H_2-Air Results from their Report

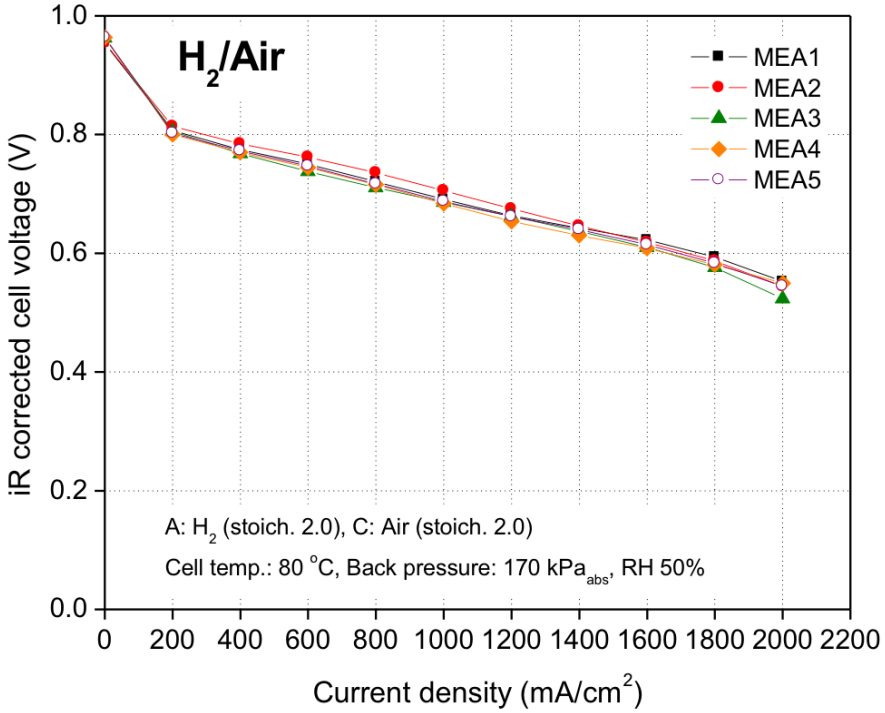

Figure 7. Comparison of initial H_2/air fuel cell performances of 30% Pt*/ACCS-2 catalyst in five MEAs assembled in fuel cell hardware for further evaluation at NREL. Catalyst loading is 0.1 mg_{Pt}/cm^2 on both the anode and cathode electrodes. The fuel cell operating conditions are: H_2/air (2/2 stoic.), 80 ° C, 50% RH, 170 kPa_{abs} back pressure. Nafion® NRE 212 membrane is used as the electrolyte.

H_2-Air Results @ NREL

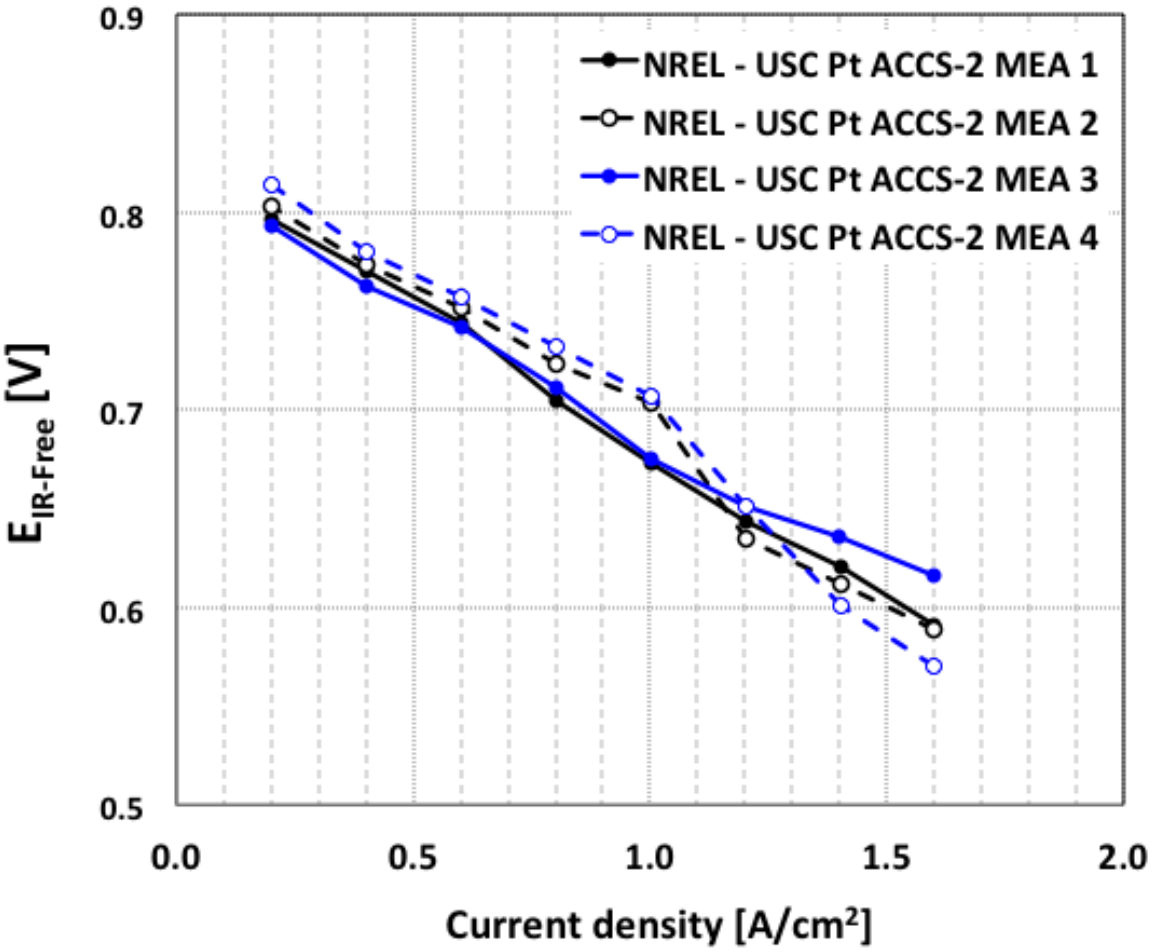

4 USC MEAs were tested at NREL referred to as: MEA1, MEA2, MEA3, MEA4.

Durability Studies

30% Pt*/ACCS-2 catalyst

Pt* stands for suppressed platinum lattice catalyst synthesized with Co doped platinum

1–1.5V Potential Cycling

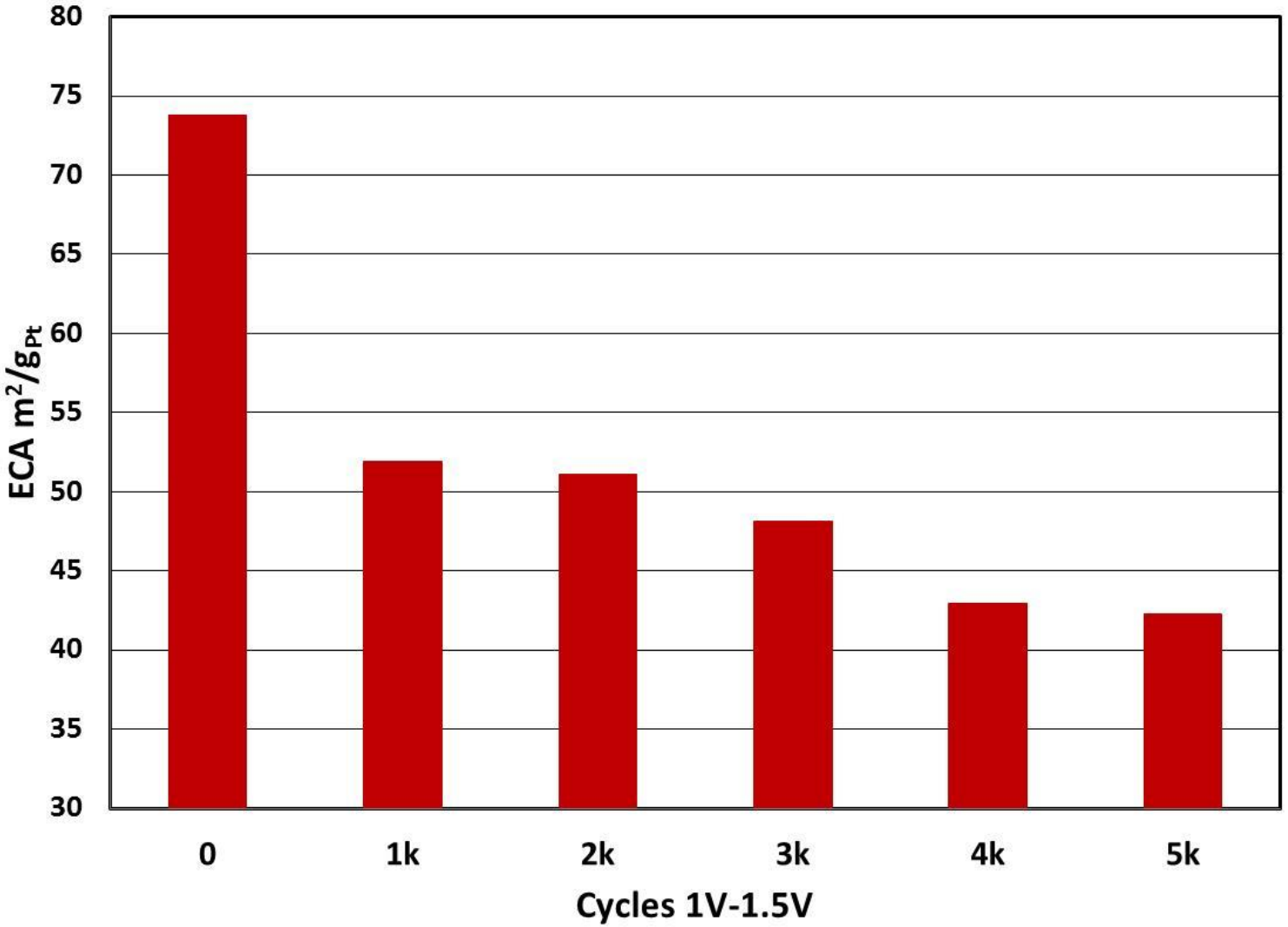

ECA losses versus number of cycles.

1–1.5V Potential Cycling

100% RH H_2/O_2 150 kPa, 80°C

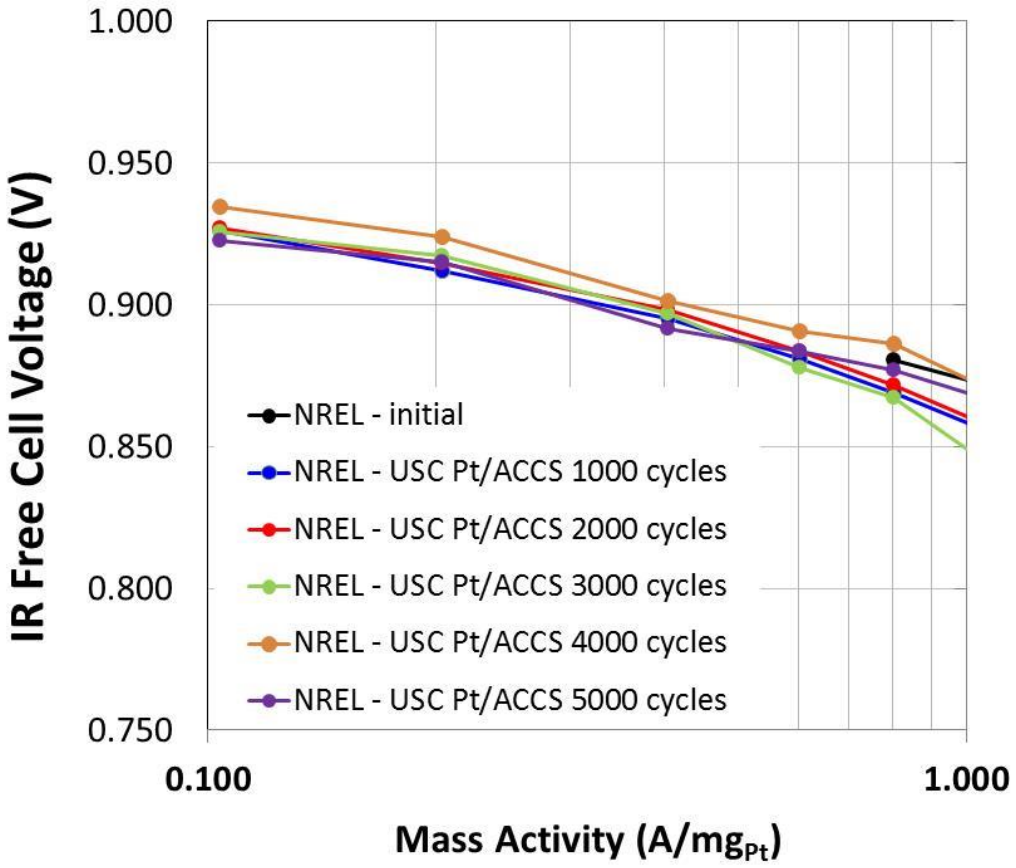

ORR activity losses versus number of cycles. Minimal losses observed.

1–1.5V Potential Cycling

40% RH H_2/Air 150 kPa, 80°C

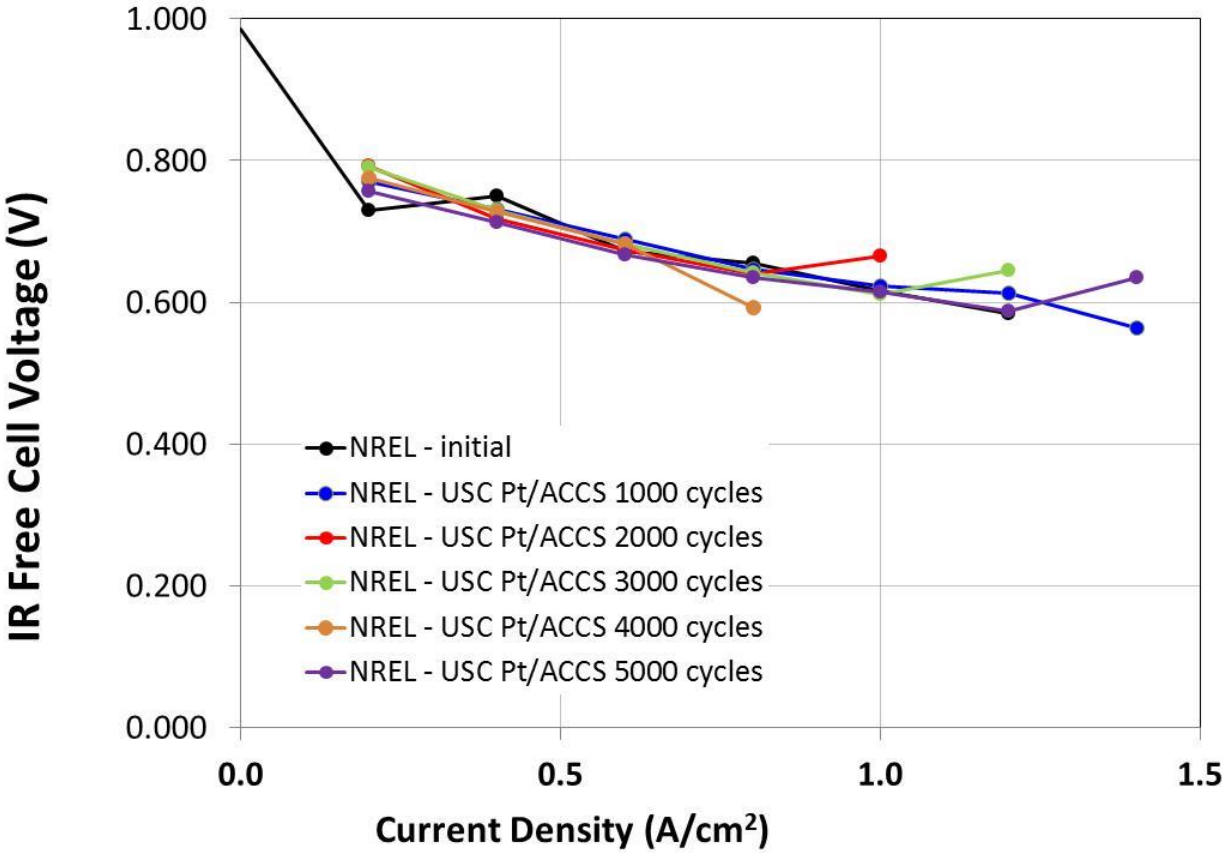

Performance losses versus number of cycles. Minimal losses observed.

0.6–1.0V Potential Cycling

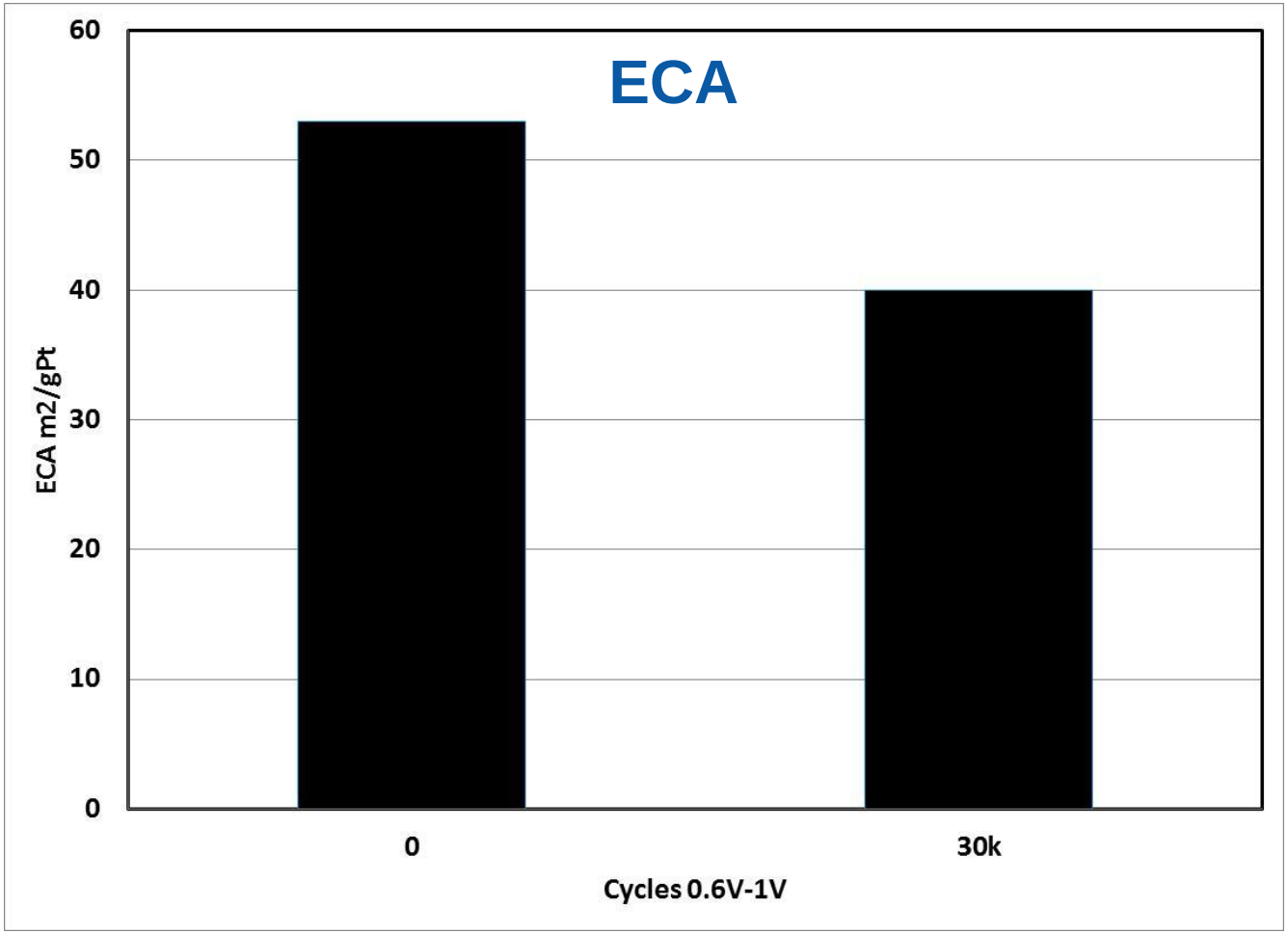

ECA losses @ BOL and @ 30,000 cycles

0.6–1.0V Potential Cycling

H_2/O_2 150 kPa, 80°C, 100%RH

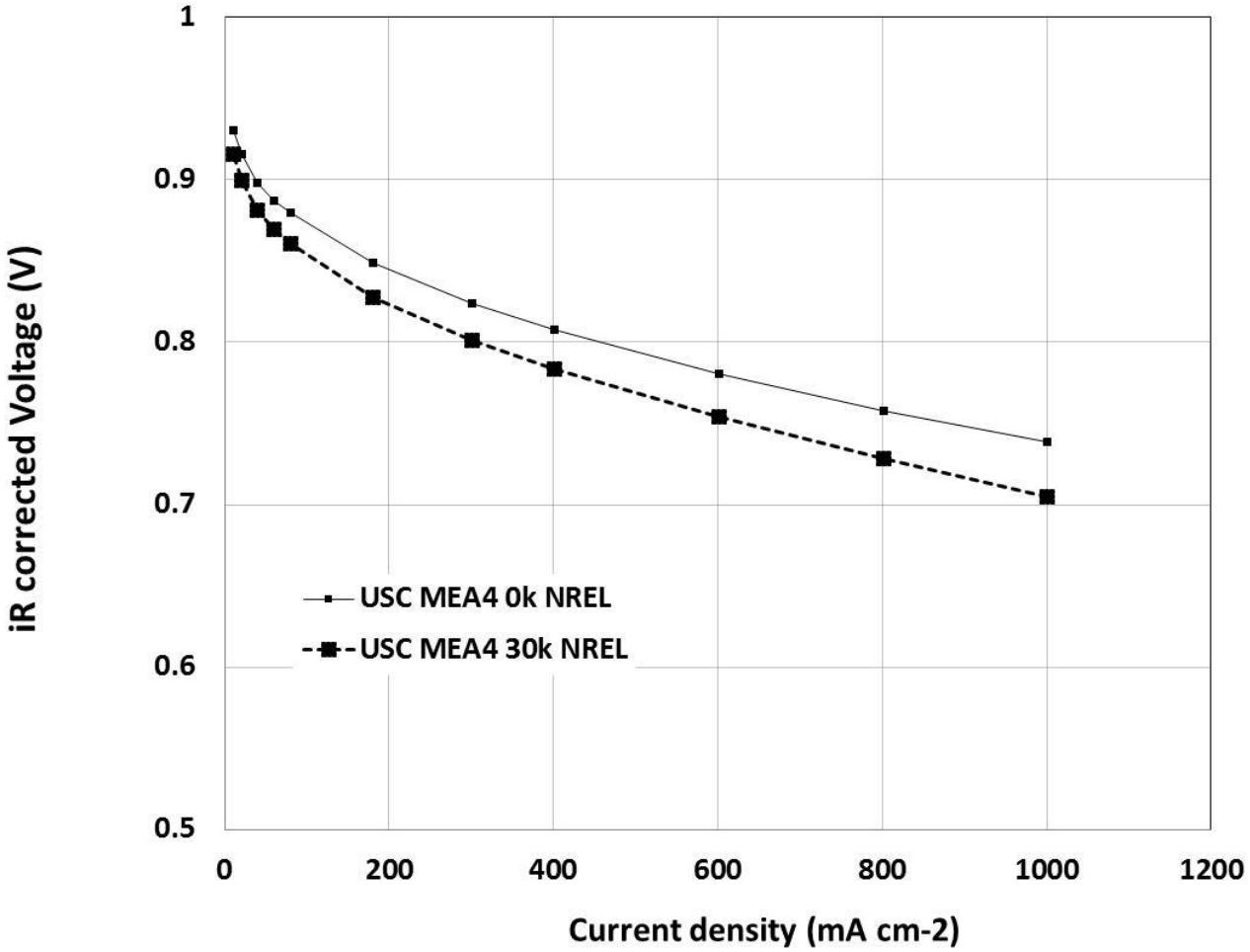

ORR activity losses @ BOL and 30,000 cycles.

0.6–1.0V Cycling

H_2/Air 150 kPa, 80°C, 60%RH

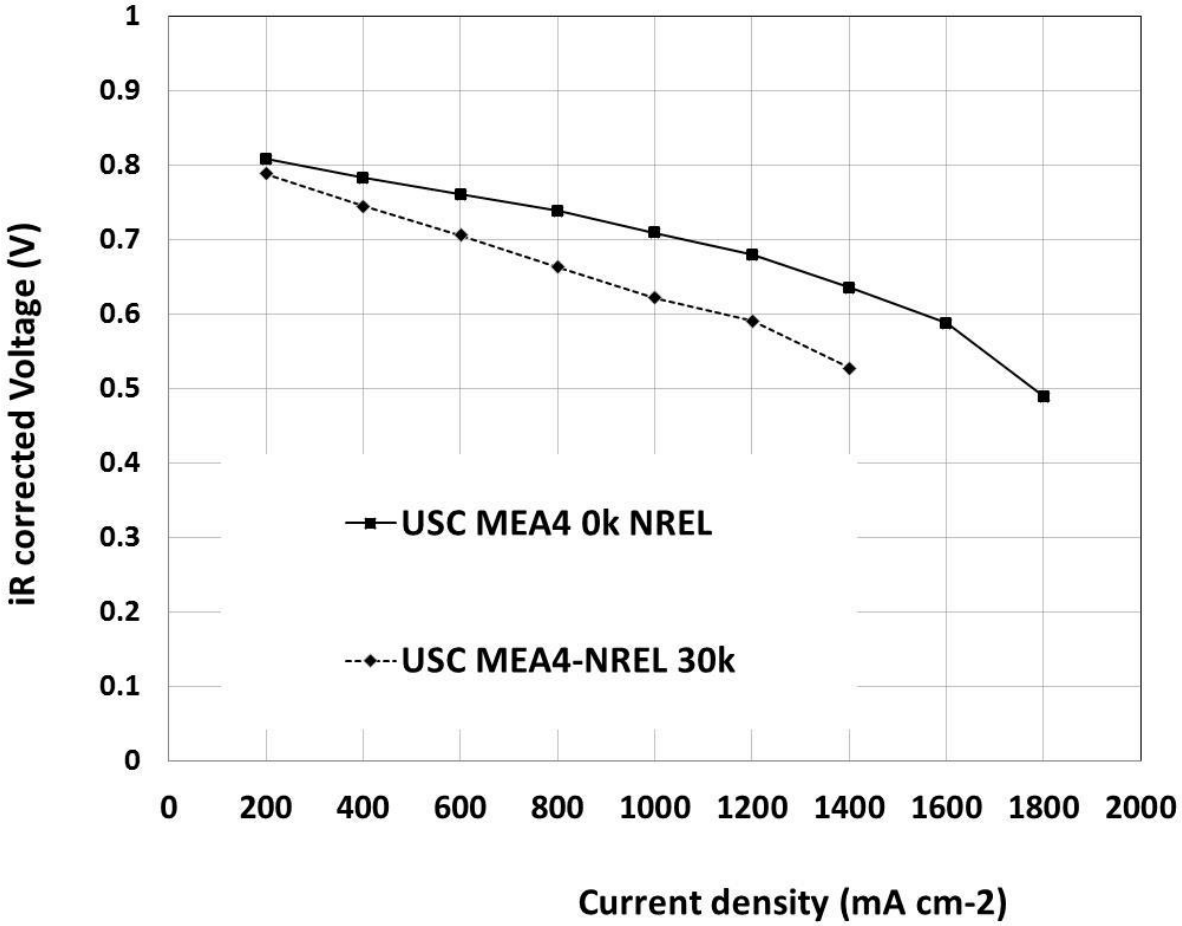

Performance losses @BOL and 30,000 cycles.

Summary Pt-ACCS-2

NREL

Catalyst/Test	Particle size (nm)	Mass activity (A/mg_{Pt})		ECSA (m^2/g_{Pt})		Cell voltage loss (mV)
		Initial	Final	Initial	Final	$\Delta V_{iR\text{-}free}$
Pt/ACCS-2 Support Stability		**0.339**	**0.295 (13% loss)** (5k cycles)	**74**	**42 (43% loss)** (5k cycles)	**no loss** at 1.2 A/cm^2 (5k cycles)
Catalyst Durability		**0.455**	**0.213 (54% loss)** (30k cycles)	**53**	**40 (24% loss)** (30k cycles)	**88 mV loss** at 1.2 A/cm^2 (30k cycles)

Summary Pt-ACCC

NREL

Catalyst/Test	Particle size (nm)	Mass activity (A/mg_{Pt})		ECSA (m^2/g_{Pt})		Cell voltage loss (mV)
		Initial	Final	Initial	Final	$\Delta V_{iR\text{-}free}$
Pt/A-CCC Support Stability	2.9	**0.23**	**0.238 (no loss)** (5k cycles)	**60**	**37 (38% loss)** (5k cycles)	**12, 35 mV loss** at 1.4, 1.6 A/cm^2 (5k cycles)
Catalyst Durability	2.9	**0.212**	**0.055 (74% loss)** (30k cycles)	**54**	**24 (56% loss)** (30k cycles)	**123 mV loss** at 0.8 A/cm^2 (30k cycles)

Summary

Initial ORR activity and performance of USC MEAs Pt*/CCS-2 under oxygen and air, evaluated at NREL, were comparable to that measured and reported by USC in their report.

Identical operating conditions and similar protocols were used in both labs.

Cyclic durability studies indicate that the Pt*/CCS-2 catalyst has minimal losses in activity and performance under 1–1.5V potential cycling indicating a robust corrosion resistant support.

The support for Pt*/CCS-2 appears to be more durable than the Pt-ACCC catalyst.

END